

Randomness in Dissipative and Chaotic Quantum Dynamics

Pablo Martínez Azcona

pablo.martinez@uni.lu

A dissertation submitted to the Faculty of Science Technology and Medicine
of the University of Luxembourg, for the degree of Doctor of Philosophy in Physics

Supervisor: Prof. Aurélia Chenu



PhD-FSTM-2025-114
Faculty of Science, Technology and Medicine

DISSERTATION

Defence held on 17 September 2025 in Luxembourg
to obtain the degree of

DOCTEUR DE L'UNIVERSITÉ DU LUXEMBOURG EN PHYSIQUE

by

Pablo MARTINEZ AZCONA

Born on 13 September 1998 in Monzón (Huesca) (Spain)

**Randomness in Dissipative and Chaotic Quantum
Dynamics**



Affidavit / Statement of originality

I declare that this thesis:

- is the result of my own work. Any contribution from any other party, and any use of generative artificial intelligence technologies have been duly cited and acknowledged;
- is not substantially the same as any other that I have submitted, and;
- is not being concurrently submitted for a degree, diploma or other qualification at the University of Luxembourg or any other University or similar institution except as specified in the text.

With my approval I furthermore confirm the following:

- I have adhered to the rules set out in the University of Luxembourg's Code of Conduct and the Doctoral Education Agreement (DEA), in particular with regard to Research Integrity.
- I have documented all methods, data, and processes truthfully and fully.
- I have mentioned all the significant contributors to the work.
- I am aware that the work may be screened electronically for originality.

I acknowledge that if any issues are raised regarding good research practices based on the review of the thesis, the examination may be postponed pending the outcome of any investigation of such issues. If a degree was conferred, any such subsequently discovered issues may result in the cancellation of the degree.

Approved on 2025-08-21

Dissertation defense committee

Prof. Aurélia Chenu, Supervisor

University of Luxembourg

Prof. Ludger Wirtz, Chairman

University of Luxembourg

Prof. Kater Murch

Washington University in Saint Louis

Prof. Andreas Buchleitner

University of Freiburg

Prof. Massimiliano Esposito

University of Luxembourg

Abstract

This thesis studies randomness in quantum dissipative and chaotic dynamics. We first focus on a detailed study of the effect of noise in the Hamiltonian of a quantum system, going beyond the noise-average and characterizing higher moments. The main quantity we introduce is the *Stochastic Operator Variance* (SOV), which is an observable characterizing the spread of trajectories around the average evolution. Interestingly, this quantity fulfills different types of uncertainty relations and is related to quantum information scrambling through out-of-time-order correlators (OTOC). We illustrate the SOV-OTOC connection in a stochastic version of the Lipkin-Meshkov-Glick (LMG) model, which shows a positive Lyapunov exponent from an unstable saddle point. We find that under the action of the noise, this Lyapunov exponent can change sign, thus stabilizing the unstable phase of the model while destabilizing the stable one. We then study the interplay between noise and decay in a non-Hermitian Hamiltonian. The noise-average evolution follows an *antidephasing* master equation beyond Lindblad form. We characterize the purity dynamics and the steady states of this master equation, and study this new evolution in a stochastically driven version of the Dissipative Qubit. By characterizing its spectral and steady state properties, we find that there are three phases: the \mathcal{PT} unbroken, \mathcal{PT} broken, and a novel Noise Induced (NI) phase where the qubit converges to the lossy state. We further investigate the validity of our model to explain experimental data, such as the *residual damping rate* of the \mathcal{PT} unbroken phase. In the last Chapter, we study randomness as a model for chaotic dynamics. In particular, leveraging a Wigner-like surmise for the k -th neighbor level spacing distribution, we compute analytically the k -th neighbor Spectral Form Factor ($kn\text{SFF}$), which characterizes the contribution of the k -th neighbor spacings to the Spectral Form Factor (SFF). We study the properties of the individual $kn\text{SFF}$ and characterize their role in building the universal ramp of the SFF. Interestingly, we find that the very short-range and very long-range spacings are the ones that contribute the most to the extent of the ramp. We finish by discussing our results and possible pathways for further research.

Acknowledgements

This thesis represents the end of a journey that has transformed me in more ways than I can tell. I am eternally grateful to all the people who have accompanied and helped me through it. Let this be my thank you to all.

I must begin by thanking my supervisor, Prof. Aurélia Chenu, for her unconditional and enthusiastic support throughout this journey, and for teaching me to always try to understand every detail to the core in a simple way. Your guidance has shaped me both as a scientist and as a person. *Je te remercie enormement pour ton encouragement pendant ces quatre ans.*

I am also very grateful to Prof. Tomáš Mančal at Charles University for welcoming me to Prague, a city that continues to fascinate me. You have shown me an example of a scientist who understands *almost* everything about a particular system or phenomenon, without forgetting about other disciplines of human knowledge, *Moc děkuji Tomáši!*

I also sincerely thank Prof. Adolfo del Campo, who has inspired me scientifically in so many ways and motivated me to always think above and beyond the current state of knowledge. *Muchas gracias Adolfo!*

I am also indebted to my collaborators, who have shaped my research and approach to life. I am grateful to Dr. Aritra Kundu for the countless inspiring discussions we had, for sharing with me his exhaustive—“*statistical-physics-like*” as he likes to call it—approach to physics, and for teaching me to only trust something that you checked through many different methods. I must also sincerely thank Dr. Ruth Shir for her thorough work, for teaching me her skepticism, and for showing me to be grateful for each discussion. I am indebted to Dr. Apollonas Matsoukas for being an older brother in physics and life, especially through his *golden rules*, for helping me survive through the inner workings of the scientific system, and for always steering me towards interesting scientific and personal discoveries. And a big thank you to the “*quantum wizard*” of Luxembourg, Dr. Matthieu Sarkis, for having helped me regain the spark for physics, for the many *melon pain*, and for showing me the beauty in the vastness of the physics that I don’t know (yet). I am also indebted to my other collaborators: Dr. Pratik Nandy, Prof. Anatoly Dymarsky, Prof. Avadh Saxena, and Prof. Alexandre Tkatchenko for their invaluable contributions to our work, and for sharing with me their approach to science.

To my friends and colleagues in Luxembourg and Prague: Leonce Dupays, Nicoletta Carabba, Federico Roccati, Federico Balducci, Niklas Hörnedal, Dan Allan, Jing Yang, Müge Doğanay, Clara, Meggy Šimčáková, Oskar Prosniak, Alice Prosniak, Komal Kumari, Mat-

teo Massaro, Kasturi Ranjan-Swain, Gaetano Sammartino, András Grabarits, Seongho Sinn, Sean Shieu, Preethi Gopalakrishnan, Eva Taupeau and Maximilian Meyer-Mölleringhof which have shared part of this journey with me. Whether in Tramways, Gudde Wellen, Vzorkovna, get-togethers at home, or even in Las Vegas, each of you has shared with me a part of your world and has shaped the person I am today. Muchas gracias también a mis amigos de Monzón, Zaragoza y Bilbao por siempre acogerme con los brazos abiertos sin importar cuanto tiempo haya pasado.

This PhD has allowed me to see parts of the world in many conferences: Bad Honnef, Zaragoza, Dresden, Paris, Las Vegas, Prague, Torun, Bielefeld, Dublin, Lindau, Chania, and Tenerife. I am grateful to each participant, speaker, and organizer for making each of them a unique experience, and especially to everyone I have discussed with, shared dinner or a drink, you have enlarged my view of physics both as a discipline and as a community. I am genuinely grateful to Aurelia for giving me the opportunity to attend them, and particularly to the *Fonds Nationales de la Recherche* for sponsoring my participation in the *Lindau Nobel Laureate meeting*, which was the most inspiring of them all.

I am also grateful to Aurelia Chenu, and Aritra Kundu for reading different parts of this thesis and to Prof. Kater Murch, Prof. Andreas Buchleitner, Prof. Ludger Wirtz, and Prof. Massimiliano Esposito for being part of the thesis jury. Lastly, a big thank you to Prof. Peter Rabl for offering me a postdoctoral position in Munich. I am looking forward to working with you!

A mi familia, Mamá, Papá, Sergio, Yayo Marcelino, Yaya Tere, Yayo Paco y Yaya Juanita, a todos mis primos y primas, tíos y tías—en especial Marimar por ser mi guía en el mundo académico—muchísimas gracias por vuestro apoyo y amor incondicional, y por siempre haberos preocupado por mi. Si he podido llegar aquí es gracias a todo vuestro esfuerzo, en la panadería, en la fábrica y en casa, y a vuestra eterna generosidad. And lastly, to Pooja Deerpalsing—*mi Poojita*— my most beautiful coincidence in Luxembourg, *mo contan twa*. Thank you for always having my back in each step of life, for making my heart happier than ever, for building a home together far from home, and for—along with the rest of the Deerpalsing family—giving me a gentle push along the right path when I needed it most.

Publications related to this thesis

This thesis is based on the following publications:

- **P. Martinez-Azcona**, A. Kundu, A. del Campo, A. Chenu
Stochastic Operator Variance: An Observable to diagnose noise and Scrambling
Physical Review Letters 131, 160202 (2023) [1] *Chapter 2*
- **P. Martinez-Azcona**, A. Kundu, A. Saxena, A. del Campo, A. Chenu
Quantum Dynamics with Stochastic Non-Hermitian Hamiltonians
Physical Review Letters 135, 010402 (2025) [2] *Chapter 3*
- **P. Martinez-Azcona**, R. Shir, A. Chenu
Decomposing the Spectral Form Factor
Physical Review B 111, 165108 (2025) [3] *Chapter 4*

During the PhD studies, the author has also published the following articles/preprints related to the topics of the thesis, but which will not be discussed in great depth

- **P. Martinez-Azcona**, A. Chenu
Analyticity constraints bound the decay of the Spectral Form Factor
Quantum 6, 852 (2022) [4]
- P. Nandy, A.S. Matsoukas-Roubeas, **P. Martinez-Azcona**, A. Dymarsky, A. del Campo
Quantum Dynamics in Krylov Space: Methods and Applications
Physics Reports, Vols. 1125–1128 Pg. 1-82 (2025) [5]
- R. Shir, **P. Martinez-Azcona**, A. Chenu
Surmise for random matrices' level spacing distributions beyond nearest-neighbors
arXiv:2504.20134 [6]
- **P. Martinez-Azcona**, M. Sarkis, A. Tkatchenko, A. Chenu
Magic steady state production: Non-Hermitian and Stochastic pathways
arXiv:2507.08676 [7]

List of acronyms

CPTP	Completely Positive Trace Preserving
TP	Trace Preserving
SFF	Spectral Form Factor
OTOC	Out of Time Ordered Correlator
FOTOC	Fidelity Out of Time Ordered Correlator
SOV	Stochastic Operator Variance
qSOV	quantum (noise) Stochastic Operator Variance
GKSL	Gorini Kossakowski Sudarshan Lindblad
OQS	Open Quantum Systems
SDQ	Stochastic Dissipative Qubit
SME	Stochastic Master Equation
SDE	Stochastic Differential Equation
NH	Non Hermitian
DM	Density Matrix
TD	Trace Decreasing
RMT	Random Matrix Theory
GOE	Gaussian Orthogonal Ensemble
GUE	Gaussian Unitary Ensemble
GSE	Gaussian Symplectic Ensemble
LMG	Lipkin Meshkov Glick
sLMG	stochastic Lipkin Meshkov Glick
NI	Noise Induced
DFS	Decoherence Free Subspace
DW	Double Well (Phase)
SW	Single Well (Phase)
LEP	Liouvillian Exceptional Point
EP	Exceptional Point
SQUID	Superconducting QUantum Interference Device
BGS	Bohigas Giannoni Schmit
nnLS	nearest neighbor Level Spacing
knLS	k -th neighbor Level Spacing
knSFF	k -th (nearest) neighbor Spectral Form Factor
SSE	Stochastic Schrödinger Equation

Contents

Abstract	v
Acknowledgements	vi
Publications related to this thesis	viii
List of acronyms	ix
Invitation to Randomness in Quantum Dynamics	xv
1 Introduction	3
1.1 Some basic notions of Quantum Information	3
1.1.1 Quantum Channels	3
1.1.2 Fidelity between states	4
1.2 Different approaches to model Open Quantum Systems	5
1.3 Gorini-Kossakowski-Sudarshan-Lindblad Equation	6
1.3.1 Vectorization of superoperators	7
1.3.2 The adjoint GKSL equation	7
1.4 Classical noise Hamiltonians	8
1.4.1 On the different conventions of Stochastic Calculus	10
1.4.2 Itô calculus	11
1.4.3 Stratonovich calculus and Novikov's theorem	12
1.4.4 Dynamics generated by a stochastic Hamiltonian	12
1.5 Non Hermitian Hamiltonians	15
1.5.1 Parity-Time Symmetry	17
1.5.2 Interlude: Quantum Jumps and Continuous Quantum Measurements	18
1.5.3 Non-Hermitian Hamiltonians from Continuous Measurements . . .	20
1.6 A crash course in Random Matrix Theory	23
1.6.1 Definition of Gaussian Random Matrix Ensembles	24
1.6.2 Unfolding the spectrum	27

1.7	Founding Conjectures of Quantum Chaos	30
1.7.1	Berry Tabor conjecture	30
1.7.2	Bohigas Giannoni Schmitt conjecture	31
1.8	Other measures of spectral Statistics	32
1.8.1	Short range: Spacing ratios	32
1.8.2	Long range: Number variance	33
1.9	Spectral Form Factor	33
1.9.1	The many faces of the Spectral Form Factor	33
1.9.2	Connected SFF	35
1.10	Out of Time Order Correlators	37
1.10.1	General definition of the OTOC	37
1.10.2	Connection to the classical limit: A semiclassical argument	38
1.10.3	A Lyapunov exponent does not imply chaos	39
1.10.4	On averaging and different OTOCs	40
1.10.5	The bound on chaos	40
1.10.6	Dissipative OTOC	41
2	Stochastic Operator Variance	45
2.1	A story for the results of this chapter	46
2.2	The Stochastic Operator Variance	50
2.2.1	Mathematical properties of the SOV	54
2.2.2	Comparison to the Variance over state	54
2.2.3	The SOV as an operation on replicated Hilbert spaces	55
2.3	SOV uncertainty relation	57
2.3.1	An operator version of the SOV uncertainty relation	59
2.3.2	Example: Stochastic Frequency Harmonic Oscillator	60
2.4	Higher order moments and cumulants	61
2.5	Steady states of the SOV	62
2.5.1	General expression in terms of conserved quantities	62
2.5.2	Example: Two qubit dissipation	64
2.6	SOV-OTOC connection	66
2.6.1	Dephasing case: Classical noise	66
2.6.2	General GKSL case: Quantum noise	68
2.6.3	Finding different OTOC's	70
2.6.4	Properties of Dissipative OTOC's	71

2.7	The Stochastic Lipkin Meshkov Glick model	73
2.7.1	Quantum stochastic LMG	73
2.7.2	Classical stochastic LMG model	78
2.8	Conclusions	86
2.8.1	Open Questions	87
3	Stochastic Non Hermitian Hamiltonians	91
3.1	Introducing Stochastic Non-Hermitian Hamiltonians	92
3.1.1	A story for the results of this chapter	92
3.1.2	Why studying Stochastic Non-Hermitian Hamiltonians?	93
3.2	Dynamics under general anti-hermitian fluctuations	96
3.2.1	The unnormalized Stochastic Master Equation	96
3.2.2	Imposing Trace Preservation	97
3.2.3	Antidephasing master equation in Stratonovich sense	100
3.2.4	Gauge transformations of the antidephasing master equation	101
3.2.5	Evolution of the purity	103
3.2.6	Long time dynamics: Steady states	104
3.3	The Stochastic Dissipative Qubit	110
3.3.1	Evolution of the Purity	113
3.3.2	Spectral and steady state Properties	114
3.3.3	Bloch sphere dynamics	126
3.3.4	Transitions between the different phases of the model	135
3.3.5	Dynamics of the SDQ	140
3.3.6	Approach to steady states	145
3.4	Single trajectory dynamics	146
3.4.1	General Equation of motion	146
3.4.2	Single trajectory dynamics of the SDQ	148
3.4.3	Noise-Induced phase in No-Pump dynamics	151
3.4.4	Justifying Trace Preservation at average level	153
3.5	Experimental results	155
3.5.1	Possible experimental implementations of the Stochastic Dissipative Qubit	155
3.5.2	Modelling noise in the Dissipative Qubit	157
3.6	Discussion	161
3.6.1	Comparison to other dynamics	161
3.6.2	What did we learn in this chapter?	163

3.6.3	Open Questions	166
4	Decomposing the spectral form factor	169
4.1	Introduction	170
4.1.1	A story for the results	170
4.1.2	Why do we decompose the SFF?	172
4.2	A Wigner-surmise for the k -th neighbor level spacing distribution	173
4.2.1	Validity of the generalized Wigner-like surmise	175
4.3	The k -th neighbor SFF	176
4.3.1	The ensemble averaged kn SFF	177
4.3.2	kn SFF for Gaussian Random Matrices	179
4.3.3	kn SFF for the Poisson ensemble	182
4.3.4	Comparison with the disordered XXZ spin chain	184
4.4	Properties of the k -th neighbor SFF	185
4.4.1	Minimum and minimum time	186
4.4.2	Deepest kn SFF	190
4.4.3	The kn SFF is not self-averaging	194
4.5	Building the full SFF	196
4.5.1	The partial SFF	196
4.5.2	Contribution from even and odd neighbors	200
4.5.3	The full SFF	201
4.5.4	What is the simplest form of the kn SFF which gives rise to a ramp?	206
4.6	A dissipative protocol to measure the kn SFF	210
4.7	Conclusion	212
4.7.1	Open questions	213
5	Discussion	217
A	Numerical solution of Stochastic Differential Equations	221
A.1	Euler-Maruyama	221
A.2	Stochastic Runge-Kutta	221
A.3	Kloeden-Platen	222

An Invitation to Randomness in Quantum Dynamics

This thesis deals with several different aspects of *randomness* in quantum dynamics. The physical world around us has a vast amount of information and fine details. However, for the purpose of modeling a particular physical phenomenon, most of this complexity is discarded, leaving only the most relevant degrees of freedom. This *reductionist* approach has been very fruitful in the past, leading to some of our best and most accurate physical theories, such as *quantum mechanics*. Precisely starting from the quantum world, we can find two objections to this reductionist approach:

- The first objection, related to the ineludible presence of an environment, comes purely from the Nature of quantum systems. Classical systems are also surrounded by an environment that leads to different phenomena, such as your coffee cooling down after some time. However, in quantum systems, the presence of an environment has a much more drastic effect due to *decoherence*. Decoherence is the physical phenomenon by which quantum systems lose some of their quantum properties and transition to an effective classical behavior, such as Schrodinger's famous cat. In its typical setup, the box containing the cat and the poison is assumed to be completely opaque. But what if the box were to be made slightly transparent? Then, some of the information from the inside would be available to an observer, and we might be able to infer whether the cat is alive or dead. This process removes the *quantum* superpositions in which the cat is dead and alive simultaneously, rendering a classical state in which the cat is either dead or alive with 50% probability. For this reason, decoherence has been proposed as a mechanism for the *emergence of the classical world* [8].

To explain this phenomenon, it becomes essential to add an extra element to the description of the relevant degrees of freedom, by either modifying the equation of motion from the Schrödinger equation to a *master equation* such as the Gorini-Kossakowski-Sudarshan-Lindblad (GKSL) equation, or by adding an element of randomness to describe the effect of external sources which interact with the system of interest — be it an environment such as a bath or an observer.

- The second, even stronger, objection to reductionism, which is ubiquitous in *Condensed Matter* and *Statistical Mechanics*, is that of *emergence*. In essence, this scientific approach poses that the whole is more than the sum of its parts, or in *Anderson*'s words “*more is different*” [9]. At every scale of complexity, collective phenomena emerge that cannot be understood as a simple combination of the be-

havior of their building blocks, e.g., knowledge of the behavior of individual spins does not explain the existence of ferromagnetism, or an understanding of human biology does not suffice to describe the behavior of societies. In this spirit, when many individual agents, be it spins, molecules, or humans, *interact* with each other, their collective behavior can change drastically and give rise to new behavior.

Understanding the interactions between many different quantum systems in quantum mechanics represents the current frontier in *many-body* quantum systems. The challenge is that very few systems are analytically tractable, sometimes only in certain restricted cases, and their exact numerical solution involves an exponentially large Hilbert space, rendering the large N limit extremely challenging to reach. The way randomness appears in complex, many-body systems is even more puzzling. Importantly, randomness leads to some universality classes, only dependent on the system's symmetries, and vastly different systems behave similarly.

These two arguments highlight the need to go beyond a reductionist approach, and motivate the two main fields that this thesis explores, namely *Open Quantum Systems* and *Quantum Chaos*.

These two fields are particularly timely, as they are important for the state of the art in quantum information. The great efforts to build a quantum computer go mainly in two directions¹: (i) *counter-act* the effects of noise on qubits, through quantum error-correction [10] or error mitigation schemes [11], and (ii) to scale up the quantum systems, by having more and more qubits, which can be controlled.

Noise, Chaos and Dissipation

“*Randomness*”, as highlighted in the title of this thesis, provides a common denominator to all the different facets of this work. The first instance of randomness we will consider is *randomness in time*, which we will call *noise*. It will be used to model dissipation, and then crafted to unveil new possible dissipative dynamics. A second instance of randomness will be in the generator of the dynamics, connecting with the theory of *Random Matrices* (RMT). In this context, the system's model (i.e., the Hamiltonian) is unknown but instead sampled from an ensemble of Hamiltonians. Surprisingly, this approach captures many of the universal features of chaotic and integrable systems. A third instance where randomness will appear is as *local disorder*. In some models we will study, introducing

¹There is actually a third key direction, that of *quantum algorithms*, which investigates what tasks can be performed more efficiently on a quantum computer.

local random parameters can drastically change their behavior, allowing us to witness a transition from chaotic to integrable dynamics.

These three sources of randomness can lead to vastly different phenomena. Figure 1 sketches the main results and concepts introduced in this thesis.

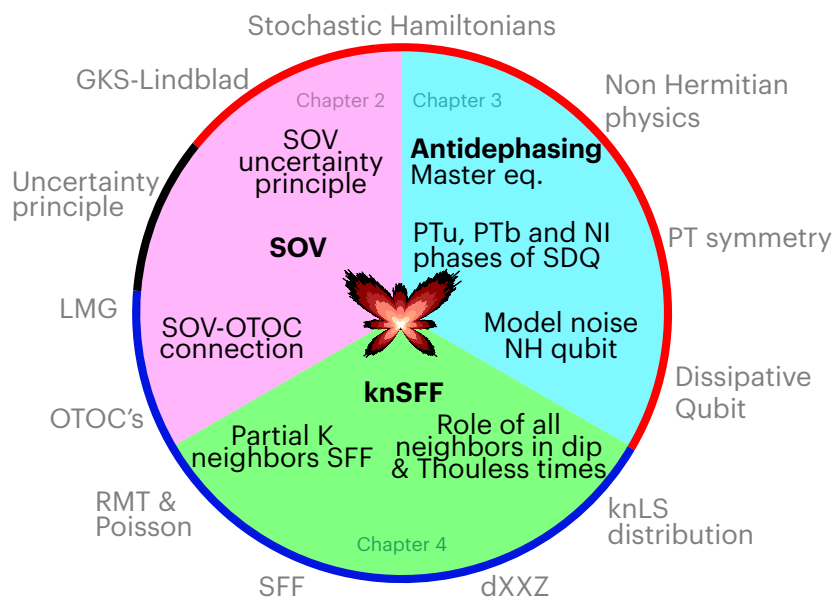


Figure 1. Conceptual map of the main results. The topics outside of the circle represent basic concepts and models on which the current thesis builds, which will be introduced in Chapter 1. The three sections of the circle represent the three chapters, along with their main results, introduced in the thesis. The outer circle denotes the parts of the thesis which deal mainly with Open Quantum Systems theory (red), Quantum Chaos and Information scrambling (blue), and standard Quantum Mechanics (black).

- **Chapter 1** will introduce the formalism to model the different sources of randomness that we consider. In doing so, we will introduce the main concepts related to *Open Quantum Systems* and *Quantum Chaos*. These include all the concepts outside the circle in Fig. 1.
- In **Chapter 2** we will study *noise as a model for dissipation*, and consider *Stochastic Hamiltonians*. Extending beyond the main approach in the field, we introduce tools to study quantities beyond the noise-average. The main quantity that we introduce is the *Stochastic Operator Variance* (**SOV**) [1], which, interestingly, fulfills an *uncertainty principle* analogous to the one obeyed by the quantum mechanical vari-

ance, and is connected to *Out-of-Time-Order Correlators* (**OTOC**'s), which define a quantum version of the Lyapunov exponent.

- In **Chapter 3** we will focus on the *effect of noise on dissipation*. In particular, we study the dynamics generated by non-Hermitian Hamiltonians, which are also subject to noise in their imaginary part, modeling noisy dissipation. Averaging over the noise, we find an exotic *anti-dephasing* master equation [2]. We illustrate our results on the Stochastic Dissipative Qubit (**SDQ**), which exhibits three distinct phases: \mathcal{PT} unbroken, \mathcal{PT} broken, and Noise-Induced. Furthermore, we study the **SDQ** as a model for the noise in the experimental realization of the non-Hermitian qubit.
- In **Chapter 4**, we will explore randomness as a model for many-body interacting systems. In particular, we consider the Random Matrix Theory description of the universal features of quantum chaotic systems and study the role played by the k -th neighbor level spacing distribution in the Spectral Form Factor (**SFF**), through the k -th neighbor SFF (**knSFF**) [3]. We compute exact and approximate analytical expressions for this quantity, study the properties of individual **knSFF**'s, and show how neighbors further apart participate in building the universal ramp of the **SFF**.

Purpose of the thesis

Physics is the study of the rules of Nature. Every human has an intuition of how certain physical properties of the natural world work, particularly those properties at our length and time scales, e.g., a kid knows how to get a ball through a hoop way before anyone teaches them Newton's laws of motion. Physics is a formalization of that intuitive understanding, which allows us to predict properties at scales outside what any human has experienced. For this reason, it should be possible to explain in simple terms the main results of physical theories, even those usually deemed hard to understand. To this end, one should be able to build a story from the developed formalism. Such a story cannot contain all the details, but it should keep the fundamental message and conceptual ideas. Indeed, the greatest physical theories often come with intriguing stories that can spark curiosity in anyone. For example, in Quantum Mechanics, fundamental concepts such as superposition, the uncertainty principle, or even path integrals can be distilled into a simple, yet puzzling, story. In the latter case, the story associated to path integrals can even be used to *quantitatively* explain phenomena in the natural world, as famously done in Feynman's *QED* book [12], which does not sacrifice the predictive power of the

theory while telling a simple, yet strange, story. With its hectic publication pace, the current academic system rarely offers space to build these stories. For this reason, and to be able to answer the ultimate question: “*What have you done in your thesis?*” I will complement the presentation of results with stories that explain them. In particular, each of the chapters contains a prelude where I build a simple story of one of the concepts or main results in a way aimed at being accessible to a non-physicist audience. To make the thesis reading easier, we compartmentalize it; each main chapter starts with a small abstract and finishes with a recap of the results.

Chapter 1

An Introduction to the theory of Open Quantum Systems and Quantum Chaos

After motivating the driving force behind this thesis, randomness as an essential concept in our understanding of the quantum world around us, we now present the technical formulation of the theories of *Open Quantum Systems* and *Quantum Chaos*. We focus primarily on introducing the techniques used in the thesis, so that the calculations in the future chapters can be understood. This means that the level of rigour varies throughout this chapter, due to two key mathematical fields used throughout the thesis: *Stochastic Calculus* and *Random Matrix Theory*. We introduce them with their proper mathematical definitions, and use them later in a less rigorous way, focusing on deriving results, rather than rigour. This chapter is structured as follows: we first introduce some basic notions of quantum information, comment on the different approaches to open quantum systems, and then introduce the Gorini-Kossakowski-Sudarshan-Lindblad (**GKSL**) master equation. We then introduce stochastic Hamiltonians as a simple, yet powerful, model for open quantum systems, and non-Hermitian Hamiltonians as an effective model for nonunitary dynamics. We then turn to the second field, Quantum Chaos, we begin by introducing random matrix theory, which lays the ground to introduce the founding conjectures of quantum chaos, we then introduce other measures of spectral statistics before focusing on a particularly relevant one for us, the *spectral form factor* (**SFF**), we finish by introducing another key quantity for the theory of quantum chaos, the *out of time order correlator* (**OTOC**) and the quantum Lyapunov exponent.

1.1 Some basic notions of Quantum Information

1.1.1 Quantum Channels

The most general *quantum channel* is given by a Completely Positive Trace Preserving (**CPTP**) linear map $\mathcal{E} : \mathcal{L}(\mathcal{H}) \rightarrow \mathcal{L}(\mathcal{H})$ [13, 14]. We now review what each of the properties means:

- A linear map fulfills the property $\mathcal{E}(a\hat{\rho} + b\hat{\sigma}) = a\mathcal{E}(\hat{\rho}) + b\mathcal{E}(\hat{\sigma})$, where $a, b \in \mathbb{C}$, $\hat{\rho}, \hat{\sigma} \in \mathcal{L}(\mathcal{H})$.

- A linear map is said to be *positive* if all positive semi-definite states $\hat{\rho} \geq 0 \mapsto \mathcal{E}[\hat{\rho}] \geq 0$ are mapped to positive semi-definite states.
- A linear map is said to be *completely positive* if the map $\mathcal{E} \otimes \text{id}_n[\bullet] : \mathcal{L}(\mathcal{H}) \otimes \mathbb{C}^{n \times n} \rightarrow \mathcal{L}(\mathcal{H}) \otimes \mathbb{C}^{n \times n}$ is positive for all n .
- A linear map is *trace preserving* if $\text{Tr}(\hat{\rho}) = \text{Tr}(\mathcal{E}[\hat{\rho}]) = 1$.

A quantum channel is therefore the most general linear map which takes valid quantum states $\hat{\rho}$, and takes them to valid quantum states, that is, positive semi-definite and with unit trace. The requirement of complete positivity implies that enlarging the system considered to have an ancilla of an arbitrary dimension n does not spoil the positivity of the channel. Owing to the **CPTP** properties, the most general quantum channel can be written in Kraus form as

$$\mathcal{E}[\bullet] = \sum_{j=1}^{N_K} \hat{K}_j \bullet \hat{K}_j^\dagger, \quad (1.1)$$

where the set of Kraus operators is $\{\hat{K}_j\}_{j=1}^{N_K}$, $N_K \leq d^2$ is the number of Kraus operators and they are subject to the constraint $\sum_{j=1}^{N_K} \hat{K}_j^\dagger \hat{K}_j = \hat{\mathbb{1}}$ which imposes Trace Preservation of the dynamics.

A notation comment is now in order: throughout the thesis we denote quantum states through the ket notation $|\psi\rangle \in \mathcal{H}$, vectors in a different vector space are generally denoted by bold-face, e.g. \mathbf{r} , we denote *operators*—that send states to states $\hat{O}|\psi\rangle = |\psi'\rangle$ —with a hat \bullet , we reserve the calligraphic letters $\mathcal{E}, \mathcal{L}, \dots$ to denote *superoperators*—which send operators to operators $\mathcal{E}[\hat{\rho}] = \hat{\rho}'$. The *Script* font $\mathcal{H}, \mathcal{L}(\mathcal{H}), \dots$ is used to denote more abstract concepts such as vector spaces. The *Fraktur* font is used as an auxiliary font to denote other objects, such as probability distributions $\mathfrak{P}(\bullet)$, or the noise average of \hat{A}_t as $\hat{\mathfrak{A}}_t$, lastly $\mathbb{E}(\bullet)$ denotes the average over the noise. In contrast, $\langle \bullet \rangle$ denotes the expectation value over a quantum state. Throughout the thesis, we work in natural units $\hbar = 1$, unless explicitly used to highlight the role of Planck's constant.

1.1.2 Fidelity between states

In many tasks in the field of quantum information science, we need to measure how close are two different states. One quantity that characterizes this is the *fidelity* F . Given two quantum states $|\psi\rangle \in \mathcal{H}$ and $|\phi\rangle \in \mathcal{H}$, the fidelity between the two is simply given by

$$F_{\psi,\phi} := |\langle \psi | \phi \rangle|^2, \quad (1.2)$$

which can take values from zero to one, $0 \leq F_{\psi,\phi} \leq 1$, with unity when both states coincide $F_{\psi,\psi} = 1$ and zero when they are orthogonal.

In the most general case, the fidelity between two density matrices $\hat{\rho} \in \mathcal{L}(\mathcal{H})$ and $\hat{\sigma} \in \mathcal{L}(\mathcal{H})$ is given by the *Uhlmann fidelity* [15, 16]

$$F_{\hat{\rho}, \hat{\sigma}} := \text{Tr} \left(\sqrt{\sqrt{\hat{\rho}} \hat{\sigma} \sqrt{\hat{\rho}}} \right)^2. \quad (1.3)$$

The density matrices are positive semidefinite $\hat{\rho} \geq 0$; thus, the square root and fidelity are well defined.

1.2 Different approaches to model Open Quantum Systems

The theory of Open Quantum Systems (OQS) provides the mathematical formalism to describe quantum systems interacting with their environment [17, 18]. There are two main approaches to this end, adopted by different communities.

- The *microscopic* approach: Here, one considers a particular (idealized) model for the environment. The “full universe” is thus partitioned into the *system* and the *bath*. We associate a Hilbert space to each of these: \mathcal{H}_S for the system and \mathcal{H}_B for the bath. Since we consider the full System + Bath to be closed, it evolves unitarily, and its states live in the product space $\mathcal{H}_{SB} = \mathcal{H}_S \otimes \mathcal{H}_B$. One could, in principle, solve the full Schrödinger equation of System + Bath, but this is only possible in simple cases. In practice, one tries to derive a closed equation for the dynamics of the system alone; this is what is known as a *quantum master equation* [17, 18]. Depending on the community and the reason for deriving a master equation the microscopic derivations may involve many approximations, e.g. if one wishes to achieve a **GKSL** master equation, i.e. a master equation that is guaranteed to evolve density matrices into density matrices, one needs to consider typically weak system-bath coupling, and perform the Born, Markov and rotating wave/secular approximations. Each of these approximations reduces the accuracy of the master equation as a description of the System coupled to the bath. For a recent critical re-evaluation of the approximations and assumptions in the microscopic derivation of the **GKSL** master equation, see [19]. On the other hand, performing fewer approximations, one can reach a *Redfield equation* [20, 21] which is consistently more accurate than other perturbative master equations [22], but does not generate a positive map and thus does not necessarily send density matrices to density matrices. Other microscopic approaches to derive a master equation involve the use of *Nakajima-Zwanzig* projection operators [23, 24], which project onto the relevant set of degrees of freedom, see [25] for a recent tutorial.
- The *macroscopic* approach postulates the properties of the dynamical map, to ensure certain properties, such as Complete positivity and Trace Preservation, or even time-locality of the master equation¹, which can be achieved through the *time convo-*

¹A master equation is said to be *time-local* if it only depends on the density matrix at time t $\hat{\rho}_t$ and not on the previous times, i.e. $\partial \hat{\rho}_t = \mathcal{L}_t[\hat{\rho}_t]$. Although the Markov approximation is sometimes called

lutionless approach [17, 26]. This approach is more common in the fields of quantum information and especially mathematical physics, in which the **GKSL** equation was originally derived. In the following sections, we will follow an approach more in line with this; we do not build a model for the bath and its interaction with the system, but rather postulate the evolution of the system to be a **CPTP** map, as was the original motivation. Similarly, the treatment of open quantum systems through a stochastic Hamiltonian can be thought of as macroscopic. We encode the details that would come from the bath in the correlations between the noise, which are chosen as part of our model, and do not come from microscopic information.

1.3 Gorini-Kossakowski-Sudarshan-Lindblad Equation

Consider the most general quantum channel \mathcal{E} , i.e., a **CPTP** evolution, furthermore, let us assume that the evolution is, in a reasonable sense, Markovian², i.e., memoryless. In here, for simplicity, we will consider the original framework developed by *Gorini, Kossakowski, Sudarshan* [29] and *Lindblad* [30] in which the evolution of the system is given by a *dynamical semigroup* \mathcal{E}_t . A dynamical semigroup is given by a family of quantum channels $\{\mathcal{E}_t | t \geq 0, \mathcal{E}_0[\hat{\rho}] = \hat{\rho} \forall \hat{\rho}\}$ which fulfills the *semigroup identity*

$$\mathcal{E}_{t+\tau}[\bullet] = \mathcal{E}_t[\mathcal{E}_\tau[\bullet]]. \quad (1.4)$$

The generator of the dynamical semigroup is then given by

$$\partial_t \hat{\rho}_t = \lim_{\Delta t \rightarrow 0} \frac{\mathcal{E}_{\Delta t}[\hat{\rho}_t] - \hat{\rho}_t}{\Delta t} = \mathcal{L}[\hat{\rho}], \quad (1.5)$$

where $\mathcal{L}[\bullet]$ is the *Lindbladian* or *Liouvillian* superoperator which generates the dynamical semigroup. The celebrated *Gorini, Kossakowski, Sudarshan, Lindblad* (**GKSL**) master equation thus reads

$$\partial_t \hat{\rho}_t = -i[\hat{H}, \hat{\rho}_t] + \sum_j^{N_c} \gamma_j \left(\hat{L}_j \hat{\rho}_t \hat{L}_j^\dagger - \frac{1}{2} \{ \hat{L}_j^\dagger \hat{L}_j, \hat{\rho}_t \} \right) =: \mathcal{L}[\hat{\rho}], \quad (1.6)$$

where $N_c \leq \dim(\mathcal{H})^2 - 1$ is the number of decoherence channels, the unitary evolution is described by the Hamiltonian $\hat{H} \in \mathcal{B}(\mathcal{H})$, and the dissipative evolution is characterized

the time-local approximation, a time-local master equation need not be Markovian. Such an equation can always be formally derived if the map $\mathcal{E}_t[\hat{\rho}]$ can be inverted as $\partial_t \hat{\rho}_t = \dot{\mathcal{E}}[\mathcal{E}^{-1}[\hat{\rho}_t]]$, see [26] for an explicit example of this construction for a single qubit.

²The subject of quantum (non) Markovianity is a fascinating field of study, about which we will not be concerned much in this thesis. In the main text we follow the standard approach by **GKSL**, let us digress on other definitions of Markovianity. A notion which generalizes the classical notion from one-point probabilities is that of *divisibility* of the channel [27], i.e. $\mathcal{E}_{t_3 \leftarrow t_1} = \mathcal{E}_{t_3 \leftarrow t_2} \circ \mathcal{E}_{t_2 \leftarrow t_1}$ for $t_3 \geq t_2 \geq t_1$. This leads to a master equation of Lindblad form with positive time-dependent rates $\gamma_k(t) \geq 0$. However, there is a whole hierarchy [28] of definitions of quantum non-Markovianity.

by the *jump operators*³ $\{\hat{L}_j \in \mathcal{B}(\mathcal{H})\}_{j=1}^{N_c}$, and $\{\gamma_j \geq 0\}_{j=1}^{N_c}$ are the decay rates. The **GKSL** master equation can always be formally solved as

$$\mathcal{E}_t[\hat{\rho}] = e^{\mathcal{L}t}[\hat{\rho}]. \quad (1.7)$$

Note that, however, this formal solution is analogous to stating that the solution of the Schrödinger equation is the propagator $e^{-i\hat{H}t}$; it is a formal statement, but we do not necessarily know an efficient way to compute the matrix exponential, especially for large-dimensional Hilbert spaces.

1.3.1 Vectorization of superoperators

There is an extra caveat which makes the solution of the **GKSL** equation more involved. \mathcal{L} is a superoperator, i.e., an object that acts on both sides of the state $\hat{\rho}$, while \hat{H} has an obvious expression as a matrix; a priori, \mathcal{L} does not. We want to find a matrix associated with the superoperator for many purposes, including implementing this formal solution as we will do in the forthcoming chapters.

There are many approaches to this end, such as the *Choi-Jamolkowski* isomorphism [33, 34]. In here, we will introduce a vectorization procedure such that operators become vectors as

$$\hat{\rho} = \sum_{i,j} \rho_{ij} |i\rangle\langle j| \in \mathcal{L}(\mathcal{H}) \mapsto |\rho\rangle = \sum_{i,j} \rho_{ij} |i\rangle \otimes |j\rangle^* \in \mathcal{H} \otimes \mathcal{H}, \quad (1.8)$$

which means that a density matrix may be understood as a state on two copies of the Hilbert space. The superoperator $\mathcal{S}[\bullet]$ can be mapped to an operator as

$$\begin{aligned} \mathcal{S}[\hat{\rho}] = \hat{A}\hat{\rho}\hat{B} &\mapsto \check{\mathcal{S}}[\rho] = (\hat{A} \otimes \hat{B}^\top)|\rho\rangle \\ \mathcal{S} \in \mathcal{L}(\mathcal{L}(\mathcal{H})) &\mapsto \check{\mathcal{S}} \in \mathcal{L}(\mathcal{H} \otimes \mathcal{H}), \end{aligned} \quad (1.9)$$

in here we used the accent $\check{\mathcal{S}}$ to denote that the superoperator is a linear operator over the doubled Hilbert space, however in the rest of this thesis we will not make this distinction since we will either deal with superoperators or with their vectorized form, but not with both at the same time so there will not be room for confusion, by the context it will be clear whether we are dealing with the superoperator or its vectorized form.

1.3.2 The adjoint GKSL equation

Even though open quantum systems studies focus extensively on dynamics of density matrices in the Schrödinger picture, the **GKSL** master equation can also be formulated

³Lindblad [30] originally considered bounded linear operators over the Hilbert space as the allowed jump operators. In physical models of the master equation, see e.g., Quantum Brownian motion, Caldeira Legett model, etc, it is common to consider unbounded jump operators like \hat{x}, \hat{p} . The extension of the mathematical formalism to the unbounded case was studied in [31, 32]

in the Heisenberg picture for a given operator \hat{A}_t . To do this, one evaluates the evolution of the expectation value

$$\begin{aligned}\partial_t \text{Tr}(\hat{A}\hat{\rho}_t) &= \text{Tr}(\hat{A}\partial_t\hat{\rho}_t) = \text{Tr}(\hat{A}\mathcal{L}[\hat{\rho}_t]) \\ &= \text{Tr}(\partial_t\hat{A}_t\hat{\rho}_t) = \text{Tr}(\mathcal{L}^\dagger[\hat{A}_t]\hat{\rho}),\end{aligned}\quad (1.10)$$

where the second line is in the Heisenberg picture. In the case that the generator \mathcal{L} is time-independent [17], the adjoint **GKSL** master equation reads

$$\partial_t\hat{A}_t = \mathcal{L}^\dagger[\hat{A}_t] = +i[\hat{H}, \hat{A}_t] + \sum_{j=1}^{N_c} \gamma_j \left(\hat{L}_j^\dagger \hat{A}_t \hat{L}_j - \frac{1}{2} \{ \hat{L}_j^\dagger \hat{L}_j, \hat{A}_t \} \right), \quad (1.11)$$

which has changed sign in the unitary evolution, as already happens between the Liouville-von Neumann $\partial_t\hat{\rho}_t = -i[\hat{H}, \hat{\rho}_t]$ and Heisenberg $\partial_t\hat{A}_t = +i[\hat{H}, \hat{A}_t]$ equations, and where the jump term changed to $\hat{L}_j^\dagger \hat{A}_t \hat{L}_j$. This master equation can still be solved formally through the map $\mathcal{E}_t^\dagger = e^{\mathcal{L}^\dagger t}$.

1.4 Classical noise Hamiltonians

One simple way to find some master equations is to consider a classical noise source ξ_t acting on the quantum Hamiltonian. This approach was originally developed by Budini [35, 36], used to develop quantum simulators of open quantum systems in [37], and extended to general sources of noise in [38]. In this thesis we will consider *Gaussian white noise*, the Gaussianity implies that the statistics of the noise is completely determined by the first two moments $\mathbb{E}(\xi_t)$ and $\mathbb{E}(\xi_t\xi_\tau)$, since all the higher moments can be expressed in terms of the first two. The white noise property amounts to considering

$$\mathbb{E}(\xi_t) = 0, \quad \mathbb{E}(\xi_t\xi_\tau) = \delta(t - \tau). \quad (1.12)$$

The first condition imposes that the stochastic process ξ_t is driftless, the second condition implies that it is *delta-correlated*, i.e. the noise ξ_t is only correlated to the noise at the same time ξ_t , and completely uncorrelated with the noise at any other time ξ_τ with $\tau \neq t$. This property defines white noise, and it implies that the process is Markovian, i.e., it has no memory. Memory effects are described by $\mathbb{E}(\xi_t\xi_\tau) \neq 0$ for $t \neq \tau$, and this provides a powerful tool to model non-markovian effects in quantum mechanics.

The idea is to consider a noise in the Hamiltonian, i.e., a driving by the function ξ_t which is unknown. Considering the noise affecting only hermitian operators, we find the stochastic Hamiltonian

$$\hat{H}_t = \hat{H}_0 + \sum_{j=1}^{N_c} \sqrt{2\gamma_j} \xi_t^{(j)} \hat{L}_j, \quad (1.13)$$

where $\gamma_j \geq 0$ are the decay rates, \hat{H}_0 is the deterministic Hamiltonian of the system, \hat{L}_j are the jump operators which are Hermitian $\hat{L}_j^\dagger = \hat{L}_j$ and the different channels are assumed to be uncorrelated $\mathbb{E}(\xi_t^{(m)} \xi_\tau^{(n)}) = \delta_{mn} \delta(t - \tau)$. Trivially, the total Hamiltonian \hat{H}_t is Hermitian $\hat{H}_t^\dagger = \hat{H}_t$. This will be the starting point of our analysis in Chapter 2, and inspired by this construction, in Chapter 3, we will consider the case in which the total Hamiltonian \hat{H}_t is non-Hermitian $\hat{H}_t^\dagger \neq \hat{H}_t$. The interesting point of this formalism is that when we average over the noise, we can recover the **GKSL** equation for the density matrix, in particular if $\hat{H}_t^\dagger = \hat{H}_t$ the **GKSL** equation necessarily describes only dephasing processes, but going beyond Hermiticity for \hat{H}_t allows us to find the most general **GKSL** master equation. Since we aim for the future chapters to be as self-contained as possible and this chapter as merely introducing the framework and formal concepts needed for the rest of the thesis, we will present the derivation of the **GKSL** equation from stochastic Hamiltonians in Sec. 1.4.4, and repeat it in Chapt. 2 for dephasing and in Chapt. 3 for the generic case.

One of the pioneering works in the study of stochastic Hamiltonians by *Budini* [35] considered the case in which jump operators are not Hermitian, $\hat{L}_j \neq \hat{L}_j^\dagger$, but where the total stochastic Hamiltonian is still Hermitian, i.e.

$$\hat{H}_t = \hat{H}_0 + \sum_{j=1}^{N_c} \sqrt{2\gamma_j} (\zeta_t^{(j)} \hat{L}_j + \zeta_t^{(j)*} \hat{L}_j^\dagger), \quad (1.14)$$

where now the white noises are complex $\zeta_t^{(j)} \in \mathbb{C}$ and fulfills

$$\begin{aligned} \mathbb{E}(\zeta_t^{(j)}) &= \mathbb{E}(\zeta_t^{(j)*}) = \mathbb{E}(\zeta_t^{(j)} \zeta_\tau^{(k)}) = \mathbb{E}(\zeta_t^{(j)*} \zeta_\tau^{(k)*}) = 0, \\ \mathbb{E}(\zeta_t^{(j)} \zeta_\tau^{(k)*}) &= \mathbb{E}(\zeta_t^{(j)*} \zeta_\tau^{(k)}) = \delta_{jk} \delta(t - \tau). \end{aligned} \quad (1.15)$$

Note that this situation can always be mapped to the real noise case by expressing the complex noise as $\zeta_t = \frac{1}{\sqrt{2}}(\xi_t^{(R)} + i\xi_t^{(I)})$ where the real and imaginary parts are uncorrelated, i.e. $\mathbb{E}(\xi_t^{(R)} \xi_\tau^{(R)}) = \mathbb{E}(\xi_t^{(I)} \xi_\tau^{(I)}) = \delta(t - \tau)$, $\mathbb{E}(\xi_t^{(R)} \xi_\tau^{(I)}) = \mathbb{E}(\xi_t^{(I)} \xi_\tau^{(R)}) = 0$. The statistical properties of the complex noise follow from

$$\begin{aligned} \frac{1}{2} \mathbb{E}((\xi_t^{(R)} \pm i\xi_t^{(I)})(\xi_\tau^{(R)} \pm i\xi_\tau^{(I)})) &= \frac{1}{2} (\mathbb{E}(\xi_t^{(R)} \xi_\tau^{(R)}) - \mathbb{E}(\xi_t^{(I)} \xi_\tau^{(I)})) = 0, \\ \frac{1}{2} \mathbb{E}((\xi_t^{(R)} \pm i\xi_t^{(I)})(\xi_\tau^{(R)} \mp i\xi_\tau^{(I)})) &= \frac{1}{2} (\mathbb{E}(\xi_t^{(R)} \xi_\tau^{(R)}) + \mathbb{E}(\xi_t^{(I)} \xi_\tau^{(I)})) = \delta(t - \tau). \end{aligned}$$

Therefore, any classical noise, hermitian, stochastic Hamiltonian can always be written as

$$\hat{H}_t = \hat{H}_0 + \sum_{j=1}^{N_c} \sqrt{2\gamma_j} (\xi_t^{(R,j)} (\hat{L}_j + \hat{L}_j^\dagger) - i\xi_t^{(I,j)} (\hat{L}_j - \hat{L}_j^\dagger)), \quad (1.16)$$

where both operators $\hat{L}_j + \hat{L}_j^\dagger$, and $-i(\hat{L}_j - \hat{L}_j^\dagger)$ are Hermitian.

1.4.1 On the different conventions of Stochastic Calculus

The white noise that we have introduced in the previous section ξ_t has the property that when integrated, it generates a *Wiener process* $W_t \equiv \int_0^t \xi_\tau d\tau$. However, the Wiener process W_t is almost nowhere differentiable⁴, and therefore $\xi_t \equiv \frac{dW_t}{dt}$ should be the “*derivative of a non-differentiable function*”. To give a more formal and consistent formulation, we must introduce *Stochastic calculus*. In this framework, one defines the *increment of the Wiener process* dW_t , which can be related to the ξ_t noise from the previous section as $dW_t \equiv \xi_t dt$ and which integrates to the Wiener process $W_t = \int_0^t dW_\tau$. Although formally dW_t is the increment of the Wiener process, we will sometimes loosely call both W_t and dW_t the Wiener process; however, by the notation, it will be clear whether we are referring to the Wiener process itself or its increment.

The theory of stochastic calculus provides the tools to formally solve a *Stochastic Differential Equation (SDE)*, which when written in “*physicists*” or Langevin notation reads

$$\dot{x}_t = a(x_t, t) + b(x_t, t)\xi_t, \quad (1.17)$$

i.e. the evolution of the variable x is determined by a *deterministic* or *drift* part given by the function $a(x, t)$ and a *stochastic* part $b(x, t)$ which is affected by white noise ξ_t . As we have already argued, ξ_t does not have a formal meaning. Whenever we consider an *SDE*, we will write it in the form

$$dx_t = a(x_t, t)dt + b(x_t, t)dW_t. \quad (1.18)$$

Stochastic Calculus has two main approaches to deal with *SDEs*, each of them with its advantages and disadvantages:

- A formal approach to deal with *SDEs* is that of **Itō calculus**. In this convention, the Wiener process dW_t is independent of the integration variable x_t , i.e., the expectation value factorizes $\mathbb{E}(f(x_t)dW_t) = \mathbb{E}(f(x_t))\mathbb{E}(dW_t) = 0$ for any function of the stochastic process x_t . In this formalism, we have to *modify* the rules of calculus and substitute them for the Itō rules, which we will introduce in the coming section. We will mostly work in Itō convention throughout this thesis, unless explicitly denoted otherwise.
- On the other hand, **Stratonovich calculus** keeps the standard rules of calculus as we know them for deterministic functions, e.g., the chain rule still applies in the usual way. This formalism does so at a high cost: dW_t and the process x_t are *not* independent, i.e., this means that $\mathbb{E}(x_t dW_t) \neq \mathbb{E}(x_t)\mathbb{E}(dW_t)$. Instead, these averages have to be computed in a special way, which we introduce in the next subsection. A

⁴By almost we mean that the set of points in which the Wiener process is differentiable is of measure zero.

Stratonovich SDE is conventionally denoted as

$$dx_t = a(x_t, t)dt + b(x_t, t) \circ dW_t, \quad (1.19)$$

where \circ denotes that the product should be understood in the Stratonovich sense.

1.4.2 Itō calculus

In standard calculus, since we consider dt to be infinitesimally small, when we perform a Taylor expansion, we only need to keep terms of $\mathcal{O}(dt)$. All the higher order terms $\mathcal{O}(dt^n)$ with $n \geq 2$ will be much smaller than dt and thus negligible.

Itō calculus changes this approach due to the *Itō rule* which states that

$$dW_t^2 = dt. \quad (1.20)$$

From a practical point of view this means that now the terms of order $\mathcal{O}(dW_t^2)$ are of the same order as dt , and therefore we have to keep them. However, terms of order $\mathcal{O}(dW_t dt)$ or $\mathcal{O}(dW_t^n)$ with $n \geq 3$ are of higher order than dt and therefore we can neglect them.

Definition 1 (Itō integral). *Consider a function G_τ , the Itō integral is defined as*

$$\int_0^t G_\tau dW_\tau := \text{ms-lim}_{n \rightarrow \infty} \sum_{i=1}^n G_{t_{i-1}} (W_{t_i} - W_{t_{i-1}}), \quad (1.21)$$

where the function G is evaluated at the beginning of the interval t_{i-1} and the mean-squared limit $\text{ms-lim}_{n \rightarrow \infty}$ is defined as $\text{ms-lim}_{n \rightarrow \infty} X_n = X \Leftrightarrow \lim_{n \rightarrow \infty} \mathbb{E}((X_n - X)^2) = 0$.

Itō's rule is a surprising result. The Wiener process dW_t is a stochastic function, but the square of the Wiener process dW_t^2 is deterministic and equal to dt . This can be proven in several ways; here, we give the main idea of two approaches with different levels of rigour and defer the interested reader to the original references. Gardiner [39] starts from the definition of the Ito integral using a test function G_t which is required to be *non-anticipating* and shows that

$$\lim_{n \rightarrow \infty} \mathbb{E} \left(\left(\sum_{i=1}^n G_{t_{i-1}} (\Delta W_i^2 - \Delta t_i) \right)^2 \right) = 0 \Rightarrow \int G_t dW_t^2 = \int G_t dt, \quad (1.22)$$

where $\Delta W_i = W_{t_i} - W_{t_{i-1}}$ is the finite Wiener increment. Jacobs [40] shows that the variance of the sum of square Wiener increments $\text{Var}(\sum_{i=1}^n \Delta W_i^2) \sim n^{-1}$, and thus vanishes in the limit of an infinite number of time-steps n . Even more, the full probability distribution of the sum of squared Wiener increments converges to a delta function

$$\mathfrak{P} \left(\sum_{i=1}^n \Delta W_i^2 \right) \rightarrow \delta \left(\sum_{i=1}^n \Delta W_i^2 - t \right). \quad (1.23)$$

This means that the sum of squared Wiener increments is exactly t and can have no other value in the limit of infinite time steps.

An important consequence of Itō's rule is that the usual chain rule of calculus does not apply and instead we need to use *Ito's formula*, also known as Itō's lemma. Consider a generic function of the stochastic process x_t given by $y = f(x)$, its derivative is thus

$$dy = \frac{df}{dx}dx + \frac{1}{2}\frac{d^2f}{dx^2}(dx)^2, \quad (1.24)$$

where now the higher order terms $(dx)^2$ need not be negligible.

1.4.3 Stratonovich calculus and Novikov's theorem

To keep the standard rules of calculus, we need to develop the Stratonovich stochastic calculus. The basic object in this convention is *Stratonovich stochastic integral*.

Definition 2 (Stratonovich integral). *Consider a function $G_{x,\tau}$, the Stratonovich integral is defined as*

$$\int_0^t G_{x_\tau, \tau} \circ dW_\tau := \text{ms-lim}_{n \rightarrow \infty} \sum_{i=1}^n G_{\bar{x}_i, t_{i-1}} (W_{t_i} - W_{t_{i-1}}), \quad (1.25)$$

where the function G is evaluated at the intermediate point $\bar{x}_i = \frac{x_{t_i} + x_{t_{i-1}}}{2}$.

The appeal for the standard rules of calculus in the Stratonovich convention is obscured by the fact that the stochastic process x_t and the white noise are not independent. To deal with expectation values of the form $\mathbb{E}(x_t \circ \xi_t^{(n)})$ we can make use of *Novikov's theorem*, also sometimes referred to as Furutsu-Novikov formula, [41] which states that

$$\mathbb{E}(x[\xi] \circ \xi_t^{(n)}) = \sum_{m=1}^{N_c} \int_0^t d\tau \mathbb{E}(\xi_t^{(n)} \xi_\tau^{(m)}) \mathbb{E} \left(\frac{\delta x[\xi]}{\delta \xi_\tau^{(m)}} \right), \quad (1.26)$$

where the process $x[\xi]$ is a functional of the white noises $\xi_t = (\xi_t^{(1)}, \dots, \xi_t^{(N_c)})$ and $\frac{\delta x[\xi]}{\delta \xi_t^{(m)}}$ is the functional derivative of the stochastic process with respect to the m -th white noise.

1.4.4 Dynamics generated by a stochastic Hamiltonian

There are three possible approaches to finding the dynamics generated by a stochastic Hamiltonian; here, we introduce them and discuss their advantages and disadvantages. For ease of notation, let us consider the single noise case, but the approaches trivially extend to more noise sources.

Purely Stratonovich approach

When we write a stochastic Hamiltonian as

$$\hat{H}_t = \hat{H}_0 + \sqrt{2\gamma}\xi_t \hat{L}. \quad (1.27)$$

We are necessarily interpreting it in Langevin or physicist's notation, and thus ξ_t should be interpreted in Stratonovich convention. The Schrödinger equation reads

$$\partial_t |\psi_t\rangle = -i(\hat{H}_0 + \sqrt{2\gamma}\xi_t \hat{L}) |\psi_t\rangle, \quad (1.28)$$

from where it is possible to find an equation for the density matrix $\hat{\rho}_t = |\psi_t\rangle \langle \psi_t|$ as

$$\partial_t \hat{\rho}_t = |\dot{\psi}_t\rangle \langle \psi_t| + |\psi_t\rangle \langle \dot{\psi}_t| = -i[\hat{H}_0, \hat{\rho}_t] - i\sqrt{2\gamma}\xi_t [\hat{L}, \hat{\rho}_t]. \quad (1.29)$$

If we average over the noise, we find an equation for $\hat{\rho}_t = \mathbb{E}(\hat{\rho}_t)$ as

$$\partial_t \hat{\rho}_t = -i[\hat{H}_0, \hat{\rho}_t] - i\sqrt{2\gamma}[\hat{L}, \mathbb{E}(\xi_t \circ \hat{\rho}_t)], \quad (1.30)$$

where now the term $\mathbb{E}(\xi_t \hat{\rho}_t)$ is cumbersome to compute, needing the use of Novikov's formula, which for this case reads

$$\mathbb{E}(\xi_t \circ \hat{\rho}_t) = \int_0^t d\tau \mathbb{E}(\xi_t \xi_\tau) \mathbb{E}\left(\frac{\delta \hat{\rho}[\xi_t]}{\delta \xi_\tau}\right). \quad (1.31)$$

Now one needs to realize that the functional derivative fulfills the Liouville-von Neumann equation [35, 37]

$$\partial_t \frac{\delta \hat{\rho}_t}{\delta \xi_\tau} = -i \left[\hat{H}_t, \frac{\delta \hat{\rho}[\xi_t]}{\delta \xi_\tau} \right], \quad (1.32)$$

and thus evolves as

$$\frac{\delta \hat{\rho}[\xi_t]}{\delta \xi_\tau} = \hat{V}_{t,\tau} (-i\sqrt{2\gamma}[\hat{L}, \hat{\rho}[\xi_\tau]]) \hat{V}_{t,\tau}^\dagger, \quad (1.33)$$

where $\hat{V}_{t,\tau} = \mathcal{T}_- \exp(-i \int_\tau^t dt' \hat{H}_{t'})$ is the propagator with the stochastic Hamiltonian. Therefore, the expectation value reads

$$\mathbb{E}(\xi_t \circ \hat{\rho}_t) = \int_0^t d\tau \mathbb{E}(\xi_t \xi_\tau) \mathbb{E}(\hat{V}_{t,\tau} (-i\sqrt{2\gamma}[\hat{L}, \hat{\rho}[\xi_\tau]]) \hat{V}_{t,\tau}^\dagger). \quad (1.34)$$

When we take white noise, we find that this expression greatly simplifies to

$$\mathbb{E}(\xi_t \circ \hat{\rho}_t) = \frac{1}{2} \sqrt{2\gamma} [\hat{L}, \hat{\rho}_t], \quad (1.35)$$

where the $1/2$ factor comes from the Stratonovich integral of Dirac's delta in one of the integrand limits $\int_0^t d\tau \delta(t - \tau) f(\tau) = \frac{1}{2} f(t)$, see Sec. 4.2.6. in Gardiner [39]. Therefore we find the dephasing **GKSL** master equation

$$\partial_t \hat{\rho}_t = -i[\hat{H}_0, \hat{\rho}_t] - \gamma[\hat{L}, [\hat{L}, \hat{\rho}_t]]. \quad (1.36)$$

The advantage of this approach is that it can deal with colored noise and Non-Markovian dynamics in a relatively easy way [35], its main disadvantage is that it is cumbersome, and if we want to derive an equation of motion for other quantities, it gets completely impractical.

Purely Itō approach

The Schrödinger equation is to be understood in the Stratonovich sense; it is, however, quite common to translate between the two conventions of stochastic calculus, at the price of adding spurious terms [39, 42, 43]. Therefore, the Itō version of the stochastic Schrödinger equation is

$$d|\psi_t\rangle = (-i\hat{H}_0 - \gamma\hat{L}^2)|\psi_t\rangle dt - i\sqrt{2\gamma}\hat{L}|\psi_t\rangle dW_t, \quad (1.37)$$

which directly gives the stochastic master equation

$$\begin{aligned} d\hat{\rho}_t &= d|\psi_t\rangle\langle\psi_t| + |\psi_t\rangle d\langle\psi_t| + d|\psi_t\rangle d\langle\psi_t| \\ &= (-i[\hat{H}_0, \hat{\rho}_t] - \gamma[\hat{L}, [\hat{L}, \hat{\rho}_t]])dt - i\sqrt{2\gamma}[\hat{L}, \hat{\rho}_t]dW_t, \end{aligned} \quad (1.38)$$

and now averaging gives the dephasing **GKSL** master equation

$$\partial_t \hat{\rho}_t = -i[\hat{H}_0, \hat{\rho}_t] - \gamma[\hat{L}, [\hat{L}, \hat{\rho}_t]]. \quad (1.39)$$

This method is technically much simpler, and can be easily extended to other quantities, at the cost of changing the rules of calculus for Itō rules. One unavoidable drawback is that one cannot extend this model to colored noise. The other drawback is that the transformation to Itō is not very rigorous, one needs to know how to transform the Stratonovich equation into Itō convention and what spurious terms should be added.

The best of both worlds: Stratonovich-Itō method

Let us now introduce the approach that we will follow in the rest of the thesis, which is conceptually the simplest.

The Stochastic Schrödinger equation (1.28) should be understood in the Stratonovich sense, this means that the standard rules of calculus apply and the propagator solves the equation

$$\hat{U}_t = \mathcal{T}_{\leftarrow} e^{-i \int_0^t d\tau (\hat{H}_0 + \sqrt{2\gamma}\xi_\tau \hat{L})}. \quad (1.40)$$

If we want to generate the infinitesimal evolution from t to $t + dt$, this propagator reads

$$\hat{U}_{dt} = \exp(-i\hat{H}_0 dt - i\sqrt{2\gamma}\hat{L}dW_t) = e^{-id\hat{H}_t}, \quad (1.41)$$

where the differential Hamiltonian is $d\hat{H}_t = \hat{H}_0 dt + \sqrt{2\gamma}\hat{L}dW_t$.

Note that this object only depends on the Wiener process dW_t and not on the state, and thus we do not need to specify a convention to write this object. The convention must only be specified when we write products with the state, e.g., $\hat{U}_t |\psi_t\rangle$ or $\hat{U}_t \circ |\psi_t\rangle$.

If we shift the focus from the stochastic Schrödinger equation to the propagator as the fundamental object, some disadvantages of the Itō approach wash away. We can obtain the spurious terms appearing in Itō convention simply as the quadratic terms in the propagator

$$d|\psi_t\rangle = \hat{U}_{dt} |\psi_t\rangle - |\psi_t\rangle = \left(-i\hat{H}_0 dt - i\sqrt{2\gamma}\hat{L}dW_t - \frac{1}{2}(\sqrt{2\gamma}\hat{L})^2 dt \right) |\psi_t\rangle. \quad (1.42)$$

This is the convention that we will follow in the rest of the thesis. Due to its simplicity, it keeps the power of the Itō method without the need to modify the equation of motion in an *ad-hoc* way to add spurious terms.

1.5 Non Hermitian Hamiltonians

The interest in Non-Hermitian Hamiltonians can be understood as an extension of quantum theory where the axiom of the hermiticity of the Hamiltonian is not postulated $\hat{H}^\dagger \neq \hat{H}$. The motivation behind Bender and Boettcher's [44] seminal work was that Non-Hermitian quantum mechanics, and in particular \mathcal{PT} symmetric quantum theory, which keeps the eigenvalues of the Hamiltonian real, could provide a new theory for fundamental physics. Nowadays, the motivation for studying Non-Hermitian Hamiltonians has changed. It is understood that a Non-Hermitian Hamiltonian provides an *effective description* of certain physical systems, which nonetheless can show fascinating phenomena, even amenable to experimental observation. In the setup we will consider mostly in this thesis, a Non-Hermitian Hamiltonian describes the nonunitary dynamics of an open quantum system undergoing a continuous measurement in the no-click limit. However, this is only one of the possible physical realizations of NH evolution, in here we briefly review the history of Non-Hermitian Quantum Mechanics and its experimental realization, and in the coming subsections, we will introduce the basic mathematical framework.

History and importance of non-Hermitian Hamiltonians

In Quantum Mechanics, the eigenvalues of an observable, i.e., the possible outcomes of a measurement of such an observable, need to be *real* because the number spit out by any measurement device is necessarily real. This motivates the postulate that observables in Quantum theory are necessarily Hermitian matrices, possessing real eigenvalues.

The reverse implication is, however, more subtle: a non-Hermitian Hamiltonian can have real eigenvalues. Bender⁵ and Boettcher realized in their seminal work [44] that the Hamiltonian

$$\hat{H} = \hat{p}^2 + i\hat{x}^3, \quad (1.43)$$

has *real spectrum*, i.e. *all* its eigenvalues are real. The physical reason this non-Hermitian Hamiltonian, which a priori could have an arbitrary complex spectrum, has a fully real spectrum was shown to be the presence of a symmetry called \mathcal{PT} *symmetry*. In the forthcoming subsection, we will define formally this symmetry, particularly for a finite-dimensional Hilbert space. The most general class of non-Hermitian Hamiltonians with a real spectrum is that of *pseudo-Hermitian* Hamiltonians [46–48], of which \mathcal{PT} symmetric systems form a subset. Another interesting type of non-Hermitian Hamiltonians arises from *non-reciprocal* interactions in a chain, which is the celebrated *Hatano-Nelson* model [49], which shows interesting topological phenomena such as the Non-Hermitian *skin effect* [50, 51] in which all eigenstates localize around the edges of the chain.

This mathematical observation could be thought to be a formal curiosity but it was realized that the Maxwell equations in a waveguide can be mapped to Schrödinger's equation with a NH, and particularly \mathcal{PT} symmetric, Hamiltonian [52, 53]. Shortly after, the first examples of NH Hamiltonians were realized experimentally [54–56]. By now, non-Hermitian systems have been engineered in many classical and quantum setups, and an extensive review can be found in [57]. This allowed for observing many phenomena without a hermitian counterpart, such as those arising from the presence of an Exceptional Point (EP) like *unidirectional invisibility* [56, 58] or EP-enhanced sensing [59–61]. \mathcal{PT} symmetric Hamiltonians provide a system whose energies are the zeros of the Riemann zeta function, thus potentially proving the Riemann hypothesis [62]. In recent years, it was shown that NH Hamiltonians enrich the Altland-Zirnbauer symmetry classification [63], allowing for novel topological phenomena without a Hermitian counterpart [64–66] which has also been studied in the context of open quantum systems with structured, topological baths [67].

There are two prominent approaches to obtaining a non-Hermitian Hamiltonian quantum mechanically. The first is based on the *Feshbach* projection approach [68–70]. In this approach, one is concerned about some energy levels, which define the *relevant* subspace of the full Hilbert space, discarding the *irrelevant* part. One reaches an effective Hamiltonian for the relevant subspace, which is in general non-Hermitian [57, 71]. The second one, which we will consider more in this thesis, is based on *quantum trajectories* and post-selection. Quantum trajectories were theoretically proposed and studied in [72–74], they can be obtained as *unravelings* of the *GKSL* master equation [17, 75] or arising from continuous quantum measurements [42, 43, 76, 77]. Quantum trajectories can be experimentally observed [78, 79] by evolving the system to a variable time t and performing full state tomography. The experimental control of quantum trajectories then allows for continuous measurements and post-selection to discard the quantum jumps. The first

⁵A historical note from Bender can be found in [45] where he mentions what inspired this Hamiltonian, and early observations by other researchers of the eigenvalues being real.

successful experimental realization of a NH system in this way was done in the Murch lab [80] using superconducting qubits. Many of the exceptional phenomena displayed by NH systems have then been experimentally tested [81–84]. Recently, similar experiments were performed in trapped ions [85] where NH Hamiltonians can show super quantum correlations, e.g., go beyond the limits posed by quantum mechanics through Legett-Garg inequalities [86]. Finally, recent proposals study the possibility of obtaining NH Hamiltonians without the need for post-selection, e.g., leveraging the symplectic transformations between the creation and annihilation operators in bilinear quantum optical models [87], or even arising from a clock in a non-inertial reference frame [88].

We now technically introduce the concept of \mathcal{PT} symmetry, particularly in the context of the NH qubit studied in [80].

1.5.1 Parity-Time Symmetry

Consider the following simple qubit Hamiltonian

$$\hat{H}_{J,G,L} = \begin{pmatrix} +iG & J \\ J & -iL \end{pmatrix}. \quad (1.44)$$

This Non-Hermitian Hamiltonian represents two states $\{|0\rangle, |1\rangle\}$. The state $|1\rangle$ has a gain term, described by $+iG$ in the diagonal, while $|0\rangle$ has a loss term described by $-iL$. Both states are coupled by a hopping J , which can induce transitions between the two states. A *Parity* transformation in this 2×2 Hamiltonian is simply given by $\hat{P} = \hat{\sigma}_x$, which exchanges sites $|0\rangle$ and $|1\rangle$. Transforming the Hamiltonian with a parity transformation $\mathcal{P}[\bullet] = \hat{P} \bullet \hat{P}$ we find

$$\mathcal{P}[\hat{H}_{J,G,L}] = \hat{\sigma}_x \hat{H}_{J,G,L} \hat{\sigma}_x = \begin{pmatrix} -iL & J \\ J & +iG \end{pmatrix}. \quad (1.45)$$

This transformed Hamiltonian has a clear meaning, exchanging the two sites, we end up with a Hamiltonian with losses $-iL$ in $|1\rangle$ and gains $+iG$ in $|0\rangle$. A *time reversal* transformation \mathcal{T} sends $t \rightarrow -t$; however, in quantum mechanics, since the propagator is $e^{-i\hat{H}t}$, this transformation can be equivalently thought of as complex conjugation $i \rightarrow -i$. Therefore $\mathcal{T}[\bullet] = \bullet^*$. If we applied the time-reversal transformation to \hat{H} , we would end up with a Hamiltonian with losses on site $|1\rangle$ described by $-iG$ and gains in site $|0\rangle$ described by $+iL$. However, note that if we apply the time-reversal transformation to the parity-transformed Hamiltonian, we find

$$\mathcal{PT}[\hat{H}_{J,G,L}] = (\hat{\sigma}_x \hat{H}_{J,G,L} \hat{\sigma}_x)^* = \begin{pmatrix} +iL & J \\ J & -iG \end{pmatrix}. \quad (1.46)$$

This is very similar to the original Hamiltonian. Indeed, if we impose the condition of *balanced gain and loss* $G = L$ [52], i.e., the amount of energy or matter going into site 1

is the same as the one exiting the system in site 0, we find that

$$\mathcal{PT}[\hat{H}_{J,G,G}] = \hat{H}_{J,G,G}, \quad (1.47)$$

and we say that the Hamiltonian has \mathcal{PT} symmetry. Bender put forward the concept of \mathcal{PT} symmetry [44] for a continuous variable setup, which involves some technical points, but is physically the same idea as the one described above [89]. The most striking consequence of \mathcal{PT} symmetry is that the Hamiltonian has real eigenvalues, albeit it is non-Hermitian; diagonalizing the Hamiltonian, we find

$$\lambda^2 + G^2 - J^2 = 0, \quad \lambda_{\pm} = \pm\sqrt{J^2 - G^2}. \quad (1.48)$$

Which has the property that when $J \geq G$, the spectrum is real, and when $G > J$, the spectrum is purely imaginary. This can be understood in the following way: when the gains and losses G are smaller than the hopping J , this parameter “compensates” for the decay and makes the spectrum real, while when the decay G is larger than the hopping J , the former dominates and makes the eigenvalues purely imaginary. This phenomena is known as \mathcal{PT} -symmetry breaking and the phases $J > G$ and $G > J$ as \mathcal{PT} unbroken ($\mathcal{PT}u$) and broken ($\mathcal{PT}b$), respectively. The reason for the name is that in the unbroken phase the eigenstates inherit the \mathcal{PT} symmetry of the Hamiltonian while in the broken phase they do not [45]. Between the two phases, when $J = G$, there is an *Exceptional Point* (EP) where both the eigenvalues and the eigenvectors coalesce, and the Hamiltonian is not diagonalizable at that point. Let us compute the (right) eigenvectors of this Hamiltonian, defined as $\hat{H} |\lambda_{\pm}^{(R)}\rangle = \lambda_{\pm} |\lambda_{\pm}^{(R)}\rangle$, which read

$$|\lambda_{\pm}^{(R)}\rangle = \begin{pmatrix} +iG \pm \sqrt{J^2 - G^2} \\ J \end{pmatrix}, \quad (1.49)$$

note that this eigenvector is *not* normalized. The left eigenvectors, defined as $\langle \lambda_{\pm}^{(L)} | \hat{H} = \lambda_{\pm} \langle \lambda_{\pm}^{(L)} |$ or equivalently $\hat{H}^\dagger |\lambda_{\pm}^{(L)}\rangle = \lambda_{\pm}^* |\lambda_{\pm}^{(L)}\rangle$, read

$$\langle \lambda_{\pm}^{(L)} | = \begin{pmatrix} -iG \pm \sqrt{J^2 - G^2} \\ J \end{pmatrix}. \quad (1.50)$$

We see that both pairs of eigenvectors coalesce at the EP $J = G$, and thus, the matrix is not diagonalizable since its eigenbasis does not span the full Hilbert space. The typical convention is to take both of these eigenvectors to be *bi-orthonormal*, as $\langle \lambda_n^{(L)} | \lambda_n^{(R)} \rangle = \delta_{mn}$ [90].

1.5.2 Interlude: Quantum Jumps and Continuous Quantum Measurements

Here we will introduce the main approach to obtaining a non-Hermitian Hamiltonian on the lab. Following Wiseman and Milburn [42], we consider that our measurement over a

time dt is described by a quantum channel

$$\hat{\rho}_{t+dt} = \mathcal{E}[\hat{\rho}_t] = \sum_r \hat{M}_r(dt) \hat{\rho}_t \hat{M}_r^\dagger(dt), \quad (1.51)$$

where the sum over r accounts for all the possible measurement's *results*. In the simplest case, we consider two operators of the form

$$\hat{M}_0(dt) = \hat{\mathbb{1}} - \left(\frac{1}{2} \hat{c}^\dagger \hat{c} + i \hat{H} \right) dt, \quad \hat{M}_1(dt) = \sqrt{dt} \hat{c}, \quad (1.52)$$

associated to measurement results $r = 0$ and $r = 1$, respectively.

Note that these are *bona fide* Kraus operators since they obey the normalization condition $\hat{M}_0^\dagger(dt) \hat{M}_0(dt) + \hat{M}_1^\dagger(dt) \hat{M}_1(dt) = \hat{\mathbb{1}}$. Starting the measurement from state $\hat{\rho}$ the probability of observing the result $r = 1$ after a time dt is given by

$$\mathfrak{P}(r = 1, dt) = \text{Tr}(\hat{\rho} \hat{M}_1^\dagger(dt) \hat{M}_1(dt)) = dt \text{Tr}(\hat{c}^\dagger \hat{c} \hat{\rho}), \quad (1.53)$$

which is infinitesimal⁶. The probability of measuring $r = 0$, the null result, is thus much larger

$$\mathfrak{P}(r = 0, dt) = 1 - dt \text{Tr}(\hat{c}^\dagger \hat{c} \hat{\rho}) = 1 - \mathcal{O}(dt). \quad (1.54)$$

If we take the operator $\hat{c} = \sqrt{\gamma} \hat{a}$ to be an annihilation operator, this continuous measurement models photodetection of a cavity. Introducing the number of photodetections up to time t as $N(t)$ and starting in a pure state $|\psi_t\rangle$ one can introduce the increment in the photodetections at time t dN_t as defined by the properties

$$dN_t^2 = dN_t, \quad \mathbb{E}(dN_t) = dt \langle \psi_t | \hat{c}^\dagger \hat{c} | \psi_t \rangle, \quad (1.55)$$

dN_t is therefore a point process [42]. The first property implies that at any time the increment is either $dN_t = 0$ or $dN_t = 1$, i.e., either we do not detect a photon or we do. The probability of detecting a photon over the time dt is given by $\mathfrak{P}(r = 1, dt) = \mathbb{E}(dN_t)$. Let us now look at how the state evolves: If we detect a photon $dN_t = 1$, the state is updated to

$$|\psi_{t+dt}^{(1)}\rangle = \frac{\hat{M}_1(dt) |\psi_t\rangle}{\sqrt{\langle \psi_t | \hat{M}_1^\dagger(dt) \hat{M}_1(dt) | \psi_t \rangle}} = \frac{\hat{c} |\psi_t\rangle}{\sqrt{\langle \psi_t | \hat{c}^\dagger \hat{c} | \psi_t \rangle}}. \quad (1.56)$$

⁶As long as $\hat{c}^\dagger \hat{c} \in \mathcal{B}(\mathcal{H})$ is a bounded linear operator over the Hilbert space, as in the original derivation of Lindblad [30, 42]

If we do not detect a photon, $dN_t = 0$, and the state is updated to

$$\begin{aligned} |\psi_{t+dt}^{(0)}\rangle &= \frac{\hat{M}_0(dt)|\psi_t\rangle}{\sqrt{\langle\psi_t|\hat{M}_0^\dagger(dt)\hat{M}_0(dt)|\psi_t\rangle}} = \frac{\left(\hat{\mathbb{1}} - \left(\frac{1}{2}\hat{c}^\dagger\hat{c} + i\hat{H}\right)dt\right)|\psi_t\rangle}{\sqrt{1 - dt\langle\psi_t|\hat{c}^\dagger\hat{c}|\psi_t\rangle}} \\ &= \left(\hat{\mathbb{1}} - dt\left(i\hat{H} + \frac{1}{2}(\hat{c}^\dagger\hat{c} - \langle\psi_t|\hat{c}^\dagger\hat{c}|\psi_t\rangle)\right)\right)|\psi_t\rangle + \mathcal{O}(dt^{3/2}). \end{aligned} \quad (1.57)$$

This evolution can be rewritten as a *nonlinear Stochastic Schrödinger equation* (SSE) of the form

$$d|\psi_t\rangle = \left\{ \left(\frac{\hat{c}}{\sqrt{\langle\hat{c}^\dagger\hat{c}\rangle_\psi}} - 1 \right) dN_t + \left(\frac{\langle\hat{c}^\dagger\hat{c}\rangle_\psi - \hat{c}^\dagger\hat{c}}{2} - i\hat{H} \right) dt \right\} |\psi_t\rangle, \quad (1.58)$$

where we introduced the short-hand notation $\langle\hat{c}^\dagger\hat{c}\rangle_\psi \equiv \langle\psi_t|\hat{c}^\dagger\hat{c}|\psi_t\rangle$ and we discarded terms of order $dN_t dt$ that come from writing the probability of the null measurement $1 - dN_t$. The case in which we observe a photodetection is called a *quantum jump*. However, it describes a “*sudden change in the observer’s knowledge, not an objective physical event*” [42], in contrast with Bohr’s original interpretation [91]. The dynamics described by the solutions of this equation are called *quantum trajectories*. These are not quantum trajectories in the Bohmian sense, or *objectively real* [76], but rather *subjectively real* in the sense that the trajectory depends on the choice of the measurement scheme chosen by the observer, however, once this scheme is chosen, all observers would agree on the result. The general approach of mapping the GKSL equation to a Stochastic Differential Equation of a certain kind is called an *unraveling* of the master equation [17]. There are several different unravelings, e.g., based on quantum jumps dN_t as described here, based on white noise dW_t like homodyne or heterodyne detection. All these unravelings give different stochastic density matrices $\hat{\rho}_t$ that reproduce the evolution of the GKSL equation on average $\hat{\rho}_t = \mathbb{E}(\hat{\rho}_t)$.

1.5.3 Non-Hermitian Hamiltonians from Continuous Measurements

Pure initial state

Leveraging the framework of quantum trajectories, there is a simple way to engineer a non-Hermitian Hamiltonian. Imagine that we do a continuous measurement up to a certain time t and we *post-select* only those trajectories that did not have a quantum jump. For these special trajectories, the evolution of the wavefunction follows the Schrödinger equation

$$i\partial_t|\psi_t\rangle = \left(\hat{H} - \frac{i}{2}\hat{c}^\dagger\hat{c} + \frac{i}{2}\langle\hat{c}^\dagger\hat{c}\rangle_\psi\right)|\psi_t\rangle. \quad (1.59)$$

Note that this equation looks like the Schrödinger equation, but there are two main differences:

- The effective Hamiltonian $\hat{H}_{\text{eff}} = \hat{H} - \frac{i}{2}\hat{c}^\dagger\hat{c}$ is *non-Hermitian* since $\hat{H}_{\text{eff}}^\dagger = \hat{H} + \frac{i}{2}\hat{c}^\dagger\hat{c} \neq \hat{H}_{\text{eff}}$. This means that it does not generate unitary evolution, which can be seen by computing the propagator $\hat{G}_t = e^{-i\hat{H}_{\text{eff}}t}$ whose hermitian conjugate is *not* its inverse $\hat{G}_t^\dagger\hat{G}_t = e^{+i\hat{H}_{\text{eff}}^\dagger t}e^{-i\hat{H}_{\text{eff}}t} \neq \hat{1}$.
- The equation is nonlinear in the wavefunction. The non-linearity arises from the state-dependent term $\langle\hat{c}^\dagger\hat{c}\rangle_\psi$. This term ensures that the wavefunction $|\psi_t\rangle$ is normalized at all times $\langle\psi_t|\psi_t\rangle = 1$.

Even though the equation is non-linear, it can be formally solved in terms of the propagator as

$$|\psi_t\rangle = \frac{\hat{G}_t|\psi_0\rangle}{\sqrt{\langle\psi_0|\hat{G}_t^\dagger\hat{G}_t|\psi_0\rangle}} = \frac{e^{-i\hat{H}_{\text{eff}}t}|\psi_0\rangle}{\sqrt{\langle\psi_0|e^{+i\hat{H}_{\text{eff}}^\dagger t}e^{-i\hat{H}_{\text{eff}}t}|\psi_0\rangle}}. \quad (1.60)$$

Generic initial state

If we allow for an initially mixed state $\hat{\rho}_0$, the generic evolution follows the non-linear master equation found by Brody and Graefe [92]

$$\partial_t\hat{\rho}_t = -i[\hat{H},\hat{\rho}_t] - \frac{1}{2}\{\hat{c}^\dagger\hat{c},\hat{\rho}_t\} + \text{Tr}(\hat{c}^\dagger\hat{c}\hat{\rho}_t)\hat{\rho}_t. \quad (1.61)$$

Note that the anti-commutator term naturally arises from the **GKSL** equation; therefore, this equation—discarding the nonlinear term, which simply enforces normalization—can be thought of as the **GKSL** equation in which we have “*killed*” the quantum jumps $\sum_j \hat{L}_j \hat{\rho} \hat{L}_j^\dagger$ [89]. Again, this nonlinear master equation can be formally solved as

$$\hat{\rho}_t = \frac{\hat{G}_t\hat{\rho}_0\hat{G}_t^\dagger}{\text{Tr}(\hat{G}_t^\dagger\hat{G}_t\hat{\rho}_0)} = \frac{e^{-i\hat{H}_{\text{eff}}t}\hat{\rho}_0e^{+i\hat{H}_{\text{eff}}^\dagger t}}{\text{Tr}(e^{+i\hat{H}_{\text{eff}}^\dagger t}e^{-i\hat{H}_{\text{eff}}t}\hat{\rho}_0)}. \quad (1.62)$$

This evolution has an interesting property: it preserves the rank of states, which allows for a purely geometric formulation of **NH** dynamics [93]. A consequence is that if the initial state is pure $\hat{\rho}_0 = |\psi_0\rangle\langle\psi_0|$, the state remains pure along the evolution. This can be easily understood for the qubit in the Bloch sphere; the trajectories that start on the surface of the sphere remain on the surface, but inside the sphere, the trajectories can have all sorts of behavior, since the evolution in general does not preserve the purity, as unitary evolution would do. This can be easily checked from the expression of the purity

$$P_t = \text{Tr}(\hat{\rho}_t^2) = \frac{\text{Tr}(\hat{G}_t^\dagger\hat{G}_t\hat{\rho}_0\hat{G}_t^\dagger\hat{G}_t\hat{\rho}_0)}{\text{Tr}(\hat{G}_t^\dagger\hat{G}_t\hat{\rho}_0)\text{Tr}(\hat{G}_t^\dagger\hat{G}_t\hat{\rho}_0)} = \begin{cases} 1 & \text{if } \hat{\rho}_0 = |\psi_0\rangle\langle\psi_0| \\ < 1 & \text{if } \text{Tr}(\hat{\rho}_0^2) < 1 \end{cases}. \quad (1.63)$$

Where the case for mixed initial state can be proved by expanding $\hat{\rho}_0 = \sum_i p_i |\psi_i\rangle \langle \psi_i|$, which gives

$$P_t = \frac{\sum_{i,j} p_i p_j |\langle \psi_j | \hat{G}_t^\dagger \hat{G}_t | \psi_i \rangle|^2}{\sum_{i,j} p_i p_j \langle \psi_i | \hat{G}_t^\dagger \hat{G}_t | \psi_i \rangle \langle \psi_j | \hat{G}_t^\dagger \hat{G}_t | \psi_j \rangle}.$$

The Cauchy-Schwarz inequality ensures that

$$|\langle \psi_j | \hat{G}_t^\dagger \hat{G}_t | \psi_i \rangle|^2 \leq \langle \psi_i | \hat{G}_t^\dagger \hat{G}_t | \psi_i \rangle \langle \psi_j | \hat{G}_t^\dagger \hat{G}_t | \psi_j \rangle,$$

and therefore $P_t \leq 1$.

Passive \mathcal{PT} symmetry

The types of NH Hamiltonians that we can achieve from continuous measurements and post-selection are always of the form $\hat{H} - \frac{i}{2}\hat{c}^\dagger \hat{c}$ note that, whatever the operator \hat{c} , the product will always be positive semi-definite $\hat{c}^\dagger \hat{c} \geq 0$. This means that, at least in this approach, it is only possible to realize NH Hamiltonians whose eigenvalues have negative imaginary part. This comes from the fact that if the quantum channel $\mathcal{E}[\bullet]$ is trace preserving, applying any post-selection strategy to choose only a subset of Kraus operators will only yield a trace decreasing map. This implies that gains, described by positive imaginary terms like $+iG$ in (1.44), cannot be implemented in quantum setups, and are hard to implement even in classical setups [89]. However, considering *non-uniform* losses can achieve the same phenomenology. This gives rise to a *passive- \mathcal{PT}* symmetric Hamiltonian [89]. In particular, the version of (1.44) that has been realized in the lab [80], which we will call the *Dissipative Qubit* can be written in the $\{|e\rangle, |f\rangle\}$ basis as

$$\hat{H}_{\text{DQ}} = \begin{pmatrix} 0 & J \\ J & -i\Gamma \end{pmatrix} = J\hat{\sigma}_x - i\Gamma |e\rangle \langle e|, \quad (1.64)$$

where the anti-Hermitian term comes from setting $\hat{c} = \sqrt{2\Gamma}\hat{\sigma}_- = \sqrt{2\Gamma}|g\rangle \langle e|$ and thus $-\frac{i}{2}\hat{c}^\dagger \hat{c} = -i\Gamma|e\rangle \langle e|$. Note that this Hamiltonian is *not* \mathcal{PT} -symmetric, however it can be mapped to a \mathcal{PT} -symmetric Hamiltonian by a constant shift of the energy $+i\Gamma/2$, which has no physical effect, provided that the evolution of the state is renormalized. This shift makes the eigenvalues purely real and purely imaginary, in the \mathcal{PT} unbroken and \mathcal{PT} broken phases, respectively.

Details on the experimental setup of the Dissipative Qubit

The first physical implementation of this system consisted of a superconducting qubit setup, particularly a transmon, which has 3 levels $\{|g\rangle, |e\rangle, |f\rangle\}$. Two Josephson junctions form the transmon circuit in a Superconducting Quantum Interference Device ([SQUID](#)) shunted by a capacitor [80, 94]. The full 3-level system is described by the master equa-

tion⁷

$$\partial_t \hat{\rho}_t = -i[\hat{H}, \hat{\rho}_t] + 2\Gamma_e \mathcal{D}_{\hat{\sigma}_-}[\hat{\rho}_t], \quad (1.65)$$

the dissipator superoperator is defined as $\mathcal{D}_{\hat{X}}[\bullet] := \hat{X} \bullet \hat{X}^\dagger - \frac{1}{2}\{\hat{X}^\dagger \hat{X}, \bullet\}$. This channel describes *spontaneous emission* from $|e\rangle \rightarrow |g\rangle$. An *Impedance mismatch element* is used to shape the density of states and thus to achieve a large decay rate Γ_e . This decay rate can be tuned by a magnetic flux Φ through the [SQUID](#), which tunes the frequency of the levels of the transmon. The circuit is embedded in a waveguide, the dispersive interaction between the transmon and the fundamental mode of the waveguide gives a *state-dependent* shift of the cavity frequency, which is detected with a *weak microwave tone*, lastly the phase shift is detected by homodyne measurement with a Josephson parametric amplifier [80]. Recently, another setup for realizing a Non-Hermitian Qubit based on trapped ions has been realized [85].

1.6 A crash course in Random Matrix Theory

Why Random Matrices?

In the 1950s, physicists were trying to characterize certain properties of heavy nuclei. These systems are composed of hundreds of nucleons that interact very strongly with each other, as Bohr pointed out [95]. Even if we had a model for the interaction of each pair of nucleons, solving it for all practical purposes would be impossible. In this context, Wigner introduced an extremely simplified model [96]; his idea was that the system under study would be so complex that its Hamiltonian would be almost *random*, or at least this could be a good model for it. The only constraint that one should impose on the randomness is that it respects the fundamental symmetries of the system. In a sense, this is a *statistical* model of the behavior of complex nuclei, instead of averaging over different initial states, as typically done in physics, Wigner's approach considered an ensemble of Hamiltonians with some common symmetry; in this way, one extracts the properties that are common to all the ensemble.

This was the original idea behind the grand development of *Random Matrix Theory* (RMT), which ever since has been explored in many different areas of physics [97–99] and mathematics [100]. See [99] for a historical account of the different periods in the development of RMT.

⁷This master equation holds when we disregard the decay channel $|f\rangle \rightarrow |e\rangle$. In reality, this channel is present, but its decay rate Γ_f is very small compared to the decay rate of the channel $|e\rangle \rightarrow |g\rangle$ given by Γ_e . For one of the particular realizations in [80] we have $\Gamma_f = 0.25\mu\text{s}^{-1}$, while $\Gamma_e = 6.7\mu\text{s}^{-1}$, which justifies this approximation. The effect of this decay rate can be accounted for by shifting the decay rate $\Gamma = \Gamma_e - \Gamma_f$.

1.6.1 Definition of Gaussian Random Matrix Ensembles

The basic object in [RMT](#) is an ensemble of random matrices $\{\hat{H}\}$, which in physical applications are typically considered to model Hamiltonians, and more importantly one needs to introduce a probability distribution $\mathfrak{P}(\hat{H})$ over this ensemble, such that we know how likely it is to sample a given matrix \hat{H} .

In the *Gaussian* random matrix ensembles, the different matrix elements H_{ij} are sampled independently from one another. This means that the probability distribution over the Hamiltonians factorizes as

$$\mathfrak{P}(\hat{H}) = \prod_{i,j=1}^N p_{ij}(H_{ij}). \quad (1.66)$$

In particular, one can show [\[101\]](#) that for the different Gaussian Random Matrix Ensembles, which we will define in this section, this expression reduces to

$$\mathfrak{P}(\hat{H}) = Ce^{-A\text{Tr}(\hat{H}^2)}, \quad (1.67)$$

where A sets the energy scale and C is a normalization factor which can be thought of as the inverse of the partition function $C = 1/Z$.

The ensembles are fundamentally characterized by their symmetries. Once the physical Hamiltonian has been block diagonalized according to its unitary symmetries, e.g., fixing the global spin, we can model it using random matrix theory. The relevant symmetries for defining the [RMT](#) are antiunitary, the most relevant symmetry for our case is *time-reversal symmetry* \hat{T} . Anti-unitary symmetry can be expressed as a product of a unitary operator \hat{U} and complex conjugation \hat{K} , i.e., $\hat{T} = \hat{U}\hat{K}$. Note that if we act twice with time-reversal symmetry, we should recover the same state, which enforces $\hat{T}^2 = \alpha\hat{1}$ with $|\alpha| = 1$. From the expression of the antiunitary operator, we find that it fulfills the property [\[101\]](#)

$$\begin{aligned} \hat{T}^2 &= \hat{U}\hat{K}\hat{U}\hat{K} = \hat{U}\hat{U}^* = \alpha \Rightarrow \hat{U}^* = \alpha\hat{U}^\dagger \Rightarrow \hat{U}^\dagger = (\hat{U}^*)^\dagger = \alpha\hat{U}^* \\ &\Rightarrow \hat{U}^* = \alpha^2\hat{U}^* \Rightarrow \alpha^2 = 1 \Rightarrow \alpha = \pm 1. \end{aligned} \quad (1.68)$$

Therefore, the square of the time-reversal operator has the two possible values $\hat{T}^2 = \pm 1$. The $\hat{T}^2 = 1$ case is obtained in spinless systems and whenever the Hamiltonian is real in a certain basis, while the $\hat{T}^2 = -1$ case can be obtained for spin $\frac{1}{2}$ systems [\[101\]](#). Therefore, according to their different behavior under time-reversal symmetry, there are three possible Gaussian Random Matrix ensembles, which is known as *Dyson's threefold way* [\[102\]](#). These three possibilities define the three basic ensembles that we will consider in the remainder of this thesis. The *Dyson index* β distinguishes between the three

- **Gaussian Orthogonal Ensemble (GOE):** If $\hat{T}^2 = +1$ the system shows conventional time reversal symmetry. In this case, the ensemble is invariant under

orthogonal transformations respecting $\hat{O}^\tau \hat{O} = \hat{O} \hat{O}^\tau = \hat{\mathbb{1}}$. This implies that

$$\mathfrak{P}^{(1)}(\hat{O} \hat{H} \hat{O}^\tau) = \mathfrak{P}^{(1)}(\hat{H}), \quad \forall \hat{O} \in \mathcal{O}(\mathcal{H}), \quad (1.69)$$

where $\mathcal{O}(\mathcal{H})$ denotes the group of *orthogonal* linear operators over the Hilbert space. This property physically represents that the ensemble should remain invariant under changes of basis that keep the Hamiltonian real. The **GOE** is characterized by $\beta = 1$. The Hamiltonians of GOE have real matrix elements $H_{ij} \in \mathbb{R}$, given a matrix \hat{X} in which all its elements are normally distributed $X_{ij} \sim \mathcal{N}(0, 1)$, with $1 \leq i, j \leq N$ we can sample a **GOE** matrix as

$$\hat{H} = \frac{\hat{X} + \hat{X}^\tau}{2}, \quad \hat{H} \in \text{GOE}(N). \quad (1.70)$$

- **Gaussian Unitary Ensemble (GUE):** When there is no time-reversal symmetry, the ensemble will be invariant under *unitary* transformations

$$\mathfrak{P}^{(2)}(\hat{U} \hat{H} \hat{U}^\dagger) = \mathfrak{P}^{(2)}(\hat{H}), \quad \forall \hat{U} \in \mathcal{U}(\mathcal{H}), \quad (1.71)$$

where $\mathcal{U}(\mathcal{H})$ denotes the group of unitary operators over the Hilbert space. Again, the physical meaning of this requirement is that the ensemble should remain invariant under a change of basis, i.e. the probability of two Hamiltonians related simply by a change of basis should be the same $\hat{H}, \hat{H}' = \hat{U}^\dagger \hat{H} \hat{U}$. The **GUE** is characterized by $\beta = 2$. The matrix elements now need not be real, however, \hat{H} still has to be Hermitian. If we sample a square matrix with complex, normally distributed variables, $X_{mn} \sim \mathcal{N}(0, 1) + i\mathcal{N}(0, 1)$, with $1 \leq m, n \leq N$, we can sample a GUE matrix as

$$\hat{H} = \frac{\hat{X} + \hat{X}^\dagger}{2}, \quad \hat{H} \in \text{GUE}(N). \quad (1.72)$$

- **Gaussian Symplectic Ensemble (GSE):** When the system is anti-symmetric under time-reversal transformations $\hat{T}^2 = -1$ the ensemble is required to be invariant under *symplectic* transformations \hat{S}

$$\mathfrak{P}^{(4)}(\hat{S} \hat{H} \hat{S}^\dagger) = \mathfrak{P}^{(4)}(\hat{H}). \quad (1.73)$$

The *symplectic* transformations are those $2N \times 2N$ matrices that satisfy

$$\hat{S}^\dagger \hat{\Omega} \hat{S} = \hat{\Omega}, \quad \text{where} \quad \hat{\Omega} = \begin{pmatrix} 0 & -1 \\ 1 & 0 \end{pmatrix} \otimes \hat{\mathbb{1}}_N. \quad (1.74)$$

The GSE is characterized by $\beta = 4$. It can be sampled by constructing the complex, normally distributed matrix $X_{mn} \sim \mathcal{N}(0, 1) + i\mathcal{N}(0, 1)$, $1 \leq m, n \leq 2N$ and

computing

$$\hat{H} = \frac{\hat{X} + \hat{X}^\dagger - \hat{\Omega}(\hat{X} + \hat{X}^\dagger)\hat{\Omega}}{2\sqrt{2}}, \quad \hat{H} \in \text{GSE}(N). \quad (1.75)$$

Due to Kramer's degeneracy [101], the eigenvalues of this ensemble come in degenerate pairs; for this reason, for the spectral analysis of this ensemble, we will only consider one energy per each degenerate pair.

A key feature of these Gaussian ensembles is that the joint probability density of all the eigenvalues is known analytically [103]

$$\rho_\beta(E_1, \dots, E_N) = C \prod_{1 \leq i < j \leq N} |E_i - E_j|^\beta e^{-A \sum_{i=1}^N E_i^2}, \quad (1.76)$$

where A is a constant that fixes the energy scale and C ensures normalization of the joint probability density. The most relevant term in this expression is the *Vandermonde determinant* $\prod_{1 \leq i < j \leq N} |E_i - E_j|^\beta$; this term describes the interaction, also called the *level repulsion*, between the eigenvalues. Interestingly, this level repulsion is stronger the higher the value of the Dyson index β of the ensemble. This is one of the key features presented by random matrices, which makes them interesting from a physical point of view, as will be discussed in the next section.

In a real system, building the joint probability density of all the eigenvalues is impractical. Thus we resort to other measures of spectral correlations which are easier to compute or measure. The most basic of these quantities is the *nearest-neighbors Level Spacing (nnLS)* distribution $\mathfrak{P}(s)$. The nearest-neighbor level spacings are defined simply as $s_n := E_{n+1} - E_n$. Given the set of all possible level spacings $\{s_n\}_{n=1}^{N-1}$ we can compute the *nnLS* distribution $\mathfrak{P}(s)$. For the Random Matrix Ensembles, this distribution is given by the *Wigner's Surmise* [104]

$$\mathfrak{P}_\beta(s) = C_\beta s^\beta e^{-A_\beta s^2}, \quad (1.77)$$

where C_β and A_β are given by [101]

$$C_\beta = \frac{2}{\Gamma(\frac{\beta+1}{2})} \left(\frac{\Gamma(\frac{\beta}{2} + 1)}{\Gamma(\frac{\beta+1}{2})} \right)^{\beta+1} = \begin{cases} \frac{\pi}{2} & \text{for } \beta = 1, \\ \frac{32}{\pi^2} & \text{for } \beta = 2, \\ \frac{2^{18}}{3^6 \pi^3} & \text{for } \beta = 4, \end{cases} \quad (1.78a)$$

$$A_\beta = \left(\frac{\Gamma(\frac{\beta}{2} + 1)}{\Gamma(\frac{\beta+1}{2})} \right)^2 = \begin{cases} \frac{\pi}{4} & \text{for } \beta = 1, \\ \frac{4}{\pi} & \text{for } \beta = 2, \\ \frac{64}{9\pi} & \text{for } \beta = 4, \end{cases} \quad (1.78b)$$

which ensures that the distribution is normalized and that the average level spacing is unity [101]

$$\int_0^\infty \mathfrak{P}(s)ds = 1, \quad \int_0^\infty s\mathfrak{P}(s)ds = 1. \quad (1.79)$$

The expressions for these distributions can be derived analytically for a 2×2 matrix, and interestingly, agree quite well with a random matrix of any dimension N , provided that one enforces the conditions (1.79), something that can be achieved through a numerical process called *unfolding the spectrum* [101, 105] which will be introduced in the next section.

1.6.2 Unfolding the spectrum

Spectra have two main contributions, a system-specific one and a universal one, which is the one we can model in the context of Random Matrices. To remove all the system-specific information and analyze only universal behavior, we typically perform a procedure called *unfolding* of the spectrum [99], which we detail in this section. Given a spectrum $\{E_n\}_{n=1}^N$, which we assume to be ordered $n \geq m \Rightarrow E_n \geq E_m$, we can compute the *density of states* $\rho(E)$

$$\rho(E) = \sum_{n=1}^N \delta(E - E_n), \quad (1.80)$$

which yields the *cumulative density of states* $\eta(E)$ defined as

$$\eta(E) = \int_{-\infty}^E \rho(E')dE' = \sum_{n=1}^N \Theta(E - E_n), \quad (1.81)$$

where $\Theta(x)$ is the *Heaviside step function*. The function $\eta(E)$ counts the number of energy levels with energy $E_n < E$, and is also sometimes referred to as the *staircase* function. This function has two different contributions: a *smooth* and a *fluctuating* one

$$\eta(E) = \bar{\eta}(E) + \eta_{\text{fl}}(E), \quad (1.82)$$

where the smooth part $\bar{\eta}(E)$ is the cumulative local density of states [99] obtained as

$$\bar{\eta}(E) = \int_{-\infty}^E \bar{\rho}(E')dE', \quad (1.83)$$

where $\bar{\rho}(E')$ is the local density of states [101]. The unfolding procedure consists of mapping each eigenvalue E_n to a new eigenvalue e_n as

$$E_n \mapsto e_n = \bar{\eta}(E_n), \quad (1.84)$$

so that now the staircase function for the *unfolded spectrum* $\{e_n\}_{n=1}^N$ reads

$$\eta(e) = e + \eta_{\text{fl}}(e), \quad (1.85)$$

which has unit-density states all over the spectrum; therefore, the spectral analysis of the unfolded spectrum should only contain universal information and should not depend on the system-specific local density of states. Of course, to unfold a given spectrum, one needs to find the staircase function $\bar{\eta}(E)$, which is generally a non-trivial task.

Analytical unfolding in Gaussian Random Matrices

We know that the local density of states of Random Matrices in the $N \rightarrow \infty$ limit is well-described by *Wigner's semicircle law* [106] as

$$\bar{\rho}(E) = \frac{1}{\pi\beta N} \sqrt{2N\beta - E^2}, \quad (1.86)$$

where we see that the local density of states is a semicircle with radius $\sqrt{2N\beta}$ depending on the dimension of the matrix and the Dyson index. For this local density of states, the staircase function can be computed analytically to be

$$\begin{aligned} \bar{\eta}(E) &= N \int_{-\infty}^E \bar{\rho}(E') dE', \\ &= \begin{cases} 0 & E < -\sqrt{2N\beta}, \\ \frac{N}{2} + \frac{E}{2\beta\pi} \sqrt{2\beta N - E^2} + \frac{N}{\pi} \arctan\left(\frac{E}{\sqrt{2\beta N - E^2}}\right) & -\sqrt{2N\beta} \leq E \leq \sqrt{2N\beta}, \\ N & E > \sqrt{2N\beta}. \end{cases} \end{aligned} \quad (1.87)$$

This analytical unfolding is essential when comparing random matrices of different dimensions, which is necessary since many of the analytical expressions such as the level spacing distribution $\mathfrak{P}(s)$ are obtained analytically for 2×2 matrices.

Numerical unfolding

In the general case, where we have obtained some spectrum numerically, we do not know an analytical expression for its local density of states. In this case, it becomes important to find a numerical procedure to find the staircase function $\bar{\eta}(E)$. Following [105], we use the following algorithm:

1. Order the energies such that $E_1 \leq E_2 \leq \dots \leq E_N$

2. Compute the staircase function $\eta(E) = \sum_{n=1}^N \Theta(E - E_n)$. In practice, we compute the histogram for the density of states

$$\rho_{\text{num}}(x_1, \dots, x_{N_{\text{bins}}}) = \sum_{n=1}^N \Theta(E_n \in [x_i, x_{i+1}])_{i=1}^{N_{\text{bins}}},$$

which depends on the number of bins N_{bins} , and compute its cumulative function $\eta_{\text{num}}(E) = \sum_{x_i < E} \rho_{\text{num}}(x_i)$.

3. We fit the staircase function $\eta_{\text{num}}(E)$ to a certain polynomial of degree κ , which is smooth in the variable $p_{\kappa}(E) = \sum_{\alpha=0}^{\kappa} c_{\alpha} E^{\alpha} = \bar{\eta}_{\text{num}}(E)$.
4. Once we have found the polynomial fit $\bar{\eta}_{\text{num}}(E) = p_{\kappa}(E)$ we find the unfolded spectrum as

$$e_n = \bar{\eta}_{\text{num}}(E_n).$$

5. This spectrum $\{e_n\}_{n=1}^N$ now should have a density of states equal to unity; however, the tails of the density of states are hard to sample properly, and we typically get some unwanted behavior in the tails. For this reason, we choose a window of energies of size N_{en} in the middle of the spectrum.

The numerical unfolding depends on two parameters [3]: the number of bins N_{bins} and the degree of the polynomial fit κ . The number of bins should be chosen in a “mesoscopic” scale: large enough such that the density of states does not change much over the the interval $[x_i, x_{i+1}]$, but small enough such that the bin size $x_{i+1} - x_i \gg \langle s \rangle$ contains enough levels. The role of the degree of the polynomial is also critical, since a high degree can lead to overfitting [107], i.e., to attributing part of the fluctuating $\eta_{\text{fl}}(E)$ to the staircase function $\bar{\eta}(E)$. To test what parameters provide the best unfolding for our case, we use the analytical unfolding known for random matrices and compare it with the numerical approach, defining a *quality of the unfolding* \mathfrak{Q} as

$$\mathfrak{Q} := \sum_{i=1}^{N_{\text{bins}}} \sum_{n=1}^{N_{\text{en}}} [\text{Hist}_i(\bar{\eta}_{\text{an}}(E_n)) - \text{Hist}_i(\bar{\eta}_{\text{num}}(E_n))]^2. \quad (1.88)$$

Figure 1.1 shows the quality of the unfolding [3] as a function of the two parameters N_{bins} and κ . We observe that unfolding with degrees 1 and 2 performs poorly, and that unfolding with degree $\kappa > 5$ performs slightly worse, which we attribute to overfitting. To avoid this, we choose a polynomial of degree $\kappa = 3$ and a number of bins $N_{\text{bins}} = 50$. As argued by Bertrand and Garcia-Garcia [107], a global unfolding, such as the one we use, keeps the long-range correlations between energies, which are critical for our work in Chap. 4.

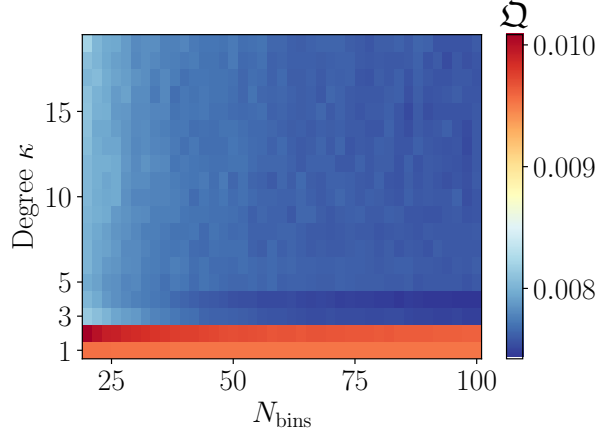


Figure 1.1. Quality of the numerical unfolding with respect to the analytical one for GOE matrices. The dimension of the random matrices is $N = 400$, we choose the central window with $N_{\text{en}} = 200$ energies and average over $N_{\text{av}} = 500$ realizations of the ensemble.

1.7 Founding Conjectures of Quantum Chaos

Having introduced the basic concepts in the theory of Random Matrices, we are now in a position to answer the question: “*why* is RMT important in physics?”, with a particular focus on the chaotic or integrable dynamics of quantum systems. The connection to these systems is through two conjectures, which we introduce now.

1.7.1 Berry Tabor conjecture

The *Berry-Tabor* conjecture [108] states that the energy levels of *integrable* quantum systems, i.e., those that are not chaotic, follow a *Poisson Point Process* on the real line. This means that they behave as if the energies were sampled randomly and independently from each other. This is also called the *Poisson* ensemble in which each energy $E_i \sim \mathcal{U}_{[-\frac{l}{2}, \frac{l}{2}]}$ is sampled independently⁸ in a certain interval. The level spacing distribution reads

$$\mathfrak{P}(s) = e^{-s}. \quad (1.89)$$

This distribution reflects a key feature of integrable systems: the value of the level spacing at $s = 0$ is $\mathfrak{P}(0) = 1$, which indicates that by randomly sampling energies it is very probable that the two neighboring energies E_n, E_{n+1} are very close, i.e. nearly degenerate⁹. This arises naturally since the energies are sampled independently and thus have no

⁸Here we sample the energies from a uniform distribution on the interval $[-l/2, l/2]$, but sampling them from a different distribution, such as normal distribution, is expected to give similar results.

⁹Note that even if the distribution is maximum at the origin, the probability of having two *exactly* degenerate levels is zero, since the set with $s = 0$ has zero measure.

repulsion. There are many possible definitions of what an *integrable* system is; for a complete discussion, see [109]. Generally, one expects an integrable quantum system to have an extensive number of conserved quantities, in terms of which the dynamics can be solved.

1.7.2 Bohigas Giannoni Schmitt conjecture

The *Bohigas-Giannoni-Schmitt* conjecture [110] states that *chaotic* quantum systems follow the spectral statistics of a Random Matrix Ensemble with the same underlying symmetries. In particular, by looking at the **nnLS** distribution one expects it to follow the Wigner's surmise (1.77)

$$\mathfrak{P}(s) = C_\beta s^\beta e^{-A_\beta s^2}, \quad (1.90)$$

where the Dyson index β is to be chosen accordingly to the underlying symmetries of the system: $\beta = 1$ for $T^2 = +1$, $\beta = 2$ for $T^2 = 0$, and $\beta = 4$ for $T^2 = -1$. The original conjecture was posed for systems with a well-defined semiclassical limit $\hbar_{\text{eff}} \rightarrow 0$ in which the dynamics is chaotic, like quantum billiards [111, 112] or the quantum kicked top [101, 113]. The most general Quantum Kicked Top [101] is given by a Floquet operator \hat{F} which describes the evolution of the system in one period—the kicks are periodic—and generally reads

$$\hat{F} = e^{-i\frac{t_x}{N}\hat{S}_x^2 - ia_x\hat{S}_x} e^{-i\frac{t_y}{N}\hat{S}_y^2 - ia_y\hat{S}_y} e^{-i\frac{t_z}{N}\hat{S}_z^2 - ia_z\hat{S}_z}, \quad (1.91)$$

which can show Poisson, GOE, or GUE statistics depending on the values of $\mathbf{a} = (a_x, a_y, a_z)$ and $\mathbf{t} = (t_x, t_y, t_z)$. As an example of integrable Kicked Top we consider $\mathbf{a} = (0, 0, 1)$ and $\mathbf{t} = (0, 0, 10)$, while as an example of GOE statistics we consider $\mathbf{a} = (1, 0, 1)$ and $\mathbf{t} = (10, 0, 0)$. The *pseudo-energies* ϵ_n can be obtained from the eigenvalues of the Floquet operator as $\hat{F}|\chi_n\rangle = e^{i\epsilon_n}|\chi_n\rangle$ [101], which give the **nnLS** as $s_n = \epsilon_{n+1} - \epsilon_n$.

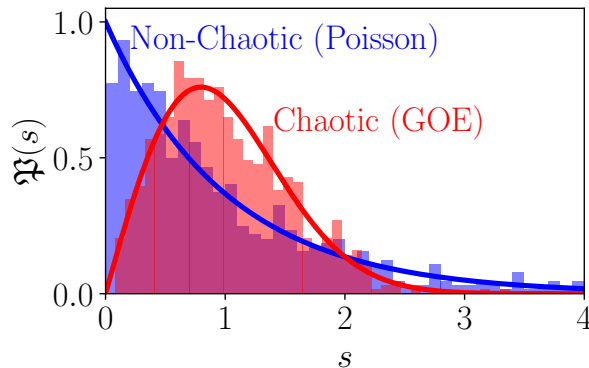


Figure 1.2. Nearest-neighbor level spacing distribution for a Quantum Kicked Top in the integrable (blue) and GOE (red) phases. The system has $S = 400$, and the pseudo energies were unfolded by a 3rd order polynomial with 50 bins.

The **nnLS** distributions for the Quantum Kicked Top in the integrable and chaotic phase are shown in Fig. 1.2, which shows good agreement with the Poisson (blue) and Wigner-Dyson (red) results, thus justifying the Berry-Tabor and Bohigas-Giannoni-Schmit conjectures. This plot clearly illustrates that in integrable systems one expects many small spacings, i.e., almost degenerate levels. In contrast, for chaotic systems the probability density at $s = 0$ vanishes, this arises from level repulsion, and grows linearly for small s as $\mathfrak{P}(s) \propto s$. Interestingly, a very large spacing $s \gtrsim 2$ is more probable when the levels are uncorrelated, a feature arising from the fact that a Gaussian approaches zero faster than an exponential.

1.8 Other measures of spectral Statistics

Although the **nnLS** is the most basic of all measures of spectral correlations, there are many other measures, which have their advantages and disadvantages. We briefly review now two that will be related to the analysis carried out in Chapter 4.

1.8.1 Short range: Spacing ratios

If one wants to see whether a given spectrum $\{E_n\}_{n=1}^N$ shows level repulsion, the level spacing distribution will in general show $\mathfrak{P}(0) = 0$ and a power law growth at small s . However, if one wants to compare with the Wigner surmise, the spectrum first has to be unfolded, as discussed in Sec. 1.6.2, to remove the dependence on the density of states $\rho(E)$. This is problematic since the unfolding procedure is not always reliable and it involves some extra processing of the spectral data, which may be a drawback in some occasions. For this reason, *Oganesyan and Huse* [114] introduced the **nnLS ratios** \tilde{r}_n as a numerical tool to determine whether a given spectrum shows level repulsion without the need for unfolding. The level spacing ratio is defined from two level spacings s_n, s_{n-1} as

$$r_n := \frac{\min(s_n, s_{n-1})}{\max(s_n, s_{n-1})}, \quad (1.92)$$

which can equivalently be re-written in terms of the ratio $\tilde{r}_n = \frac{s_n}{s_{n-1}}$ as $r_n = \min(\tilde{r}_n, \tilde{r}_n^{-1})$ [115, 116]. The advantage of the ratio is that by comparing s_n with s_{n-1} , all the energies have approximately the same density of states $\rho(E_n)$, and thus this contribution is removed from \tilde{r}_n . The probability distribution for the ratios \tilde{r}_n can be computed for RMT [115]

$$\mathfrak{P}^{(\beta)}(\tilde{r}) = \frac{1}{Z_\beta} \frac{(\tilde{r} + \tilde{r}^2)^\beta}{(1 + \tilde{r} + \tilde{r}^2)^{1+\frac{3}{2}\beta}}, \quad (1.93)$$

where Z_β is some normalization constant [115], while for Poisson “ $\beta = 0$ ” it reads [114, 115]

$$\mathfrak{P}^{(0)}(\tilde{r}) = \frac{1}{(1 + \tilde{r})^2}. \quad (1.94)$$

Similarly to the level spacing distribution, the ratio distribution vanishes at $\tilde{r} = 0$ for RMT, while it is maximum at $s = 0$ for Poisson, thus showcasing level repulsion. To compare numerical data with RMT, it is also customary to introduce the average of the ratio r_n as a simple measure of spectral correlations, in particular, the exact values for the average read [114, 115]

$$\langle r \rangle = \begin{cases} 2 \ln 2 - 1 \approx 0.39 & \text{Poisson,} \\ 4 - 2\sqrt{3} \approx 0.53 & \text{GOE,} \\ \frac{2\sqrt{3}}{\pi} - \frac{1}{2} \approx 0.60 & \text{GUE,} \\ \frac{32\sqrt{3}}{15\pi} - \frac{1}{2} \approx 0.67 & \text{GSE.} \end{cases} \quad (1.95)$$

1.8.2 Long range: Number variance

Correlations are present all over the spectrum of random matrices, with the nnLS being only one indication of the correlation to nearest neighbors. A more thorough study of spectral correlations in random matrices or quantum chaotic systems necessitates measures of correlations at all possible spectral distances. Throughout the thesis, we will study the spectral form factor in depth, encompassing all correlations. However, for completeness, we review other measures of long-range correlations.

The easiest of such measures is the *number variance* $\Sigma^2(\epsilon)$, introduced by Dyson and Mehta [99, 117], which is given in terms of the number of levels $N(x_s, \epsilon) = \sum_{n=1}^N \Theta(E_n \in [x_s, x_s + \epsilon])$ on the interval $[x_s, x_s + \epsilon]$, where x_s is the starting energy of the interval and ϵ is the length of the energy window. The number variance is therefore defined as

$$\Sigma^2(\epsilon) := \mathbb{E}_{x_s} (N(x_s, \epsilon)^2) - \mathbb{E}_{x_s} (N(x_s, \epsilon))^2, \quad (1.96)$$

where the average is performed over the starting points of the interval. For Poisson, this quantity is well-known to grow linearly $\Sigma^2(\epsilon) = \epsilon$, while for the random matrix ensembles, it behaves logarithmically $\Sigma^2(\epsilon) \sim \log(\epsilon)$, see [99] for the exact expression.

1.9 Spectral Form Factor

1.9.1 The many faces of the Spectral Form Factor

The spectrum arising from a random matrix is not only correlated to its nearest neighbors, but instead shows correlations between all the different eigenvalues. Some indicators, such as the number variance discussed in Sec. 1.8.2, focus on the long-range spectral correlations. However, a more interesting one is the *Spectral Form Factor* (SFF), which takes all the possible energy ranges into account. Berry studied this quantity [118] and can be computed analytically for random matrices [103]. This quantity was also introduced as a numerical tool by *Leviandier et al.* [119], which allowed for the analysis of correlations in spectra with possibly missing levels [120–122].

There are many possible different definitions of the **SFF**, at a finite temperature T it can be written in terms of the partition function $Z_\beta = \sum_{n=1}^N e^{-\beta E_n}$ analytically continued to complex β [123–126]

$$S_{\beta,t} := \left\langle \left| \frac{Z_{\beta+it}}{Z_\beta} \right|^2 \right\rangle = \left\langle \frac{1}{Z_\beta^2} \sum_{m,n=1}^N e^{-\beta(E_m+E_n)} e^{-it(E_m-E_n)} \right\rangle, \quad (1.97)$$

where $\beta = 1/(k_B T)$ is the inverse temperature, and $\langle \bullet \rangle$ denotes a suitable average, as discussed more carefully in Sec. 4.3.1, which is needed since the **SFF** is *not* self-averaging [127]. Interestingly, we found that, similarly to the universal bound on the Lyapunov exponent by *Maldacena, Shenker, and Stanford* [128], the early time exponential decay of the **SFF** $S_{\beta,t} \sim e^{-\eta t}$ is also universally bounded by [4]

$$\eta \leq \frac{\pi}{2\beta}. \quad (1.98)$$

The **SFF** that we will consider mostly in Chapter 4 will be at infinite temperature $\beta = 0$, which simply reads

$$S_t := \frac{1}{N^2} \left\langle \sum_{m,n=1}^N e^{-it(E_m-E_n)} \right\rangle. \quad (1.99)$$

For a generic system, this quantity shows a very distinctive shape, at time zero it is $S_0 = 1$, due to the normalization, after that it starts decaying in the slope, showing some oscillations. Then, if the system is chaotic, it grows back in a *linear ramp*, and saturates to a plateau given by $\lim_{t \rightarrow \infty} S_t = \frac{1}{N}$. The plateau arises due to the different oscillation frequencies $\omega_{mn} = E_m - E_n$ not having rational relations with each other and thus cancelling each other out. In the case of certain integrable models, such as the Harmonic Oscillator or the Calogero-Sutherland model [4, 129], there exist frequencies such that their ratio is rational $\omega_{mn}/\omega_{kl} \in \mathbb{Q}$, these oscillations are in phase and thus in the long-time limit they do not simply cancel out, in this case the **SFF** does not show a plateau but rather oscillatory behavior. Lastly, in a generic integrable system, the oscillation frequencies will not show rational ratios. Thus the **SFF** converges to a plateau, but since the spectrum does not show level-repulsion, it will not show a linear ramp.

In general, one can consider a general filtering function for the spectrum $f(E)$ and define the **SFF** as [130]

$$S_t = \frac{1}{Z} \left\langle \left| \sum_{n=1}^N f(E_n) e^{-iE_n t} \right|^2 \right\rangle, \quad (1.100)$$

where Z is simply a normalization factor. The introduction of filters or different averages is equivalent to breaking unitarity of the evolution [131], which reduces the effects of quantum noise, rendering the **SFF** to be self-averaging, a feature observed in [132]. Lastly, the **SFF** can be understood as a fidelity for a special initial state, such as the *coherent Gibbs*

state $|\psi_\beta\rangle = \sum_n \frac{e^{-\frac{\beta}{2}E_n}}{\sqrt{Z_\beta}} |E_n\rangle$, or the *Thermofield Double State* $|\text{TFD}_\beta\rangle = \sum_n \frac{e^{-\frac{\beta}{2}E_n}}{\sqrt{Z_\beta}} |E_n\rangle_1 \otimes |E_n\rangle_2$ [129]

$$S_{\beta,t} = \left| \langle \psi_\beta | e^{-i\hat{H}t} | \psi_\beta \rangle \right|. \quad (1.101)$$

Lastly, perhaps the most common definition of the **SFF** is as a Fourier Transform of the two-point correlation function $\langle \rho(E)\rho(E') \rangle$ of the level density $\rho(E)$ as

$$S_{\beta,t} = \iint dE dE' \langle \rho(E)\rho(E') \rangle e^{-\beta(E+E')} e^{-it(E-E')}. \quad (1.102)$$

1.9.2 Connected SFF

The **SFF** can generally be split in three main contributions¹⁰ [124, 126, 129]

$$S_{\beta,t} \propto \langle Z_{2\beta} \rangle + \langle Z_{\beta+it} \rangle \langle Z_{\beta-it} \rangle + S_{\beta,t}^{(c)}, \quad (1.103)$$

where the three terms correspond to the *plateau*, *disconnected*, and *connected* parts of the **SFF**. The most interesting part is the connected one, defined from the *connected* two point correlation function $\langle \rho(E)\rho(E') \rangle_c = \langle \rho(E)\rho(E') \rangle - \langle \rho(E) \rangle \langle \rho(E') \rangle$

$$S_{\beta,t}^{(c)} = \iint dE dE' \langle \rho(E)\rho(E') \rangle_c e^{-\beta(E+E')} e^{-it(E-E')}. \quad (1.104)$$

The connected part encodes the universal features of the spectral statistics of the model; these are the correlations that are well described by **RMT**. The level repulsion between the eigenvalues gives rise to the *universal ramp* of the **SFF**, a feature widely considered a signature of quantum chaos. In particular, for the Gaussian ensembles of Random Matrices, one can compute analytical expressions for the connected **SFF** $b(t)$ [103]. We adapt these by setting the plateau time to $t_p = 2\pi$ —which is the Heisenberg or plateau time for an unfolded spectrum with $\int_0^\infty s\mathfrak{P}(s)ds = 1$ —and the plateau value to $1/N$. The

¹⁰Here we disregard the proportionality factors since they obscure our reasoning, particularly because averages of the form $\left\langle \frac{Z_{\beta+it}}{Z_\beta} \right\rangle$ cannot be computed analytically and one instead takes the “annealed” averages [126] $\left\langle \frac{Z_{\beta+it}}{\langle Z_\beta \rangle} \right\rangle$. These two averages are approximately equal in the high temperature $\beta \ll 1$ limit. However, in Chap. 4 we will only deal with infinite T and this will not be an issue, so we will not comment on it. A solution to this issue is to multiply by a term of the form $\frac{\langle |Z_\beta|^2 \rangle}{\langle Z_\beta \rangle^2}$ as in [130].

connected SFFs read [133]

$$b_{\text{GOE}}(t) = \begin{cases} \frac{t}{\pi N} - \frac{t}{2\pi N} \log \left(1 + \frac{t}{\pi} \right) & \text{for } t \leq 2\pi, \\ \frac{2}{N} - \frac{t}{2\pi N} \log \frac{t + \pi}{t - \pi} & \text{for } t > 2\pi, \end{cases} \quad (1.105a)$$

$$b_{\text{GUE}}(t) = \begin{cases} \frac{t}{2\pi N} & \text{for } t \leq 2\pi, \\ \frac{1}{N} & \text{for } t > 2\pi, \end{cases} \quad (1.105b)$$

$$b_{\text{GSE}}(t) = \begin{cases} \frac{t}{4\pi N} - \frac{t}{8\pi N} \log \left(1 - \frac{|t|}{2\pi} \right) & \text{for } t \leq 4\pi, \\ \frac{1}{N} & \text{for } t > 4\pi. \end{cases} \quad (1.105c)$$

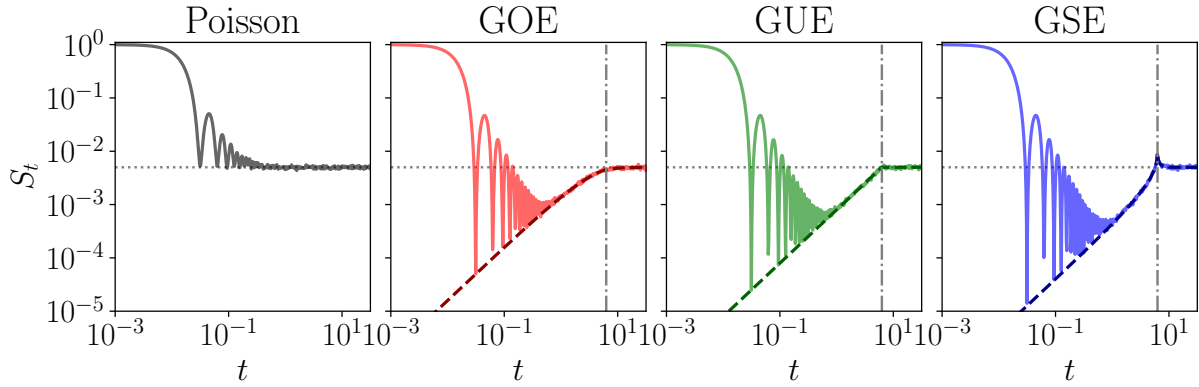


Figure 1.3. Spectral Form Factor for the Random Matrix Ensembles: The SFF numerically generated (solid lines), along with the universal connected SFF $b(t)$ (1.105) (dashed lines). We indicate the plateau value $S_{t \rightarrow \infty} = \frac{1}{N}$ (dotted gray), as well as the Heisenberg or plateau time $t_p = 2\pi$ (dash dotted gray). The numerical results are obtained for $N = 200$ and averaged over $N_{\text{av}} = 500$ realizations of the RMT ensemble. The spectrum was unfolded analytically, see Sec. 1.6.2.

Figure 1.3 shows the time evolution of the SFF for the different ensembles. The three main contributions of the SFF now have a clear interpretation: the plateau sets the saturation value at long times, the disconnected SFF is responsible for the early time decay and the oscillations of the SFF, and the connected SFF gives rise to the universal ramp. In Fig. 1.3 we see that the Poisson ensemble shows no correlation hole, thus saturating directly to the plateau value. In contrast, the other ensembles display a *correlation hole* with the characteristic linear ramp. This ramp is well characterized by the connected SFF $b(t)$ (dashed lines). Interestingly, the different symmetries of the ensembles cause a difference in the transition from the ramp to the plateau: GOE shows a smooth transition; while GUE shows a sharp transition, which is called the *kink*; lastly, GSE shows an

increase around $t_p = 2\pi$, before saturating to the plateau, which is called the *spike*. These are related to the different amounts of level repulsion between the eigenvalues in the different **RMT** ensembles. Therefore, the presence of the correlation hole and the ramp is widely regarded as one of the *signatures* of Quantum Chaos [118, 133–135] even when no semiclassical limit is available [136].

Let us now address a natural question: “*do we need to perform spectral unfolding to use the SFF as a signature of quantum chaos?*” The answer is that it depends on what we want to use the **SFF** for: if we want to inspect a plot looking for the correlation hole and we will take that observation as a signature of quantum chaos, then we do not need to perform unfolding, as long as the spectrum shows level repulsion, the **SFF** will show a correlation hole with a linear ramp; However, if we want to compare to the analytical expressions from **RMT** for the connected SFF (1.105), then we do need to perform unfolding, since the dependence on the density of states $\rho(E)$ will give a non-universal contribution to the **SFF**, which cannot be well captured by the universal **RMT** results.

1.10 Out of Time Order Correlators

1.10.1 General definition of the OTOC

One fundamental limitation of taking the **SFF**, or the **nnLS** distribution, as a signature of Quantum Chaos is that we do not have a natural notion of *Lyapunov exponent* λ , as we have classically. Thus the classical-quantum correspondence for a chaotic system remained elusive. To bridge the notions of classical and quantum chaos, Kitaev [137, 138] proposed to study an object of the form

$$C_t := -\langle [\hat{A}_t, \hat{B}_0]^2 \rangle, \quad (1.106)$$

where $\hat{A}_t = e^{+i\hat{H}t} \hat{A} e^{-i\hat{H}t}$ and \hat{B}_0 are two hermitian operators in Heisenberg picture, but critically the former is evaluated at time t . In contrast, the latter is evaluated at time 0, in here $\langle \bullet \rangle$ represents a suitable average, which will be particularized to different cases. This quantity is called an *Out-of-Time-Order-Correlator* (**OTOC**). The quantity is composed of two types of terms

$$C_t = \langle \hat{A}_t \hat{B}_0 \hat{B}_0 \hat{A}_t \rangle + \langle \hat{B}_0 \hat{A}_t \hat{A}_t \hat{B}_0 \rangle - 2\text{Re}(\langle \hat{A}_t \hat{B}_0 \hat{A}_t \hat{B}_0 \rangle), \quad (1.107)$$

where the first two terms are time-ordered and the last term is the one that is genuinely out of time order, therefore it is also sometimes called the **OTOC** [139].

This quantity had been studied already by Larkin and Ovchinnikov [140] in the context of a quasiclassical theory of superconductivity, but had not received much attention back then. The reason why such a quantity is interesting is that if the system shows a Lyapunov exponent, it is expected to grow exponentially as

$$C_t \sim \varepsilon e^{\lambda t}, \quad (1.108)$$

for a certain window of times between the dissipation $t_d \sim \lambda^{-1}$ and the *Ehrenfest* or scrambling time $t_E \sim \lambda^{-1} \log(\frac{1}{\epsilon})$ [128]. The parameter $\epsilon \ll 1$ is small, so there is a long range of times in the window $[t_d, t_E]$, to which we can fit a Lyapunov exponent. The existence of this small parameter implies that the Lyapunov regime can only be seen in systems with a semiclassical limit, as we will introduce in the next section, or with a large N limit such as the *Sachdev-Ye-Kitaev* model [138, 141–143].

If the operators $\hat{A}_{x,t}$ and $\hat{B}_{0,0}$ are space-separated, one expects the OTOC to show a light cone as

$$C(x,t) = -\langle [\hat{A}_{x,t}, \hat{B}_{0,0}]^2 \rangle \sim e^{\lambda(t-|x|/v_B)}, \quad (1.109)$$

where v_B is the *butterfly velocity*, characterizing the speed of spread of information in these systems, and related to the Lieb-Robinson bound [144]. Recently, it has been found that many other types of behavior are possible beyond this linear light cone [145–147].

For systems with small local Hilbert space dimension, such as spin $\frac{1}{2}$ spin chains, there is in general no Lyapunov regime, however, even in these systems, OTOC's still contain relevant information, particularly related to the spreading of quantum information in the system and operator growth [148] which can also be conveniently formulated in Krylov space [5, 149]. Consider the case of a spin chain, let us take an initial local operator in site j , e.g., $\hat{A}_{j,0} = \hat{\sigma}_x^{(j)}$, and a Hamiltonian \hat{H} with nearest-neighbor interactions, the time evolution in the Heisenberg picture gives

$$\hat{A}_{j,t} = \hat{e}^{+i\hat{H}t} \hat{\sigma}_x^{(j)} e^{-i\hat{H}t} = \hat{\sigma}_x^{(j)} - it[\hat{H}, \hat{\sigma}_x^{(j)}] - \frac{t^2}{2}[\hat{H}, [\hat{H}, \hat{\sigma}_x^{(j)}]] + \dots \quad (1.110)$$

so we see that at time zero the operator only lives on site j , at times of order $\mathcal{O}(t)$ it involves operators in the sites $[j-1, j, j+1]$, at times of order $\mathcal{O}(t^2)$ operators in the $[j-2, j-1, j, j+1, j+2]$ sites, and so on [148]. This phenomenon is known as *quantum information scrambling*, and the idea is that local information such as that codified in the operator $\hat{\sigma}_x^{(j)}$, becomes increasingly non-local under many-body dynamics, and cannot be recovered by local measurements, only by global ones.

The OTOC then only starts to grow when the time evolution of \hat{A}_t reaches the support of the operator \hat{B} , thus encoding locality in many-body dynamics.

1.10.2 Connection to the classical limit: A semiclassical argument

The reason why this quantity is related to the Lyapunov can be seen choosing the operators $\hat{A} = \hat{x}$ and $\hat{B} = \hat{p}$, and, through the correspondence principle, we know that in the semiclassical limit the commutator is related to the Poisson bracket $-\frac{i}{\hbar}[\bullet, \bullet] \leftrightarrow \{\bullet, \bullet\}_{\text{PB}}$. Recall that for a classical phase space with two degrees of freedom (x, p) , the Poisson bracket is defined as $\{f, g\}_{\text{PB}} := \frac{\partial f}{\partial x} \frac{\partial g}{\partial p} - \frac{\partial f}{\partial p} \frac{\partial g}{\partial x}$, which implies that the semiclassical $\hbar_{\text{eff}} \rightarrow 0$

of the OTOC reads [128, 140]

$$C_t = -\langle [\hat{x}_t, p_0]^2 \rangle \sim \varepsilon e^{\lambda t} \xrightarrow{\hbar_{\text{eff}} \rightarrow 0} C_t^{(\text{cl})} = \hbar^2 \langle \{x_t, p_0\}_{\text{PB}}^2 \rangle = \hbar^2 \left\langle \left(\frac{\partial x_t}{\partial x_0} \right)^2 \right\rangle \sim \hbar^2 e^{2\lambda_{\text{cl}} t}, \quad (1.111)$$

where $\frac{\partial x_t}{\partial x_0}$ is a quantity characterizing the sensitivity to initial conditions of a classical system. From this semiclassical argument, we see that the quantum Lyapunov exponent is related to the classical one as $\lambda \approx 2\lambda_{\text{cl}}$ and that the small parameter is given by Planck's constant $\varepsilon = \hbar^2$. This classical argument can be refined through a phase space formulation [150], which shows that the Lyapunov growth is the dominant term of the expansion, until the Ehrenfest time t_E at which quantum corrections become dominant.

1.10.3 A Lyapunov exponent does not imply chaos

The connection between the classical and quantum Lyapunov exponents is not as transparent as it seems from this simple semiclassical argument, since the classical Lyapunov is the average over phase space of the logarithm of the sensitivity, and the quantum one is the log of the average over phase space, the relation between the Lyapunov exponents actually holds as [151]

$$\lambda \geq 2\lambda_{\text{cl}}, \quad (1.112)$$

which was numerically observed in a chaotic system with a well-defined semiclassical limit, the quantum kicked rotor [152]. The interpretation of this Lyapunov exponent as a measure of chaos is, however, weakened by the fact that there exist several integrable models [153, 154], such as the Lipkin-Meshkov-Glick model, which we will introduce in the next section, that show a positive quantum Lyapunov exponent. Xu *et al.* showed that unstable saddle points in phase space provide a possible mechanism for the emergence of exponential growth of OTOC's without chaotic behavior. Indeed this provides a further lower bound on the Lyapunov exponent

$$\lambda \geq \lambda_{\text{saddle}}, \quad (1.113)$$

and even in chaotic systems, the scrambling can be dominated by saddle points, i.e., the bound by the properties of the saddle (1.113) can be tighter than the bound by the classical Lyapunov exponent (1.112), such as in the Feingold-Peres model [151].

This leads to a separation in terminology between *scrambling*, which refers here to exponential growth of out of time order correlators, and *quantum chaos*, which is most typically defined through the connection to random matrices through the Bohigas-Giannoni-Schmitt conjecture [110]. The OTOC, as a quantity which is related to the Lyapunov exponent, does of course carry certain information about quantum chaos, but it is a *necessary, not sufficient* condition for chaos [155]. This is similar to the case in classical chaos, a positive Lyapunov exponent is one of the necessary conditions for chaos, but there are

integrable systems which have positive Lyapunov exponents, e.g. an inverted harmonic oscillator, for this reason in a reasonable definition of classical chaos one also asks for extra conditions, such as: *aperiodicity* of the trajectories at long times [156], the system to present *mixing* [105] or even *topological transitivity* and *dense periodic points* such as in Devaney's definition [157], which imply exponential sensitivity on initial conditions [158].

1.10.4 On averaging and different OTOCs

There are many different types of OTOCs, which are used in different contexts. In Sec. 2.6.3, we will introduce the ones relevant for this thesis. One of the reasons why different OTOCs are introduced is due to various choices for the thermal average; let us comment on these briefly now.

The most typical case is to consider the thermal average $\langle \bullet \rangle_\beta = \text{Tr}(\bullet \hat{\rho}_\beta)$, which involves an average with a thermal state $\hat{\rho}_\beta = \frac{1}{Z_\beta} e^{-\beta \hat{H}}$, which also includes the infinite temperature limit $\beta = 0$, in which $\hat{\rho}_\beta$ becomes the maximally mixed state $\hat{\rho}_{\beta=0} = \frac{\hat{1}}{N}$. However, to obtain one of the most striking results associated with the quantum Lyapunov exponent, Maldacena, Shenker, and Stanford [128] used a *regularized* version of the 4-point OTOC as

$$\tilde{C}_{\beta,t}^{(\text{reg})} = \frac{1}{Z_\beta} \text{Tr}(\hat{A}_t e^{-\frac{\beta}{4} \hat{H}} \hat{B}_0 e^{-\frac{\beta}{4} \hat{H}} \hat{A}_t e^{-\frac{\beta}{4} \hat{H}} \hat{B}_0 e^{-\frac{\beta}{4} \hat{H}}). \quad (1.114)$$

This regularization is needed in quantum field theories since evaluating the standard thermal average leads to some operators being inserted at the same spacetime point, which can produce short-distance divergences in quantum field theory [159]. Another common regularization strategy is to split the thermal factor into two

$$C_{\beta,t}^{(\text{reg})} = \frac{1}{Z_\beta} \text{Tr}([\hat{A}_t, \hat{B}_0] e^{-\frac{\beta}{2} \hat{H}} [\hat{A}_t, \hat{B}_0] e^{-\frac{\beta}{2} \hat{H}}). \quad (1.115)$$

A one-parameter family of possible regularizations was introduced by Tsuji *et al.* [160], which leads to an alternative proof of the Maldacena-Shenker-Stanford bound [128]. The dependence of the Lyapunov exponent on the different regularization contours and the difference between regularized and unregularized Lyapunov exponents have been studied in [161–163].

1.10.5 The bound on chaos

Maldacena, Shenker, and Stanford [128] proved that the Lyapunov exponent of a given system cannot be arbitrarily large, and that it fulfills the universal bound

$$\lambda \leq \frac{2\pi}{\beta \hbar}. \quad (1.116)$$

This bound is physically motivated from the point of view of holography, in which black holes are conjectured to be the fastest scramblers in nature [164], i.e., those showing fastest growth of **OTOCs**, and their Lyapunov exponent is $\frac{2\pi}{\beta\hbar}$, the universal upper bound. Even more surprisingly, any system that saturates the bound (1.116), such as the Sachdev Ye Kitaev model for low temperature [142, 143], is conjectured to be holographically dual to a black hole. The early time exponential decay of the **SFF**, $S_t \sim e^{-\eta t}$ also obeys a very similar universal bound $\eta \leq \frac{\pi}{2\beta\hbar}$ [4, 165]. This bound can be understood simply in the semiclassical limit [166, 167], derived through different regularizations [160] and relates to the fluctuation dissipation theorem [168, 169].

1.10.6 Dissipative OTOC

A natural extension of **OTOC**'s is to consider the time evolution to be given by a **CPTP** map $\mathcal{E}_t^\dagger[\bullet] = e^{\mathcal{L}^\dagger t}$ instead of being simply unitary. In this case the dissipative **OTOC** reads

$$C_t := -\langle [\mathcal{E}_t^\dagger(\hat{A}), \hat{B}]^2 \rangle. \quad (1.117)$$

This quantity was originally studied by Syzranov *et al.* [170] for finite open systems in the dephasing case, and afterwards studied for the average bipartite case [171], for spreading of quantum information in spin chains [172, 173], these works seem to suggest a non-trivial interplay between growth due to scrambling and decay due to decoherence [174].

Recap of main concepts of the introduction

- The most general *completely positive, trace preserving* (**CPTP**) quantum channel can be written in Kraus form as (1.1)

$$\mathcal{E}[\bullet] = \sum_{j=1}^{N_K} \hat{K}_j \bullet \hat{K}_j^\dagger.$$

- The *Gorini-Kossakowski-Sudarshan-Lindblad* (**GKSL**) master equation (1.6) describes the most general generator of a Markovian **CPTP** map and reads

$$\partial_t \hat{\rho}_t = -i[\hat{H}, \hat{\rho}_t] + \sum_j^{N_c} \gamma_j \left(\hat{L}_j \hat{\rho}_t \hat{L}_j^\dagger - \frac{1}{2} \{ \hat{L}_j^\dagger \hat{L}_j, \hat{\rho}_t \} \right) =: \mathcal{L}[\hat{\rho}],$$

where $\mathcal{L}(\bullet)$ is the *Lindbladian* superoperator.

- The increment of the Wiener process, also called simply Wiener process $dW_t = \xi_t dt$, can be understood formally in two different conventions for *stochastic calculus*:

- In the Itō convention, it obeys the Itō rule $dW_t^2 = dt$, which changes the standard rules of calculus, and is independent of the variable $\mathbb{E}(dW_t f(x_t)) = \mathbb{E}(dW_t) \mathbb{E}(f(x_t)) = 0$.
- In the Stratonovich convention, we keep the standard rules of calculus, at the price of averages of the form $\mathbb{E}(x_t \circ \xi_t)$ being cumbersome to compute using Novikov's formula (1.26).
- A *non-Hermitian* \mathcal{PT} symmetric Hamiltonian is invariant under the combined action of parity and time-reversal $\mathcal{PT}[\hat{H}] = \hat{H}$. It has a phase with purely real spectrum (\mathcal{PT} unbroken) and one with purely imaginary spectrum (\mathcal{PT} broken). A system has *passive* \mathcal{PT} symmetry if the Hamiltonian with a certain imaginary constant $\hat{H} + iE_0$ has \mathcal{PT} symmetry. A non-Hermitian Hamiltonian can be realized through continuous quantum measurements and post-selection of the jumps. The *Dissipative Qubit*

$$\hat{H}_{\text{DQ}} = \begin{pmatrix} 0 & J \\ J & -i\Gamma \end{pmatrix} = J\hat{\sigma}_x - i\Gamma |e\rangle\langle e|,$$

illustrates many of the features of non-Hermitian Hamiltonians and is amenable to experimental realization.

- There are three Gaussian ensembles of random matrices, distinguished by the Dyson index: **GOE** $\beta = 1$, **GUE** $\beta = 2$, and **GSE** $\beta = 4$. The joint probability distribution of their eigenvalues is (1.76)

$$\rho_\beta(E_1, \dots, E_N) = C \prod_{1 \leq i < j \leq N} |E_i - E_j|^\beta e^{-A \sum_{i=1}^N E_i^2}.$$

The spectrum of random matrices shows level repulsion, which can be studied through their *level spacing distribution*, with the nearest neighbor level spacings $s_n = E_{n+1} - E_n$, which obeys the *Wigner surmise* (1.77)

$$\mathfrak{P}_\beta(s) = C_\beta s^\beta e^{-A_\beta s^2}.$$

To compare with this analytical expression, a general spectrum has to be *unfolded*, cf. Sec. 1.6.2, either numerically or analytically.

- The study of quantum chaos builds on two conjectures, cf. Sec 1.7
 - The *Berry-Tabor* states that integrable quantum systems show spectral statistics consistent with the *Poisson* ensemble in which each of the energies is sampled independently.
 - The *Bohigas-Giannoni-Schmitt* conjecture states that chaotic quantum systems have the spectral statistics predicted by random matrices.

- One of the most commonly used signatures of quantum chaos is the *spectral form factor* (**SFF**) defined for infinite temperature as

$$S_t := \frac{1}{N^2} \left\langle \sum_{m,n=1}^N e^{-it(E_m - E_n)} \right\rangle,$$

which shows a universal linear ramp for random matrices, and thus the ramp can be taken as a signature that the quantum system is chaotic.

- The *out-of-time-order correlator* (**OTOC**) is a correlation function defined from two operators in the Heisenberg picture as (1.106)

$$C_t = -\langle [\hat{A}_t, \hat{B}_0]^2 \rangle.$$

If this quantity grows exponentially in a certain window of time, it defines the *quantum Lyapunov exponent* λ as

$$C_t \sim e^{\lambda t}.$$

The time evolution can be generalized by a dissipative quantum channel, thus generalizing this quantity to a *dissipative OTOC*.

Chapter 2

Stochastic Hamiltonians: Beyond the noise average

“And if the cloud bursts thunder in your ear,
You shout and no one seems to hear,
And if the band you’re in starts playing different tunes,
I’ll see you on the dark side of the moon”
Pink Floyd

Abstract of this chapter

- The main objective of this chapter is to characterize the dynamics of stochastic Hamiltonians of the form $\hat{H}_t = \hat{H}_0 + \sqrt{2\gamma}\xi_t\hat{L}$ going beyond the noise average. For this, we define the **Stochastic Operator Variance (SOV)** as

$$\Delta\hat{A}_t^2 = \mathbb{E}(\hat{A}_t^2) - \mathbb{E}(\hat{A}_t)^2.$$

This observable characterizes the deviation of trajectories from the average. We show that this quantity can be expressed in terms of the adjoint Liouvillian \mathcal{L}^\dagger as

$$\Delta\hat{A}_t^2 = e^{\mathcal{L}^\dagger t}[\hat{A}^2] - (e^{\mathcal{L}^\dagger t}[\hat{A}])^2.$$

- The SOV’s of two different operators fulfill the uncertainty-like relationship

$$\langle\Delta\hat{A}_t^2\rangle\langle\Delta\hat{B}_t^2\rangle \geq \frac{D_+^2(\hat{A}, \hat{B}) - D_-^2(\hat{A}, \hat{B})}{4},$$

where the lower bound is determined by the difference between the time-evolved (anti)commutator and the (anti)commutator of the time-evolved operators

$$D_\pm(\hat{A}, \hat{B}) = \langle\mathcal{E}_t^\dagger([\hat{A}, \hat{B}]_\pm)\rangle - \langle[\mathcal{E}_t^\dagger(\hat{A}), \mathcal{E}_t^\dagger(\hat{B})]_\pm\rangle,$$

where we use the general notation for (anti)commutators $[\hat{A}, \hat{B}]_\pm = \hat{A}\hat{B} \pm \hat{B}\hat{A}$.

- The **SOV** is related to a dissipative Out-of-Time-Order-Correlator (**OTOC**) C_t through the **SOV-OTOC connection**

$$\frac{1}{N} \partial_t \text{Tr}(\Delta \hat{A}_t^2) = 2\gamma C_t.$$

- We study as an example the *Lipkin-Meshkov-Glick LMG* model subject to energy dephasing. In the thermodynamical limit, we find that the Lyapunov exponent of the origin of the system is well-modeled by the SOV through the SOV-OTOC relation. As the noise increases, the Double Well (**DW**) phase stabilizes, i.e., its Lyapunov exponent becomes negative. In contrast, the Single Well (**SW**) phase becomes unstable and acquires a positive-Lyapunov exponent. This noise-induced stabilization is analogous to the *Kapitza pendulum*, but here obtained from stochastic driving.

This chapter studies quantum systems coupled to classical noise beyond the noise average. The standard setup in quantum mechanics assumes that we have full knowledge of the Hamiltonian generating the system's evolution. This is, however, an idealization, since even in the most controlled quantum setups, the parameters of the evolution are subject to errors and fluctuations. The unavoidable presence of noise motivates referring to current quantum devices as *Noisy Intermediate Scale Quantum* (NISQ) devices [175, 176]. In the context of Quantum Computing, although the errors that occur in quantum circuits are modeled in discrete time, the quantum system in the lab does not evolve in discrete chunks of time but rather continuously in time. It is subject to different sources of noise. These can be accounted for in terms of *Stochastic Hamiltonians* [35] which include a noisy term in the generator of the evolution, and can be understood as arising from the different unravelings of the master equation [42, 72, 75, 177–179]. When we consider an average over the noise, the equation of motion for the system reduces to a master equation for the noise-averaged state of the system. In particular, if the noise on the Hamiltonian is *white noise*, the master equation will be Markovian, and we can recover certain GKSL master equations.

Here, we go beyond the paradigm of studying noise-averaged evolution and characterize the noise-induced fluctuations. In particular, we will focus on the *Stochastic Operator Variance*, an observable that we introduce to characterize the variance (over the classical noise) of any given quantum mechanical operator in the Heisenberg picture. We will show how this quantity characterizes scrambling properties, particularly the Lyapunov exponent, and obeys a generalized uncertainty relation.

2.1 A story for the results of this chapter

A quantum state¹ can be represented by different numbers on a matrix. Basically, it is a “*table of numbers*”, each entry having two values, the real and imaginary part of a

¹For the sake of simplicity in the analogy, let us consider only finite-dimensional Hilbert spaces.

complex number. Your phone's screen is a familiar device that acts similarly; each pixel in the screen contains three values for the amount of red, green, and blue it should show. Therefore, a quantum state can be conceived as analogous to a picture on your phone. The main purpose of studying quantum dynamics is to understand how different quantum states evolve in time, i.e., to witness the sequence of quantum “pictures” as time passes, essentially like a film.

There is a myriad of possible quantum dynamics, but in a broad sense, they can be classified into *unitary* and *dissipative* dynamics. The defining feature of unitary dynamics is that no matter the current picture in the film, it is always possible to “*rewind*” the dynamics and find the first photograph of the movie. On the other hand, dissipative dynamics tends to a particular end, which physicists call a *steady state*. There can be several possible ends, but in many relevant cases, there is a single ending to the dynamics—in other words, we know the end of the story, like in *Titanic*. Note that the existence of a single end to the story prevents us from rewinding time and finding out what the first frame of the movie was, since different starting images could have led to the same ending.

Imagine that we were recording an animal daily, say a rabbit, to track its position in a forest. Every day, the animal sleeps in the same den, and each day it goes in a different direction: perhaps some days it goes to a river nearby, other days to a field to eat some wheat, or runs away from a predator. At the end of the day, the rabbit returns to its den, and everything repeats the next morning, so each film is, in a sense, “*unitary*”. Now imagine that the films from all the different days were played simultaneously on your phone; in other words, that you only had access to the film *averaged* over all the days. You would see something quite weird: the rabbit would appear to split into many copies and, at the same time, go to the river, go to the field, and run from the predator. However, watching all of the recordings one by one would take a lot of time. In quantum systems subject to noise, the story is quite similar; we let them evolve with many realizations of a random process, and then look at the average over all possible random processes. In this chapter, we propose to go beyond the average picture and understand deviations from it, without the full complexity of considering all the possible realizations of the random process. To this end, we introduce a quantity, which we call the *Stochastic Operator Variance*, which characterizes how far away the trajectories of the rabbit are from the “average” film. For quantum systems, it captures how much we can trust the average evolution.

Figure 2.1 provides a pictorial illustration of this concept². We have three rabbits with different “*levels of randomness*” which illustrate how strong the noise in our quantum evolution is. The way to compute the quantum variance of each of these is: at a given time, the rabbit reached several points, but when we measure where the rabbit is on a given day, it can only be in one place, and thus the state “*collapses*” and we find one

²For completeness, let us describe how the trajectories in the “cellular automaton” were generated. We have a 22×22 grid, and we generate $N_{\text{trajs}} = 40$ trajectories with $N_t = 20$ time-steps. At each step we generate a random number $r \sim \mathcal{U}([0, 1])$ and if it is smaller than a certain threshold $r < p_{\text{th}}$ we generate a random evolution which uniformly chooses either 0 or 1 for each of the directions x and y , if the random number is larger than the threshold $r > p_{\text{th}}$ we move in diagonal $x_{i+1} = x_i + 1$, $y_{i+1} = y_i + 1$. Rabbit 1 is not very random with $p_{\text{th}} = 0.05$, Rabbit 2 has $p_{\text{th}} = 0.4$ and Rabbit 3 has $p_{\text{th}} = 1$.

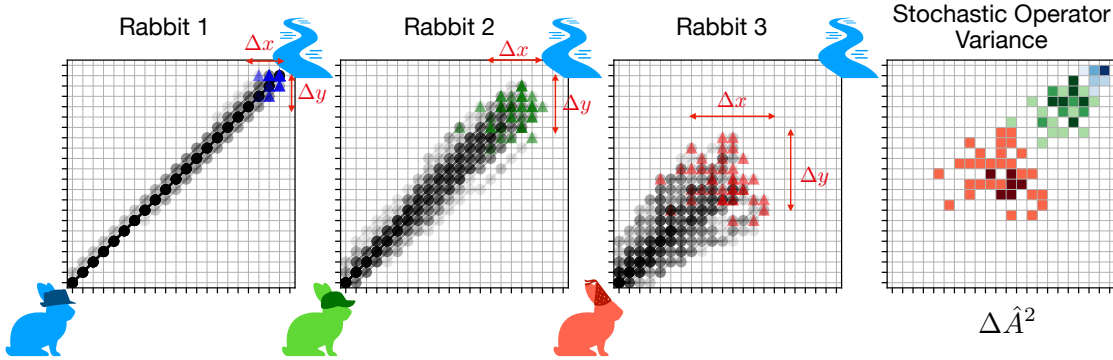


Figure 2.1. Pictorial representation of the Stochastic Operator Variance and its difference with the quantum mechanical variance. We show three different rabbits that are going to the river: Rabbit 1 is very deterministic, every day he follows the shortest path and deviates very little from it, Rabbit 2 has a medium probability of deviating from the path, and Rabbit 3 has a very high probability of deviating from the shortest path. The grid shows the average picture—analogous to the *quantum state*—for each of these rabbits. The colored triangles (blue, green, and red) highlight the last position reached in each trajectory of the rabbit. The spread of the positions, as characterized by a single number, is given by the standard quantum mechanical variance Δx , Δy and is highlighted in the red arrows. The rightmost image shows the Stochastic Operator Variance of the trajectories of the different rabbits (blue, green, red) at the last time step. This is an operator, i.e., a picture instead of a number, which characterizes how far each of the trajectories is from the average one at a given time. Since the trajectories reach different parts of the grid, we were able to superimpose the three in one image for simplicity, but each color represents a different picture.

position of the rabbit. Repeating this experiment over the days, we find that each day the rabbit reached a different point, and we can find the spread of these points, which is a single number called the *quantum variance* Δx or Δy in Fig. 2.1. The *Stochastic Operator Variance* that we introduce does things differently, instead of asking for the spread of positions reached by the rabbit, we measure *how far is a trajectory from the average trajectory*, i.e. given the blob of points reached by the rabbit throughout all the days, how far from that blob are we? It does not require collapsing the state many times, and it has more information, since a picture contains more information than a single number. In essence, while the quantum variance is a number that measures how spread out the position of the rabbit is, the *Stochastic Operator Variance* is a full picture, which for every position in the grid measures how far a trajectory of the rabbit in that position is from the average trajectory over all the days.

Perhaps one of the most mind-boggling features of quantum mechanics is *Heisenberg's uncertainty principle*. It tells us that in the quantum world, it is impossible to determine with arbitrary precision the speed and at the same time the position of a quantum particle:

If we know with perfect accuracy the position of a quantum particle we do not know its speed, and if we know perfectly well the speed of the particle we have no knowledge of its position. This arises because properties of quantum objects are not described by numbers but by *matrices* —remember the pixels in your phone screen—. When multiplying these objects, we get a different result if we multiply the first by the second than if we multiply the second by the first. A simple example of two everyday actions that do not commute is putting on your sock and then your shoe, which is not the same as putting your shoe on first and then your sock. In the case of the rabbits if we were to measure the spread in positions that the rabbit reached Δx and the spread of the velocities at which the rabbit reached Δp , these two quantities cannot be known at the same time with arbitrary precision, this is, by knowing that the rabbit reached a position with complete certainty, the speed at which it reached is entirely unknown. One of the main results of this chapter is that the Stochastic Operator Variance, i.e., the picture that measures how far away we are from the average evolution, also fulfills an uncertainty relation. This means that the distance from the average trajectory of two different evolutions cannot be smaller than a certain value. Throughout the chapter we will study various versions of this new uncertainty principle: the closest to Heisenberg's uncertainty principle involves getting an average value of this Stochastic Operator Variance over the grid, and therefore is an inequality between numbers, just like the uncertainty principle; a second stronger version of the uncertainty principle that we will introduce poses a constraint to the full operator, i.e. the full picture, and says that the stochastic Operator Variances of two different operator need to follow a certain inequality.

The second main result of this chapter has to do with the *Butterfly effect*, which is shown by physical systems that we call *chaotic*. These systems are very sensitive to the initial conditions, which means that starting them from one position or another position very close will show two extremely different evolutions, the popular way of presenting this phenomenon states that “*the flap of the wings of a butterfly*” [a very small perturbation to the initial conditions of a certain system] “*can cause a tornado in the other side of the world*” [can lead to vastly different outcomes]. Lorenz realized that a very simplified model of the Earth's atmosphere was showing chaos [180], in particular, this is what we call the *Lorenz attractor*, which has a very characteristic shape akin to a butterfly's wings. However, a very natural question arises: “*If I have a chaotic system and I start it from two slightly different initial conditions, how fast will I see a deviation of the trajectories?*” this is what the *Lyapunov exponent* measures, how fast is the *exponential* separation of the neighboring trajectories.

The extension of this concept to the quantum world is quite involved, one reason being that if we measure the position of a quantum system, we collapse its wavefunction and drastically change its behavior. One tool physicists recently introduced to study this quantity is called the *Out of Time Order Correlator*, which, in essence, measures the sensitivity to initial conditions by considering the effect of different quantities at different times that are not ordered. The most common case is to consider a certain quantity at time 0, evolve it to time t , evolve it “*backwards in time*” to time 0, and then back to time t . This quantity provides a way to define a Lyapunov exponent for a quantum system and characterizes how entanglement spreads in a quantum system. Furthermore, black

holes have been conjectured to be highly chaotic quantum systems, because they scramble information in the fastest possible way, saturating a universal bound on the Lyapunov exponent. Our second main result on this chapter is to establish a connection between the *Stochastic Operator Variance* and *Out of Time Order Correlators*, this physically means that if the rabbits were chaotic in some way, for example one could think that the grid is not in a flat euclidean space, but rather on a more interesting curved space such as *hyperbolic space*, the distance between two different initial conditions could grow exponentially in time with a Lyapunov exponent, and the Stochastic Operator Variance would characterize the chaos in this system. Fig. 2.2 shows two sample paths of rabbits in this hyperbolic geometry described by the Poincaré disk, where the distance between the two rabbits can grow exponentially in time, therefore illustrating the possible presence of chaos in these systems.

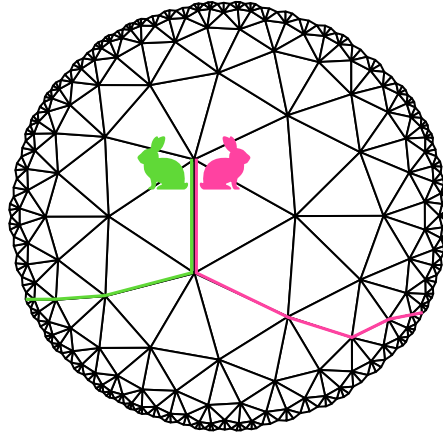


Figure 2.2. Adding chaos to Fig. 2.1. The image shows two sample paths (green and pink) of two rabbits in hyperbolic space represented by a Poincaré disk, with $p = 3$, $q = 7$ generated using [hypertiling](#) [181]

2.2 The Stochastic Operator Variance

Let us consider the most general Stochastic Hamiltonian, with N_c sources of *classical, white noise*

$$\hat{H}_t = \hat{H}_0 + \sum_{n=1}^{N_c} \sqrt{2\gamma_n} \xi_t^{(n)} \hat{L}_n, \quad (2.1)$$

where $\{\gamma_n | \gamma_n \in \mathbb{R}, \gamma_n \geq 0\}_{n=1}^{N_c}$ is the set of the noise strengths associated to the n -th noise channel, $\xi_t^{(n)}$ is the n -th classical white noise which obeys $\mathbb{E}(\xi_t^{(n)}) = 0$, and $\mathbb{E}(\xi_t^{(n)} \xi_{t'}^{(m)}) = \delta_{nm} \delta(t - t')$; and $\{\hat{L}_n | \hat{L}_n^\dagger = \hat{L}_n, \hat{L}_n \in \mathcal{B}(\mathcal{H})\}_{n=1}^{N_c}$ is the set of operators that characterize how the n -th source of noise affects the Hamiltonian of the system, which, as

we shall see below, correspond to the *jump operators* in the [GKSL](#) equation. For a formal treatment of ξ_t , it is useful to introduce the differential of the Hamiltonian $d\hat{H}_t$, which describes the evolution over a small time dt and depends on the increment of the Wiener process $dW_t \equiv \xi_t dt$. This definition has some subtleties when working in the Heisenberg picture, which we discuss now.

Throughout this chapter, we will be interested in the time evolution of operators \hat{A}_t in the *Heisenberg picture*. Let us first review the evolution of a deterministic operator under an explicitly time-dependent Hamiltonian \hat{H}_t . We know that the states evolve according to the Schrödinger equation $\partial_t |\psi_t\rangle = -i\hat{H}_t |\psi_t\rangle$, whose solution reads $|\psi_t\rangle = \hat{U}_t |\psi_0\rangle = \mathcal{T}_{\leftarrow} e^{-i \int_0^t \hat{H}_\tau d\tau} |\psi_0\rangle$, where \mathcal{T}_{\leftarrow} denotes the chronological time ordering operator and \hat{U}_t is the propagator between times 0 and t . We make no assumptions in the structure of the Hamiltonian, in particular, the Hamiltonian does not commute with itself at different times, $[\hat{H}_t, \hat{H}_\tau] \neq 0$ for $t \neq \tau$. The expectation value of \hat{A} evolves as $\langle \hat{A}_t \rangle = \langle \psi_0 | \hat{U}_t^\dagger \hat{A} \hat{U}_t | \psi_0 \rangle = \langle \psi_t | \hat{A} | \psi_t \rangle = \langle \psi_0 | \hat{A}_t | \psi_0 \rangle$ where the expression can be equivalently understood in Schrödinger $|\psi_t\rangle$ or Heisenberg \hat{A}_t pictures. In the latter, the operator evolves as

$$\hat{A}_t = \hat{U}_t^\dagger \hat{A} \hat{U}_t. \quad (2.2)$$

The Heisenberg equation in this case reads $\partial_t \hat{A}_t = +i[\hat{H}_t^{(\text{H})}, \hat{A}_t]$ where $\hat{H}_t^{(\text{H})} = \hat{U}_t^\dagger \hat{H}_t \hat{U}_t \neq \hat{H}_t$ is the Hamiltonian in the interaction picture with respect to itself. Note that, due to the non-commutativity of the Hamiltonian with itself at different times, the Hamiltonian in the Heisenberg picture $\hat{H}_t^{(\text{H})}$ is not equal to the time-dependent Hamiltonian \hat{H}_t . Solving the Heisenberg equation yields the evolution of the operator in the Heisenberg picture \hat{A}_t . However, the same evolution can also be written in terms of the original propagator \hat{U}_t as in (2.2). Thus, we do not need to consider the Hamiltonian in the Heisenberg picture. Importantly for our analysis, operators in the Heisenberg picture evolve “*backwards in time*”. To show this, let us split the propagator into two: one evolution from 0 to t_1 and another from t_1 to t_2 . Doing so, one finds

$$\langle \hat{A}_{t_2} \rangle = \langle \psi_0 | \mathcal{T}_{\rightarrow} e^{-i \int_0^{t_1} \hat{H}_\tau d\tau} \mathcal{T}_{\rightarrow} e^{-i \int_{t_1}^{t_2} \hat{H}_\tau d\tau} \hat{A} \mathcal{T}_{\leftarrow} e^{-i \int_{t_1}^{t_2} \hat{H}_\tau d\tau} \mathcal{T}_{\leftarrow} e^{-i \int_0^{t_1} \hat{H}_\tau d\tau} | \psi_0 \rangle,$$

where $\mathcal{T}_{\rightarrow}$ represents the anti-chronological time ordering operator—backwards evolution. From this expectation value, it is clear that while states evolve forwards in time from $0 \rightarrow t_1$ and from $t_1 \rightarrow t_2$, shifting the evolution to operators results in them evolving in the opposite order, from $t_2 \rightarrow t_1$ and from $t_1 \rightarrow 0$. This is not a physical “*backwards in time*” evolution but an artifact of the Heisenberg picture.

This detail will be quite important for our argument. Indeed, as already explained in Sec. 1.4.2, the Itō convention of Stochastic calculus imposes a discretization of the time interval $[t, t + dt]$, where the noise needs to be evaluated at the beginning of the interval t . In the Heisenberg picture, since we evolve backwards in time, to describe the evolution in the interval $[t - dt, t]$, the noise should be evaluated at dW_{t-dt} to respect the Itō convention. A similar noise evaluation has been introduced in adjoint Stochastic Master Equations for continuous measurements [182, 183]. The differential of the Hamiltonian in

the Heisenberg picture is thus

$$d\hat{H}_t = \hat{H}_0 dt + \sum_{n=1}^{N_c} \sqrt{2\gamma_n} dW_{t-dt}^{(n)} \hat{L}_n. \quad (2.3)$$

Following the simple approach described in Sec. 1.4.4, we shift the focus from the Hamiltonian to its associated differential propagator, which reads

$$\hat{U}_{dt} = e^{-i d H_t} = \exp \left(-i \hat{H}_0 dt - i \sum_{n=1}^{N_c} \sqrt{2\gamma_n} dW_{t-dt}^{(n)} \hat{L}_n \right). \quad (2.4)$$

Since the operator evolves backwards in time, we have that the propagator acts as $\hat{A}_{t-dt} = \hat{U}_{dt}^\dagger \hat{A}_t \hat{U}_{dt}$, i.e., acting on the operator at time t , on \hat{A}_t , gives the operator at time $t - dt$. This allows us to find a Stochastic Differential Equation for the evolution of the operator. In particular, by introducing the backwards differential $d\hat{A}_t = \hat{A}_{t-dt} - \hat{A}_t$, we find the adjoint Stochastic Master Equation

$$\begin{aligned} d\hat{A}_t &= \left(+i[\hat{H}_0, \hat{A}_t] - \sum_{n=1}^{N_c} \gamma_n [\hat{L}_n, [\hat{L}_n, \hat{A}_t]] \right) dt + i \sum_{n=1}^{N_c} \sqrt{2\gamma_n} [\hat{L}_n, \hat{A}_t] dW_{t-dt}^{(n)} \\ &=: \mathcal{L}^\dagger[\hat{A}_t] dt + i \sum_{n=1}^{N_c} \sqrt{2\gamma_n} [\hat{L}_n, \hat{A}_t] dW_{t-dt}^{(n)}, \end{aligned} \quad (2.5)$$

where we have introduced the adjoint Lindbladian $\mathcal{L}^\dagger[\bullet]$. Averaging this equation over the noise $\hat{\mathbf{A}}_t = \mathbb{E}(\hat{A}_t)$, the second term cancels out for driftless noise, leading to the adjoint GKSL equation

$$\partial_t \hat{\mathbf{A}}_t = +i[\hat{H}_0, \hat{\mathbf{A}}_t] - \sum_{n=1}^{N_c} \gamma_n [\hat{L}_n, [\hat{L}_n, \hat{\mathbf{A}}_t]] = \mathcal{L}^\dagger[\hat{\mathbf{A}}_t]. \quad (2.6)$$

This equation describes dephasing caused by the Hermitian jump operators \hat{L}_n . We now introduce the main quantity studied throughout this chapter.

Definition 3 (Stochastic Operator Variance). *Given an operator evolving in the Heisenberg picture \hat{A}_t under a Stochastic Hamiltonian, the Stochastic Operator Variance (SOV) $\Delta \hat{A}_t^2$ is defined as the variance over the classical noise and reads*

$$\Delta \hat{A}_t^2 := \mathbb{E}(\hat{A}_t^2) - \mathbb{E}(\hat{A}_t)^2. \quad (2.7)$$

Figure 2.3 schematically illustrates the meaning of the SOV. The figure shows many different evolutions of the operator $\hat{A}_t = \hat{U}_t^\dagger \hat{A}_0 \hat{U}_t$ with different noise realizations. The average over the noise (thick black line) gives the evolution predicted by GKSL. However, the single trajectories have much more information; particularly, they can substantially deviate from the mean. The Stochastic Operator Variance characterizes a part of this

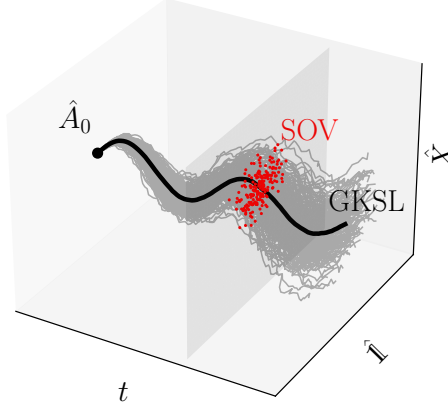


Figure 2.3. Illustration of the SOV: Illustration of the Stochastic Operator Variance (red). An operator \hat{A} evolves in the Hilbert space of operators $\mathcal{B}(\mathcal{H})$ with different realizations (gray) of a stochastic Hamiltonian. We show a 2-dimensional subspace of the Hilbert space of operators spanned by the identity $\hat{1}$ and a generic operator \hat{X} . The noise-averaged evolution (black) follows the adjoint GKSL equation. The SOV $\Delta\hat{A}_t^2$ characterizes the deviation of different trajectories (red). The figure is only an illustration, for a simulation of the evolution of the SOV in the Hilbert space of operators, we refer the reader to Fig. 2.9.

information and captures the spread of all the stochastic single trajectories around the average.

The expression for the SOV can be greatly simplified by leveraging the unitarity at single trajectories property of \hat{U}_t , particularly $\hat{U}_t^\dagger \hat{U}_t = \hat{1}$. The second moment over the noise thus simplifies to

$$\mathbb{E}(\hat{A}_t^2) = \mathbb{E}(\hat{U}_t^\dagger \hat{A} \hat{U}_t \hat{U}_t^\dagger \hat{A} \hat{U}_t) = \mathbb{E}(\hat{U}_t^\dagger \hat{A}^2 \hat{U}_t) = e^{\mathcal{L}^\dagger t} [\hat{A}^2], \quad (2.8)$$

where we used the fact that the average of any operator $\mathbb{E}(\hat{X}_t)$ evolves according to the adjoint GKSL equation $\partial_t \mathbb{E}(\hat{X}_t) = \mathcal{L}^\dagger [\mathbb{E}(\hat{X}_t)]$, to formally write $\mathbb{E}(\hat{U}_t^\dagger \bullet \hat{U}_t) = e^{\mathcal{L}^\dagger t} [\bullet]$. The SOV then reduces to

$$\Delta\hat{A}_t^2 = e^{\mathcal{L}^\dagger t} [\hat{A}^2] - e^{\mathcal{L}^\dagger t} [\hat{A}] \cdot e^{\mathcal{L}^\dagger t} [\hat{A}]. \quad (2.9)$$

Note that the evolution is a CPTP map. Writing it as $\mathcal{E}_t^\dagger [\bullet] = e^{\mathcal{L}^\dagger t} [\bullet]$ the SOV becomes the variance $\Delta\hat{A}_t^2 = \mathcal{E}_t^\dagger [\hat{A}^2] - \mathcal{E}_t^\dagger [\hat{A}]^2$ of a Hermitian matrix under the evolution of a positive unital linear map—Recall that a map is *unital* if it preserves the identity $\mathcal{E}^\dagger[\hat{1}] = \hat{1}$. This quantity has been studied in the context of the theory of *positive definite matrices* [184]. Below, we detail some of its properties.

2.2.1 Mathematical properties of the SOV

Since the Lindbladian $\mathcal{L}^\dagger[\bullet]$ is the generator of a **CPTP** map $e^{\mathcal{L}^\dagger t}[\bullet]$, it also preserves Hermiticity. This means that if the initial operator is Hermitian $\hat{A}^\dagger = \hat{A}$, the **SOV** $\Delta\hat{A}_t^2$ is also Hermitian $(\Delta\hat{A}_t^2)^\dagger = \Delta\hat{A}_t^2$, and thus an observable.

Another key property of the **SOV** is that it is positive semi-definite. This ensures that the variance is non-negative. This can be proven using *Kadison's inequality* [185]. Kadison's inequality states that for a linear map $\mathcal{E}^\dagger[\bullet]$ that is *positive* $\hat{X} \geq 0 \Rightarrow \mathcal{E}^\dagger[\hat{X}] \geq 0$, and *unital* $\mathcal{E}^\dagger[\hat{1}] = \hat{1}$, given a Hermitian operator $\hat{X}^\dagger = \hat{X}$, the following inequality holds

$$\mathcal{E}^\dagger[\hat{X}^2] \geq \mathcal{E}^\dagger[\hat{X}]^2. \quad (2.10)$$

Note that $e^{\mathcal{L}^\dagger t}[\bullet]$ is (completely) positive and unital, which implies that the **SOV** is positive semidefinite $\Delta\hat{A}_t^2 = e^{\mathcal{L}^\dagger t}[\hat{A}^2] - (e^{\mathcal{L}^\dagger t}[\hat{A}])^2 \geq 0$.

Another interesting property of the **SOV** which comes from the connection to the variance of positive definite matrices is that, if the operator is bounded from below and above $m\hat{1} \leq \hat{A} \leq M\hat{1}$, then the **SOV** is bounded from above by [184]

$$\Delta\hat{A}_t^2 \leq \left(\frac{M-m}{2}\right)^2 \hat{1}. \quad (2.11)$$

Let a_j be the spectrum of the operator $\hat{A}|a_j\rangle = a_j|a_j\rangle$, which is well defined given that $\hat{A}^\dagger = \hat{A}$. A particularly simple case of this inequality follows since $\min_j a_j \hat{1} \leq \hat{A} \leq \max_j a_j \hat{1}$

$$\Delta\hat{A}_t^2 \leq \frac{(\max_j a_j - \min_j a_j)^2}{4} \hat{1}. \quad (2.12)$$

So that this bound implies that if \hat{A} is a bounded operator, the **SOV** is also bounded from above.

2.2.2 Comparison to the Variance over state

The standard quantum mechanical variance of operator \hat{A} over a state $\hat{\rho}$ reads

$$\text{Var}(\hat{A}, \hat{\rho}) = \text{Tr}(\hat{A}^2 \hat{\rho}) - \text{Tr}(\hat{A} \hat{\rho})^2. \quad (2.13)$$

If we assume an initially pure state and a dissipative GKSL dynamics, we have

$$\begin{aligned} \text{Var}(\hat{A}, e^{\mathcal{L} t}[\langle \psi_0 | \psi_0 \rangle]) &= \text{Tr}(\hat{A}^2 e^{\mathcal{L} t}[\langle \psi_0 | \psi_0 \rangle]) - \text{Tr}(\hat{A} e^{\mathcal{L} t}[\langle \psi_0 | \psi_0 \rangle])^2, \\ &= \langle \psi_0 | e^{\mathcal{L}^\dagger t}[\hat{A}^2] | \psi_0 \rangle - \langle \psi_0 | e^{\mathcal{L}^\dagger t}[\hat{A}] | \psi_0 \rangle^2, \\ &= \text{Var}(e^{\mathcal{L}^\dagger t}[\hat{A}], |\psi_0\rangle \langle \psi_0|) \equiv \text{Var}(\hat{\mathfrak{A}}_t, \psi_0). \end{aligned} \quad (2.14)$$

The dissipative dynamics can be equivalently applied to the state in the Schrödinger picture or to the observable in the Heisenberg picture.

The quantum variance (2.14) appears to be similar to the **SOV** (2.9). To make explicit the difference between the two approaches, let us look at the expectation value of the **SOV** over the initial state $|\psi_0\rangle$

$$\langle\psi_0|\Delta\hat{A}_t^2|\psi_0\rangle = \langle\psi_0|e^{\mathcal{L}^\dagger t}[\hat{A}^2]|\psi_0\rangle - \langle\psi_0|e^{\mathcal{L}^\dagger t}[\hat{A}]\cdot e^{\mathcal{L}^\dagger t}[\hat{A}]|\psi_0\rangle. \quad (2.15)$$

The difference between the two quantities then reduces to

$$\langle\psi_0|\Delta\hat{A}_t^2|\psi_0\rangle - \text{Var}(\hat{\mathbf{A}}_t, \psi_0) = \langle\psi_0|e^{\mathcal{L}^\dagger t}[\hat{A}]\hat{\mathbf{Q}}e^{\mathcal{L}^\dagger t}[\hat{A}]|\psi_0\rangle, \quad (2.16)$$

where $\hat{\mathbf{Q}} = \hat{\mathbb{1}} - |\psi_0\rangle\langle\psi_0|$ is the projector over the complementary subspace of $|\psi_0\rangle\langle\psi_0|$. We can then conclude that the expectation value of the **SOV** contains the information contained in the quantum variance plus the information in which $\hat{\mathbf{A}}_t$ leaves the subspace spanned by $|\psi_0\rangle$. In particular, writing this projector in the basis of the complementary subspace $\{|\phi_n\rangle\mid\langle\phi_n|\psi_0\rangle=0\}_{n=1}^{d-1}$ as $\hat{\mathbf{Q}} = \sum_{n=1}^{d-1}|\phi_n\rangle\langle\psi_n|$, allows to express the expectation value of the **SOV** as

$$\langle\psi_0|\Delta\hat{A}_t^2|\psi_0\rangle = \text{Var}(\hat{\mathbf{A}}_t, \psi_0) + \sum_{n=1}^{d-1}|\langle\psi_0|\hat{\mathbf{A}}_t|\phi_n\rangle|^2. \quad (2.17)$$

So the term additional to the quantum mechanical variance is given by the transition amplitude of $\hat{\mathbf{A}}_t$ outside of the $|\psi_0\rangle$ subspace.

Another difference between the **SOV** and the quantum variance over a state is that given any basis $\{|\psi_n\rangle\}_{n=1}^d$ since $\Delta\hat{A}_t^2$ is an operator it has both diagonal matrix elements $\langle\psi_n|\Delta\hat{A}_t^2|\psi_n\rangle$, which are the ones that are given by the quantum variance plus transitions out of the $|\psi_n\rangle$ subspace, but it also has off-diagonal matrix elements $\langle\psi_n|\Delta\hat{A}_t^2|\psi_m\rangle$ which have no analog in the variance over a state.

2.2.3 The SOV as an operation on replicated Hilbert spaces

We now turn to an alternative representation to provide further understanding of the **SOV**. Expression (2.9), in terms of the **CPTP** map, can be understood with two replicas of the Hilbert space $\mathcal{H}\otimes\mathcal{H}$. In each of these, we consider an initial operator $\hat{A}\in\mathcal{B}(\mathcal{H})$ living in the space of operators over the Hilbert space. We denote each Hilbert space by a subscript 1 and 2, respectively. In particular, we consider an operator in each of the original Hilbert spaces, i.e. $\hat{X}\in\mathcal{B}(\mathcal{H})_1$ and $\hat{Y}\in\mathcal{B}(\mathcal{H})_2$, we further introduce an “interaction” between the two replicas $\mathfrak{J}:\hat{X}\in\mathcal{B}(\mathcal{H})\times\hat{Y}\in\mathcal{B}(\mathcal{H})\mapsto\hat{X}\hat{Y}\in\mathcal{B}(\mathcal{H})$, which gives the product $\hat{X}\hat{Y}$. One way to produce this interaction is through a partial trace and a *swap* operation. The swap operation acts on a general state of the doubled Hilbert space $|\psi\rangle_1\otimes|\phi\rangle_2\equiv|\psi_1,\phi_2\rangle\in\mathcal{H}\otimes\mathcal{H}$ simply as $\mathbb{S}|\psi_1,\phi_2\rangle=|\phi_1,\psi_2\rangle$ [169, 186].

We thus obtain the operator product from

$$\begin{aligned}
 \mathfrak{J}(\hat{X}, \hat{Y}) &= \text{Tr}_2((\hat{X} \otimes \hat{Y}) \mathbb{S}) \\
 &= \sum_{n_1, m_1, n_2, m_2} \text{Tr}_2(X_{n_1 m_1} Y_{n_2 m_2} |n_1, n_2\rangle \langle m_1, m_2| \mathbb{S}) \\
 &= \sum_{n_1, m_1, n_2, m_2} \text{Tr}_2(X_{n_1 m_1} Y_{n_2 m_2} |n_1, n_2\rangle \langle m_2, m_1|) \\
 &= \sum_{n_1, m_1, n_2, m_2, k_2} X_{n_1 m_1} Y_{n_2 m_2} |n_1\rangle \langle m_2| \delta_{k_2, n_2} \delta_{k_2, m_1} \\
 &= \sum_{n, m, k} X_{n k} Y_{k m} |n\rangle \langle m| = \hat{X} \hat{Y},
 \end{aligned} \tag{2.18}$$

where we denote the matrix element $X_{nm} = \langle n | \hat{X} | m \rangle$. Note that performing the partial trace over the first copy instead also leads to the product of two matrices but in a different order, i.e., $\text{Tr}_1((\hat{X} \otimes \hat{Y}) \mathbb{S}) = \hat{Y} \hat{X}$.

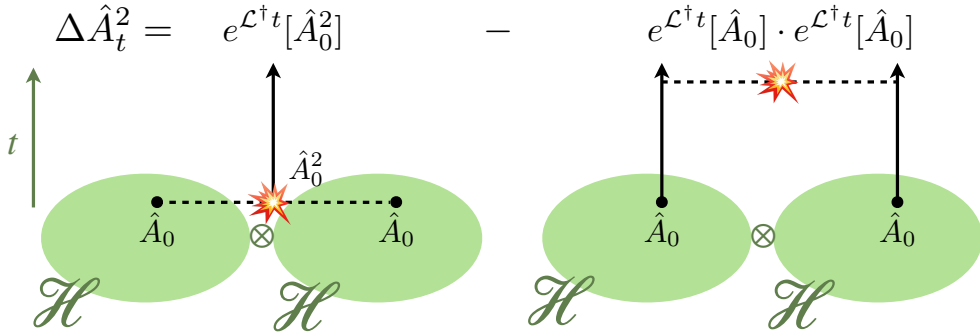


Figure 2.4. Replica interpretation of the SOV. The SOV is the difference between two protocols (left and right) on a doubled Hilbert space $\mathcal{H} \otimes \mathcal{H}$. The interaction (black dashed line) is given by $\mathfrak{J}(\bullet, \bullet)$ (2.18) and the time evolution (vertical black line) is given by the CPTP map $e^{\mathcal{L}^\dagger t}[\bullet]$.

Figure 2.4 illustrates the SOV as a difference of two protocols on two replicas of a Hilbert space. The first protocol, associated to the term $e^{\mathcal{L}^\dagger t}[\hat{A}_0^2]$, starts by making the two copies interact at time $t = 0$ to give \hat{A}_0^2 , and lets the squared operator evolve dissipatively in time to produce $\mathbb{E}(\hat{A}_t^2) = e^{\mathcal{L}^\dagger t}[\hat{A}_0^2]$. The second protocol lets each of the copies evolve in time first, thus producing two copies of $\hat{A}_t = e^{\mathcal{L}^\dagger t}[\hat{A}_0]$, and makes them interact at time t to give $(\hat{A}_t)^2 = (e^{\mathcal{L}^\dagger t}[\hat{A}_0])^2$. The SOV then is the difference between these two protocols. This interpretation also provides a simple intuition for why the SOV is positive semidefinite, $\Delta \hat{A}_t^2 \geq 0$, since the first protocol involves one dissipative time evolution, while the second one involves two. So the second protocol will be subject to more decoherence.

2.3 SOV uncertainty relation

As discussed in Sec. 2.2.2, the **SOV** contains the quantum variance and some extra information. Perhaps the most interesting property of the quantum variance is *Heisenberg's uncertainty relation* [187] which states that the product of the variances of two non-commuting operators cannot be arbitrarily close to zero, but there is a fundamental limit to the precision with which the expectation value of two non-commuting operators can be known. This section explores similar uncertainty relations for the **SOV**.

Before considering the case of operators, let us motivate our derivation by considering functions. The variance of a function is defined as $\text{var}(f) := \langle f^* f \rangle - \langle f \rangle^* \langle f \rangle$, where the expectation value $\langle \bullet \rangle = \int \bullet d\mu$ is to be understood with respect to a proper measure of L_2 functions. The covariance of two functions is defined as $\text{cov}(f, g) := \langle f^* g \rangle - \langle f \rangle^* \langle g \rangle$. The Cauchy-Schwarz inequality then gives an inequality between the variance and the covariance, namely

$$\text{var}(f)\text{var}(g) \geq |\text{cov}(f, g)|^2.$$

We now turn to the operator case. As previously discussed, for the **CPTP** map $\mathcal{E}_t^\dagger[\bullet] = e^{\mathcal{L}^\dagger t}[\bullet]$, the **SOV** is the variance of operators with respect to that map. Analogously, one can define the *covariance* of two operators \hat{A}, \hat{B} with respect to the map [184] as

$$\Delta \widehat{AB}_t := \mathcal{E}_t^\dagger[\hat{A}^\dagger \hat{B}] - \mathcal{E}_t^\dagger[\hat{A}]^\dagger \mathcal{E}_t^\dagger[\hat{B}], \quad (2.19)$$

Note that the map preserves hermiticity, so we can drop the conjugation for Hermitian operators. It is then possible to find an analogous statement to the variance-covariance inequality [184, 188]. If $\mathcal{E}_t^\dagger[\bullet]$ is a completely positive, unital, linear map, the following $2N \times 2N$ matrix is positive semidefinite

$$\begin{pmatrix} \Delta \hat{A}_t^2 & \Delta \widehat{AB}_t \\ \Delta \widehat{AB}_t^\dagger & \Delta \hat{B}_t^2 \end{pmatrix} \geq 0. \quad (2.20)$$

The Heisenberg uncertainty relation involves a non-commuting pair of operators and a quantum state. To find an expression closer to the uncertainty relation, we take the expectation value of this inequality over a certain state $\langle \bullet \rangle_\rho = \text{Tr}(\bullet \hat{\rho})$, which gives the 2×2 matrix

$$\begin{pmatrix} \langle \Delta \hat{A}_t^2 \rangle_\rho & \langle \Delta \widehat{AB}_t \rangle_\rho \\ \langle \Delta \widehat{AB}_t^\dagger \rangle_\rho & \langle \Delta \hat{B}_t^2 \rangle_\rho \end{pmatrix} \geq 0. \quad (2.21)$$

Sylvester's criterion states that a matrix is positive semidefinite $\hat{X} \geq 0$ if and only if its principal minors—the determinants of the matrix where the columns and rows with the same index are removed—are positive. For our matrix, this implies the following three

inequalities

$$\langle \Delta \hat{A}_t^2 \rangle_\rho \geq 0, \quad \langle \Delta \hat{B}_t^2 \rangle_\rho \geq 0, \quad \langle \Delta \hat{A}_t^2 \rangle_\rho \langle \Delta \hat{B}_t^2 \rangle_\rho - |\langle \Delta \widehat{AB}_t \rangle_\rho|^2 \geq 0. \quad (2.22)$$

The first two conditions are satisfied because of the positive semidefiniteness of the **SOV** and the density matrix; thus, they do not impose extra conditions. The third condition imposes an analog of the Cauchy-Schwarz inequality for the **SOV** and the stochastic operator covariance

$$\langle \Delta \hat{A}_t^2 \rangle_\rho \langle \Delta \hat{B}_t^2 \rangle_\rho \geq |\langle \Delta \widehat{AB}_t \rangle_\rho|^2. \quad (2.23)$$

Let us now re-express this inequality in terms of the commutator and anticommutator of the operators. To simplify the notation In particular, using the identities $\hat{A}\hat{B} = \frac{1}{2}(\{\hat{A}, \hat{B}\} + [\hat{A}, \hat{B}])$ and $\hat{B}\hat{A} = \frac{1}{2}(\{\hat{A}, \hat{B}\} - [\hat{A}, \hat{B}])$

$$\begin{aligned} |\langle \Delta \widehat{AB}_t \rangle_\rho|^2 &= (\langle \mathcal{E}_t^\dagger(\hat{A}\hat{B}) \rangle_\rho - \langle \hat{\mathbf{A}}_t \hat{\mathbf{B}}_t \rangle_\rho)(\langle \mathcal{E}_t^\dagger(\hat{B}\hat{A}) \rangle_\rho - \langle \hat{\mathbf{B}}_t \hat{\mathbf{A}}_t \rangle_\rho) \\ &= \frac{1}{4} \left(\langle \mathcal{E}_t^\dagger(\{\hat{A}, \hat{B}\}) \rangle_\rho^2 - \langle \mathcal{E}_t^\dagger([\hat{A}, \hat{B}]) \rangle_\rho^2 - 2\langle \mathcal{E}_t^\dagger(\{\hat{A}, \hat{B}\}) \rangle_\rho \langle \{\hat{\mathbf{A}}_t, \hat{\mathbf{B}}_t\} \rangle_\rho \right. \\ &\quad \left. + 2\langle \mathcal{E}_t^\dagger([\hat{A}, \hat{B}]) \rangle_\rho \langle [\hat{\mathbf{A}}_t, \hat{\mathbf{B}}_t] \rangle_\rho + \langle \{\hat{\mathbf{A}}_t, \hat{\mathbf{B}}_t\} \rangle_\rho - \langle [\hat{\mathbf{A}}_t, \hat{\mathbf{B}}_t] \rangle_\rho^2 \right) \\ &= \frac{1}{4} \left(\langle \mathcal{E}_t^\dagger(\{\hat{A}, \hat{B}\}) \rangle_\rho - \langle \{\hat{\mathbf{A}}_t, \hat{\mathbf{B}}_t\} \rangle_\rho \right)^2 - \frac{1}{4} \left(\langle \mathcal{E}_t^\dagger([\hat{A}, \hat{B}]) \rangle_\rho - \langle [\hat{\mathbf{A}}_t, \hat{\mathbf{B}}_t] \rangle_\rho \right)^2 \\ &= \frac{1}{4} \left(D_+^2(\hat{A}, \hat{B}) - D_-^2(\hat{A}, \hat{B}) \right). \end{aligned}$$

The expectation value of the covariance is thus determined by the following quantities

$$D_\pm(\hat{A}, \hat{B}) := \langle \mathcal{E}_t^\dagger([\hat{A}, \hat{B}]_\pm) \rangle_\rho - \langle [\mathcal{E}_t^\dagger(\hat{A}), \mathcal{E}_t^\dagger(\hat{B})]_\pm \rangle_\rho, \quad (2.24)$$

where in this last line we used the common notation for commutators and anticommutators $[\hat{A}, \hat{B}]_\pm = \hat{A}\hat{B} \pm \hat{B}\hat{A}$ such that $[\bullet, \bullet]_+ = \{\bullet, \bullet\}$ and $[\bullet, \bullet]_- = [\bullet, \bullet]$. Therefore, the uncertainty relation for the **SOV** reads

$$\text{Tr}(\Delta \hat{A}_t^2 \hat{\rho}) \text{Tr}(\Delta \hat{B}_t^2 \hat{\rho}) \geq \frac{1}{4} \left(D_+^2(\hat{A}, \hat{B}) - D_-^2(\hat{A}, \hat{B}) \right). \quad (2.25)$$

The D_\pm functions represent the expectation value of the difference between evolving an (anti)commutator in time and taking the (anti)commutator of the time-evolved operators, which is reminiscent of the replica interpretation of the **SOV**, cf. Sec. 2.2.3. Also note that since the commutator of two Hermitian operators is anti-Hermitian, D_- is purely imaginary and thus $D_-^2 < 0$; while the anticommutator of two Hermitian operators is Hermitian and thus $D_+^2 > 0$. This implies that $D_+^2(\hat{A}, \hat{B}) - D_-^2(\hat{A}, \hat{B}) \geq 0$. Also note that when $\hat{A} = \hat{B}$, the inequality is trivially saturated since $\Delta \widehat{AA} = \Delta \hat{A}^2$. It is possible to derive the Heisenberg uncertainty principle [187], depending only on the commutator of the two operators, from the Robertson-Schrödinger uncertainty relation [189, 190], which

depends on both the commutator and anticommutator of the two operators. Similarly, we can find a looser inequality which only depends on the commutator of operators, in particular in the difference of the time evolution of the commutator and the commutator of the time-evolved operators as

$$\begin{aligned}\langle \Delta \hat{A}_t^2 \rangle_\rho \langle \Delta \hat{B}_t^2 \rangle_\rho &\geq \frac{1}{4} \left| D_-(\hat{A}, \hat{B}) \right|^2, \\ &\geq \frac{1}{4} \left| \langle \mathcal{E}_t^\dagger([\hat{A}, \hat{B}]) \rangle_\rho - \langle [\mathcal{E}_t^\dagger(\hat{A}), \mathcal{E}_t^\dagger(\hat{B})] \rangle_\rho \right|^2,\end{aligned}\quad (2.26)$$

where we used the fact that $D_+^2(\hat{A}, \hat{B}) \geq 0$ to derive this version of the inequality.

2.3.1 An operator version of the SOV uncertainty relation

A matrix of the form $\begin{pmatrix} \hat{X} & \hat{Y} \\ \hat{Y}^\dagger & \hat{Z} \end{pmatrix} \geq 0$ is positive semidefinite if and only if $\hat{X} \geq 0$, $\hat{Z} \geq 0$ and $\hat{X} \geq \hat{Y} \hat{Z}^{-1} \hat{Y}^\dagger$ [188, 191, 192], where the inverse is to be understood as the generalized inverse if \hat{Z} is not invertible. This immediately implies an operator version of the variance-covariance inequality [188]

$$\Delta \hat{A}_t^2 \geq \Delta \widehat{AB}_t (\Delta \hat{B}_t^2)^{-1} \Delta \widehat{AB}_t^\dagger. \quad (2.27)$$

In statistics it is common to introduce the *Pearson Correlation coefficient* between two random variables as $\text{corr}(x, y) = \frac{\text{cov}(x, y)}{\sigma_x \sigma_y}$. This quantity provides a normalized version of the covariance of the two variables, normalized by the standard deviations of each of the variables $\sigma_{x,y}$, and it is upper and lower bounded as $-1 \leq \text{corr}(x, y) \leq +1$. Interestingly, it is possible to introduce a Pearson Correlation Operator for two observables under a quantum channel, as

$$\text{corr}_t(\hat{A}, \hat{B}) := \Delta \hat{A}_t^{-1} \Delta \widehat{AB}_t \Delta \hat{B}_t^{-1}, \quad (2.28)$$

where we introduced the Operator standard deviation $\Delta \hat{A}_t := \sqrt{\Delta \hat{A}_t^2}$, which is well defined since the **SOV** is positive semidefinite $\Delta \hat{A}_t \geq 0$. Assuming that the two **SOV**'s are invertible, i.e., positive definite $\Delta \hat{A}_t^2, \Delta \hat{B}_t^2 > 0$, the operator version of the variance-covariance inequality implies that the operator correlation is upper bounded as

$$\text{corr}_t(\hat{A}, \hat{B}) \text{corr}_t(\hat{A}, \hat{B})^\dagger \leq \hat{1}. \quad (2.29)$$

2.3.2 Example: Stochastic Frequency Harmonic Oscillator

To illustrate the **SOV** uncertainty relation, we consider a harmonic oscillator with a stochastically driven frequency, i.e.

$$\hat{H}_t = (\omega + \sqrt{2\gamma}\xi_t)\hat{a}^\dagger\hat{a}, \quad (2.30)$$

where we set the ground state energy to zero. Similar systems, with a stochastic position of a harmonic trap $\hat{V}(\hat{x}) \propto (\hat{x} - \xi_t \hat{1})^2$, were studied for quantum control [193]. The creation and annihilation operators in this model evolve as

$$\hat{a}_t = e^{-i(\omega t + \sqrt{2\gamma}W_t)}\hat{a}, \quad \hat{a}_t^\dagger = e^{+i(\omega t + \sqrt{2\gamma}W_t)}\hat{a}^\dagger, \quad (2.31)$$

where we introduced the Wiener process $W_t = \int_0^t dW_{t'} \equiv \int_0^t \xi_{t'} dt'$ as the integral of the Wiener increment dW . This gives the evolution of these operators at the average level as

$$\mathbb{E}(\hat{a}_t) = e^{-i\omega t - \gamma t}\hat{a}, \quad \mathbb{E}(\hat{a}_t^\dagger) = e^{+i\omega t - \gamma t}\hat{a}^\dagger. \quad (2.32)$$

These expressions can be understood through a complex frequency $\omega - i\gamma$ and thus can be thought of as a mapping to a non-Hermitian Hamiltonian, which provides a further connection to the next Chapter 3. From these expressions, the noise-averaged evolution of the position and momentum observables follows directly as

$$\hat{x}_t = \frac{e^{-\gamma t}}{2} (e^{-i\omega t}\hat{a} + e^{i\omega t}\hat{a}^\dagger), \quad \hat{p}_t = \frac{e^{-\gamma t}}{2i} (e^{-i\omega t}\hat{a} - e^{i\omega t}\hat{a}^\dagger). \quad (2.33)$$

It is also simple to obtain the bilinears of the creation and annihilation operators as

$$\mathbb{E}(\hat{a}_t^2) = e^{-2i\omega t - 2\gamma t}\hat{a}^2, \quad (2.34a)$$

$$\mathbb{E}(\hat{a}_t^{\dagger 2}) = e^{+2i\omega t - 2\gamma t}\hat{a}^{\dagger 2}, \quad (2.34b)$$

$$\mathbb{E}(\hat{a}_t^\dagger\hat{a}_t) = \hat{a}^\dagger\hat{a}, \quad (2.34c)$$

$$\mathbb{E}(\hat{a}_t\hat{a}_t^\dagger) = \hat{a}\hat{a}^\dagger. \quad (2.34d)$$

The third of these equations implies that the photon number is conserved through the evolution, which was expected since it commutes with the Hamiltonian $[\hat{H}_t, \hat{a}^\dagger\hat{a}] = 0$. These expressions directly yield the **SOV** of the position and momentum to be

$$\Delta\hat{x}_t^2 = \frac{1 - e^{-2\gamma t}}{4} \{\hat{a}, \hat{a}^\dagger\} = \Delta\hat{p}_t^2. \quad (2.35)$$

We can also compute the covariance of the two operators and find

$$\Delta\hat{x}\hat{p}_t = i\frac{1 - e^{-2\gamma t}}{4} [\hat{a}, \hat{a}^\dagger] = i\frac{1 - e^{-2\gamma t}}{4}, \quad (2.36)$$

which gives the **SOV** uncertainty relation for the stochastic frequency-driven HO as

$$\langle \Delta \hat{x}_t^2 \rangle_\rho \langle \Delta \hat{p}_t^2 \rangle_\rho \geq \left(\frac{1 - e^{-2\gamma t}}{4} \right)^2. \quad (2.37)$$

Substituting the exact expressions for the time evolution of the **SOV**'s of the model, the inequality reduces to

$$\langle 2\hat{n} + 1 \rangle_\rho^2 \geq 1. \quad (2.38)$$

Since the covariance is proportional to unity, the operator version of the uncertainty relation provides the following operator inequality

$$\Delta \hat{x}_t \Delta \hat{p}_t^2 \geq \left(\frac{1 - e^{-2\gamma t}}{4} \right)^2 \hat{1}, \quad (2.39)$$

or equivalently

$$(2\hat{n} + 1)^2 \geq \hat{1}. \quad (2.40)$$

Several observations are apparent from this example:

- Since the noise affects only the frequency of the harmonic oscillator, it affects all the Hamiltonian in the same way, and does not have any effect on the Fock basis $|n\rangle$. This may be the reason behind the **SOV** for the position and the momentum to be the same.
- Expression (2.38) and its operator version (2.40) are always fulfilled since the number operator is positive semidefinite $\hat{n} \geq 0$.
- One of the most interesting features of the Heisenberg uncertainty relation is the existence of *coherent states* which saturate the uncertainty principle. However, at least in this case, the only state which saturates the **SOV** uncertainty relation (2.38) is the ground state $\hat{\rho} = |0\rangle \langle 0|$. Any other state, no matter if pure or mixed, will have $\text{Tr}(\hat{n}\hat{\rho}) > 0$ and the inequality will not be saturated.

2.4 Higher order moments and cumulants

In this section, we explore the behavior of higher-order moments and cumulants of the time-evolved operator averaged over the noise. In particular, unitarity at single trajectories yields that the n -th moment over the noise is

$$\hat{M}_t^{(n)} = \mathbb{E}(\hat{A}_t^n) = \mathbb{E}(\hat{U}_t^\dagger \hat{A} \hat{U}_t \hat{U}_t^\dagger \hat{A} \hat{U}_t \dots \hat{U}_t^\dagger \hat{A} \hat{U}_t) = \mathbb{E}(\hat{U}_t^\dagger \hat{A}^n \hat{U}_t), \quad (2.41)$$

and thus it follows the same adjoint GKSL master equation $\partial_t \mathbb{E}(\hat{A}_t^n) = \mathcal{L}^\dagger[\mathbb{E}(\hat{A}_t^n)]$, which implies that the adjoint Liouvillian generates the evolution of all the moments through

$$\hat{M}_t^{(n)} = \mathbb{E}(\hat{A}_t^n) = e^{\mathcal{L}^\dagger t}[\hat{A}^n]. \quad (2.42)$$

Moments can also be computed by differentiation of the *moment generating function* $\hat{\varphi}(\alpha)$ as

$$\hat{M}_t^{(n)} = \left. \frac{\partial^n}{\partial \alpha^n} \hat{\varphi}(\alpha) \right|_{\alpha=0},$$

where the moment generating function $\hat{\varphi}(\alpha)$ is defined as

$$\hat{\varphi}(\alpha) := \mathbb{E}(e^{\alpha \hat{A}_t}). \quad (2.43)$$

Expanding this function gives all the moments

$$\hat{\varphi}(\alpha) = \sum_{n=0} \frac{\alpha^n}{n!} \mathbb{E}(\hat{A}_t^n) = \sum_{n=0} \frac{\alpha^n}{n!} e^{\mathcal{L}^\dagger t}[\hat{A}^n] = e^{\mathcal{L}^\dagger t}[e^{\alpha \hat{A}}], \quad (2.44)$$

where we used the linearity of the **CPTP** map in the last equality.

In a similar spirit, it is possible to introduce the cumulant generating function $\hat{K}(\alpha)$, taking the natural logarithm, now understood in the operator sense, of the moment generating function

$$\hat{K}(\alpha) = \log(\hat{\varphi}(\alpha)) = \log(e^{\mathcal{L}^\dagger t}[e^{\alpha \hat{A}}]), \quad (2.45)$$

which gives the n -th cumulant over the noise $\hat{\kappa}_t^{(n)}$ by simple differentiation

$$\hat{\kappa}_t^{(n)} = \left. \frac{\partial^n}{\partial \alpha^n} \hat{K}(\alpha) \right|_{\alpha=0}. \quad (2.46)$$

A natural extension of this analysis is to look at what properties of chaos show up in the fluctuations beyond the (operator) variance. It is known that high order cumulants are essential to understand the formation of topological defects through a quantum phase transition [194], so it is expected that higher order moments over the noise characterize certain information of the chaotic properties, such as generalized Lyapunov exponents [195] characterizing the behavior of higher point **OTOC**'s, or spectral correlations.

2.5 Steady states of the SOV

2.5.1 General expression in terms of conserved quantities

The **SOV** $\Delta \hat{A}_t^2$ is a time-evolving quantity; it is thus natural to wonder about the values of the **SOV** in the long-time limit $t \rightarrow \infty$, i.e., what is its steady state. This is not only a theoretical curiosity; the preparation of non-trivial steady states is one of the possible

approaches to dissipative quantum computing [196], which has been used experimentally to prepare highly entangled states [197]. By computing the steady state of the **SOV**, we can then characterize the effect of fluctuations around the steady state of a given operator. Introducing the eigenvalues and eigenvectors of the adjoint Lindbladian $\mathcal{L}^\dagger[\hat{R}_i] = -\lambda_i \hat{R}_i$, where the eigenvalues are non-positive and thus we add a negative sign such that $\lambda_i \geq 0$, and the left eigenvectors of the adjoint Lindbladian³ \hat{L}_i , which are the right eigenvectors of the Lindbladian $\mathcal{L}^{\dagger\dagger}[\hat{L}_i] = \mathcal{L}[\hat{L}_i] = -\lambda_i^* \hat{L}_i$. The **SOV** in the Lindbladian eigenbasis reads

$$\Delta \hat{A}_t^2 = \sum_{i=1}^{N^2} e^{-\lambda_i t} (\hat{L}_i, \hat{A}^2) \hat{R}_i - \sum_{i,j=1}^{N^2} e^{-(\lambda_i + \lambda_j)t} (\hat{L}_i, \hat{A})(\hat{L}_j, \hat{A}) \hat{R}_i \hat{R}_j, \quad (2.47)$$

where the inner product is defined as

$$(\hat{X}, \hat{Y}) := \text{Tr}(\hat{X}^\dagger \hat{Y}), \quad (2.48)$$

Therefore in the long time limit the only contributions that survive are the ones with $\lambda_i = \lambda_j = 0$, i.e. the projections over the kernel of \mathcal{L}^\dagger . Therefore at long times the **SOV** reads

$$\lim_{t \rightarrow \infty} \Delta \hat{A}_t^2 = \Delta \hat{A}_\infty^2 = \sum_{i \in \ker(\mathcal{L}^\dagger)} (\hat{L}_i, \hat{A}^2) \hat{R}_i - \sum_{i,j \in \ker(\mathcal{L}^\dagger)} (\hat{L}_i, \hat{A})(\hat{L}_j, \hat{A}) \hat{R}_i \hat{R}_j. \quad (2.49)$$

Since the map $e^{\mathcal{L}^\dagger t}[\bullet]$ is unital, i.e. $e^{\mathcal{L}^\dagger t}[\hat{1}] = \hat{1}$, the identity lives in the kernel of the adjoint Lindbladian $\mathcal{L}^\dagger[\hat{1}] = 0$. If there is a *unique* steady state of the Lindbladian $\mathcal{L}[\rho^s] = 0$, the identity $\hat{1}$ may be understood as the left-eigenvector associated to the right-eigenvector $\hat{\rho}^s$, or conversely, the identity is the right eigenvector of the adjoint lindbladian and $\hat{\rho}^s$ is the left eigenvector. In this case, the only eigenstate in the kernel of the adjoint Lindbladian $\ker(\mathcal{L}^\dagger)$ is the identity $\hat{R}_1 = \hat{1}$. In this case, the steady state of the **SOV** is simply

$$\Delta \hat{A}_\infty^2 = \left(\text{Tr}(\hat{\rho}^s \hat{A}^2) - \text{Tr}(\hat{\rho}^s \hat{A})^2 \right) \hat{1}. \quad (2.50)$$

This result implies that at long times, when the steady state is unique, the **SOV** converges to a quantity proportional to the identity with a proportionality constant which is the variance over the steady state $\hat{\rho}^s$.

Multiple steady states

The identity $\hat{1}$ is always in the kernel of the adjoint Lindbladian; therefore, even in the case with multiple steady states, there will be a term proportional to the identity in the same way as (2.50). The elements of the kernel of the adjoint Lindbladian $\ker(\mathcal{L}^\dagger)$ are the *conserved quantities* studied by Albert *et al.* [198, 199], also referred to as *invariant*

³Here we use a *sans serif* font to differentiate between the left eigenvectors \hat{L}_i and the jump operators \hat{L}_i .

observables by Baumgartner *et al.* [200]. Note that if the Lindbladian has a *strong symmetry* \hat{S} in the sense of Buča and Prosen [201] the operator \hat{S} commutes with the Hamiltonian and the jump operators

$$[\hat{S}, \hat{H}] = [\hat{S}, \hat{L}_k] = 0, \forall k. \quad (2.51)$$

The presence of a *strong symmetry* \hat{S} implies that \hat{S} is a conserved quantity, or invariant observable, $\mathcal{L}^\dagger[\hat{S}] = 0$, but the converse is not true, i.e. there may be quantities \hat{J} which are conserved as a whole $\mathcal{L}^\dagger[\hat{J}] = 0$ but not individually by the Hamiltonian and jump operators $[\hat{J}, \hat{H}] \neq 0, [\hat{J}, \hat{L}_k] \neq 0$, which are also referred as *weak symmetries*. Following the notation of Albert [198], the right eigenvectors of the adjoint Lindbladian $\hat{R}_i \leftrightarrow \hat{J}_i$, while the left eigenvectors of the adjoint Lindbladian are $\hat{L}_i \leftrightarrow \hat{M}_i$.

Let $\mathbb{J} = \{\hat{J}_i\}$ be the set of all conserved quantities, then the steady state of the **SOV** can be written in terms of the conserved quantities as

$$\Delta\hat{A}_\infty^2 = \sum_{J_i \in \mathbb{J}} \text{Tr}(\hat{M}_i^\dagger \hat{A}^2) \hat{J}_i - \sum_{J_i, J_j \in \mathbb{J}} \text{Tr}(\hat{M}_i^\dagger \hat{A}) \text{Tr}(\hat{M}_j^\dagger \hat{A}) \hat{J}_i \hat{J}_j, \quad (2.52)$$

unfortunately, in general \mathbb{J} does not form a Lie algebra, see example 5.0.3 of [200]. This implies that the product of $\hat{J}_i \hat{J}_j$, and thus the whole **SOV** $\Delta\hat{A}_\infty^2$, is not necessarily an element of \mathbb{J} . However, if we restrict the conserved quantities to the steady state subspace $\ker(\mathcal{L})$, introducing the projection onto the steady state subspace $\mathcal{P}_s[\bullet]$, we can find the matrices $\hat{j}_i = \mathcal{P}_s[\hat{J}_i]$ and $\hat{m}_i = \mathcal{P}_s[\hat{M}_i]$ such that $\mathbf{j} = \{\hat{j}_i\}$ forms a Lie algebra [198]. Therefore the **SOV** steady state $\Delta\hat{A}_\infty^2$ projected to the steady state subspace

$$\Delta\hat{A}_{\infty,s}^2 = \sum_{j_i \in \mathbf{j}} \text{Tr}(\hat{m}_i^\dagger \hat{A}^2) \hat{j}_i - \sum_{j_i, j_k \in \mathbf{j}} \text{Tr}(\hat{m}_i^\dagger \hat{A}) \text{Tr}(\hat{m}_k^\dagger \hat{A}) \hat{j}_i \hat{j}_k, \quad (2.53)$$

is an element of the Lie algebra \mathbf{j} . Therefore, we have shown that the steady state of the **SOV** depends only on the conserved quantities (also known as invariant observables or simply elements of the kernel of the adjoint Lindbladian). Particularly through the projections of \hat{A} , \hat{A}^2 on the conserved quantities, and the products between the conserved quantities. The steady state of the **SOV** is not a conserved quantity in general $\mathcal{L}^\dagger[\Delta\hat{A}_\infty^2] \neq 0$, but it becomes one when $\Delta\hat{A}_{\infty,s}^2$ is built from the conserved quantities projected on the steady state subspace, i.e. $\mathcal{L}^\dagger[\Delta\hat{A}_{\infty,s}^2] = 0$.

2.5.2 Example: Two qubit dissipation

To illustrate the above computation, we choose case III.2 of [198] based on a similar Lindbladian considered by Barreiro *et al.* [197] to engineer a Lindbladian with a Bell

steady state. The system has two qubits, no free Hamiltonian, and a single jump operator⁴

$$\hat{L} = \frac{1}{2}(\hat{\mathbb{1}} - \hat{Z}_1 \hat{Z}_2) \hat{X}_2. \quad (2.54)$$

Interestingly, this system has a *decoherence free subspace* (DFS) [202]. Since the jump operator is Hermitian, the Lindbladian is of the form

$$\mathcal{L}[\bullet] = -\frac{\gamma}{4}[(\hat{\mathbb{1}} - \hat{Z}_1 \hat{Z}_2) \hat{X}_2, [(\hat{\mathbb{1}} - \hat{Z}_1 \hat{Z}_2) \hat{X}_2, \bullet]]. \quad (2.55)$$

Note that, due to the absence of Hamiltonian and the hermiticity of the jump operators, the adjoint Lindbladian is equal to the Lindbladian $\mathcal{L} = \mathcal{L}^\dagger$. The conserved quantities of this Lindbladian read [198]

$$\hat{J}_{00} = \frac{\hat{\mathbb{1}} + \hat{Z}_1}{2}, \quad (2.56a)$$

$$\hat{J}_{01} = \frac{\hat{X}_1 + i\hat{Y}_1}{2} \hat{X}_2 = \hat{J}_{10}^\dagger, \quad (2.56b)$$

$$\hat{J}_{11} = \frac{\hat{\mathbb{1}} - \hat{Z}_1}{2} = \hat{\mathbb{1}} - \hat{J}_{00}, \quad (2.56c)$$

which can be equivalently written in matrix form

$$\hat{J}_{00} = \begin{pmatrix} 1 & 0 & 0 & 0 \\ 0 & 1 & 0 & 0 \\ 0 & 0 & 0 & 0 \\ 0 & 0 & 0 & 0 \end{pmatrix}, \quad \hat{J}_{01} = \begin{pmatrix} 0 & 0 & 0 & 1 \\ 0 & 0 & 1 & 0 \\ 0 & 0 & 0 & 0 \\ 0 & 0 & 0 & 0 \end{pmatrix}. \quad (2.57)$$

In this case, the conserved quantities form a Lie algebra, so the steady-state subspace projection is not necessary. The Bell-state representation of these conserved quantities is [199]

$$\hat{J}_{kl} = |\Psi_k\rangle \langle \Psi_l| + |\Psi_k^\perp\rangle \langle \Psi_l^\perp|, \quad \hat{M}_{kl} = |\Psi_k\rangle \langle \Psi_l|, \quad (2.58)$$

where the Bell states are defined as

$$|\Psi_k\rangle = \frac{|01\rangle + (-1)^k |10\rangle}{\sqrt{2}}, \quad |\Psi_k^\perp\rangle = \frac{|00\rangle + (-1)^k |11\rangle}{\sqrt{2}},$$

which naturally obey the orthonormality properties $\langle \Psi_k | \Psi_l \rangle = \langle \Psi_k^\perp | \Psi_l^\perp \rangle = \delta_{kl}$ and $\langle \Psi_k^\perp | \Psi_l \rangle = 0$. Using these properties, the product between two conserved quantities reduces to

$$\hat{J}_{ij} \hat{J}_{kl} = |\Psi_i\rangle \langle \Psi_j | \Psi_k \rangle \langle \Psi_l| + |\Psi_i^\perp\rangle \langle \Psi_j^\perp | \Psi_k^\perp \rangle \langle \Psi_l^\perp| = \delta_{jk} \hat{J}_{il}. \quad (2.59)$$

⁴In this subsection, for convenience, we shift notation for the Pauli matrices from $\sigma_i^z = Z_i, \dots$

The steady **SOV** can be written in terms of the conserved quantities as

$$\Delta \hat{A}_\infty^2 = \sum_{i,j} \text{Tr}(\hat{M}_{ij}^\dagger \hat{A}^2) \hat{J}_{ij} - \sum_{i,j,k,l} \text{Tr}(\hat{M}_{ij}^\dagger \hat{A}) \text{Tr}(\hat{M}_{kl}^\dagger \hat{A}) \hat{J}_{ij} \hat{J}_{kl}, \quad (2.60)$$

which, substituting the products between the Lie algebra of conserved quantities, gives

$$\Delta \hat{A}_\infty^2 = \sum_{i,j} \left(\text{Tr}(\hat{M}_{ij}^\dagger \hat{A}^2) - \sum_k \text{Tr}(\hat{M}_{ik}^\dagger \hat{A}) \text{Tr}(\hat{M}_{kj}^\dagger \hat{A}) \right) \hat{J}_{ij}. \quad (2.61)$$

The projections of the initial operator \hat{A} and the operator squared \hat{A}^2 can be written as matrix elements between Bell states

$$\text{Tr}(\hat{M}_{kl}^\dagger \hat{A}) = \langle \Psi_k | \hat{A} | \Psi_l \rangle, \quad (2.62)$$

$$\text{Tr}(\hat{M}_{kl}^\dagger \hat{A}^2) = \langle \Psi_k | \hat{A}^2 | \Psi_l \rangle. \quad (2.63)$$

Using the completeness of the Bell-state basis $\sum_k |\Psi_k\rangle \langle \Psi_k| + \sum_k |\Psi_k^\perp\rangle \langle \Psi_k^\perp| = \hat{1}$ it is possible to write the steady **SOV** as

$$\Delta \hat{A}_\infty^2 = \sum_{i,j,k} \langle \Psi_i | \hat{A} | \Psi_k^\perp \rangle \langle \Psi_k^\perp | \hat{A} | \Psi_j \rangle (|\Psi_i\rangle \langle \Psi_j| + |\Psi_i^\perp\rangle \langle \Psi_j^\perp|). \quad (2.64)$$

The **DFS** is spanned by the Bell states $\{|\Psi_k^\perp\rangle\}$. It is interesting to note that if the initial operator \hat{A} is started either entirely in the **DFS** or entirely out of the **DFS**, the **SOV** in the steady state will completely vanish. The first observation can be intuitively understood in the following way, when restricted to the **DFS** $\hat{P}_{\text{DFS}} = \sum_k |\Psi_k\rangle \langle \Psi_k|$, the evolution generated by the Quantum channel is effectively unitary $\hat{P}_{\text{DFS}} \mathcal{E}^\dagger[\bullet] \hat{P}_{\text{DFS}} \equiv \hat{U}_{\text{DFS}} \bullet \hat{U}_{\text{DFS}}^\dagger$, and the **SOV** of a unitary channel identically vanishes.

2.6 SOV-OTOC connection

2.6.1 Dephasing case: Classical noise

Throughout this Chapter, we have introduced the Stochastic Operator Variance and studied some of its properties. We show that this quantity is related to an Out of Time Order Correlator (**OTOC**).

We begin by deriving the equation of motion, followed by the **SOV**. We know that the second moment $\mathbb{E}(\hat{A}_t^2)$ evolves following the **GKSL** equation, see eq. 2.8 $\partial_t \mathbb{E}(\hat{A}_t^2) = \mathcal{L}^\dagger[\mathbb{E}(\hat{A}_t^2)]$. For the noise-average evolution squared, we have

$$\partial_t \hat{\mathbf{A}}_t^2 = \mathcal{L}^\dagger[\hat{\mathbf{A}}_t] \hat{\mathbf{A}}_t + \hat{\mathbf{A}}_t \mathcal{L}^\dagger[\hat{\mathbf{A}}_t]. \quad (2.65)$$

In deriving an equation of motion for the **SOV** $\Delta\hat{A}_t^2$, it is convenient to write the equation with a homogeneous term of the form $\mathcal{L}^\dagger[\Delta\hat{A}_t^2]$ plus an inhomogeneous term. To bring it to this form, we need a term of the form $\mathcal{L}^\dagger[\hat{\mathbf{A}}_t^2]$ in the equation for the evolution of the second moment squared $\partial_t\hat{\mathbf{A}}_t^2$. Let us see how this simplifies

$$\begin{aligned}\partial_t\hat{\mathbf{A}}_t^2 - \mathcal{L}^\dagger[\hat{\mathbf{A}}_t^2] &= \{\mathcal{L}^\dagger[\hat{\mathbf{A}}_t], \hat{\mathbf{A}}_t\} - \mathcal{L}^\dagger[\hat{\mathbf{A}}_t^2], \\ &= -\sum_{n=1}^{N_c} \gamma_n \left(\{[\hat{L}_n, [\hat{L}_n, \hat{\mathbf{A}}_t]], \hat{\mathbf{A}}_t\} - [\hat{L}_n, [\hat{L}_n, \hat{\mathbf{A}}_t^2]] \right), \\ &= -2 \sum_{n=1}^{N_c} \gamma_n \left(\hat{\mathbf{A}}_t \hat{L}_n^2 \hat{\mathbf{A}}_t + \hat{L}_n \hat{\mathbf{A}}_t^2 \hat{L}_n - \hat{L}_n \hat{\mathbf{A}}_t \hat{L}_n \hat{\mathbf{A}}_t - \hat{\mathbf{A}}_t \hat{L}_n \hat{\mathbf{A}}_t \hat{L}_n \right), \\ &= +2 \sum_{n=1}^{N_c} \gamma_n [\hat{L}_n, \hat{\mathbf{A}}_t]^2.\end{aligned}\tag{2.66}$$

Interestingly, the right-hand side of this expression represents the *dissipation function* introduced by *Lindblad* [30], which provides a partial order over Lindbladians.

The equation of motion for the **SOV** then reduces to

$$\frac{d(\Delta\hat{A}_t^2)}{dt} = \mathcal{L}^\dagger[\Delta\hat{A}_t^2] - 2 \sum_{n=1}^{N_c} \gamma_n [\hat{L}_n, \hat{\mathbf{A}}_t]^2.\tag{2.68}$$

For simplicity, we now take the case with a single noise channel $N_c = 1$, in which the **SOV** evolves according to

$$\frac{d(\Delta\hat{A}_t^2)}{dt} = \mathcal{L}^\dagger[\Delta\hat{A}_t^2] - 2\gamma[\hat{L}, \hat{\mathbf{A}}_t]^2.\tag{2.69}$$

Taking the expectation value of this equation of motion over the maximally mixed state $\hat{\rho}_0 = \hat{\mathbb{1}}/N$, we find the **SOV-OTOC connection**. It states that the trace of the time-derivative of the **SOV** is equal to a dissipative **OTOC** between the jump operator \hat{L} and the noise-averaged operator $\hat{\mathbf{A}}_t$. The proportionality constant between these quantities is nothing but the noise strength γ

$$\frac{1}{N} \frac{d\text{Tr}(\Delta\hat{A}_t^2)}{dt} = -\frac{2\gamma}{N} \text{Tr}([\hat{L}, \hat{\mathbf{A}}_t]^2) = 2\gamma C_t.\tag{2.70}$$

The connection is illustrated in Fig. 2.5. The **SOV** (red) is related to the spread of trajectories around the average; when this quantity is projected over the identity, its time derivative gives the **OTOC** (blue). The dissipative **OTOC** C_t can then be written as

$$C_t = \frac{1}{2\gamma N} \frac{d\text{Tr}(\Delta\hat{A}_t^2)}{dt} \sim \epsilon e^{\lambda_q t},\tag{2.71}$$

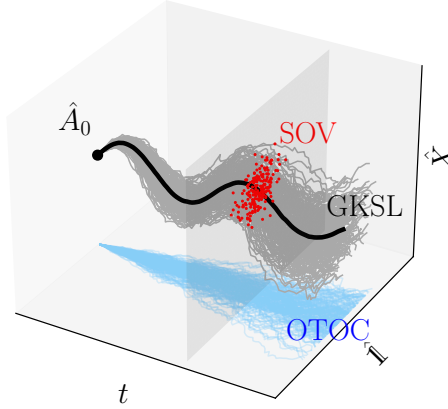


Figure 2.5. Illustration of the SOV-OTOC connection: Illustration of the Stochastic Operator Variance (red) and its connection to the Out-of-Time-Order Correlator (blue). The projection over the identity of the time-derivative of the SOV gives a dissipative OTOC (2.70). Figure adapted from [1].

where the exponential growth only applies in systems with scrambling, in the appropriate time window $t_d \ll t \ll t_E$ between the dissipation $t_d \sim 1/\lambda_Q$ and Ehrenfest $t_d \sim \log(\hbar_{\text{eff}}^{-1})/\lambda_Q$ times [128], recall Sec. 1.10. Due to the dissipation, the Lyapunov regime in the dissipative OTOC may be more difficult to observe. If this regime is present, it tells us that the trajectories are separating exponentially fast from the GKSL average behavior, at least in their projection over the identity.

2.6.2 General GKSL case: Quantum noise

We consider now a setup slightly different from the rest of the chapter. We want to find a SOV-OTOC connection for the most general GKSL equation with non-Hermitian jump operators $\hat{L}_n^\dagger \neq \hat{L}_n$, i.e., with Lindbladian

$$\mathcal{L}^\dagger[\bullet] = \sum_j \gamma_j \left(2\hat{L}_j^\dagger \bullet \hat{L}_j - \{\hat{L}_j^\dagger \hat{L}_j, \bullet\} \right).$$

This master equation can be derived considering a Stochastic Hamiltonian with quantum noise [203], i.e. the white noise $\hat{\xi}_t$ is now an operator such that $[\hat{\xi}_t, \hat{\xi}_{t'}^\dagger] = \delta(t - t') \neq 0$. Therefore, the stochastic Hamiltonian now is $\hat{H}_t = \hat{H}_0 + \sqrt{2\gamma} \hat{\xi}_t \hat{L}$ where now $\hat{L} \neq \hat{L}^\dagger$.

Using quantum noise, we generalize the SOV and define the *quantum Stochastic Operator Variance (qSOV)* as

$$\Delta \hat{A}_t^2 := \mathbb{E}_q(\hat{A}_t^2) - \mathbb{E}_q(\hat{A}_t)^2. \quad (2.72)$$

where the *vacuum conditional expectation map* was defined by Hudson and Parthasarathy [204] as

$$\begin{aligned}\mathbb{E}_q(\bullet) : \mathcal{B}(\tilde{\mathcal{H}}) &\rightarrow \mathcal{B}(\mathcal{H}), \\ \langle u | \mathbb{E}_q(\hat{J}) | v \rangle &= \langle u \otimes \psi_0 | J | v \otimes \psi_0 \rangle,\end{aligned}\tag{2.73}$$

where $u, v \in \mathcal{H}$, $\hat{J} \in \mathcal{B}(\mathcal{H})$. We now want to find its equation of motion. We can introduce the analog of the Wiener increment $d\hat{B}_t$, which now obeys the following Itô properties [203]

$$d\hat{B}_t d\hat{B}_t^\dagger = (\bar{N} + 1) dt, \quad d\hat{B}_t^\dagger d\hat{B}_t = \bar{N} dt,\tag{2.74}$$

where all other products vanish and \bar{N} is the average number of photons. Even if noise is quantum, the propagator

$$\hat{Q}_t = \mathcal{T}_{\leftarrow} \exp \int_0^t \left(\hat{H} dt' + \hat{L} d\hat{B}_{t'} \right),$$

is still unitary and thus respects $\hat{Q}_t^\dagger \hat{Q}_t = \hat{Q}_t \hat{Q}_t^\dagger = \hat{\mathbb{1}}$. Unitarity implies that the second moment over the noise reduces as

$$\mathbb{E}_q(\hat{A}_t^2) = \mathbb{E}_q(\hat{Q}_t^\dagger \hat{A} \hat{Q}_t \hat{Q}_t^\dagger \hat{A} \hat{Q}_t) = \mathbb{E}_q(\hat{Q}_t^\dagger \hat{A}^2 \hat{Q}_t) = e^{\mathcal{L}^\dagger t} [\hat{A}^2],\tag{2.75}$$

which means that it still obeys the GKSL equation $\partial_t \mathbb{E}_q(\hat{A}_t^2) = \mathcal{L}^\dagger [\mathbb{E}_q(\hat{A}_t^2)]$. In the same way as before, we want to express the derivative of the first moment squared $\partial_t \hat{\mathfrak{A}}_t^2 = \{\mathcal{L}^\dagger[\hat{\mathfrak{A}}_t], \hat{\mathfrak{A}}_t\}$, as the adjoint Lindbladian acting on the first moment squared and extra terms. In this case, we have

$$\partial_t \hat{\mathfrak{A}}_t^2 - \mathcal{L}^\dagger[\hat{\mathfrak{A}}_t^2] = \{\mathcal{L}^\dagger[\hat{\mathfrak{A}}_t], \hat{\mathfrak{A}}_t\} - \mathcal{L}^\dagger[\hat{\mathfrak{A}}_t^2],\tag{2.76}$$

$$\begin{aligned}&= \sum_{j=1}^{N_c} \left(\left\{ (2\hat{L}_j^\dagger \hat{\mathfrak{A}}_t \hat{L}_j^\dagger - \{\hat{L}_j^\dagger \hat{L}_j, \hat{\mathfrak{A}}_t\}), \hat{\mathfrak{A}}_t \right\} - (2\hat{L}_j^\dagger \hat{\mathfrak{A}}_t^2 \hat{L}_j^\dagger - \{\hat{L}_j^\dagger \hat{L}_j, \hat{\mathfrak{A}}_t^2\}) \right), \\ &= \sum_{j=1}^{N_c} 2\gamma_j \left(\hat{L}_j^\dagger \hat{\mathfrak{A}}_t \hat{L}_j \hat{\mathfrak{A}}_t + \hat{\mathfrak{A}}_t \hat{L}_j^\dagger \hat{\mathfrak{A}}_t \hat{L}_j - \hat{\mathfrak{A}}_t \hat{L}_j^\dagger \hat{L}_j \hat{\mathfrak{A}}_t - \hat{L}_j^\dagger \hat{\mathfrak{A}}_t^2 \hat{L}_j \right), \\ &= -2 \sum_{j=1}^{N_c} \gamma_j [\hat{L}_j, \hat{\mathfrak{A}}_t]^\dagger [\hat{L}_j, \hat{\mathfrak{A}}_t],\end{aligned}\tag{2.77}$$

where we used the Hermiticity property of the observable $\hat{\mathfrak{A}}_t^\dagger = \hat{\mathfrak{A}}_t$ to simplify the expression. Therefore, we find the equation of motion for the **qSOV** to be

$$\partial_t \Delta \hat{A}_t^2 = \mathcal{L}^\dagger[\Delta \hat{A}_t^2] + 2 \sum_{j=1}^{N_c} \gamma_j [\hat{L}_j, \hat{\mathfrak{A}}_t]^\dagger [\hat{L}_j, \hat{\mathfrak{A}}_t],\tag{2.78}$$

which averaging over the maximally mixed state $\rho = \hat{\mathbb{1}}/N$ gives the **qSOV-OTOC** connection as

$$\frac{1}{N} \partial_t \text{Tr}(\Delta \hat{A}_t^2) = \frac{2}{N} \sum_{j=1}^{N_c} \gamma_j \text{Tr}([\hat{L}_j, \hat{\mathbf{A}}_t]^\dagger [\hat{L}_j, \hat{\mathbf{A}}_t]), \quad (2.79)$$

or in the case of a single noise channel $N_c = 1$

$$\frac{1}{N} \partial_t \text{Tr}(\Delta \hat{A}_t^2) = 2\gamma C_t, \quad (2.80)$$

where the **OTOC** for non-Hermitian operators is defined as $C_t := \langle [\hat{B}, \hat{A}_t]^\dagger [\hat{B}, \hat{A}_t] \rangle$ [148].

2.6.3 Finding different OTOC's

Unregularized thermal OTOC

There are many different versions of the **OTOCs** considered in the literature, used in different contexts. First of all, one may be interested in considering the average over a thermal state $\hat{\rho}_\beta = e^{-\beta \hat{H}}/Z_\beta$. This is a *unregularized thermal OTOC* $C_{\beta,t}^{(u)}$ [160, 168] and the **SOV-OTOC** connection reads

$$\begin{aligned} \frac{1}{Z_\beta} \frac{d\text{Tr}(\Delta \hat{A}_t^2 e^{-\beta \hat{H}})}{dt} &= \frac{\text{Tr}(\mathcal{L}^\dagger [\Delta \hat{A}_t^2] e^{-\beta \hat{H}})}{Z_\beta} - \frac{2\gamma}{Z_\beta} \text{Tr}([\hat{L}, \hat{\mathbf{A}}_t]^2 e^{-\beta \hat{H}}), \\ &= \langle \mathcal{L}^\dagger [\Delta \hat{A}_t^2] \rangle_\beta + 2\gamma C_{\beta,t}^{(u)}. \end{aligned} \quad (2.81)$$

Note the appearance of an extra term in the **SOV-OTOC** relation. This additional term comes from the fact that the expectation value over a maximally mixed state of the adjoint Lindbladian acting on any operator vanishes due to trace preservation $\text{Tr}(\mathcal{L}^\dagger[\bullet]) = 0$, but this is not the case for any general state. In the case of the **qSOV** however, if the Lindbladian has a thermal steady state and we average over this state $\text{Tr}(\mathcal{L}^\dagger [\Delta \hat{A}_t] e^{-\beta \hat{H}}) = \text{Tr}(\Delta \hat{A}_t^2 \mathcal{L}[e^{-\beta \hat{H}}]) = 0$ the extra term cancels out leaving the derivative of the thermal expectation value of the **qSOV** directly related to the unregularized thermal **OTOC**.

Regularized thermal OTOC

In certain quantum field theories, the previous expression may give rise to diverging results [128]. For this reason, when studying the Lyapunov exponent of a quantum system at finite temperature, it is customary to introduce a certain regularization scheme. There are many possible regularizations of the thermal **OTOC**, for instance one can split the thermal factor $e^{-\beta \hat{H}}$ in two to define an regularized thermal **OTOC** as

$$C_{\beta,t}^{(r,2)} = \frac{1}{Z_\beta} \text{Tr}([\hat{B}, \hat{A}_t] e^{-\frac{\beta}{2} \hat{H}} [\hat{B}, \hat{A}_t] e^{-\frac{\beta}{2} \hat{H}}). \quad (2.82)$$

Perhaps the most commonly used way to regularize this quantity [128] is to split the thermal factor in four and define the **OTOC** as

$$\tilde{C}_{\beta t}^{(r,4)} = \frac{1}{Z_\beta} \text{Tr}(\hat{A}_t e^{-\frac{\beta}{4}\hat{H}} \hat{B} e^{-\frac{\beta}{4}\hat{H}} \hat{A}_t e^{-\frac{\beta}{4}\hat{H}} \hat{B} e^{-\frac{\beta}{4}\hat{H}}), \quad (2.83)$$

note that this expression involves only the out-of-time-order terms and thus not all of the terms in the squared commutator, we add the tilde to the quantity \tilde{C} to stress out this difference.

If we transform the jump operators in the way $\hat{L}_\beta = e^{-\frac{\beta}{4}\hat{H}} \hat{L} e^{-\frac{\beta}{4}\hat{H}}$ and we trace over the maximally mixed state we can find the **SOV**-regularized **OTOC** connection as

$$\frac{1}{N} \frac{d\text{Tr}(\Delta\hat{A}_t)}{dt} = -\frac{2\gamma}{N} \text{Tr}([\hat{L}_\beta, \hat{A}_t]^2) = 2\gamma C_t^{(r,4)}, \quad (2.84)$$

where the Liouvillian term vanishes since $\text{Tr}(\mathcal{L}_\beta^\dagger[\bullet]) \sim -\gamma \text{Tr}([\hat{L}_\beta, [\hat{L}_\beta, \bullet]]) = 0$.

Fidelity OTOC

A certain class of **OTOC**'s, which is known as *Fidelity OTOC (FOTOC)* $C_t^{(\psi)}$, can be written as a fidelity between two quantum states [205] and allows to map the **OTOC** to a Loschmidt echo. It is customary to take the operator that does not evolve in time to be a projector over a certain pure state $\hat{B} = |\psi\rangle\langle\psi|$. Taking the jump operator in the stochastic Hamiltonian to be a projector $\hat{L} = |\psi\rangle\langle\psi|$ directly gives a **SOV-FOTOC** relation

$$\frac{1}{N} \partial_t \text{Tr}(\Delta\hat{A}_t) = -\frac{2\gamma}{N} \text{Tr}([|\psi\rangle\langle\psi|, \hat{A}_t]^2) = C_t^{(\psi)}. \quad (2.85)$$

Microcanonical OTOC

Lastly one other interesting **OTOC** is the *microcanonical OTOC* $C_t^{(E_n)}$ [151, 206]. This expression takes the expectation value over an energy eigenstate $|E_n\rangle$. In a similar way to what was done for the thermal **OTOC**, we find the connection to the microcanonical one as

$$\begin{aligned} \partial_t \langle E_n | \Delta\hat{A}_t^2 | E_n \rangle &= \langle E_n | \mathcal{L}^\dagger[\Delta\hat{A}_t^2] | E_n \rangle - 2\gamma \langle E_n | [\hat{L}, \hat{A}_t]^2 | E_n \rangle \\ &= \langle \mathcal{L}^\dagger[\Delta\hat{A}_t^2] \rangle_{E_n} + 2\gamma C_t^{(E_n)}. \end{aligned} \quad (2.86)$$

2.6.4 Properties of Dissipative OTOC's

In the previous subsection, we found a connection between different expectation values of the Stochastic Operator Variance and different Out of Time Order Correlators. However, there is something that all the different **OTOC**'s have in common: they are *dissipative OTOC*'s, in which the time evolution is given by some dissipative dynamics of the form

$\hat{\mathfrak{A}}_t = e^{\mathcal{L}^\dagger t}[\hat{A}]$. Dissipative OTOC's have been studied previously in the literature [170–172, 174, 207]. Crucially, dissipation alters their structure, and many of their defining features, such as the Lyapunov regime, can be hidden due to the presence of dissipation. In here, we study some generic features of dissipative OTOC's, which provide further understanding of the OTOC side of the SOV-OTOC connection.

Short time expansion of the Dissipative OTOC

The short-time expansion of the time evolution of the observable \hat{A} is

$$\hat{\mathfrak{A}}_t = \hat{A} + t\mathcal{L}^\dagger[\hat{A}] + \mathcal{O}(t^2).$$

Substituting this expression in the Dissipative OTOC, which is related to the SOV gives

$$\begin{aligned} NC_t &= -\text{Tr} \left(\left[\hat{L}, \hat{A} + t\mathcal{L}^\dagger[\hat{A}] + \mathcal{O}(t^2) \right]^2 \right), \\ &= -\text{Tr} \left([\hat{L}, \hat{A}]^2 + 2t[\hat{L}, \hat{A}][\hat{L}, \mathcal{L}^\dagger[\hat{A}]] \right) + \mathcal{O}(t^2). \\ &\approx -\text{Tr}([\hat{L}, \hat{A}]^2) - 2t \left(i\text{Tr}([\hat{L}, \hat{A}][\hat{L}, [\hat{H}_0, \hat{A}]]) - \gamma\text{Tr}([\hat{L}, \hat{A}][\hat{L}, [\hat{L}, [\hat{L}, \hat{A}]]]) \right). \end{aligned} \quad (2.87)$$

The first of the two linear terms provides some imaginary contribution, which induces oscillations in the dissipative OTOC, while the second term provides an exponential decay at short times. This is the dissipation time τ_D and using the property $\text{Tr}(\hat{X}[\hat{Y}, \hat{Z}]) = \text{Tr}([\hat{X}, \hat{Y}]\hat{Z})$ of the trace, with $\hat{X} = [\hat{L}, \hat{A}]$, $\hat{Y} = \hat{L}$ and $\hat{Z} = [\hat{L}, [\hat{L}, \hat{A}]]$, it can be rewritten as the Hilbert Schmidt norm of the dissipator $\text{Tr}([\hat{L}, [\hat{L}, \hat{A}]]^2)$. Introducing the initial value of the OTOC as $C_0 = -\frac{\text{Tr}([\hat{L}, \hat{A}]^2)}{N}$ the dissipation time of the OTOC is given by

$$-C_0 \frac{t}{\tau_D} = -2\gamma t \text{Tr}([\hat{L}, [\hat{L}, \hat{A}]]^2), \quad (2.88)$$

$$\tau_D = \frac{C_0}{2\gamma \text{Tr}([\hat{L}, [\hat{L}, \hat{A}]]^2)}. \quad (2.89)$$

Therefore the dissipative OTOC which connects to the SOV decays as $C_t = C_0(1 - \frac{t}{\tau_D} + \mathcal{O}(t^2))$ at short times. Note that it is also possible to resum some of the terms in the Taylor expansion to argue that it decays as $C_t \approx C_0 e^{-t/\tau_D}$.

Dissipative OTOC in dephasing dynamics

If we assume that the jump operator and the Hamiltonian commute $[\hat{H}_0, \hat{L}] = 0$ they can be diagonalized simultaneously in the eigenbasis $\hat{H}_0 |n\rangle = e_n |n\rangle$, $\hat{L} |n\rangle = l_n |n\rangle$. In this eigenbasis, the operator evolves as

$$\hat{\mathfrak{A}}_t = \sum_{m,n} \hat{A}_{mn} e^{i(E_m - E_n)t - \gamma(l_m - l_n)^2 t} |m\rangle \langle n|, \quad (2.90)$$

where $\hat{A}_{mn} = \langle m | \hat{A} | n \rangle$ is the matrix element of the operator between different eigenvectors of the basis. Using this expression, we find that the **OTOC** is given by a term of the form

$$\text{Tr}([\hat{L}, \hat{A}_t]^2) = \sum_{m,k=1}^N (l_m - l_k)^2 |\hat{A}_{km}(t)|^2 = \sum_{m,k=1}^N (l_m - l_k)^2 e^{-2\gamma(l_m - l_n)^2 t} |\hat{A}_{km}|^2,$$

which yields the dissipative **OTOC** as

$$C_t = \frac{1}{N} \sum_{m,n} (l_m - l_n)^2 e^{-2\gamma(l_m - l_n)^2 t} |A_{nm}|^2. \quad (2.91)$$

The behavior of the dissipative **OTOC** for dephasing dynamics was studied originally by *Syzranov et al.* [170]. One of their main results is that the dissipative **OTOC** should show two different exponentially decaying regimes and a saturation at longer times. The case of commuting Hamiltonian and jump provides dephasing since the dynamics' effect simply dampens all the coherences in the common eigenbasis. This decomposition of the dephasing **OTOC** shows that the maximum difference between eigenvalues and the minimum difference, respectively, gives the two decaying exponentials. At the transition between the two exponentially decaying regimes, we expect to see a contribution from the intermediate differences $l_m - l_n$.

2.7 The Stochastic Lipkin Meshkov Glick model

The *Lipkin-Meshkov-Glick* (LMG) model [208] describes the behavior of many two-level systems interacting all-to-all through a collective operator. Initially introduced in the context of nuclear physics, this model shows scrambling coming from the presence of a saddle point, while still being integrable [151, 154, 209]. It has been realized experimentally with trapped ions [210] where scrambling may improve certain tasks in quantum metrology [211].

2.7.1 Quantum stochastic LMG

We begin our study by considering the fully quantum version of the model. The LMG model describes the collective motion of N identical two-level systems interacting all-to-all with the same coupling strength [208]. The Hamiltonian of the system reads

$$\hat{H}_{\text{LMG}} = \Omega \hat{S}_z - \frac{2}{N} \hat{S}_x^2, \quad (2.92)$$

where Ω is the frequency of the two-level systems in units of the coupling strength and \hat{S}_j are the spin S operators. The total spin S of the collective operators is related to the number of two-level systems through $S = N/2$. The first term of the Hamiltonian describes the energy of each of the two-level systems, while the second term describes the

interactions between them through a $\hat{\sigma}_x^{(i)}\hat{\sigma}_x^{(j)}$ coupling. The total spin $\hat{\mathbf{S}}^2 = \hat{S}_x^2 + \hat{S}_y^2 + \hat{S}_z^2$ commutes with all the operators $[\hat{\mathbf{S}}^2, \hat{S}_j] = 0$, and thus the total angular momentum is conserved. Furthermore, due to time-translational symmetry, the energy of the system is conserved. This implies that the system is integrable since it only has one degree of freedom. When the continuous time-translational symmetry is broken through some periodic kicks in \hat{S}_x^2 , this model is the Quantum Kicked Top [113, 133], which displays many of the features of quantum chaos. In here, we break time translational symmetry by adding some stochastic terms to the Hamiltonian. In general, it reads

$$\hat{H}_t = \hat{H}_{\text{LMG}} + \sum_{n=1}^{N_c} \sqrt{2\gamma_n} \hat{L}_n \xi_t^{(n)}. \quad (2.93)$$

However, for many of the results we will consider a simple case in which there is only one source of noise $N_c = 1$ which affects the whole Hamiltonian $\hat{L} = \hat{H}_{\text{LMG}}$, i.e.

$$\hat{H}_t = \hat{H}_{\text{LMG}} (1 + \sqrt{2\gamma} \xi_t). \quad (2.94)$$

This stochastic Hamiltonian describes energy dephasing dynamics, i.e., dephasing in the energy eigenbasis of \hat{H}_{LMG} . To characterize the evolution of the **SOV** in time, it is helpful to consider the eigenvalues and eigenvectors of the **SOV**

$$\Delta \hat{A}_t^2 |v_k(t)\rangle = \Lambda_k(t) |v_k(t)\rangle.$$

Since the **SOV** is hermitian and positive semidefinite its eigenvalues fulfill $\Lambda_k(t) \in \mathbb{R}$, $\Lambda_k(t) \geq 0$. We order the eigenvalues in ascending order $\Lambda_0(t) \leq \Lambda_1(t) \leq \dots \leq \Lambda_{N-1}(t)$. This eigen-decomposition also allows to find the state *minimally affected by the noise* at long times as the eigenstate with the smallest eigenvalue of the **SOV** in the $t \rightarrow \infty$ limit

$$|\Psi\rangle = \lim_{t \rightarrow \infty} |v_0(t)\rangle. \quad (2.95)$$

Starting in this state guarantees that at long times the **SOV** acquires its smallest value and thus the dynamics is protected from the noise in a certain way, since this state only “feels” the smallest possible value of the **SOV**.

Figure 2.6 (a) shows the evolution of the eigenvalues of the **SOV**. We see that the eigenvalues initially grow in time and then generally saturate to a given value, although some still show non-trivial dynamics at long times. In this particular case, we have energy dephasing; we observe that the smallest eigenvalue grows in time as $\Lambda_0(t) \sim t^{3/2}$, which is reminiscent of superdiffusive behavior in the context of quantum transport [212, 213]. However, most of the eigenvalues, especially the largest ones, show a diffusive scaling in which the variance grows linearly in time $\Lambda_k(t) \sim t$. Lastly, the expectation value of the **SOV** in the $|\Psi\rangle$ state $\langle \Psi | \Delta \hat{A}_t^2 | \Psi \rangle$ (black dash-dotted)

Interestingly, in the case where $[\hat{H}_0, \hat{L}] \neq 0$, shown in Fig. 2.7, it is possible to get ballistic scalings $\Lambda_k(t) \sim t^2$, as well as diffusive and superdiffusive, for specific windows of time. Another interesting feature of this case is that at long times all the eigenvalues collapse to

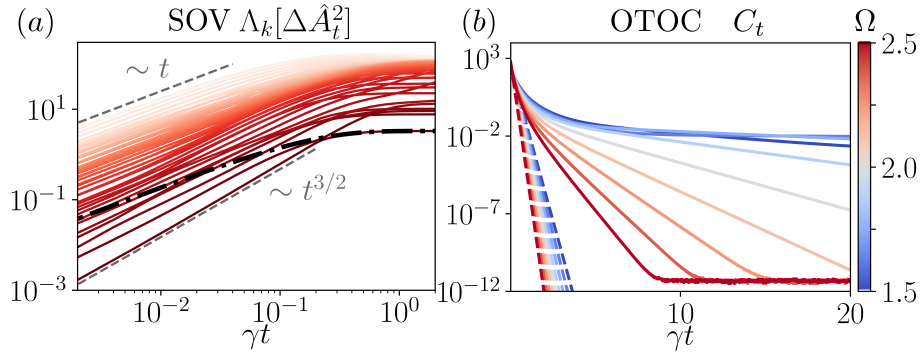


Figure 2.6. Evolution of (a) the **SOV** eigenvalues, and (b) the **OTOC** C_t for the quantum sLMG model. The operator $\hat{A} = \frac{1}{\sqrt{3}}(\hat{S}_x + \hat{S}_y + \hat{S}_z)$ evolves under the stochastic Hamiltonian (2.94) with $\gamma = 2$, $\Omega = 1$, and $S = 20$. (a) Eigenvalues of the **SOV** as a function of time (solid red, colorscale indicates k and can be seen in Fig. 2.7) and expectation value of the **SOV** for the state which minimized the deviation at long time, $\langle \Psi | \Delta\hat{A}_t^2 | \Psi \rangle$ (black dash-dotted). (b) Dissipative **OTOC** obtained from the **SOV-OTOC** relation (2.70) (solid line) and short-time expansion (dashed line) for different values of Ω (colorbar) across the phase transition—at $\Omega_c = 2$. Figure adapted from [1].

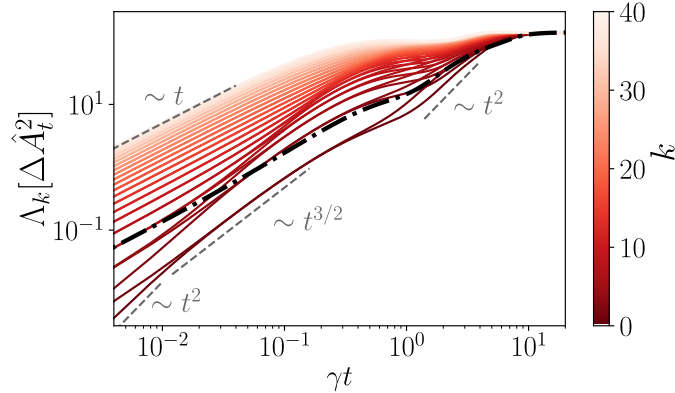


Figure 2.7. Eigenvalues of the **SOV** as a function of time for noncommuting Hamiltonian and Jump operator $[\hat{H}_0, \hat{L}] \neq 0$ (red colorscale), as well as the expectation value over the minimum **SOV** state $\langle \Psi | \Delta\hat{A}_t^2 | \Psi \rangle$ (black dash-dotted). The parameters are $\gamma = 2, \Omega = 1, S = 20, \hat{A} = (\hat{S}_x + \hat{S}_y + \hat{S}_z)/\sqrt{3}$ and $\hat{L} = \hat{S}_x$.

the same value. This implies that all the initial states see the same value of the **SOV** and that the **SOV** is proportional to the identity, as found in the case of a single steady state (2.50), which was expected since in this case the Hamiltonian \hat{H}_{LMG} is not a conserved quantity.

Figure 2.6 (b) shows the behavior of the dissipative **OTOC** $C_t = \text{Tr}([\hat{L}, \hat{A}_t]^2)/N$, as computed through the **SOV-OTOC** connection, for different values of the parameter Ω . As will be discussed in the coming sections, the LMG model shows a transition from a double-

well-like, ferromagnetic phase when $\Omega < 2$ to a paramagnetic, single-well-like phase when $\Omega > 2$. This difference in behavior manifests in the dissipative OTOC, which shows some decay for Ω below the transition, but above the transition, shows very clearly the two exponential decays and saturation expected from [170], or from our previous analysis of the dissipative OTOC when $[\hat{H}_0, \hat{L}] = 0$ (2.91).

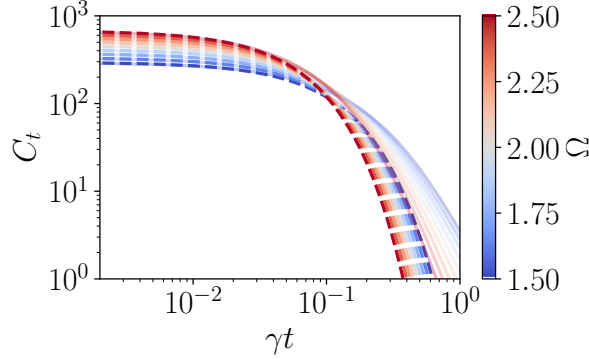


Figure 2.8. Short-time behavior of the OTOC as computed from the SOV-OTOC relation. Full OTOC (solid line) and short-time expansion (2.89) (dashed line). The crossover between the two exponentially decaying regimes is seen around $\gamma t \approx 0.1$.

Furthermore, the short-time exponential decay $C_0 e^{-t/\tau_D}$ (2.89) (dashed line in Fig. 2.6 (b)) describes well the first exponential decay of the dissipative OTOC. This can be more easily inspected from Fig. 2.8, which focuses on the early time decay of the dissipative OTOC in a log-log scale.

Figure 2.3 illustrates the information in the SOV. Taking the stochastic LMG model as a playground, we now build a more quantitative version of the previous figure. For this, we compute the SOV exactly in the sLMG with energy dephasing, in the double well phase of the model. Figure 2.9 shows the evolution of the SOV for two different strengths of the noise ($\gamma = 0.1$ upper and $\gamma = 2$ lower). In particular, Fig. 2.9 (a) shows the Stochastic Operator Standard deviation $\Delta \hat{A}_t = \sqrt{\Delta \hat{A}_t^2}$ as the error bar on top of the GKSL evolution, in particular through all its projections, in the Hilbert-Schmidt sense, over the three spin operators $\{\hat{S}_x, \hat{S}_y, \hat{S}_z\}$. In particular, to ensure that different spin operators are orthonormal, the normalization in the Hilbert-Schmidt inner product is chosen as

$$(\hat{A}, \hat{B})_s = \frac{3}{S(S+1)(2S+1)} \text{Tr}(\hat{A}^\dagger \hat{B}), \quad (2.96)$$

which ensures that $(\hat{S}_i, \hat{S}_j)_s = \delta_{ij}$, however note that the identity is not normalized $(\hat{1}, \hat{1})_s = \frac{3}{S(S+1)} \neq 1$.

The flow of time is indicated by the colorscale (from black to yellow). We see that the weak noise case $\gamma = 0.1$ shows underdamped dynamics in which the observables oscillate before

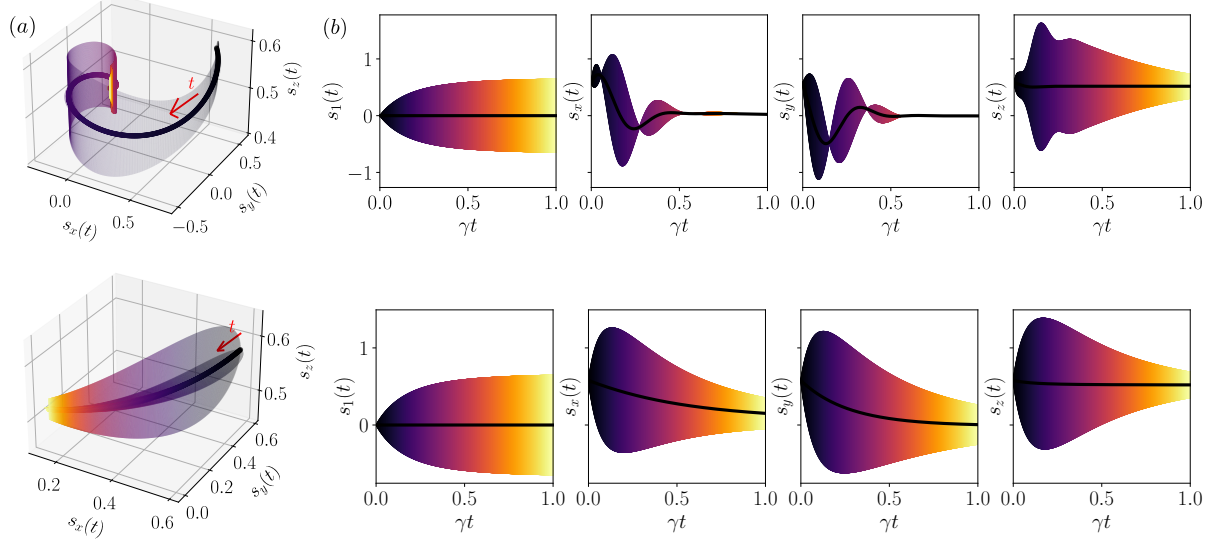


Figure 2.9. Visualization for the evolution of the stochastic operator variance and its standard deviation for the quantum sLMG model. (a) Projection over the different spin operators of the noise averaged observable $(\hat{A}_t, \hat{S}_j)_S$ (solid line) and the Stochastic Operator Standard Deviation $(\Delta \hat{A}_t, \hat{S}_j)_S$ (error bar), with the flow of time indicated by the color scale and the red arrow. (b) Projections of the noise-averaged observable (black line) $(\hat{A}_t, \hat{X})_S$ and the SOV $(\Delta \hat{A}_t^2, \hat{X})_S$ (error bar) over $\hat{X} \in \{\hat{1}, \hat{S}\}$. The initial operator is $\hat{A} = (\hat{S}_x + \hat{S}_y + \hat{S}_z)/\sqrt{3}$. The parameters are $S = 20$ and $\Omega = 1.5$, with $\gamma = 0.1$ (upper) or $\gamma = 2$ (lower). The times for which the error bar vanishes correspond to the SOV being orthogonal to the projected operator.

reaching the steady state, while the strong noise case $\gamma = 2$ shows overdamped dynamics with direct convergence to the steady state, without showing oscillations. Figure 2.9 (b) shows the projection of the SOV $\Delta \hat{A}_t^2$ over different operators $\{\hat{1}, \hat{S}\}$. We see that the projection of the SOV over the identity, related to the integral of the OTOC, grows in time for both strengths of the noise. However, the projection of the SOV over the spin operators shows a more non-trivial evolution, for instance, when the noise is weak the projection over the operators \hat{S}_x and \hat{S}_y can become zero, which implies that the SOV is orthogonal to the operator at that time, in the same case the projection over \hat{S}_z quickly grows, then decreases, stays almost constant, and then finally decreases at long times. The strong noise case shows a simpler evolution; the projections of the SOV quickly grow and decay. One further comment is in order, the z projection of the average $(\hat{A}_t, \hat{S}_z)_S$ shows almost no dynamics, this makes the range spanned by the z projection much smaller compared to the range spanned by the other coordinates, making the projection of the SOSD over the z coordinate $(\Delta \hat{A}_t, \hat{S}_z)$ appear much larger than the other projections. Looking at the projection of the SOV with the same scale for all the axes, cf. Fig. 2.9, we see that even if the projection of the SOV over \hat{S}_z is larger than those over \hat{S}_x, \hat{S}_y for weak noise, the difference is not as big as that apparent from (a). The large noise case

has a **SOV** with similar projection over the three operators, and from (a) the projection over \hat{S}_x, \hat{S}_y looks much smaller.

These results can be further understood in terms of the steady state analysis performed in Sec. 2.5. The identity is *always* a conserved quantity, and therefore the projection of the steady state **SOV** $\Delta\hat{A}_\infty^2$ is non-zero; for this reason, its projection over the identity grows until it reaches the steady state. The spin operators \hat{S}_j are *not* conserved quantities, and thus the projection of the **SOV** onto them decreases at long times, eventually reaching zero. Lastly, even before performing a full analysis of the conserved quantities of the model, in this case \hat{H}_{LMG} is a *strong symmetry* of the system, and thus will be preserved. Therefore, we expect the projection of the **SOV** over $\hat{H}, (\hat{H}, \Delta\hat{A}_t^2)$ to have a similar behavior at long times as the projection over the identity. It is also interesting to note that since the operator \hat{A} is traceless, its projection over the identity (black solid line in the leftmost plot of (b)) stays at zero.

2.7.2 Classical stochastic LMG model

Classical limit of the spin Hamiltonian

The classical limit of the LMG model captures some of the features expected from its quantum counterpart[154, 209]. In particular, it explains the presence of an unstable saddle point, which is the cause for the presence of scrambling in the system, despite its integrability [151]. We will first detail how to take the classical limit of the spin Hamiltonian, and then introduce noise in this model.

The *coherent $SU(2)$ states* are defined as [214]

$$|\zeta\rangle = \frac{e^{\zeta\hat{S}_+}}{(1 + |\zeta|^2)^S} |S, -S\rangle, \quad (2.97)$$

where $\hat{S}_+ = \hat{S}_x + i\hat{S}_y$ is the raising operator and $|S, -S\rangle$ is the common eigenstate of $\hat{\mathbf{S}}^2$ and \hat{S}_z with the smallest eigenvalue of \hat{S}_z , furthermore $e^{\zeta\hat{S}_+}$ is the generalized displacement operator of the $SU(2)$ group. Physically, the states $|\zeta\rangle$ correspond to wavepackets with the minimum width allowed by the uncertainty principle. The parameter ζ is a complex number given by $\zeta = -\tan\frac{\theta}{2}e^{-i\phi}$, where the angles θ, ϕ determine the location of the coherent $SU(2)$ state $|\zeta\rangle$ centered at coordinates $\mathbf{n} = (\sin\theta\cos\phi, \sin\theta\sin\phi, \cos\theta)$. Note that ζ plays the role of a stereographic projection of the surface of the sphere into the complex plane. The classical limit of the Hamiltonian is thus defined as the expectation value of the Hamiltonian between coherent $SU(2)$ states in the limit of large spin

$$H_{\text{LMG}} = \lim_{S \rightarrow \infty} \frac{\langle \zeta | \hat{H}_{\text{LMG}} | \zeta \rangle}{S}. \quad (2.98)$$

Note that since the collective spin was related to the number of two-level systems in the fully connected spin chain model for LMG $S = \frac{N}{2}$, the semiclassical limit is also a thermodynamical limit. This semiclassical limit has an effective Planck's constant $\hbar_{\text{eff}} = 1/S$,

which vanishes in the large spin limit. This can be understood as \hbar_{eff} provides a measure for the separation between different quantized levels, and in the semiclassical limit, the difference between quantum levels vanishes and becomes a continuum. Introducing the rescaled variables $\hat{s}_j = \hat{S}_j/S$ we see that in the large spin limit the rescaled variables commute since $[\hat{s}_i, \hat{s}_j] = i\hbar_{\text{eff}}\epsilon_{ijk}\hat{s}_k \xrightarrow{S \rightarrow \infty} 0$ and thus are classical [151].

To compute the expectation value of the Hamiltonian between coherent $\text{SU}(2)$ states, we will use the following results [214]

$$\begin{aligned}\langle \mathbf{n} | \hat{S}_z | \mathbf{n} \rangle &= -S \cos \theta, \\ \langle \mathbf{n} | \hat{S}_x^2 | \mathbf{n} \rangle &= S(S - \frac{1}{2}) \sin^2 \theta \cos^2 \phi + \frac{S}{2},\end{aligned}$$

from which we find that the classical limit of the Hamiltonian is

$$\frac{\langle \zeta | \hat{H}_{\text{LMG}} | \zeta \rangle}{S} = -\Omega \cos \theta - \sin^2 \theta \cos^2 \phi + \mathcal{O}(S^{-1}). \quad (2.99)$$

where the sub-extensive terms vanish in the semiclassical limit. Following Pilatowsky-Cameo *et al.* [154], we introduce two canonically conjugated variables Q, P , analogous to the classical position and momentum, which characterize the real and imaginary part of the ζ variable. In particular

$$\zeta = \frac{Q - iP}{\sqrt{4 - (Q^2 + P^2)}} = -\tan \frac{\theta}{2} e^{-i\phi},$$

or more explicitly $\frac{Q}{\sqrt{4 - Q^2 - P^2}} = -\tan \frac{\theta}{2} \cos \phi$, $\frac{P}{\sqrt{4 - Q^2 - P^2}} = -\tan \frac{\theta}{2} \sin \phi$, from where it is possible to express the angles as

$$\tan \phi = \frac{P}{Q}, \quad \tan^2 \frac{\theta}{2} = \frac{Q^2 + P^2}{4 - (Q^2 + P^2)}, \quad (2.100)$$

which yields the classical Hamiltonian expressed in position and momentum as

$$H_{\text{LMG}}(Q, P) = \frac{\Omega}{2}(Q^2 + P^2) - \Omega - \frac{1}{4}(4Q^2 - Q^2P^2 - Q^4), \quad (2.101)$$

which can be written in a more transparent way as

$$H_{\text{LMG}}(Q, P) = \frac{\Omega}{2}P^2 + \left(\frac{\Omega}{2} - 1\right)Q^2 + \frac{1}{4}(Q^2P^2 + Q^4). \quad (2.102)$$

Inspecting the quadratic term Q^2 clearly shows that this Hamiltonian shows a transition from a double-well potential, with a negative Q^2 term, when $\Omega < 2$, to a single-well potential, when $\Omega > 2$. In the two spin chain picture, these phases correspond to a *ferromagnetic* phase, where the ground state has non-zero magnetization, and a *paramagnetic* phase, where the ground state has zero magnetization.

The effects of noise

We now turn on the noise in this system, i.e., we consider the classical *stochastic Lipkin-Meshkov-Glick* (sLMG) model. The most generic case is to consider N_c sources of noise

$$H_{\text{sLMG}}(t, Q, P) = H_{\text{LMG}}(Q, P) + \sum_{n=1} \sqrt{2\gamma_n} \xi_t^{(n)} L_n(Q, P). \quad (2.103)$$

But as already done previously for simplicity, we consider a single source of noise $N_c = 1$, such that the jump operator is equal to the Hamiltonian, i.e.

$$H_{\text{sLMG}}(t, Q, P) = (1 + \sqrt{2\gamma} \xi_t) H_{\text{LMG}}(Q, P), \quad (2.104)$$

which physically describes fluctuations in the energy scale of the system. Introducing the Poisson bracket $\{f, g\}_P = \frac{\partial}{\partial Q} f \frac{\partial}{\partial P} g - \frac{\partial}{\partial P} f \frac{\partial}{\partial Q} g$ between two classical functions $f(Q, P, t)$, $g(Q, P, t)$ of the phase space variables, which is related to the quantum commutator through the correspondence principle $\{A, B\}_P \leftrightarrow -i[\hat{A}, \hat{B}]$, we can write the analogous classical evolution to energy dephasing dynamics

$$\partial_t \mathbf{A}_t = -\{H_{\text{LMG}}, \mathbf{A}_t\}_P + 2\gamma \{H_{\text{LMG}}, \{H_{\text{LMG}}, \mathbf{A}_t\}_P\}_P, \quad (2.105)$$

similar equations, in the classical limit of the Schrödinger picture, i.e. in terms of the probability distribution over phase space $\rho(x, p, t) = \lim_{\hbar \rightarrow 0} \hat{\rho}_t$, have been considered to describe the effect of decoherence due to clocks with errors, which does not only show up in the quantum realm [215].

The most interesting feature of the LMG model for our purpose is that a very simple system, integrable, and with a well-defined classical limit, shows scrambling and has a positive quantum Lyapunov exponent. The existence of such integrable models is the reason why the presence of a positive quantum Lyapunov exponent is not considered sufficient to claim that a quantum system is chaotic. For this reason, we turn to computing the value of the Lyapunov exponent λ for the sLMG model with energy dephasing. We consider three different complementary approaches to compute this value.

Approach 1 (van Kampen's method). *The analytical approach of van Kampen [216, 217] yields the Lyapunov exponent of the sLMG model to be*

$$\lambda^{(vK)} = \sqrt{2\Omega - \Omega^2} - \gamma(2\Omega - \Omega^2). \quad (2.106)$$

Proof. We consider a classical vector \mathbf{u}_t subject to deterministic and stochastic external perturbations, referred to as \mathbf{A}_d and $\mathbf{A}_s(t)$. Its equation of motion is described by the stochastic differential equations

$$\dot{\mathbf{u}}_t = [\mathbf{A}_d + \sqrt{2\gamma} \mathbf{A}_s(t)] \mathbf{u}_t. \quad (2.107)$$

Following van Kampen [217], we move to the interaction picture with respect to the deterministic evolution, $\mathbf{v}_t = e^{-\mathbf{A}_d t} \mathbf{u}_t$. Expanding up to second order in $\sqrt{\gamma}$, the noise-averaged evolution in the interaction picture, with $\mathbf{v}_t = \mathbb{E}(\mathbf{v}_t)$ reads

$$\mathbf{v}_t = \mathbf{v}_0 + 2\gamma \int_0^t dt_1 \int_0^{t_1} d\tau e^{-t_1 \mathbf{A}_d} \mathbb{E}(\mathbf{A}_s(t_1) e^{\tau \mathbf{A}_d} \mathbf{A}_s(t_1 - \tau)) e^{(t_1 - \tau) \mathbf{A}_d} \mathbf{v}_0, \quad (2.108)$$

which is valid for $\sqrt{2\gamma}t \ll 1$. We recognize the solution to order γ of the linear differential equation, also known as Bourett's integral equation, which gives an equation of motion for the noise-averaged variable $\mathbf{u}_t = \mathbb{E}(\mathbf{u}_t)$ [216]

$$\partial_t \mathbf{u}_t = \left[\mathbf{A}_d + 2\gamma \int_0^t \mathbb{E}(\mathbf{A}_s(t) e^{\mathbf{A}_d \tau} \mathbf{A}_s(t - \tau)) e^{-\mathbf{A}_d \tau} d\tau \right] \mathbf{u}_t. \quad (2.109)$$

This equation is derived by assuming the standard rules of calculus and, thus, assumes Stratonovich formalism. In this formalism of Stochastic calculus, the integral of a delta function in one of the boundaries of the integration contour is defined as $\int_0^t \delta(t - \tau) f(\tau) d\tau = \frac{1}{2} f(t)$ [39]. In the case that \mathbf{A}_d and \mathbf{A}_s commute, and for $\mathbf{A}_s(t) = \xi_t \mathbf{A}_s$ fluctuating with Gaussian white noise, Eq. (2.109) simplifies to

$$\frac{\partial}{\partial t} \mathbf{u}_t = \left(\mathbf{A}_d - 2\gamma \mathbf{A}_d^2 \int_0^t \mathbb{E}(\xi_t \xi_{\tau'}) d\tau' \right) \mathbf{u}_t = (\mathbf{A}_d - \gamma \mathbf{A}_d^2) \mathbf{u}_t,$$

where the change of integration variable $\tau' = t - \tau$ brings the minus sign. In systems exhibiting chaos, the Lyapunov exponent gives the exponential divergence between neighboring trajectories. We interpret this as the maximum eigenvalue of the matrix $\mathbf{A}_d - \gamma \mathbf{A}_d^2$. The LMG at the origin, $Q = P = 0$, can be linearized into the harmonic oscillator $H = \frac{1}{2}[\Omega P^2 + (\Omega - 2)Q^2]$. Hamilton's equation of motion gives a system of differential equations for the variables \dot{Q}_t and \dot{P}_t which read

$$\begin{cases} \dot{Q}_t &= P_t \left(\Omega + \frac{1}{2} Q_t^2 \right) \\ \dot{P}_t &= -Q_t^3 - Q_t \left(\frac{1}{2} P_t^2 + (\Omega - 2) \right) \end{cases} \quad (2.110)$$

The Jacobian around a fixed point characterizes its Lyapunov exponent in the largest eigenvalue [154]. Linearizing the system of equations around the origin $Q^* = P^* = 0$, we find the Jacobian to be given by

$$\frac{d}{dt} \begin{pmatrix} Q_t \\ P_t \end{pmatrix} = \begin{pmatrix} 0 & 2 - \Omega \\ \Omega & 0 \end{pmatrix} \begin{pmatrix} Q_t \\ P_t \end{pmatrix} \equiv \mathbf{A}_d \mathbf{u}_t, \quad (2.111)$$

whose eigenvalues are simply $\lambda_{\text{LMG}} = \pm \sqrt{\Omega(2 - \Omega)}$. Note that the spectrum is real when $\Omega < 2$, thus describing the instability of the origin in the double well potential.

It is also possible to find the evolution of the quadratic terms as [216]

$$\frac{d}{dt} \begin{pmatrix} Q_t^2 \\ P_t^2 \\ Q_t P_t \end{pmatrix} = \begin{pmatrix} 0 & 0 & \Omega \\ 0 & 0 & -(\Omega-2) \\ -\frac{\Omega-2}{2} & \frac{\Omega}{2} & 0 \end{pmatrix} \begin{pmatrix} Q_t^2 \\ P_t^2 \\ Q_t P_t \end{pmatrix}. \quad (2.112)$$

The maximum eigenvalue of this matrix is $\lambda_{\text{LMG}} = \sqrt{2\Omega - \Omega^2}$, agreeing with the largest eigenvalue of the Jacobian \mathbf{A}_d , and the Lyapunov exponent at the origin in the noiseless LMG model [154]. For the sLMG, we add noise in the energy scale and consider an evolution dictated by

$$\dot{\mathbf{u}}_t = \mathbf{A}_d(1 + \sqrt{2\gamma}\xi_t)\mathbf{u}_t,$$

where ξ_t is Gaussian white noise. The maximum eigenvalue of $\mathbf{A}_d - \gamma\mathbf{A}_d^2$ thus gives the average Lyapunov exponent as

$$\lambda = \sqrt{2\Omega - \Omega^2} - \gamma(2\Omega - \Omega^2).$$

□

Approach 2 (Numerical implementation). *A purely numerical approach consists in computing the evolution of two trajectories in phase space (Q_t, P_t) and (Q'_t, P'_t) , from the stochastic Hamilton's equations*

$$\begin{cases} dQ_t &= P_t (\Omega + \frac{1}{2}Q_t^2) (dt + \sqrt{2\gamma}dW_t) \\ dP_t &= -Q_t (Q_t^2 + \frac{1}{2}P_t^2 + \Omega - 2) (dt + \sqrt{2\gamma}dW_t) \end{cases} \quad (2.113)$$

ensuring that the noise realization dW_t is the same for both trajectories. This system of coupled SDE's is solved through the stochastic Runge-Kutta method, cf. App. A.

The initial values of these trajectories are constructed in the way $Q'_0 = Q_0 + \varepsilon\zeta$ and $P'_0 = P_0 + \varepsilon\zeta$, where the variable ε is very small, e.g. in Fig. 2.10 it is chosen as $\varepsilon = 10^{-20}$, and $\zeta \sim \mathcal{N}(0, 1)$ is a normal random variable. Defining the L_2 distance in phase space between the two trajectories as $\ell_t^2 := (Q_t - Q'_t)^2 + (P_t - P'_t)^2$, the Lyapunov exponent is given by

$$\lambda^{(\text{num})} = \lim_{t \rightarrow \infty} \mathbb{E} \left(\frac{1}{t} \log \frac{\ell_t}{\ell_0} \right) \quad (2.114)$$

Approach 3 (SOV-OTOC connection). *It is possible to compute the Lyapunov exponent using the SOV-OTOC relation. In particular, taking the position as the observable $A_t = Q_t$, which is obtained from solving the stochastic Hamilton's equations (2.113), and computing the classical SOV $\Delta Q_t^2 = \mathbb{E}(Q_t^2) - \mathbb{E}(Q_t)^2$. This yields a Lyapunov exponent*

through the **SOV-OTOC** relation as

$$\lambda^{(\text{sov-OTOC})} = \lim_{t \rightarrow \infty} \frac{1}{2(t - t_r)} \log \left(\frac{\partial_t \Delta Q_t^2}{\partial_t \Delta Q^2|_{t_r}} \right). \quad (2.115)$$

Note that the denominator acquires a factor 2 because the classical limit of the **OTOC** grows as $e^{2\lambda t}$. Furthermore, the derivative of the classical **SOV** is compared to the derivative at a given reference time $t_r = 1$ to ensure that the **OTOC** is in the Lyapunov regime.

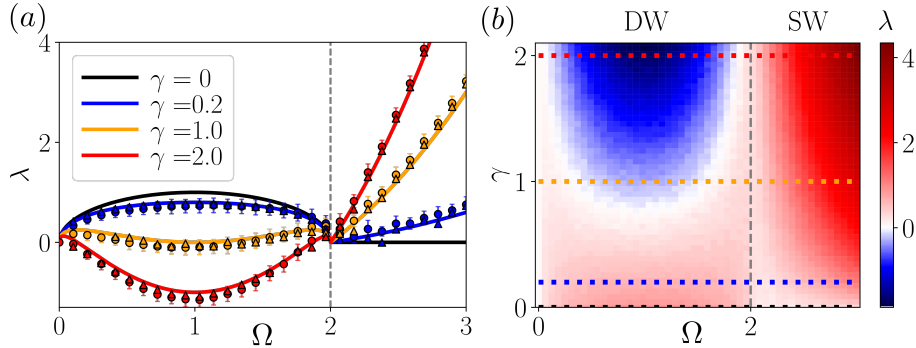


Figure 2.10. Lyapunov exponent of the classical sLMG model at the saddle point $Q^* = P^* = 0$ as a function of Ω (a) for different values of the noise strength γ and (b) over the phase diagram. (a) The Lyapunov exponent λ is computed through the three approaches: Approach 1 analytically using van Kampen's method $\lambda^{(vK)}$ (solid lines), (ii) numerically as in Approach 2, $\lambda^{(\text{num})}$ (circles with errorbar), and (iii) from the **SOV-OTOC connection as in Approach 3, $\lambda^{(\text{sov-OTOC})}$ (triangles). The known results for the LMG correspond to $\gamma = 0$ (black). (b) **Phase diagram.** The color scale represents the Lyapunov exponent $\lambda^{(\text{num})}$ as a function of the two-level frequency in units of the coupling strength Ω and the noise strength γ . A positive value of λ (red) implies exponential divergence of close initial conditions, while a negative value (blue) indicates exponential convergence. The dotted horizontal lines represent the values of γ sampled in (a). The vertical dashed gray line represents the transition between the double well ($\Omega < 2$) and single well ($\Omega \geq 2$) phase. Figure adapted from [1].**

Figure 2.10 (a) compares the Lyapunov exponent using the three approaches. We observe excellent agreement between the different approaches, which indicates their consistency. The fact that the three approaches yield similar results indicates the validity of the **SOV-OTOC** relation, even in the classical setup, in which it was not derived. Now, let us analyze the physics that the system describes. In the noiseless limit $\gamma = 0$, the double well (DW) phase of the model, $\Omega < 2$, shows a positive Lyapunov exponent, because the origin is an unstable fixed point of the model, while in the single well (SW) phase $\Omega > 2$ the Lyapunov vanishes since the origin is a stable fixed point. Under the application of a small noise, the Lyapunov exponent of the DW phase decreases slightly, while the SW phase acquires a small but positive Lyapunov exponent. In particular, from the analytical expression it is easy to show that the largest Lyapunov exponent of the DW

phase, happening at $\Omega = 1$ is equal to $\max_{\text{DW}, \gamma < \frac{1}{2}} \lambda^{(vK)} = 1 - \gamma$. When the strength of the noise is larger, like $\gamma = 1$, the Lyapunov of the DW phase is even smaller, with the point $\Omega = 1$, which had the maximum Lyapunov, now having the smallest Lyapunov, close to zero. The SW phase acquires an even bigger Lyapunov exponent. A simple computation of the second derivative with respect to Ω ,

$$\frac{\partial^2 \lambda}{\partial \Omega^2} \Big|_{\Omega=1} = -2 \left(\frac{1}{2} - \gamma \right),$$

shows that the point $\Omega = 1$ changes from the point with maximum Lyapunov of the DW phase to a relative minimum of the Lyapunov at $\gamma = 1/2$. When $\gamma > 1/2$, the two points with the largest Lyapunov exponent in the DW phase occur at $\Omega_{\pm} = 1 \pm \sqrt{1 - \frac{1}{4\gamma^2}}$. Lastly, when the strength of the noise is large $\gamma > 1$, see $\gamma = 2$ in Fig. 2.10 (a), the Lyapunov exponent in the DW phase becomes negative in the interval

$$\Omega \in \left(1 - \sqrt{1 - \frac{1}{\gamma^2}}, 1 + \sqrt{1 - \frac{1}{\gamma^2}} \right),$$

which covers the full DW phase in the limit $\gamma \rightarrow \infty$. This implies that in this regime of parameters, the origin becomes stable through the action of the noise. Trajectories converge exponentially fast to the origin $Q = P = 0$.

This behavior is analogous to *Kapitza's pendulum* [218, 219], in this setup, one considers a rigid pendulum of length L in a gravitational field given by g , whose suspension point is being periodically driven with an amplitude A and frequency ω . The standard pendulum without driving has two fixed points, with the pendulum facing up and down; the former is unstable, while the latter is stable. However, Kapitza realized that this does not have to be the case in the driven pendulum. In particular, if the amplitude and frequency obey $A^2\omega^2 \geq 2gL$, the pendulum being up becomes a stable fixed point [218]. This *dynamical stability* has also been found in quantum and many-body systems [220, 221]. Here, we find a similar behavior to dynamic stabilization but with stochastic driving instead of periodic driving.

Heuristic reason for the dynamical stabilization of sLMG

It is possible to understand the noise-induced stabilization from a heuristic argument. Let us consider the energy landscapes of the classical limit of the LMG Hamiltonian $H_{\text{LMG}}(Q, P)$ as shown in Fig. 2.11. The noiseless Hamiltonian is shown in Fig. 2.11 (c) for the DW phase and (e) for the SW phase. At all times, the Hamiltonian is multiplied by the value $1 + \sqrt{2\gamma}\xi_t$. When $\sqrt{2\gamma} \ll 1$, the Hamiltonian is very rarely flipped, and the majority of the realizations of the noise give a Hamiltonian that looks like (c) or (e) with a different coefficient $1 + \sqrt{2\gamma}\xi_t$, which is very close to 1. The small noise slightly diminishes the Lyapunov exponent of the origin in the DW phase, and slightly increases it in the SW phase.

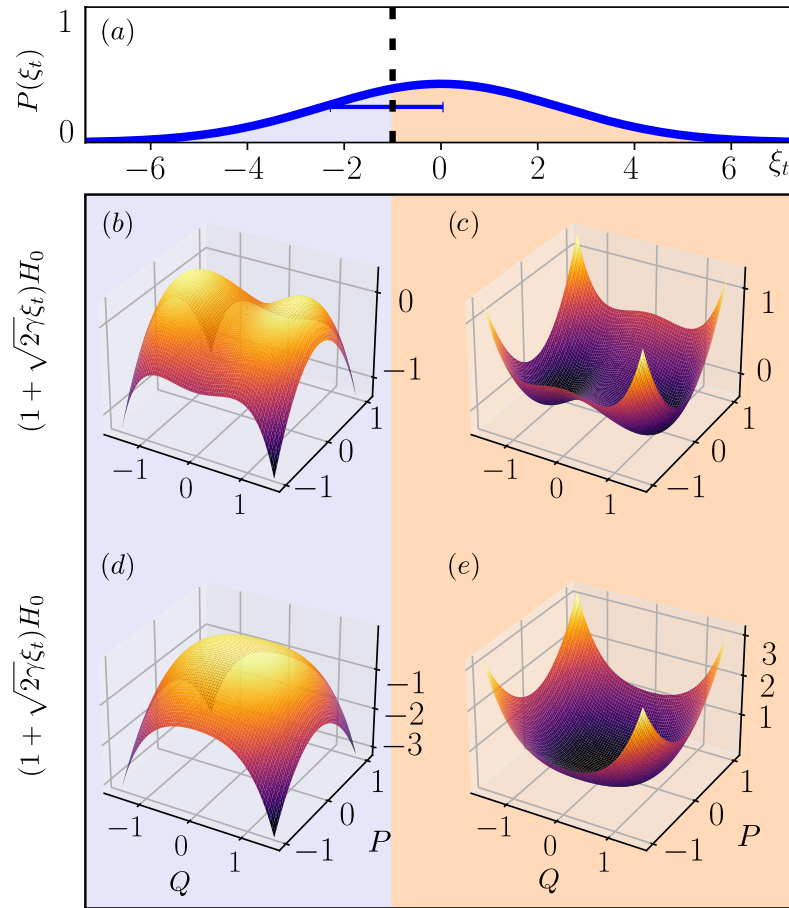


Figure 2.11. Visualization of the sLMG model. (a) Histogram of the possible values of the white noise ξ_t . The horizontal blue line indicates the standard deviation of the normal distribution. The vertical (black dashed) line indicates where $1 + \sqrt{2\gamma}\xi_t = 0$, therefore $1 + \sqrt{2\gamma}\xi_t < 0$ (blue region), and $1 + \sqrt{2\gamma}\xi_t > 0$ (orange region). LMG Hamiltonian as a function of Q, P in the double well (b,c) and single well (d,e) phases, multiplied by a negative (b,d) or positive (c,e) value of $1 + \sqrt{2\gamma}\xi_t$.

The large noise limit $\sqrt{2\gamma} \gg 1$ allows us to understand the physics better; in this limit, the noise distribution is so wide that almost half of the realizations flip the sign of the Hamiltonian. Let us see now how this brings an important difference between the SW and DW phases, consider the discretization of time $\{t_n\}$

- **Single Well phase:**

- If $1 + \sqrt{2\gamma}\xi_{t_n} > 1 + \sqrt{2\gamma}\xi_{t_{n-1}}$ all points in phase space (Q, P) gain energy. The points further away from the origin gain more energy than the points closer to the origin. In the extreme case in which the prefactor is negative at t_{n-1} and positive at t_n , we go from (d) \rightarrow (e) in Fig. 2.11.

- If $1 + \sqrt{2\gamma}\xi_{t_n} < 1 + \sqrt{2\gamma}\xi_{t_{n-1}}$ all points in phase space (Q, P) lose energy. The points further away from the origin lose more energy than the points closer to the origin. In the extreme case in which the prefactor is positive at t_{n-1} and negative at t_n , we go from (e) \rightarrow (d) in Fig. 2.11.

- **Double Well phase:**

- If $1 + \sqrt{2\gamma}\xi_{t_n} > 1 + \sqrt{2\gamma}\xi_{t_{n-1}}$, the points inside the wells lose energy, while the points outside the wells gain energy. In the extreme case in which the prefactor is negative at t_{n-1} and positive at t_n , we go from (b) \rightarrow (c) in Fig. 2.11.
- If $1 + \sqrt{2\gamma}\xi_{t_n} < 1 + \sqrt{2\gamma}\xi_{t_{n-1}}$, the points inside the wells gain energy, while the points outside the wells lose energy. In the extreme case in which the prefactor is positive at t_{n-1} and negative at t_n , we go from (c) \rightarrow (b) in Fig. 2.11.

This difference between the different points in phase space provides an intuitive view of the difference between the two phases and may explain the stabilization.

2.8 Conclusions

Throughout this chapter, we have investigated the evolution generated by stochastic Hamiltonians beyond the noise-average. The main quantity we have focused on is the *Stochastic Operator Variance*, introduced in (2.7). Interestingly, leveraging the unitarity of stochastic Hamiltonians at single trajectories, the **SOV** can be expressed as the variance of a hermitian matrix over a **CPTP** linear map (2.9). This connection allows us to find several formal mathematical properties of the **SOV**, cf. Sec. 2.2.1, show that the **SOV** contains the information in the quantum mechanical variance plus transitions outside the subspace spanned by the initial state, cf. Sec. 2.2.2, and provide an interpretation of the **SOV** as an operation on two copies of the Hilbert space, cf. Sec. 2.2.3.

The first main result that we find in the chapter is that the expectation value of the **SOV**'s of two different operators $\langle \Delta \hat{A}_t^2 \rangle_\rho$, $\langle \Delta \hat{B}_t^2 \rangle_\rho$ fulfill an uncertainty relation (2.25). Interestingly, a stronger inequality directly on the **SOV**, without the need for expectation value over any state, can also be derived, cf. eqs. (2.27) and (2.29). In Sec. 2.3.2, we provided an example of these inequalities for the case of a Harmonic Oscillator with stochastically driven frequency.

Section 2.4 investigates higher-order moments beyond the variance. We find that unitarity at single trajectories brings the same simplification to higher order moments as it did to the second moment (2.42); this implies that the adjoint Lindbladian characterizes the evolution of all the moments for stochastic Hermitian Hamiltonians. We find expressions for the moment and cumulant generating functions from where the moments and cumulants may be found upon differentiation, only with knowledge of the propagator $e^{\mathcal{L}^\dagger t}[\bullet]$.

In Section 2.5, we study the **SOV** at very long times, when the system has converged to its steady state. We find that it can be written in terms of the elements of the kernel of \mathcal{L}^\dagger . In the case of a unique steady state, it simply gives the variance over the steady state multiplied by the identity (2.50). In the case of multiple steady states, the long-time limit

of the **SOV** can be written in terms of the conserved quantities of the system [199] (2.52). In Sec. 2.5.2, we study two-qubit dissipation, which shows a non-trivial Decoherence Free subspace, and compute the steady state of the **SOV** (2.64).

Section 2.6 introduces the second main result of our analysis, the **SOV-OTOC** relation. This connection provides a deep link between the spread of trajectories in the Hilbert space of operators with quantum information scrambling and the quantum Lyapunov exponent. We showed explicitly that the connection holds for many different **OTOC**'s, which shows that this is not a coincidence and that the **SOV** is encoding information similar to the different **OTOC**'s. We exemplified this connection in the stochastic **LMG** model, cf. Sec. 2.7 both in its quantum and classical limit. In the quantum case, we found that the behavior of dissipative **OTOC**'s is drastically affected by dissipation and that the eigenvalues of the **SOV** can show diffusive, superdiffusive, and even ballistic scaling. In the classical limit, we showed several ways of computing the Lyapunov exponent, analytically, numerically, and using the **SOV-OTOC** connection, all of these agree on the Lyapunov exponent of the unstable point of **sLMG**, which becomes negative in the double well phase, thus showing noise-induced stabilization, and becomes positive in the single well phase.

2.8.1 Open Questions

We list here several open questions and avenues for further study:

- Most of the analysis of the **SOV** comes from the great simplification brought by unitary single trajectories. Can the **SOV** be computed in cases where single trajectories are *not* unitary, such as a continuous measurement? What type of **SOV-OTOC** connection holds in such systems?
- What information is carried in the higher-order moments and cumulants of the operator over the noise?
- Can we explain the growth rates of the **SOV** eigenvalues through hydrodynamics?
- From the mathematical properties of the **SOV** we see that it is quite similar to a Hamiltonian, also in the evolution of the eigenvalues, cf. Fig. 2.6, the spectrum behaves similarly to the spectrum of a driven Hamiltonian. In this plot, we see a few but not many avoided crossings, and we observe more avoided crossings in the non-commuting case, Fig. 2.7. One natural question arises: do the eigenvalues of the **SOV** show level repulsion? Is there a universal prediction for the **SOV** in the context of random matrices?
- Given two operators \hat{A} and \hat{B} what are the states $\hat{\rho}$ that saturate the **SOV** uncertainty relation?
- Can we derive quantum speed limits for open systems [222, 223] from either the **SOV** uncertainty relation or its operator version?
- The operator versions of the **SOV** uncertainty relation seem to be stronger, since they set an inequality between operators instead of scalars, but what is the real advantage of this? Can we find an extension of the operator correlation bound (2.28) to the case where $\Delta\hat{A}$ or $\Delta\hat{B}$ are non-invertible?

- What is the meaning of the **SOV** in a decoherence-free subspace in the case where \hat{A} is not completely in or out of the **DFS**?
- Is it possible to find a relation to higher point **OTOCs** from the higher order cumulants?
- The dissipative **OTOC** for dephasing seems to have a very different behavior than the unitary one. Is it, however, possible to witness a *Lyapunov regime* in the dissipative **OTOC** for small γ and large N ? In principle, the saddle point is the only source of scrambling in the **LMG** model. Can we then find a similar phase diagram for the Lyapunov in the quantum case?
- What is the dynamics generated by the classical analog of energy dephasing (2.105)?
- Can van Kampen's method be extended to the case with $[\mathbf{A}_d, \mathbf{A}_s] \neq 0$?
- Can we find a quantitative theory that predicts under what conditions systems with noisy driving will show a similar noise-induced stabilization? Can we prove that the heuristic energetic argument is behind the stabilization?
- What is the complexity of measuring the **SOV**? Naïvely, one expects it to be as complicated as doing full-state tomography. Is there a more efficient way to measure this, such as using *classical shadows* [224]?
- What is the **SOV** of a system showing localization, either single-body or many-body?
- How does the **SOV** of an operator in Krylov space [5] look like?
- If the **SOV** and higher moments can be measured experimentally, can these provide a more stringent test of the foundations of quantum mechanics, such as ruling out different collapse theories [225]?
- In the *post-quantum* theory of gravity developed by Oppenheim [226], which proposes a stochastic coupling between gravity and matter, in such theories, what does the hybrid **SOV** with classical and quantum degrees of freedom look like?
- Different unravelings of master equations reproduce the same average evolution, using the **SOV**, can we differentiate between these different unravelings?
- What is the classical limit of the **SOV** uncertainty relation?
- Is it possible to *squeeze* the **SOV** such that two operators fulfill the **SOV**-uncertainty relation but the expectation value of one of them is much larger than the other?
- The **SOV**, when properly re-normalized, fulfills all the properties of a quantum mechanical state. Can we exploit this connection and test whether non-classicality shows up in the **SOV**, either in the form of Wigner negativity [227] or as non-stabilizerness [7, 228]?
- Is it possible to compute the evolution of the **SOV** for random quantum circuits [229, 230] or for systems showing noise-induced synchronization [231, 232]?

Recap of the results of Chapter 2

- The *stochastic operator variance* (SOV) for a stochastic Hamiltonian $\hat{H}_0 + \sqrt{2\gamma}\xi_t\hat{L}$ can be expressed in terms of the adjoint Lindbladian \mathcal{L}^\dagger simply as (2.9)

$$\Delta\hat{A}_t^2 = e^{\mathcal{L}^\dagger t}(\hat{A}^2) - e^{\mathcal{L}^\dagger t}(\hat{A}) \cdot e^{\mathcal{L}^\dagger t}(\hat{A}),$$

where $\mathcal{L}^\dagger(\bullet) = +i[\hat{H}_0, \bullet] - \gamma[\hat{L}, [\hat{L}, \bullet]]$.

- The SOV is Hermitian, positive semidefinite, and bounded from above, cf. Sec. 2.2.1.
- The SOV and the quantum variance are related by (2.17), cf. Sec. 2.2.2

$$\langle\psi_0|\Delta\hat{A}_t^2|\psi_0\rangle = \text{Var}(\hat{A}_t, \psi_0) + \sum_{n=1}^{d-1} |\langle\psi_0|\hat{A}_t|\phi_n\rangle|^2.$$

- The SOV can be interpreted as a protocol on two replicas of a Hilbert space, see Fig. 2.4.
- The expectation value of the SOV for two different operators fulfills the uncertainty relation (2.25)

$$\text{Tr}(\Delta\hat{A}_t^2\hat{\rho})\text{Tr}(\Delta\hat{B}_t^2\hat{\rho}) \geq \frac{1}{4} \left(D_+^2(\hat{A}, \hat{B}) - D_-^2(\hat{A}, \hat{B}) \right),$$

where $D_\pm(\hat{A}, \hat{B}) = \langle\mathcal{E}_t^\dagger([\hat{A}, \hat{B}]_\pm)\rangle - \langle[\mathcal{E}_t^\dagger(\hat{A}), \mathcal{E}_t^\dagger(\hat{B})]_\pm\rangle$ Furthermore, we found stronger, operator versions of this inequality, in which there is no notion of state such as (2.27) and (2.29),

$$\Delta\hat{A}_t^2 \geq \Delta\widehat{AB}_t(\Delta\hat{B}_t^2)^{-1}\Delta\widehat{AB}_t^\dagger,$$

$$\text{corr}_t(\hat{A}, \hat{B}) \text{corr}_t(\hat{A}, \hat{B})^\dagger \leq \hat{\mathbb{1}},$$

where $\text{corr}_t(\hat{A}, \hat{B}) = \Delta\hat{A}_t^{-1}\Delta\widehat{AB}_t\Delta\hat{B}_t^{-1}$ is an operator analog of *Pearson's correlation coefficient* (2.28). These inequalities were illustrated for a Stochastic Frequency Harmonic Oscillator, cf. Sec. 2.3.2.

- We studied higher-order moments and cumulants. In particular, unitarity at single trajectories implies (2.42)

$$\hat{M}_t^{(n)} = \mathbb{E}(\hat{A}_t^n) = e^{\mathcal{L}^\dagger t}[\hat{A}^n],$$

we also compute formal expressions for the *cumulant* and *moment generating functions*, cf. Sec. 2.4.

- We studied the long-time behavior of the SOV, cf. Sec. 2.5. If there is a unique steady state of the dynamics, it simplifies to (2.50)

$$\Delta\hat{A}_\infty^2 = \left(\text{Tr}(\hat{\rho}^s\hat{A}^2) - \text{Tr}(\hat{\rho}^s\hat{A})^2 \right) \hat{\mathbb{1}}.$$

In the general case, it is a superposition of the conserved quantities of the system; we exemplified this in a system with a Decoherence Free Subspace, cf. Sec. 2.5.2.

- We found that the time derivative of the SOV is related to a dissipative OTOC through the **SOV-OTOC** relation (2.70)

$$\frac{1}{N} \frac{d\text{Tr}(\Delta \hat{A}_t^2)}{dt} = -\frac{2\gamma}{N} \text{Tr}([\hat{L}, \hat{A}_t]^2) = 2\gamma C_t.$$

This connection also holds in the case of a non-Hermitian jump operator and quantum noise, cf. Sec. 2.6.2, and connects to many types of OTOCs, cf. Sec 2.6.3, such as: thermal, regularized, fidelity, and microcanonical.

- We characterize certain properties of dissipative OTOCs, cf. Sec. 2.6.4, such as their dissipation time (2.89)

$$\tau_D = \frac{C_0}{2\gamma \text{Tr}([\hat{L}, [\hat{L}, \hat{A}]]^2)},$$

and found an exact expression for the dissipative OTOC in dephasing dynamics (2.91)

$$C_t = \frac{1}{N} \sum_{m,n} (l_m - l_n)^2 e^{-2\gamma(l_m - l_n)^2 t} |A_{nm}|^2$$

- We study the example of the stochastic **LMG** model, with Hamiltonian (2.94) $\hat{H}_t = \left(\Omega \hat{S}_z - \frac{2}{N} \hat{S}_x^2\right) (1 + \sqrt{2\gamma} \xi_t)$. In this system, we find that the eigenvalues of the SOV $\Lambda(t)$ can scale: diffusively $\Lambda(t) \sim t$, superdiffusively $\Lambda(t) \sim t^{3/2}$ or ballistically $\Lambda(t) \sim t^2$, cf. Figs. 2.6, 2.7.
- If we know the spectrum and eigenstates of the SOV, it is possible to compute the state *minimally affected* by the noise at long times $|\Psi\rangle$ (2.95).
- In the classical or thermodynamic limit $N \rightarrow \infty$, we study the stability of the origin for the stochastic **LMG** model with Hamiltonian (2.104)

$$H_{s\text{LMG}} = (1 + \sqrt{2\gamma} \xi_t) \left(\frac{\Omega}{2} P^2 + \left(\frac{\Omega}{2} - 1 \right) Q^2 + \frac{1}{4} (Q^2 P^2 + Q^4) \right)$$

We compute the Lyapunov exponent with three different, complementary approaches: analytically (Appr. 1)

$$\lambda^{(vK)} = \sqrt{2\Omega - \Omega^2} - \gamma(2\Omega - \Omega^2),$$

numerically (Appr. 2), and using the SOV-OTOC connection (Appr. 3). The three approaches agree in their value for the Lyapunov exponent. The origin becomes stable under the action of the noise in the **DW** phase, similarly to the Kapitza pendulum, but under stochastic driving, while it becomes unstable in the **SW** phase, cf. Fig. 2.10. We propose some heuristic energetic arguments for why this stabilization could happen, cf. Fig. 2.11.

Chapter 3

Stochastic Non Hermitian Hamiltonians

“Ven aquí, se rompe el telón con el ruido,
Ven aquí, con cierta pasión por el ruido”
Barricada

Abstract of this chapter

- The basic problem that we are interested in here is to characterize the dynamics of Stochastic Non-Hermitian Hamiltonians. In particular, we consider a Hamiltonian subject to noise in its anti-Hermitian part $\hat{H}_t = \hat{H}_0 - i(1 + \sqrt{2\gamma}\xi_t)\hat{L}$.
- The noise-averaged dynamics follows a nonlinear master equation beyond [GKSL](#) form, which follows *antidephasing* dynamics, characterized by a dissipator with a double anticommutator $+\gamma\{\hat{L}, \{\hat{L}, \bullet\}\}$. We study the evolution of quantities which showcase interesting phenomena arising in this new type of dynamics, namely: the *purity*, the *steady states*, the *dissipative gap*, and the *oscillating frequency*.
- We extensively study a physical system, namely the *Dissipative Qubit*, subject to antidephasing dynamics. We find that this system has three possible phases in its steady state: \mathcal{PT} unbroken, \mathcal{PT} broken, and Noise-Induced. The latter phase was not observed or predicted before, and in it, the system converges to a state with losses. We analyze the dynamics, the transitions between the phases, the presence of Liouvillian Exceptional Points, and the evolution of purity, and compare them with single trajectories of the noise. In the last section, we show how this model can explain the *residual damping rate* of the \mathcal{PT} unbroken phase observed experimentally.

In this chapter, we introduce the general theory of *Stochastic Non-Hermitian Hamiltonians*. The axioms of Quantum Mechanics state that the Hamiltonian of a closed quantum system is a Hermitian operator. Going beyond this axiom leads to *Non-Hermitian Quantum Mechanics*, describing systems that can gain or lose energy and or particles, which were introduced in Sec. 1.5. Furthermore, the Hamiltonian operator is typically assumed to be known; this condition can be relaxed in the context of *Stochastic Hamiltonians*, which naturally allow to include some level of uncertainty, or some fluctuations, in the operator that generates the evolution. This provides a simple way to model certain open

quantum systems, as introduced in Sec. 1.4, and to study the behavior beyond the noise average, as we did in Chapt. 2. In this chapter, we consider the following situation: the Hamiltonian is non-Hermitian, and thus gains or loses energy, but furthermore, we do not have full knowledge of this generator, meaning that either some of its parameters are unknown and subject to fluctuations.

3.1 Introducing Stochastic Non-Hermitian Hamiltonians

3.1.1 A story for the results of this chapter

Imagine that you are attending a magic show. The magician asks three different people, who are named Alice, Bob, and Charlie, to come to the stage to assist him with his next magic trick. There are two buckets on the stage, and the magician gives each person the following instructions:

- Alice will take a hose and throw water into bucket 1 at a rate Γ . The hose throws water at very high pressure, so that we are far from the equilibrium situation in which water is added slowly.
- Bob will adjust the opening between the two buckets, allowing for more or less water to pass from one to another. The amount of water that can flow from one bucket to the other is J .
- Charlie will take water out of bucket 2 at exactly the same rate that Alice fills up bucket 1 Γ so that the total amount of water on both buckets stays constant.

The two buckets [89, 233] are essentially analogous to a system described by a Non-Hermitian Hamiltonian, in particular, it is a \mathcal{PT} -symmetric Hamiltonian [234], introduced in Sec. 1.5.1. In this particular case, the *Parity* transformation refers to exchanging box 1 for box 2, and the *Time reversal* symmetry refers to changing losses for pumps and pumps for losses. If we perform both transformations at the same time, i.e., Charlie pumps water into bucket 1 and Alice extracts water from bucket 2, the system remains the same. These systems are also sometimes referred to as systems with *Balanced Gain and Loss*. The special feature of these systems is that they can have real energies, meaning that even when they are constantly gaining and losing energy, the system behaves in a similar way to a closed system and thus shows oscillations between the two buckets. At a particular point, we observe the so-called \mathcal{PT} -breaking transition, at which the energies stop being real and become imaginary, which introduces decay in the dynamics.

The magician starts the trick by showing these two possible behaviors. Alice starts pumping water into bucket 1, Charlie removes water from bucket 2 at the same rate, and Bob opens the pipe between the two buckets so that the pipe can transport more water than what Alice is throwing. The water thrown by Alice is very fast and thus creates a wave¹,

¹The analogy originally considers two boxes in which some quantity, either matter or energy, is being pumped in and out [233]. In here, I considered the case in which water is pumped, since it is a case with which many people are familiar. This is a double-edged sword since water has dynamics in which there is friction and viscosity, and thus the oscillations of the \mathcal{PT} unbroken phase will be fastly

which can pass the pipe without deforming, fills up bucket 2, and then bounces back and goes back to bucket 1, assuming no friction in the water or with the bucket walls, these oscillations do not vanish. This is what we call \mathcal{PT} symmetric, or *unbroken* phase, and has oscillations which arise from the energies being real.

The magician now repeats the trick, but this time asks Bob to close the pipe between the two buckets so that the water that flows between the buckets is smaller than the water that Alice pumps in and the water that Charlie pumps out. This means that all the water that passes through the pipe to bucket 2 is pumped out. The system then tends to a state where all the water is in bucket 1, and bucket 2 is completely empty. This is what is known as the \mathcal{PT} -broken phase, and happens because the energies associated with the system when $\Gamma \gg J$ are imaginary, and thus give exponential decay.

At this point, these two tricks may have surprised some of the audience, but in the last row of the theater, there is a small group of physicists who work with non-Hermitian Hamiltonians, who are not surprised at all. They start arguing that this is not anything new and that has been predicted and observed in many different cases, e.g., [54, 80].

The magician then starts his third trick: He changes Alice's and Charlie's hoses for much older ones, which cannot keep a constant flux of water, showing large fluctuations around the average flux of water Γ , and tells Bob to keep the size of the pipe small compared to the average flux of water. The water starts flowing and then, to everyone's surprise, including the group of physicists, the bucket 2 starts filling up. After a bit of time, the system ends up in a state with Bucket 1 completely empty and Bucket 2 completely full. Not only that, but this stationary situation, which we call *steady state*, is reached very fast, much faster than what happened in trick 2. In the middle of everyone's applause, the magician clarifies that this behavior is only possible thanks to the presence of noise, and especially the interplay between the noise and the gains and losses, and thus calls this the *Noise Induced* phase of the system.

This story illustrates one of the main results, perhaps the most counterintuitive, of this chapter. In the remainder of this chapter we will set up the stage, provide the mathematical framework which models systems subject to noisy gains and losses, and study the analogous quantum system to the two buckets of water with noisy gains and losses, the *Stochastic Dissipative Qubit*, which shows three distinct phases, with similar behavior to the three tricks performed by the magician.

3.1.2 Why studying Stochastic Non-Hermitian Hamiltonians?

We can study Stochastic and Non-Hermitian Hamiltonians, but why should we consider them together? After much thought to this question, we have come up with several different reasons, which we review now:

1. Consider first a pragmatic and practical point of view. Recently, it has become possible to generate *purely quantum* Non-Hermitian Hamiltonians in the lab. These use

suppressed. To get as close as possible to the case we are interested in, we set the water to be very fast, so that the situation is far from equilibrium, and at least some oscillations may be seen.

different cutting-edge platforms for their qubits, such as superconducting circuits [80] or trapped ions [235]. However, we know that these platforms are currently very noisy since we are in the NISQ era [175]. This is not only the case in quantum realizations of NH Hamiltonians; classical realizations of these dynamics, such as those based on waveguides [54, 56], will also be subject to fluctuations in the parameters. This means that generally, NH systems are subject to all sorts of environmental noise, which needs to be included in the description to have a full model for the behavior of the system. One example of this need appears in Naghiloo *et al.* [80]. The authors observed a residual decay rate in the \mathcal{PT} symmetric phase of their model, which is attributed to “*charge and flux noise*”, but which still remains unexplained theoretically. In here, we provide the formalism to model the effect of noise, which can even model the lack of information about certain terms of the generator, on quantum systems subject to gains and losses.

2. From a *quantum dynamicist*² From this perspective, we are looking for all sorts of new, exotic, quantum evolution, and want to characterize their properties. In particular, the space of all possible dissipative quantum evolutions is vast and different subfields of research prefer to stay in different corners of this space, as we already discussed in Sec. 1.2. From this point of view we have Non-hermitian dynamics on the one hand, showing that dissipative phenomena may be tamed and used to our advantage in building new possible evolutions, and stochastic Hamiltonians on the other, giving rise to: (i) a subclass of Lindblad master equations at the average level and (ii) noisy quantum dynamics at single trajectory level. The evolution generated by considering these two approaches together gives a new type of dynamics, which we here name *antidephasing*, which constitutes a new kind of master equation, followed by certain quantum systems.
3. A motivation more in line with some other chapters of this thesis comes from the point of view of Random Matrix Theory, as already introduced in 1.6.1. In this context, one typically considers for the model a full Random Matrix, with many elements sampled from a probability distribution. The number of real random variables in this model will be N for the Poisson ensemble, $N(N + 1)/2$ for GOE, and N^2 for GUE, $2N^2$ for Ginibre. Realistic physical models used in the study of Quantum Chaos, such as the disordered XXZ chain, see Chap. 4, have a much smaller number of random variables, since it typically is $L \sim \log(N)$, a random potential for each site, and the dimension of the Hilbert space would be $N = 2^L$. Stochastic Non-Hermitian Hamiltonians can help bridge this gap, going from full random matrices to matrices in which only one of the elements is fluctuating. Indeed, the spectra of these matrices show very interesting behavior since it does not follow the well-known analytical results for full random matrices, such as the circular or semicircle law.
4. Lastly, one of the main limitations of classical noise Stochastic *Hermitian* Hamiltonians is that from them it is not possible to derive the most general GKSL master equation. Instead, the equations you can derive have always the same decay rate, i.e., the decay channel $\gamma_{\hat{L}} \mathcal{D}[\hat{L}]$ and the decay channel $\gamma_{\hat{L}^\dagger} \mathcal{D}[\hat{L}^\dagger]$ with the conjugate

²Taking the term *dynamicist* from Strogatz [236].

jump operator will always have the same decay rate $\gamma_{\hat{L}} = \gamma_{\hat{L}^\dagger}$. Therefore, with a classical noise stochastic hermitian Hamiltonian, one can just describe *dephasing* dynamics. One of the main problems of this approach is that there is a big interest in having a master equation that has a thermal steady state $\hat{\rho}_\beta = e^{-\beta\hat{H}}/\text{Tr}(e^{-\beta\hat{H}})$. The condition that a master equation has to fulfill to show this interesting steady state is named *Kubo-Martin-Schwinger* or *quantum detailed balance*, which imposes a symmetry on the rates of the Davies generator³ $\gamma_{\alpha\beta}(-\omega) = e^{-\beta\omega}\gamma_{\beta\alpha}(-\omega)$. This condition cannot be fulfilled for finite temperature $\beta \neq 0$ if $\gamma_{\hat{L}} = \gamma_{\hat{L}^\dagger}$ and thus classical noise *Hermitian* Hamiltonians do not have finite temperature steady states.

This is one of the motivations typically put forward for introducing quantum noise [203], in which ξ_t is promoted to an operator $\hat{\xi}_t$ such that $[\hat{\xi}_t, \hat{\xi}_t^\dagger] \neq 0$. This allows us to find the most general GKSL master equation. However, this increases the complexity of our model, losing the nice, simple properties of classical noise stochastic Hamiltonians. There is another way to go around it, similar to what we do here. If we give up the hermiticity condition of the dynamics and consider generic classical noise stochastic non-Hermitian Hamiltonians, then we can find the most general GKSL master equation, as was recognized by Burgarth *et al.* [237, 238]. This can considerably reduce the complexity of simulating a generic Lindblad master equation, since now, instead of dealing with superoperators of size $N^2 \times N^2$, with $2N^4$ degrees of freedom, we can simulate a general non-Hermitian Hamiltonian of size $N \times N$ with N_{av} noise realizations, which gives $2N^2N_{\text{av}}$ degrees of freedom, giving a better scaling.

In this chapter, we study the possible dynamics that a *stochastic* and *non-hermitian* Hamiltonian can generate, thus building a path between the two types of evolution. We will find that the dynamics described by such a system follows a master equation beyond GKSL form, which we call *antidephasing* master equation. We first consider the case in which the noise affects only the anti-Hermitian part of the Hamiltonian, which is due to the anti-Hermitian part characterizing dissipation and non-unitary behavior, so that we expect the most interesting behavior to manifest in this case. For simplicity and analytical tractability of the formalism, we will also consider *gaussian*, *white* and *classical* noise.

³The Davies generator is written in the energy eigenbasis as $\mathcal{D}[\bullet] = \sum_\omega \sum_{\alpha,\beta} \gamma_{\alpha\beta}(\omega) \left(\hat{A}_\beta(\omega) \bullet \hat{A}_\alpha^\dagger(\omega) - \frac{1}{2} \{ \hat{A}_\alpha^\dagger(\omega) \hat{A}_\beta(\omega), \bullet \} \right)$ where the jump operators are eigenoperators of the unitary Liouvillian $[\hat{H}, \hat{A}_\alpha(\omega)] = -\omega \hat{A}_\alpha(\omega)$, $[\hat{H}, \hat{A}_\alpha^\dagger(\omega)] = +\omega \hat{A}_\alpha^\dagger(\omega)$ which additionally fulfill $\hat{A}_\alpha^\dagger(\omega) = \hat{A}_\alpha(-\omega)$ [17, 18].

3.2 Dynamics under general anti-hermitian fluctuations

3.2.1 The unnormalized Stochastic Master Equation

The most general Stochastic Non-Hermitian Hamiltonian with classical Gaussian white noise on its anti-hermitian part reads

$$\hat{H}_t = \hat{H}_{\text{R}} - i\hat{H}_{\text{I}} - i \sum_{n=1}^{N_{\text{C}}} \sqrt{2\gamma_n} \hat{L}_n \xi_t^{(n)}, \quad (3.1)$$

where N_{C} represents the number of noise channels, $\{\hat{L}_n\}_{n=1}^{N_{\text{C}}}$ represents the set of Hermitian $\hat{L}_n^\dagger = \hat{L}_n$ and positive semi-definite $\hat{L}_n \geq 0$ jump operators, γ_n is the noise-strength and $\xi_t^{(n)}$ are the different classical real white noises. These are characterized by zero mean $\mathbb{E}(\xi_t^{(n)}) = 0$ and with correlations given in the most general form by $\mathbb{E}(\xi_t^{(m)} \xi_{t'}^{(n)}) = \delta(t-t') M_{mn}$, where M_{mn} is a $N_{\text{C}} \times N_{\text{C}}$ matrix that defines the correlations. In the simplest case, it will be the identity $M_{mn} = \delta_{mn}$ describing independent sources of noise. Even in the case in which the noises are correlated, they can always be mapped to independent noise channels through the transformation described by Jacobs (cf. Sec. 3.8 [40]).

We now want to find an equation that allows us to describe the evolution of the state of the system under one particular realization of the Stochastic Non-Hermitian Hamiltonian, i.e., the *Stochastic Master Equation* (SME). To derive the SME associated with this Hamiltonian, we follow the simple approach described in Sec. 1.4.4, and shift the focus from the Hamiltonian to its associated propagator. We first express the propagator over a short time dt as

$$\hat{U}_{dt} = \exp \left(-i\hat{H}_{\text{R}} dt - \hat{H}_{\text{I}} dt - \sum_{n=1}^{N_{\text{C}}} \sqrt{2\gamma_n} \hat{L}_n dW_t^{(n)} \right), \quad (3.2)$$

where $dW_t^{(n)}$ are Wiener processes that obey Itô's rules, cf. Sec. 1.4.2. The evolution that this propagator generates for density matrices is given by $\tilde{\varrho}_{t+dt} = \hat{U}_{dt} \tilde{\varrho}_t \hat{U}_{dt}^\dagger$. After expanding the propagator according to Itô's rules, we find the SME associated with the Stochastic Non-Hermitian Hamiltonian (3.1) to be

$$\begin{aligned} d\tilde{\varrho}_t &= \left(-i[\hat{H}_{\text{R}}, \tilde{\varrho}_t] - \{\hat{H}_{\text{I}}, \tilde{\varrho}_t\} + \sum_{m,n=1}^{N_{\text{C}}} \sqrt{\gamma_m \gamma_n} M_{mn} \{\hat{L}_m, \{\hat{L}_n, \tilde{\varrho}_t\}\} \right) dt \\ &\quad - \sum_{n=1}^{N_{\text{C}}} \sqrt{2\gamma_n} \{\hat{L}_n, \tilde{\varrho}_t\} dW_t^{(n)} \\ &= \tilde{\mathcal{L}}_{\hat{H}_{\text{R}}, \hat{H}_{\text{I}}, \hat{\mathbf{L}}}^{\text{AD}} [\tilde{\varrho}_t] dt + \sum_{n=1}^{N_{\text{C}}} \tilde{\mathcal{M}}_{\hat{L}_n} [\tilde{\varrho}_t] dW_t^{(n)} \end{aligned} \quad (3.3)$$

This evolution involves a unitary and deterministic evolution with \hat{H}_R , a nonunitary deterministic evolution with \hat{H}_I , a dissipative term involving a double anticommutator with two jump operators, \hat{L}_m and \hat{L}_n , and lastly a stochastic, non-unitary evolution with the jump operator \hat{L}_n . Here a comment on the notation is needed; we use the tilde \bullet to denote the objects that are either: not normalized, such as the density matrices $\tilde{\rho}$, $\tilde{\rho}$, or do not generate a trace-preserving evolution, such as the superoperators $\tilde{\mathcal{L}}$, $\tilde{\mathcal{M}}$. Furthermore, we use $\hat{\rho}$ to denote that the density matrix depends on the single realization of the noise, in contrast to $\hat{\rho}$, which is averaged over the noise.

We will refer to this equation as the *anti-dephasing* (AD) SME since the dissipator involves dephasing with a double anticommutator, instead of a double commutator as is typically the case with dephasing. We have introduced the *antidephasing Liouvillian*

$$\tilde{\mathcal{L}}_{\hat{H}_R, \hat{H}_I, \hat{\mathbf{L}}}^{\text{AD}}[\bullet] := -i[\hat{H}_R, \bullet] - \{\hat{H}_I, \bullet\} + \sum_{m,n=1}^{N_c} \sqrt{\gamma_m \gamma_n} M_{mn} \{\hat{L}_m, \{\hat{L}_n, \bullet\}\}, \quad (3.4)$$

characterizing the *drift* term of the SME, where $\hat{\mathbf{L}} \equiv (\sqrt{\gamma_1} \hat{L}_1, \dots, \sqrt{\gamma_{N_c}} \hat{L}_{N_c})$ represents a vector of the jump operators, weighted by their dissipation rates. Furthermore, the *measurement superoperators*

$$\tilde{\mathcal{M}}_{\hat{L}_n}[\bullet] := -\sqrt{2\gamma_n} \{\hat{L}_n, \bullet\} \quad (3.5)$$

characterize the stochastic term associated to noise $dW_t^{(n)}$ in the SME.

In the case that the noises are uncorrelated $M_{mn} = \delta_{mn}$ the antidephasing Liouvillian simplifies to

$$\tilde{\mathcal{L}}_{\hat{H}_R, \hat{H}_I, \hat{\mathbf{L}}}^{\text{AD}}[\bullet] := -i[\hat{H}_R, \bullet] - \{\hat{H}_I, \bullet\} + \sum_{n=1}^{N_c} \gamma_n \{\hat{L}_n, \{\hat{L}_n, \bullet\}\}. \quad (3.6)$$

This form can always be achieved, in a similar way to standard OQS theory derivations of the diagonal form of the Lindblad equation [17]. In particular, the strategy is to diagonalize the matrix (M_{mn}) , and rotate the jump operators $\sqrt{\gamma'_m} \hat{L}'_m = \sum_n u_{mn} \sqrt{\gamma_n} \hat{L}_n$ into the eigenbasis, where (u_{mn}) is a unitary matrix. The matrix (M_{mn}) has to be symmetric $M_{mn} = M_{nm}$ because of Onsager reciprocity [239], if we impose the extra condition that its elements are real $M_{mn} \in \mathbb{R}$, the matrix (M_{mn}) is diagonalizable and thus this argument is justified.

3.2.2 Imposing Trace Preservation

The dynamics generated by (3.3) is, in general, not Trace Preserving (TP). This means that the solution of the SME, $\tilde{\rho}_t$, is not a proper density matrix since its populations do not sum to identity $\text{Tr}(\tilde{\rho}_t) \neq 1$. Physical dynamics must be trace preserving; for this reason, we will transform the dynamics to some associated nonlinear evolution, which is TP, in the same way as *Brody and Graefe* [92] did for standard non-Hermitian Hamiltonians.

However, since we include noise in the evolution, there are two possible approaches that can be followed to arrive at physical TP dynamics:

- We can impose that all trajectories, i.e., all possible realizations of the noise, show physical dynamics which preserve the trace of the density matrix. This is, in principle, the approach that will best describe the evolution of a Stochastic Non-Hermitian Hamiltonian in the lab. If our focus is to find an equation for the noise-averaged density matrix, this approach has a great disadvantage. A non TP evolution, e.g. $\partial_t \tilde{\rho} = \tilde{\mathcal{L}}[\tilde{\rho}]$ is associated to a nonlinear master equation $\partial_t \hat{\rho} = \tilde{\mathcal{L}}[\hat{\rho}] - \text{Tr}(\tilde{\mathcal{L}}[\hat{\rho}])\hat{\rho}$ such that the trace of $\hat{\rho}$ is preserved [92]. If we now apply this approach to single trajectories and then take an expectation value over the noise, the evolution of the first moment $\mathbb{E}(\hat{\rho}_t)$ depends on the second moment through $\mathbb{E}(\text{Tr}(\tilde{\mathcal{L}}[\hat{\rho}_t])\hat{\rho}_t)$. This creates a hierarchy of equations in which every moment $\mathbb{E}(\hat{\rho}_t^n)$ depends on higher order moments $\mathbb{E}(\hat{\rho}_t^m)$, with $m > n$. This hierarchy is not closed and, thus, very difficult to deal with. For this reason, we will study the behavior of single trajectories, solving directly the full SME, and only then averaging the results.
- The second possibility is to first take the average over the noise and then impose trace preservation. Even if this does not generate normalized single-trajectory dynamics, it allows us to find closed equations for the noise-averaged density matrix. We will follow this approach here and in Sec. 3.4.4 we will provide a justification for this choice, and a careful study of its range of validity.

We follow the latter approach; for this, we first take the noise-average of the SME, transforming it to a simpler ODE, which we will call the *antidephasing master equation*. We thus find that

$$\begin{aligned} \partial_t \tilde{\rho}_t &= \tilde{\mathcal{L}}_{\hat{H}_R, \hat{H}_I, \hat{\mathbf{L}}}^{\text{AD}}[\tilde{\rho}_t], \\ &= -i[\hat{H}_R, \tilde{\rho}_t] - \{\hat{H}_I, \tilde{\rho}_t\} + \sum_{n=1}^{N_C} \gamma_n \{\hat{L}_n, \{\hat{L}_n, \tilde{\rho}_t\}\}, \end{aligned} \quad (3.7)$$

where we use the diagonal representation of the channels, since, as argued before, such an expression can always be found, even for correlated noise. Note that the noise-averaged density matrix $\tilde{\rho}_t = \mathbb{E}(\tilde{\rho}_t)$ is still not unit trace. To solve this issue, we can renormalize the noise-averaged DM at all times as $\hat{\rho}_t = \frac{\tilde{\rho}_t}{\text{Tr}(\tilde{\rho}_t)}$. Since this quantity is not stochastic, we can apply the standard rules of calculus to derive an auxiliary equation for $\hat{\rho}_t$

$$\begin{aligned} \partial_t \hat{\rho}_t &= \frac{\dot{\tilde{\rho}}_t}{\text{Tr}(\tilde{\rho}_t)} - \frac{\tilde{\rho}_t \text{Tr}(\dot{\tilde{\rho}}_t)}{\text{Tr}(\tilde{\rho}_t)^2}, \\ &= \tilde{\mathcal{L}}_{\hat{H}_R, \hat{H}_I, \hat{\mathbf{L}}}^{\text{AD}}[\hat{\rho}_t] - \hat{\rho}_t \text{Tr}(\tilde{\mathcal{L}}_{\hat{H}_R, \hat{H}_I, \hat{\mathbf{L}}}^{\text{AD}}[\hat{\rho}_t]). \end{aligned} \quad (3.8)$$

Thus, to every non-TP linear evolution, we can associate a non-linear evolution, in the density matrix, such that the evolution is TP. Note that the second term involves the product of two density matrices. In particular, the most general antidephasing nonlinear

master equation reads

$$\begin{aligned}\partial_t \hat{\rho} = & -i[\hat{H}_R, \hat{\rho}_t] - \{\hat{H}_I, \hat{\rho}_t\} + \sum_{n=1}^{N_c} \gamma_n \{\hat{L}_n, \{\hat{L}_n, \hat{\rho}_t\}\} \\ & - \hat{\rho}_t \left(-2\text{Tr}(\hat{H}_I \hat{\rho}_t) + 4 \sum_{n=1}^{N_c} \gamma_n \text{Tr}(\hat{L}_n^2 \hat{\rho}_t) \right).\end{aligned}\quad (3.9)$$

When dealing with non-TP generators, the nonlinear master equation provides a physical TP evolution. There are, however, other approaches, such as the *Quantum Doob Transform* [240–242], which constructs a physical CPTP generator associated with the non-trace-preserving one. To the best of our knowledge, it remains an open question whether these two strategies generate the same or markedly different dynamics.

On the Positivity of the antidephasing channel

The unnormalized infinitesimal evolution generated by the antidephasing Liouvillian $\tilde{\mathcal{L}}_{\hat{H}_R, \hat{H}_I, \hat{L}}^{\text{AD}}$ can be written in terms of non-TP linear map

$$\tilde{\rho}_{t+\text{dt}} = \tilde{\mathcal{E}}_{\text{dt}}[\tilde{\rho}_t] = e^{\tilde{\mathcal{L}}_{\text{dt}}[\tilde{\rho}_t]} = \sum_{j=0}^{N_c} \hat{K}_j(\text{dt}) \tilde{\rho}_t \hat{K}_j^\dagger(\text{dt}), \quad (3.10)$$

where the operators read [243, 244]

$$\hat{K}_0(\text{dt}) = \hat{\mathbb{1}} - i\hat{H}_R \text{dt} - \hat{H}_I \text{dt} + \sum_{n=1}^{N_c} \gamma_n \hat{L}_n^2, \quad (3.11)$$

$$\hat{K}_n(\text{dt}) = \sqrt{2\gamma_n \text{dt}} \hat{L}_n, \quad n \in [1, 2, \dots, N_c]. \quad (3.12)$$

This map generates the evolution over an infinitesimal time dt , and thus for longer times a different set of Kraus gives better results [243].

Since the map admits this Kraus decomposition and the rates are positive $\gamma_n \geq 0$, it is *completely positive*, but not necessarily trace preserving since

$$\sum_{j=0}^{N_c} \hat{K}_j^\dagger(\text{dt}) \hat{K}_j(\text{dt}) = \hat{\mathbb{1}} - 2\hat{H}_I \text{dt} + 4 \sum_{n=1}^{N_c} \gamma_n \hat{L}_n^2 \text{dt} + \mathcal{O}(\text{dt}^2), \quad (3.13)$$

which is in general not equal to the identity and thus the map is in general not TP.

The evolution of the normalized density matrix then follows as

$$\hat{\rho}_{t+\text{dt}} = \frac{\sum_{j=0}^{N_c} \hat{K}_j(\text{dt}) \tilde{\rho}_t \hat{K}_j^\dagger(\text{dt})}{\text{Tr}(\sum_{i=0}^{N_c} \hat{K}_i^\dagger(\text{dt}) \hat{K}_i(\text{dt}) \tilde{\rho}_t)}. \quad (3.14)$$

Now we see that the numerator is a completely positive linear map, and the denominator is a number, which at first order in time will always be positive since the terms that change sign are first order in dt

$$\text{Tr} \left(\sum_{j=0}^{N_c} \hat{K}_j^\dagger(dt) \hat{K}_j(dt) \tilde{\rho}_t \right) = \text{Tr}(\tilde{\rho}_t) - 2\text{Tr}(\hat{H}_1 \tilde{\rho}_t)dt + 4 \sum_{n=1}^{N_c} \gamma_n \text{Tr}(\hat{L}_n^2 \tilde{\rho}_t)dt > 0, \quad (3.15)$$

as long as the averages $\text{Tr}(\hat{H}_1 \tilde{\rho}_t)$, $\text{Tr}(\hat{L}_n^2 \tilde{\rho}_t)$ are finite, which is guaranteed in the finite dimensional case, and in the infinite dimensional case can be achieved by taking these operators to be bounded $\hat{H}_1, \hat{L}_n \in \mathcal{B}(\mathcal{H})$.

Therefore, we can claim the nonlinear antidephasing map is *positive* since it is the ratio between a completely positive linear map and a positive scalar, which depends on the state $\tilde{\rho}_t$. Determining whether the antidephasing channel is also *completely* positive requires an extension of complete positivity to nonlinear maps and thus is non-trivial, although Geller [245] has claimed that nonlinear maps that are “*nonlinear in normalization only*”, such as the antidephasing one, are only positive trace-preserving (PTP) and not completely positive.

3.2.3 Antidephasing master equation in Stratonovich sense

The formalism of *stochastic calculus* has two different inequivalent approaches, which were properly introduced in Sec. 1.4.2. Throughout this chapter, we will consider only Itō calculus for convenience in the analytical results. However, the same results would follow for the noise average dynamics if we considered Stratonovich calculus, as done in [35, 37]. Here, for completeness, we provide a derivation of the same master equation in the Stratonovich convention. The antidephasing SME in Stratonovich reads

$$\dot{\tilde{\rho}}_t = -i[\hat{H}_R, \tilde{\rho}_t] - \{\hat{H}_1, \tilde{\rho}_t\} - \sum_{n=1}^{N_c} \sqrt{2\gamma_n} \{\hat{L}_n, \tilde{\rho}_t\} \circ \xi_t^{(n)}, \quad (3.16)$$

where \circ denotes that the product is to be understood in the Stratonovich sense, and for notational convenience, we use ξ_t instead of dW_t .

In the Stratonovich convention, the variable is not stochastically independent of the noise, i.e., $\mathbb{E}(\tilde{\rho}_t \circ \xi_t^{(n)}) \neq \mathbb{E}(\tilde{\rho}_t)\mathbb{E}(\xi_t^{(n)})$, instead the average of their product is given by Novikov’s theorem [41], also known as Furutsu-Novikov formula

$$\mathbb{E}(\tilde{\rho}_t \circ \xi_t^{(n)}) = \sum_{m=1}^{N_c} \int_0^t d\tau \mathbb{E}(\xi_t^{(n)} \xi_\tau^{(m)}) \mathbb{E} \left(\frac{\delta \tilde{\rho}_t}{\delta \xi_\tau^{(m)}} \right). \quad (3.17)$$

The functional derivative [35, 37], reads

$$\frac{\delta \tilde{\rho}_t}{\delta \xi_\tau^{(m)}} = -\sqrt{2\gamma_m} \hat{V}_{t,\tau} \{\hat{L}_m, \tilde{\rho}_\tau\} \hat{V}_{t,\tau}^\dagger, \quad (3.18)$$

where the propagator with the stochastic Hamiltonian reads $\hat{V}_{t,\tau} = \mathcal{T}e^{-i\int_{\tau}^t d\tau' \hat{H}_{\tau'}}$, where \mathcal{T} is the time ordering operator. Now we substitute the properties of white noise with uncorrelated channels $\mathbb{E}(\xi_t^{(n)} \xi_{\tau}^{(m)}) = \delta_{mn} \delta(t - \tau)$ and the identity $\hat{V}_{t,t} = \hat{\mathbb{1}}$, and we find that the expression for the average simplifies to

$$\mathbb{E}(\tilde{\varrho}_t \circ \xi_t^{(n)}) = -\frac{1}{2} \sqrt{2\gamma_n} \{\hat{L}_n, \tilde{\varrho}_t\}, \quad (3.19)$$

where we used that in Stratonovich convention the integral of Dirac's delta in one of the integrand limits obeys $\int_0^t d\tau f(\tau) \delta(\tau - t) = \frac{1}{2} f(t)$, cf. Sec. 1.4.4. This gives the expression for the noise-averaged unnormalized density matrix in the Stratonovich sense to be the same antidephasing master equation as in Itō

$$\dot{\tilde{\rho}}_t = -i[\hat{H}_R, \tilde{\rho}_t] - \{\hat{H}_I, \tilde{\rho}_t\} + \sum_{n=1}^{N_c} \gamma_n \{\hat{L}_n, \{\hat{L}_n, \tilde{\rho}_t\}\}. \quad (3.20)$$

3.2.4 Gauge transformations of the antidephasing master equation

We now want to characterize the Gauge transformations of the antidephasing master equation, since, as is well-known in OQS theory [17], the Lindbladian does not uniquely determine the Hamiltonian and jump operators in the GKSL equation. In other words, we want to find the ways in which we can transform \hat{H}_R , \hat{H}_I , $\hat{\mathbf{L}}$ such that the master equation remains invariant. The gauge transformations are:

- Shifting the hermitian part of the hamiltonian as $\hat{H}_R \rightarrow \hat{H}_R + E_0 \hat{\mathbb{1}}$, i.e., choosing a different zero of energy, does of course leave the master equation invariant since $[\hat{\mathbb{1}}, \hat{\rho}] = 0 \forall \hat{\rho}$.

Perhaps less trivial is the realization that one can shift the zero of the antihermitian part of the Hamiltonian $\hat{H}_I \rightarrow \hat{H}_I + a\hat{\mathbb{1}}$. Note that this transformation does not leave the Liouvillian $\tilde{\mathcal{L}}_{\hat{H}_R, \hat{H}_I, \hat{\mathbf{L}}}^{\text{AD}}[\bullet]$ invariant since

$$\tilde{\mathcal{L}}_{\hat{H}_R, \hat{H}_I + a\hat{\mathbb{1}}, \hat{\mathbf{L}}}^{\text{AD}}[\bullet] = \tilde{\mathcal{L}}_{\hat{H}_R, \hat{H}_I, \hat{\mathbf{L}}}^{\text{AD}}[\bullet] - 2a \bullet.$$

However, the full nonlinear master equation is invariant, since the extra term cancels out with the term coming from the nonlinear renormalization. Both of these conditions show that a complex zero of energy does not affect the renormalized dynamics of the NHSH master equation (3.9).

Note that this invariance is also present if we renormalized the single trajectories, as will be done in Sec. 3.4, because the previous transformation of the Liouvillian does not depend on what matrix it acts on, in particular, it could be $\hat{\rho}$, $\tilde{\rho}$, $\tilde{\rho}$ or $\hat{\rho}$, and as long as the dynamics is renormalized, i.e., considering either $\hat{\rho}$ or $\hat{\rho}$, the extra term will be cancelled.

- The jump operators do not uniquely determine the Liouvillian. In particular, consider an orthogonal transformation of the jump operators as

$$\sqrt{\gamma'_n} \hat{L}'_n = \sum_m \mathbf{O}_{nm} \sqrt{\gamma_m} \hat{L}_m, \quad (3.21)$$

where \mathbf{O} is an orthogonal matrix⁴ obeying $\mathbf{O}^\top \mathbf{O} = \mathbf{O} \mathbf{O}^\top = \mathbf{1}$, or equivalently expressed in components as $\sum_k (\mathbf{O}^\top)_{nk} \mathbf{O}_{km} = \sum_k \mathbf{O}_{kn} \mathbf{O}_{km} = \delta_{nm}$. The transformed Liouvillian then reads

$$\begin{aligned} \tilde{\mathcal{L}}_{\hat{H}_R, \hat{H}_I, \mathbf{O} \hat{\mathbf{L}}}^{\text{AD}}[\bullet] &= -i[\hat{H}_R, \bullet] - \{\hat{H}_I, \bullet\} + \sum_{m,l=1} \sqrt{\gamma_m \gamma_l} \overbrace{\sum_n \mathbf{O}_{nm} \mathbf{O}_{nl}}^{\delta_{ml}} \{\hat{L}_m, \{\hat{L}_l, \bullet\}\} \\ &= \tilde{\mathcal{L}}_{\hat{H}_R, \hat{H}_I, \hat{\mathbf{L}}}^{\text{AD}}[\bullet]. \end{aligned} \quad (3.22)$$

Therefore, the Liouvillian is invariant under orthogonal transformations of the jump operators. Note that for a general GKSL equation, the gauge freedom is unitary transformations of the jump operators [17], which reduces to orthogonal transformations if we impose hermiticity of the jump operators, i.e., restrict to *dephasing* processes.

Since the Liouvillian is invariant under the transformation, this is a symmetry of the antidephasing SME, which will be inherited by any renormalization strategy.

- Let us now consider a shift of the jump operators as $\hat{L}'_n = \hat{L}_n + b_n \hat{\mathbb{1}}$, where $b_n \in \mathbb{R}$ to respect their hermiticity. This is called a *inhomogeneous transformation* [17]. The Liouvillian transforms to

$$\tilde{\mathcal{L}}_{\hat{H}_R, \hat{H}_I, \hat{\mathbf{L}} + \mathbf{b} \hat{\mathbb{1}}}^{\text{AD}}[\bullet] = -i[\hat{H}_R, \bullet] - \left\{ \hat{H}_I - 4 \sum_{n=1}^{N_c} \gamma_n b_n \hat{L}_n, \bullet \right\} + \sum_{n=1}^{N_c} \gamma_n \{\hat{L}_n, \{\hat{L}_n, \bullet\}\}.$$

Therefore, if the anti-hermitian Hamiltonian is shifted so as to cancel the extra terms

$$\begin{cases} \hat{L}_n \rightarrow \hat{L}_n + b_n \hat{\mathbb{1}}, \\ \hat{H}_I \rightarrow \hat{H}_I + 4 \sum_{n=1}^{N_c} \gamma_n b_n \hat{L}_n, \end{cases} \quad (3.23)$$

the Liouvillian remains invariant. Defining $\mathbf{b} = (\sqrt{\gamma_1} b_1, \dots, \sqrt{\gamma_{N_c}} b_{N_c})$ for notational convenience, we find that the following transformation does not change the Liouvillian

$$\tilde{\mathcal{L}}_{\hat{H}_R, \hat{H}_I + 4\mathbf{b} \cdot \hat{\mathbf{L}}, \hat{\mathbf{L}} + \mathbf{b} \hat{\mathbb{1}}}^{\text{AD}}[\bullet] = \tilde{\mathcal{L}}_{\hat{H}_R, \hat{H}_I, \hat{\mathbf{L}}}^{\text{AD}}[\bullet]. \quad (3.24)$$

⁴ \mathbf{O} is a transformation of the vector of jump operators into the jump operators, i.e., $\mathbf{O} : \hat{\mathbf{L}} \in \mathcal{L}(\mathcal{H})^{N_c} \mapsto \mathcal{L}(\mathcal{H})^{N_c}$ where $\hat{\mathbf{L}}' = \mathbf{O} \hat{\mathbf{L}}$. Therefore $\mathbf{O} \in \mathcal{M}^{N_c \times N_c}$. Since it is not an operator on the Hilbert space, but rather a transformation over jump operators, we do not use the standard notation for quantum operators \bullet .

This invariance, as in the standard GKSL case, always allows to choose traceless jump operators. Again, since the Liouvillian is invariant under the transformation, both the unnormalized antidephasing master equation and its normalized nonlinear version have this gauge invariance.

We have seen that there are two possible classes of transformations: those that leave the Liouvillian invariant, like the orthogonal transformation of jumps, or the inhomogeneous transformation, and those that only leave the nonlinear master equation invariant, such as the shift of the anti-hermitian Hamiltonian.

In principle one could consider some more transformations of the master equation which would only be a symmetry for certain possible dynamics, i.e., $\hat{H}_R \rightarrow \hat{H}_R + \hat{A}_\rho$ or $\hat{H}_I \rightarrow \hat{H}_I + \hat{B}_\rho$ with the extra condition that the shift operator always commutes $[\hat{A}_\rho, \hat{\rho}_t] = 0 \forall t$ or anticommutes $\{\hat{B}_\rho, \hat{\rho}_t\} = 0 \forall t$ with the density matrix. But these transformations would have to be fine-tuned to respect the full dynamics, and thus we do not consider them here.

3.2.5 Evolution of the purity

One of the key differences between Non-Hermitian Hamiltonians and GKSL dynamics is that while the latter generally decoheres most states and makes them mixed, the former keeps pure states pure while only changing the purity of mixed states. In here, we consider the dynamics generated by (3.9) and find the differential equation for the evolution of the purity of any state $P_t = \text{Tr}(\hat{\rho}_t^2)$

$$\begin{aligned} \frac{dP_t}{dt} &= 2\text{Tr}(\tilde{\mathcal{L}}_{\hat{H}_R, \hat{H}_I, \hat{\mathbf{L}}}^{\text{AD}}[\hat{\rho}_t]\hat{\rho}_t) - 2\text{Tr}(\tilde{\mathcal{L}}_{\hat{H}_R, \hat{H}_I, \hat{\mathbf{L}}}^{\text{AD}}[\hat{\rho}_t])P_t, \\ &= 4\text{Tr}\left(\hat{H}_I(\hat{\rho}_t P_t - \hat{\rho}_t^2)\right) + 4 \sum_{n=1}^{N_c} \gamma_n \left(\text{Tr}(\hat{L}_n^2 \hat{\rho}_t^2) + \text{Tr}(\hat{L}_n \hat{\rho}_t \hat{L}_n \hat{\rho}_t) - 2\text{Tr}(\hat{L}_n^2 \hat{\rho}_t)P_t\right). \end{aligned} \quad (3.25)$$

Interestingly, this expression contains out-of-time-order terms reminiscent of OTOC's [1] and generalizes the known evolution for NH Hamiltonians [246]. This expression is related to the decoherence time $\frac{1}{\tau_P} = \frac{dP_t}{dt}|_{t=0}$ [247], but generalizes the concept by describing the evolution of the purity for any general state $\hat{\rho}_t$. If the state $\hat{\rho}_t$ is pure at any given time t , $\hat{\rho}_t^2 = \hat{\rho}_t = |\psi_t\rangle\langle\psi_t|$, i.e., $P_t = 1$, the first term vanishes, as expected because pure NH evolution keeps a pure state pure, and the contribution from the second term greatly simplifies to

$$\frac{dP_t}{dt} = -4 \sum_{n=1}^{N_c} \left(\langle\psi_t|\hat{L}_n^2|\psi_t\rangle - \langle\psi_t|\hat{L}_n|\psi_t\rangle^2 \right), \quad (3.26)$$

which means that the change in purity is given by the sum of the variances of the jump operators over the particular state. This result is identical to the decoherence time of pure states in a dephasing channel and quantum Brownian motion [8, 17, 248].

Note that, since a pure state cannot get *more pure*, this expression in non-positive $\frac{dP_t}{dt} \leq 0$; furthermore, each of the terms in the sum is non-positive, due to the properties of the variance. The equality, $\frac{dP_t}{dt} = 0$, is found when $|\psi_t\rangle$ is an eigenstate to all the jump operators $\{\hat{L}_n\}_{n=1}^{N_c}$. But, under what conditions can N_c matrices share a common eigenvector? A sufficient condition is that they all pairwise commute; however, this is too strong a requirement if we are interested in a single common eigenvector. For two matrices, this is answered by the *Shemesh criterion* [249], which is generalized to N matrices by Jamolkowski and Pastuszak [250]. Beyond pure states and for a single noise channel, there are many mixed states whose purity will be preserved; in Sections 3.3.1 and 3.3.3, we will provide a full characterization of all the mixed states fulfilling this property for a particular physical system.

3.2.6 Long time dynamics: Steady states

The solution of the master equation (3.9) can be formally written in terms of the antidephasing Liouvillian $\tilde{\mathcal{L}}$ simply as

$$\hat{\rho}_t = \frac{e^{\tilde{\mathcal{L}}t}[\hat{\rho}_0]}{\text{Tr}(e^{\tilde{\mathcal{L}}t}[\hat{\rho}_0])}. \quad (3.27)$$

Now, assuming that the antidephasing Liouvillian can be diagonalized, we can write the right and left eigendecomposition

$$\tilde{\mathcal{L}}[\hat{\rho}_\nu] = \tilde{\lambda}_\nu \hat{\rho}_\nu, \quad \tilde{\mathcal{L}}^\dagger[\hat{\rho}_\nu^{(L)}] = \tilde{\lambda}_\nu^* \hat{\rho}_\nu^{(L)}, \quad (3.28)$$

where, importantly, the eigenmatrices are biorthogonal [90]

$$(\hat{\rho}_\mu^{(L)}, \hat{\rho}_\nu) \propto \delta_{\mu\nu}. \quad (3.29)$$

Furthermore, we introduce the following renormalization of the eigenbasis as

$$\begin{cases} \hat{\sigma}_\nu = \frac{\hat{\rho}_\nu}{\text{Tr}(\hat{\rho}_\nu)} & \text{if } \text{Tr}(\hat{\rho}_\nu) \neq 0, \\ \hat{\sigma}_\nu = \hat{\rho}_\nu & \text{if } \text{Tr}(\hat{\rho}_\nu) = 0. \end{cases} \quad (3.30)$$

Furthermore, we order the basis in a way such that we have N_p physical eigenstates, i.e., $\hat{\sigma}_\mu \geq 0$ and $\text{Tr}(\hat{\sigma}_\mu) = 1$ for $1 \leq \mu \leq N_p$. Then, we have $N_t - N_p$ traceful but unphysical states, i.e., $\hat{\sigma}_\mu \not\geq 0$ and $\text{Tr}(\hat{\sigma}_\mu) = 1$ for $N_p < \mu \leq N_t$. Lastly, we have $N^2 - N_p$ traceless states, i.e., $\text{Tr}(\hat{\sigma}_\mu) = 0$ for $\mu > N_t$. Furthermore, inside these three sets of indices, the eigenvectors are ordered by decreasing eigenvalue.

The solution can simply be written in this basis as

$$\hat{\rho}_t = \frac{\sum_{\mu=1}^{N^2} c_\mu e^{\tilde{\lambda}_\mu t} \hat{\sigma}_\mu}{\sum_{\kappa=1}^{N_t} c_\kappa e^{\tilde{\lambda}_\kappa t}}, \quad (3.31)$$

where the coefficients are given by $c_\mu = \frac{(\hat{\sigma}_\mu^{(L)}, \hat{\rho}_0)}{(\hat{\sigma}_\mu^{(L)}, \hat{\sigma}_\mu)} = \frac{\text{Tr}(\hat{\sigma}_\mu^{(L)\dagger} \hat{\rho}_0)}{\text{Tr}(\hat{\sigma}_\mu^{(L)\dagger} \hat{\sigma}_\mu)}$. Note that there is a key difference between the dynamics generated by these dynamics and by solving the GKSL equation. In the standard GKSL master equation, all eigenvectors are traceless, except for those with $\lambda_\nu = 0$, which are the steady states. In the dynamics described by (3.37), all the traceful states, no matter if they are unphysical, contribute to the renormalization. This changes the possible dynamics described by the evolution, in particular, as we shall see next, it can lead to an oscillating trace, like in the \mathcal{PT} symmetric phase of Dissipative Qubit [80].

Let us introduce the sets \mathbb{M}_1 as the set of indices with the largest real part over which the initial state has support, i.e.,

$$\mathbb{M}_1 := \{m \text{ such that } \text{Re}(\tilde{\lambda}_\mu) = \max_\kappa \text{Re}(\tilde{\lambda}_\kappa), c_\mu \neq 0\},$$

as well as the same set but with the extra condition that the eigenstate is traceful

$$\mathbb{M}_1^{(T)} := \{m \text{ such that } \text{Re}(\tilde{\lambda}_\mu) = \max_\kappa \text{Re}(\tilde{\lambda}_\kappa), c_\mu \neq 0, \text{Tr}(\hat{\sigma}_\mu) = 1\}.$$

Also the set of the second largest real part

$$\mathbb{M}_2 := \{m \text{ such that } \text{Re}(\tilde{\lambda}_\mu) = \max_{\kappa \notin \mathbb{M}_1} \text{Re}(\tilde{\lambda}_\kappa), c_\mu \neq 0\}.$$

The *dissipative gap* is defined as the difference in the real part of the eigenspaces with the two largest real parts

$$\Delta := \text{Re}(\tilde{\lambda}_{\mathbb{M}_1}) - \text{Re}(\tilde{\lambda}_{\mathbb{M}_2}) > 0$$

and the *oscillating eigenfrequencies* are defined as the imaginary part of any eigenvalue

$$\omega_\nu = \text{Im}(\lambda_\nu).$$

Note that all of the notions, including the sets \mathbb{M}_n , depend on the initial state of the system since they are subject to the condition $c_\mu \neq 0$.

Assuming a single eigenvalue with the largest real part, the long-time dynamics follows from expanding the trace as $\sum_{\kappa=1}^{N_T} c_\kappa e^{\tilde{\lambda}_\kappa t} \sim c_0 e^{\tilde{\lambda}_0 t}$ and gives the evolution

$$\hat{\rho}_t \xrightarrow{t \rightarrow \infty} \hat{\sigma}_0 + e^{-\Delta t} \sum_{\nu \in \mathbb{M}_2} \frac{c_\nu e^{i\omega_\nu t}}{c_0} \hat{\sigma}_\nu. \quad (3.32)$$

The state $\hat{\sigma}_0$ is the *stable steady state*; we provide a proof for its stability in the next section.

In the case where there are several states in \mathbb{M}_1 a similar approach applies changing the expansion of the trace of the state to

$$\sum_{\kappa=1}^{N_T} c_\kappa e^{\tilde{\lambda}_\kappa t} \sim e^{\text{Re}(\tilde{\lambda}_0)t} \sum_{\kappa \in \mathbb{M}_1^{(T)}} c_\kappa e^{i\omega_\kappa t},$$

where interestingly we find that the trace can oscillate, given that $\omega_\mu \neq 0$ for some $\mu \in \mathbb{M}_1^{(T)}$. This yields a stable steady state

$$\hat{\rho}_t \xrightarrow{t \rightarrow \infty} \sum_{\nu \in \mathbb{M}_1} \frac{c_\nu e^{i\omega_\nu t}}{\sum_{\mu \in \mathbb{M}_1^{(T)}} c_\mu e^{i\omega_\mu t}} \hat{\sigma}_\nu + e^{-\Delta t} \sum_{\nu \in \mathbb{M}_2} \frac{c_\nu e^{i\omega_\nu t}}{\sum_{\mu \in \mathbb{M}_1^{(T)}} c_\mu e^{i\omega_\mu t}} \hat{\sigma}_\nu. \quad (3.33)$$

From this expression, it is apparent that the steady state can show oscillations and even an oscillating trace, given that the number of states in \mathbb{M}_1 is larger than one, and they have nonzero oscillating eigenfrequencies. This is equivalent to the behavior displayed in the standard Lindblad case by the *oscillating coherences* [198], with the difference that the oscillating coherences have no effect on the trace of the state, and thus only affect the off-diagonals of the density matrix, while the oscillating trace affects the whole DM.

The dissipative gap Δ characterizes the decay towards the steady state eigenspace of the density matrix. One possible situation is that if we measure a certain expectation value in the lab $\langle \chi | \hat{\rho}_t | \chi \rangle$ the expectation value of all the eigenstates in the second largest eigenspace \mathbb{M}_2 vanishes $\langle \chi | \hat{\sigma}_\nu | \chi \rangle = 0$. If this is the case, the dynamics of that expectation value will seem to have a faster convergence to the steady state than the one predicted by Δ , with a larger χ -dependent *effective dissipative gap* given by

$$\Delta_{\text{eff}}^{(\chi)} = \text{Re}(\lambda_{\mathbb{M}_1}) - \text{Re}(\lambda_{\mathbb{M}_n}), \text{ where } n = \min_m \{m | \langle \chi | \sigma_\nu | \chi \rangle \neq 0, \sigma_\nu \in \mathbb{M}_m\}. \quad (3.34)$$

By construction, this effective dissipative gap is always larger or equal to the dissipative gap $\Delta_{\text{eff}}^{(\chi)} \geq \Delta$ and thus the dissipative gap in this case can still serve as the *slowest possible speed of convergence* to the steady state.

Dynamics at a Liouvillian Exceptional Point

So far, we have considered the simple case in which the Liouvillian was diagonalizable. If this is not the case, we necessarily are at a Liouvillian Exceptional Point (LEP) [251, 252]. In this case, the Liouvillian can be brought to a Jordan block form in which the exponential reads (see eq. (27) in [57])

$$e^{\tilde{\mathcal{L}}t} = \sum_{j=1}^J e^{\tilde{\lambda}_j t} \left(\mathcal{P}_j + \sum_{\alpha=1}^{m_j^g} \sum_{p=1}^{n_{j\alpha}-1} \frac{t^p}{p!} \mathcal{N}_{j\alpha}^p \right), \quad (3.35)$$

where m_j^g is the geometric multiplicity of the eigenvalue, i.e., how many blocks are there with the $\tilde{\lambda}_j$ eigenvalue, $n_{j\alpha}$ is the size of each of those blocks, \mathcal{P}_j is a rank $n_{j\alpha}$ projector and $\mathcal{N}_{j\alpha}$ is a nilpotent matrix. Note that we use calligraphic letters because these are to be understood as matrices only in the vectorized space.

For the sake of simplicity, we consider first the case in which we have a single LEP of order 2. In this case the matrix is block diagonal with all blocks of size one except for one of size 2, and let us denote: λ_{LEP} the eigenvalue associated to the LEP and let \mathbb{M}_{LEP} the set of indices whose eigenvectors are in the LEP. This means that the equation $(\tilde{\mathcal{L}} - \lambda_{\text{LEP}}) \hat{\sigma}_{\text{LEP}} = 0$

only admits one solution $\hat{\sigma}_{\text{LEP}}^{(1)}$. However, one can introduce a generalized eigenmatrix $\hat{\sigma}_{\text{LEP}}^{(2)}$ [251] defined as $(\tilde{\mathcal{L}} - \lambda_{\text{LEP}})\hat{\sigma}_{\text{LEP}}^{(2)} = \hat{\sigma}_{\text{LEP}}^{(1)}$, which can be reexpressed in matrix notation in the Jordan block as

$$\begin{pmatrix} \lambda_{\text{LEP}} & 1 \\ 0 & \lambda_{\text{LEP}} \end{pmatrix} \begin{pmatrix} 0 \\ 1 \end{pmatrix} = \begin{pmatrix} 1 \\ \lambda_{\text{LEP}} \end{pmatrix}, \quad (3.36)$$

and clearly shows the role of the generalized eigenmatrix as an eigenstate of the diagonal part of the Liouvillian.

In this case, the dynamics reads

$$\hat{\rho}_t = \frac{\sum_{\mu=1 \notin \mathbb{M}_{\text{LEP}_2}}^{N^2} c_\mu e^{\tilde{\lambda}_\mu t} \hat{\sigma}_\mu + e^{\tilde{\lambda}_{\text{LEP}} t} (c_{\text{LEP}}^{(1)} \hat{\sigma}_{\text{LEP}}^{(1)} + t c_{\text{LEP}}^{(2)} \hat{\sigma}_{\text{LEP}}^{(2)})}{\sum_{\kappa=1 \notin \mathbb{M}_{\text{LEP}_2}}^{N_{\text{T}}} c_\kappa e^{\tilde{\lambda}_\kappa t} + e^{\tilde{\lambda}_{\text{LEP}} t} (c_{\text{LEP}}^{(1)} \text{Tr}(\hat{\sigma}_{\text{LEP}}^{(1)}) + t c_{\text{LEP}}^{(2)} \text{Tr}(\hat{\sigma}_{\text{LEP}}^{(2)}))}, \quad (3.37)$$

where the coefficients are given by the inner product with the left generalized eigenmatrices $c_{\text{LEP}}^{(n)} = \frac{(\hat{\sigma}_{\text{LEP}}^{(\text{L},1)} \dagger, \hat{\rho}_0)}{(\hat{\sigma}_{\text{LEP}}^{(\text{L},n)} \dagger, \hat{\sigma}_{\text{LEP}}^{(n)})}$. We see that the effect of the LEP in the dynamics is to introduce a polynomial contribution multiplying the exponential. In the case of a general order n LEP, the evolution of the unnormalized DM is given by

$$\tilde{\rho}_t = \sum_{\mu=1 \notin \mathbb{M}_{\text{LEP}_n}}^{N^2} c_\mu e^{\tilde{\lambda}_\mu t} \hat{\sigma}_\mu + e^{\tilde{\lambda}_{\text{LEP}} t} \sum_{k=0}^{n-1} c_{\text{LEP}}^{(k)} \frac{t^k}{k!} \hat{\sigma}_{\text{LEP}}^{(k)}, \quad (3.38)$$

so we see that the evolution acquires a polynomial of degree $n - 1$.

If the LEP is not in the eigenspace with the largest real part, it will have an effect on the dynamics, but not in the steady state. This can be seen using the fact that the exponential grows faster at large t than any polynomial, i.e., $\lim_{t \rightarrow \infty} e^{bt} - t^n e^{at} = \lim_{t \rightarrow \infty} e^{at} (e^{(b-a)t} - t^n) > 0$ if $b > a$; no polynomial can make the exponential with smaller exponent win at long times over the exponential with larger exponent. The example in which this will be most apparent is in the case where the LEP lives in the eigenspace with the second largest real part; the dynamics will not be characterized only by the dissipative gap Δ and the oscillation frequencies ω_ν in that eigenspace, but there will also be a polynomial contribution affecting the convergence to the steady state. The convergence to the steady state, considering only the highest order contribution, is changed to

$$t \sim \frac{n-1}{\Delta} w \left(\frac{\Delta e^{-\frac{1}{n-1}}}{n-1} \Gamma(n)^{\frac{1}{n-1}} \right), \quad (3.39)$$

where $w(z)$ is the principal branch of the *Lambert* or product logarithmic function. Interestingly, the polynomial causes the contribution from the eigenspace with the second largest real part of the eigenvalue to be small for short times, but that gives a *revival* at larger times before it finally dies out.

The steady states can be affected in the case in which the LEP lives in the eigenspace with the largest real part, and the eigenvectors that coalesce are physical and traceful. In this case we will observe a convergence at times $t \sim \Delta^{-1}$ to the eigenspace with largest real part of the eigenvalues, but the dynamics in this eigenspace will not remain constant or oscillatory, it will show a power law convergence to one of the eigenstates of the diagonal part of the Liouvillian. In particular, after the inverse dissipative gap $t \gtrsim \Delta^{-1}$, the only contribution to the dynamics will come from the eigenspace with the largest real part. If a LEP is present and the eigenmatrices of the LEP are traceful, the term with the largest trace at long times will be $\frac{t^{n-1}}{(n-1)!} c_{\text{LEP}}^{(k-1)} \text{Tr}(\hat{\sigma}_{\text{LEP}}^{(n-1)})$. This will cause a power law convergence to $\rho_t \rightarrow \hat{\sigma}_{\text{LEP}}^{(n-1)}$ where the contributions from other states in the LEP $\hat{\sigma}^k$, $k < n-1$ are suppressed by a power law of the form $\propto t^{-(n-1-k)}$.

Properties of the steady states

Lemma 1. *Let the Liouvillian $\tilde{\mathcal{L}}$ be diagonalizable. All steady states of the nonlinear Master Equation are eigenvectors of the non-Trace Preserving Liouvillian $\tilde{\mathcal{L}}[\bullet]$.*

Proof. To prove this, we proceed by contradiction. Assume that there exists a density matrix $\hat{\varsigma}$ such that:

- (i) It is a steady state of the nonlinear Master equation $\partial_t \hat{\varsigma} = \tilde{\mathcal{L}}[\hat{\varsigma}] - \hat{\varsigma} \text{Tr}(\tilde{\mathcal{L}}[\hat{\varsigma}]) = 0$,
- (ii) Is not an eigenstate of the nTPL $\tilde{\mathcal{L}}[\hat{\varsigma}] \neq \lambda \hat{\varsigma}$

Expressing such operator in the operator eigenbasis gives $\hat{\varsigma} = \sum_n c_n \hat{\sigma}_n$, where the unit trace condition imposes $\sum_{n=1}^{N_p} c_n = 1$. The (i) condition can be stated as

$$\partial_t \hat{\varsigma} = \sum_{n=1}^{N^2} c_n \left(\lambda_n - \sum_{m=1}^{N_p} c_m \lambda_m \right) \hat{\sigma}_n = 0. \quad (3.40)$$

Since the nTPL is diagonalizable, the eigenbasis elements are linearly independent and thus the (i) condition is equivalent to

$$c_n \lambda_n = c_n \sum_{m=1}^{N_p} c_m \lambda_m, \quad \forall n. \quad (3.41)$$

Now by virtue of (ii) we look for at least two non-zero coefficients $c_k, c_l \neq 0$ and different eigenvalues $\lambda_k \neq \lambda_l$ such that $\tilde{\mathcal{L}}[c_k \hat{\sigma}_k + c_l \hat{\sigma}_l] = c_k \lambda_k \sigma_k + c_l \lambda_l \sigma_l \neq \lambda(c_k \hat{\sigma}_k + c_l \hat{\sigma}_l)$. However, from (3.41) both of these eigenvalues should be equal to $\sum_m^{N_p} c_m \lambda_m$ and thus $\lambda_k = \lambda_l$ so we arrive at a contradiction and thus all the steady states of the nonlinear Master Equation need to be eigenstates of the non Trace Preserving Liouvillian $\tilde{\mathcal{L}}[\bullet]$. \square

Lemma 2. *The only stable steady states $\hat{\rho}^s$ are those with largest real part of their eigenvalue*

Proof. Consider a physical state steady state, $\hat{\rho}_s$ such that $\tilde{\mathcal{L}}[\hat{\rho}_s] = \lambda_s \hat{\rho}_s$ and $\text{Tr}(\hat{\rho}_s) = 1$, that is slightly perturbed as $\hat{\rho}_s + \epsilon \delta \hat{\rho}$, where the perturbation $\delta \hat{\rho}$ is traceless—the latter ensures physicality. As commonly done in the study of nonlinear dynamical systems [236], we linearize the dynamics around this steady state,

$$d_t \delta \hat{\rho} \approx \tilde{\mathcal{L}}[\delta \hat{\rho}] - \text{Tr}(\tilde{\mathcal{L}}[\hat{\rho}_s]) \delta \hat{\rho} - \text{Tr}(\tilde{\mathcal{L}}[\delta \hat{\rho}]) \hat{\rho}_s \equiv \mathcal{A}[\delta \hat{\rho}], \quad (3.42)$$

and define the linear superoperator \mathcal{A} by discarding quadratic terms in ϵ . Diagonalizing this super-operator, $\mathcal{A}[\hat{A}_\nu] = a_\nu \hat{A}_\nu$, gives the stability with respect to perturbations along \hat{A}_ν , as determined by the eigenvalue a_ν ; specifically, the system is stable for $\text{Re}(a_\nu) < 0$ and unstable otherwise.

We first consider traceless directions along the zero-trace eigenstates, that is, $\delta \hat{\rho} = \hat{\sigma}_\nu$ for $\nu > N_p$. Then $\mathcal{A}[\hat{\sigma}_\nu] = (\lambda_\nu - \lambda_s) \hat{\sigma}_\nu$, so the perturbations are stable for $\text{Re}(\lambda_s) > \text{Re}(\lambda_\nu)$. This implies that the only stable steady state with respect to perturbations along the traceless eigenvectors is the one whose eigenvalue has the largest real part. However, the choice of the traceless $\hat{\sigma}_\nu$ does not cover all the possible traceless perturbations. For example, the perturbation $\delta \hat{\rho} = \hat{\sigma}_\kappa - \hat{\sigma}_\mu$, written from the difference of two physical and traceful eigenstates $\hat{\sigma}_\kappa$ and $\hat{\sigma}_\mu$, may lead to an unstable steady state. To study perturbations in these directions, we compute the action on $\hat{\sigma}_\nu - \hat{\rho}_s$

$$\mathcal{A}[\hat{\sigma}_\nu - \hat{\rho}_s] = (\lambda_\nu - \lambda_s)(\hat{\sigma}_\nu - \hat{\rho}_s), \quad \nu \leq N_p, \quad (3.43)$$

and find it is diagonal—the eigenvalues of the \mathcal{A} superoperator are $\lambda_\nu - \lambda_s$ and their associated eigenvectors are $\hat{\sigma}_\nu - \hat{\rho}_s$. The stability condition thus is as in the previous case, namely $\text{Re}(\lambda_s) > \text{Re}(\lambda_\nu)$. \square

In conclusion, only the eigenstates whose eigenvalues have the largest real part are stable under all possible perturbations. This result generalizes the well-known result that the eigenvalues of the Lindbladian have a negative real part and that the zero eigenvalue subspace, the one with the largest real part, contains the steady states.

Lemma 3. *All physical eigenstates have real eigenvalues of $\tilde{\mathcal{L}}$*

Proof. Consider a physical DM $\hat{\rho} \geq 0$, $\hat{\rho} \neq 0$, and let us assume that it is an eigenstate of the nTPL $\tilde{\mathcal{L}}[\hat{\rho}] = \lambda \hat{\rho}$. We consider the most general form of a non-TP Liouvillian $\tilde{\mathcal{L}}[\bullet] = -i[\hat{H}, \bullet] + \sum_{n=1}^{N_c} \hat{L}_n \bullet \hat{L}_n^\dagger + \{\hat{\Gamma}, \bullet\}$. Due to the positivity of the DM, it can be written as $\hat{\rho} = \hat{A}^\dagger \hat{A}$, then the trace of the eigenstate condition gives

$$\lambda \text{Tr}(\hat{\rho}) = \text{Tr}(2\hat{\Gamma}\hat{\rho}) + \sum_{n=1}^{N_c} \text{Tr}(\hat{L}_n \hat{\rho} \hat{L}_n^\dagger),$$

where we introduced the first term is real since $\text{Tr}(\hat{\Gamma}\hat{\rho}) = \text{Tr}(\hat{A}\hat{\Gamma}\hat{A}^\dagger)$ and $\hat{A}\hat{\Gamma}\hat{A}^\dagger$ is a hermitian operator, with real trace. The second term is positive since it is the product of positive operators $\hat{L}^\dagger \hat{L} \geq 0$ and $\hat{\rho}$, and thus its trace is positive. This implies that $\lambda \text{Tr}(\hat{\rho}) \in \mathbb{R}$ but since $\hat{\rho}^\dagger = \hat{\rho}$ the trace is real, therefore $\lambda \in \mathbb{R}$. Furthermore, if the antihermitian part of the generator is positive semidefinite $\hat{\Gamma} \geq 0$, the eigenvalue is positive. \square

3.3 The Stochastic Dissipative Qubit

The simplest example showing the properties of Non-Hermitian Quantum Mechanics is the Dissipative Qubit. There are several possible physical realizations of this system; here, we will follow the approach by Naghiloo *et al.* [80]. In it a 3-level system described by the states $\{|g\rangle, |e\rangle, |f\rangle\}$ undergoes dissipative evolution, with continuous measurements (photodetection) of the $|e\rangle \rightarrow |g\rangle$ channel. After this, only the trajectories with no jumps to the $|g\rangle$ state are post-selected, effectively “killing” the jump term and leaving only non-Hermitian dynamics. The effective Non-Hermitian Hamiltonian

$$\hat{H}_{\text{DQ}} = J\hat{\sigma}_x - i\Gamma|e\rangle\langle e| = \begin{pmatrix} 0 & J \\ J & -i\Gamma \end{pmatrix}, \quad (3.44)$$

describes the no-jump dynamics. This system has passive \mathcal{PT} symmetry, which means that a shifted version of the Hamiltonian $\hat{H}_{\text{DQ}} + i\frac{\Gamma}{2}\hat{1}$ has \mathcal{PT} symmetry. The phenomenology and dynamics described by both hamiltonians are the same, given that the state is renormalized. This shift can be thought of as moving to a frame with a constant decay on both levels such that the state $|e\rangle$ has losses and the state $|f\rangle$ has the same amount of gain, showing balanced Gain and Loss. The reason for this is that gains, i.e., positive imaginary terms in the diagonal, are unstable and hard to achieve in a quantum mechanical setup.

Our aim here is to study a stochastic version of this model, which we call the *Stochastic Dissipative Qubit* (SDQ), with white noise in the anti-hermitian part. This physically corresponds to noise in the parameter Γ , which is known to be present in the experimental setup of Naghiloo *et al.* [253], see Sec. 3.5 for a discussion of the experimental details of the implementation. Considering a single noise channel, the Hamiltonian for the SDQ reads

$$\hat{H}_{\text{SDQ}} = J\hat{\sigma}_x - i\Gamma(1 + \sqrt{2\gamma}\xi_t)\hat{\Pi}, \quad (3.45)$$

where for convenience we introduced the projector over state $|e\rangle$ as $\hat{\Pi} = |e\rangle\langle e|$. This corresponds to choosing $N_c = 1$, and $\hat{H}_i = \hat{L} = \Gamma\hat{\Pi}$. Therefore, we can directly write the unnormalized Liouvillian as

$$\begin{aligned} \tilde{\mathcal{L}}_{\text{SDQ}}[\bullet] &:= \tilde{\mathcal{L}}_{J\hat{\sigma}_x, \Gamma\hat{\Pi}, \Gamma\hat{\Pi}}^{\text{AD}}[\bullet] \\ &= -iJ[\hat{\sigma}_x, \bullet] - \Gamma\{\hat{\Pi}, \bullet\} + \gamma\Gamma^2\{\hat{\Pi}, \{\hat{\Pi}, \bullet\}\}. \end{aligned} \quad (3.46)$$

This superoperator can be conveniently written as a matrix in a doubled Hilbert space using the Choi-Jamiolkowski isomorphism [33, 34], which reads

$$\tilde{\mathcal{L}}_{\text{SDQ}} = J \begin{pmatrix} 0 & i & -i & 0 \\ i & \frac{\Gamma}{J}(\gamma\Gamma - 1) & 0 & -i \\ -i & 0 & \frac{\Gamma}{J}(\gamma\Gamma - 1) & -i \\ 0 & -i & i & 2\frac{\Gamma}{J}(2\gamma\Gamma - 1) \end{pmatrix}, \quad (3.47)$$

where the basis is ordered as $\{|ff\rangle, |fe\rangle, |ef\rangle, |ee\rangle\}$, which means that the first and last element act on the populations of the density matrix, and the second and the third act on the coherence.

Note that the dynamics generated by this Liouvillian depend on two dimensionless parameters Γ/J quantifying the strength of the Non-hermiticity and γJ quantifying the strength of the noise. Both of these are given in units of the coupling strength J , which gives the frequency scale, and thus $\tau = Jt$ is the dimensionless time. Note that dimensionally, the strength of the non-Hermiticity has units of frequency $[\Gamma] = T^{-1}$ while the strength of the noise has units of time $[\gamma] = T$. For notational convenience we define the quantities $A = \frac{\Gamma}{J}(\gamma\Gamma - 1)$ and $B = 2\frac{\Gamma}{J}(2\gamma\Gamma - 1)$, which describe, respectively, the evolution of the coherence $\tilde{\rho}_{ef}$ and of the population $\tilde{\rho}_{ee}$.

The master equation for the normalized DM reads

$$\begin{aligned} \partial_t \hat{\rho}_t = & -iJ[\hat{\sigma}_x, \hat{\rho}_t] - \Gamma(1 - \gamma\Gamma)\{\hat{\Pi}, \hat{\rho}_t\} + 2\gamma\Gamma^2\hat{\Pi}\hat{\rho}_t\hat{\Pi} \\ & + 2\Gamma(1 - 2\gamma\Gamma)\text{Tr}(\hat{\Pi}\hat{\rho}_t)\hat{\rho}_t, \end{aligned} \quad (3.48)$$

where we used the property of projector $\hat{\Pi}^2 = \hat{\Pi}$. This equation can be rewritten in dimensionless form as

$$\partial_\tau \hat{\rho} = -i[\hat{\sigma}_x, \hat{\rho}] + A\{\hat{\Pi}, \hat{\rho}\} + (B - 2A)\hat{\Pi}\hat{\rho}\hat{\Pi} - B\rho_{ee}\hat{\rho}, \quad (3.49)$$

where we used the identity $\text{Tr}(\hat{\Pi}\hat{\rho}) = \langle e|\hat{\rho}|e\rangle = \rho_{ee}$. The trace of the unnormalized Liouvillian is given by $\text{Tr}(\tilde{\mathcal{L}}_{\text{SDQ}}[\hat{\rho}]) = 2\Gamma(2\gamma\Gamma - 1)\rho_{ee} = JB\rho_{ee}$, which characterizes the non-linear term of the dynamics, and only depends on the population of the $|e\rangle$ state. In particular, when $2\gamma\Gamma - 1 < 0$ the dynamics inhibits the state $|e\rangle$ and when $2\gamma\Gamma - 1 > 0$ the dynamics favours the $|e\rangle$ state.

Therefore, the dynamics shows a change in behavior at $\gamma^* = \frac{1}{2\Gamma}$. Interestingly, at this point, the trace of the Liouvillian vanishes, and the dynamics is CPTP, generated by the standard GKSL master equation

$$\partial_t \hat{\rho}_t = -iJ[\hat{\sigma}_x, \hat{\rho}_t] + \Gamma \left(\hat{\Pi}\hat{\rho}_t\hat{\Pi} - \frac{1}{2}\{\hat{\Pi}^2, \hat{\rho}_t\} \right). \quad (3.50)$$

Furthermore, since $\rho_{ee} \geq 0$, the dynamics of the unnormalized Liouvillian $\tilde{\mathcal{L}}_{\text{SDQ}}[\bullet]$ is Trace Decreasing if $\gamma < \frac{1}{2\Gamma}$ and Trace Increasing if $\gamma > \frac{1}{2\Gamma}$. However, since Trace Increasing dynamics are sometimes deemed “unphysical” [13] we stress that with a proper shift of the Liouvillian $\tilde{\mathcal{L}}_{\text{SDQ}}[\bullet] \rightarrow \tilde{\mathcal{L}}_{\text{SDQ}}[\bullet] - 2a$ such as the one described in Sec. 3.2.4 the dynamics can always be made Trace-Decreasing (TD). In particular, the shift has to obey the condition

$$a \geq 2\Gamma(2\gamma\Gamma - 1)\rho_{ee}. \quad (3.51)$$

This is a state-dependent bound giving the minimum choice of the shift which ensures TD dynamics for every value of the population ρ_{ee} . Since $\rho_{ee} \leq 1$ we can find a state-

independent condition that a has to fulfill to give TD dynamics as

$$a \geq 2\Gamma(2\gamma\Gamma - 1). \quad (3.52)$$

Another interesting feature that we observe in the SDQ model is the effect of the noise on the *success rate*. The success rate is defined as the amount of trajectories with no quantum jumps, and comes directly from the continuous measurement + post-selection realization of NH dynamics, therefore, since we do not have a full theory of post-selection in stochastic non-Hermitian Hamiltonians, we will assume that the success rate is still given by the trace of the unnormalized state $SR_t = \text{Tr}(\tilde{\rho}_t)$, which represents the ratio of trajectories with no quantum jumps up to time t , divided by the total number of trajectories.

Under this assumption, we find that the trace of the unnormalized state evolves as

$$\partial_t \text{Tr}(\tilde{\rho}) = \dot{\rho}_{ee} + \dot{\rho}_{ff} = 2\Gamma(2\gamma\Gamma - 1)\rho_{ee} = B\rho_{ee}. \quad (3.53)$$

This can be written as an inhomogeneous differential equation in the success rate

$$\partial_t SR_t = B(SR - \rho_{ff}(t)), \quad (3.54)$$

whose solution reads

$$SR = e^{Bt}(c_0 - B \int_{-\infty}^t e^{-Bs} \rho_{ff}(s) ds). \quad (3.55)$$

When approaching the $\gamma\Gamma = 1/2$ line, B is negative and approaches zero, which makes the exponential decay slower since the exponent gets close to zero.

The previous analysis relies on the assumption that the success rate is simply the trace of the unnormalized state, a more in-depth theory would entail considering the full three level system $\{|g\rangle, |e\rangle, |f\rangle\}$ and doing post-selection of the quantum jumps in a master equation of the form

$$\partial_t \hat{\rho}_t = -i[\hat{H}_0, \hat{\rho}_t] + \Gamma(1 + \sqrt{2\gamma}\xi_t)\mathcal{D}_{|g\rangle\langle e|}[\hat{\rho}], \quad (3.56)$$

where $\mathcal{D}_{\hat{L}}[\bullet] = \hat{L} \bullet \hat{L}^\dagger - \frac{1}{2}\{\hat{L}^\dagger \hat{L}, \bullet\}$ is the standard **GKSL** dissipator. Doing post-selection in this setup has the added difficulty of the rate $\Gamma(1 + \sqrt{2\gamma}\xi_t)$ acquiring negative values at some times, therefore it is a non-Markovian master equation. Pure state unravelings of master equations were originally introduced by Diosi *et al.* [254] for the diffusive case, and extended to jump processes by Gambetta *et al.* [255]. However, their physical interpretation [256] has been contested by Wiseman and Gambetta [257].

A theory of post-selection for stochastic non-Hermitian Hamiltonians may be hindered by these interpretational issues. If this were the case, a possibility to overcome these interpretational difficulties is to study the “*no-Pump*” version, as studied in Sec. 3.4.3,

of this master equation, which is Markovian

$$\partial_t \hat{\rho}_t = -i[\hat{H}_0, \hat{\rho}_t] + \Gamma(1 + \sqrt{2\gamma}\zeta_t)\mathcal{D}_{|g\rangle\langle e|}[\hat{\rho}], \quad (3.57)$$

since the rate $\Gamma(1 + \sqrt{2\gamma}\zeta_t)$ is always positive. The main issue is that this would provide only a similar model to the full white noise, only for the small noise regime.

3.3.1 Evolution of the Purity

We will now study how the purity of the dynamics of the SDQ evolves in time. In particular, we are interested in studying how different states gain or lose purity. Any state of a qubit is characterized by its Bloch coordinates $\mathbf{r} = (x, y, z)$ which give the state as $\hat{\rho} = \frac{1}{2}(\hat{\mathbb{1}} + \mathbf{r} \cdot \hat{\boldsymbol{\sigma}})$ where $\hat{\boldsymbol{\sigma}} = (\hat{\sigma}_x, \hat{\sigma}_y, \hat{\sigma}_z)$ denotes the vector containing all the Pauli matrices. Substituting our model in the general expression for the evolution of the purity (3.25) and introducing spherical coordinates in the Bloch sphere, we find

$$\partial_t P_t = \Gamma r_t ((2\gamma\Gamma - 1)(r_t^2 - 1) \cos(\theta_t) - \gamma\Gamma r_t \sin^2(\theta_t)). \quad (3.58)$$

This is closely related to the decoherence time of the purity, in particular $\partial_t P_t|_{t=0} = \tau_P^{-1}$. Let us analyze the behavior of this equation, which is illustrated in Fig. 3.1. The first property that we observe is that, apart from the common factor Γ which just sets the scale of how strong the decoherence is, the expression for the evolution of the purity only depends on the product $\gamma\Gamma$, in particular it has no dependence on J . The second interesting property is that it only depends on r and θ but not on the azimuthal angle ϕ , which allows us to study a cross-section of the Bloch sphere, since we know that the evolution of the purity will be the same for all the other states with different ϕ .

We now check for consistency with deterministic NH dynamics, for $\gamma = 0$, the equation reduces to

$$\partial_t P_t = \Gamma r(1 - r^2) \cos(\theta_t), \quad (3.59)$$

which vanishes for $r = 1$, as expected for deterministic NH Hamiltonians, which is shown in white in the surface of the Bloch sphere in Fig. 3.1. Furthermore, due to the cosine function, it is positive when $\theta \in (-\frac{\pi}{2}, \frac{\pi}{2})$ and $r \in (0, 1)$, represented by blue in the north hemisphere in Fig. 3.1, and negative (red) in the southern hemisphere. This is consistent with what is known about the \mathcal{PT} broken phase of this model, there are two steady states if the dynamics, $|e\rangle$ and $|f\rangle$, with $|e\rangle$ and unstable point and $|f\rangle$ the attractor of the dynamics. Note that for $\theta = \pm\frac{\pi}{2}$ the rhs also vanishes due to the cosine function.

When $\gamma > 0$, both of the terms in the rhs are nonzero; however, the second one is always negative since $\gamma > 0$, $\Gamma > 0$, $r_t > 0$, $\sin^2(\theta) > 0$. When $0 < \gamma < \gamma^* = \frac{1}{2\Gamma}$, we see that some of the states in the northern Hemisphere have decreasing purity. This can be understood in the following way, if $\gamma < \gamma^*$ the term $2\gamma\Gamma - 1 < 0$ is still negative, which means that the previous argument still applies and it purifies states in the north pole, however, the

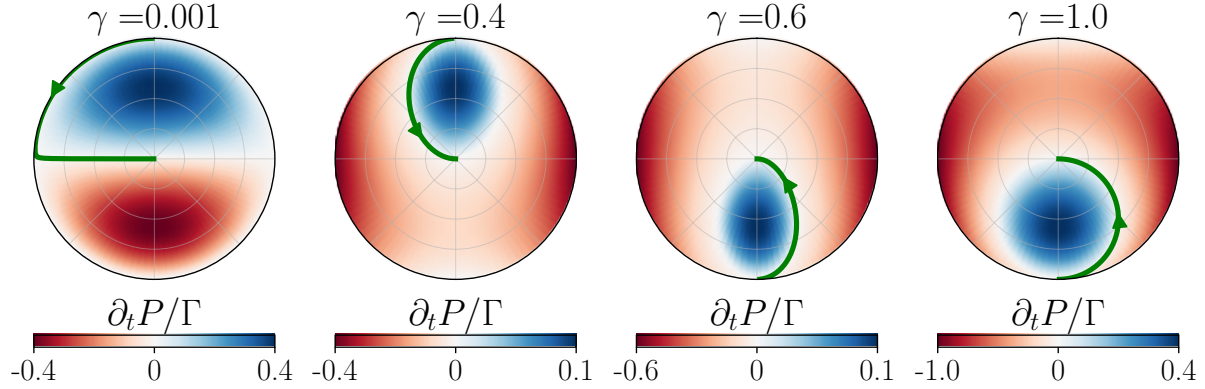


Figure 3.1. Purity evolution for different strengths of the noise as given by (3.58) in a cross-section of the Bloch sphere. Figure adapted from [2].

second term, always negative, now has a more relevant contribution and thus “shrinks” the purifying region with respect to the noiseless case.

Exactly at $\gamma = \gamma^*$, the first term completely vanishes and thus there are no purifying regions in the Bloch sphere, in particular, the equation for the evolution of the purity reduces to

$$\partial_t P_t = -\frac{\Gamma}{2} r^2 \sin^2(\theta), \quad (3.60)$$

which can only vanish at $r = 0$ or $\theta = 0, \pi$. This means that all the Bloch sphere loses purity, i.e., decoheres, except for the z axis, whose purity stays constant. We will come back to this point in the next section when we study the dynamics generated in the Bloch sphere.

When $\gamma > \gamma^*$, the first term changes sign and thus the purifying states move to the southern hemisphere. We see that as we increase γ , the region with purifying states grows in size.

3.3.2 Spectral and steady state Properties

A key part of the previous general analysis of the dynamics relied on the eigenvalues and eigenvectors of the Liouvillian. The Liouvillian reads

$$\tilde{\mathcal{L}} = J \begin{pmatrix} 0 & i & -i & 0 \\ i & A & 0 & -i \\ -i & 0 & A & i \\ 0 & -i & i & B \end{pmatrix}, \quad (3.61)$$

whose eigenvalues Λ are the solutions to the characteristic polynomial

$$(A - \Lambda)(\Lambda^3 - \Lambda^2(A + B) + \Lambda(4 + AB) - 2B) = 0. \quad (3.62)$$

This equation already tells us that $\Lambda = A$ is an eigenvalue. To compute the remaining eigenvalues, we define the cubic polynomial as

$$f(\Lambda) = \Lambda^3 - \Lambda^2(A + B) + \Lambda(4 + AB) - 2B.$$

We want to compute the roots of the polynomial. We start by shifting the variable, using $z = \Lambda - (A + B)/3$, which yields a *depressed* cubic, i.e., a cubic equation without the quadratic term, of the form

$$f(z) = z^3 + 3Cz + D = 0, \quad (3.63)$$

where we have introduced the constants

$$C = -\left(\frac{A+B}{3}\right)^2 + \frac{4+AB}{3}, \quad D = \frac{A+B}{3}(4 + AB) - 2B - 2\left(\frac{A+B}{3}\right)^3.$$

We then use Cardan's trick [258], also known as Vieta's substitution, that is, we set $z = U + \frac{a}{U}$, choosing a such that it exactly cancels the terms in U and $1/U$, i.e., $a = -C$. This leads to a quadratic equation in U^3 ,

$$(U^3)^2 + DU^3 - C^3 = 0, \quad (3.64)$$

with solutions

$$U_{m,\pm} = e^{mi\frac{2\pi}{3}} \left[-\frac{D}{2} \pm \sqrt{\left(\frac{D}{2}\right)^2 + C^3} \right]^{1/3},$$

where $m = (0, \pm 1)$. With this, we find the Liouvillian eigenvalues to be given by

$$\Lambda_{m,\pm} = J \left(U_{m,\pm} - \frac{C}{U_{m,\pm}} + \frac{A+B}{3} \right). \quad (3.65)$$

Note that we seem to have obtained six solutions from a cubic equation, which would be wrong. However, three pairs of solutions are the same. To show this, let $V = -\frac{D}{2} \pm \sqrt{\frac{D^2}{4} + C^3} \equiv U_{m,\pm}^3$ denote any nonzero root of the quadratic equation (3.64). If V is a root then $\frac{-C^3}{V}$ is also a root, since

$$V^2 + DV - C^3 = 0 \xrightarrow[V^2]{\times \frac{-C^3}{V^2}} -C^3 + D(-\frac{C^3}{V}) + (-\frac{C^3}{V})^2 = 0.$$

Therefore, if we change $+\rightarrow-$ in $\Lambda_{m,\pm}$ we exchange the terms $U_{m,\pm}$ with the term $-\frac{C}{U_{m,\pm}}$. This implies that it is enough to consider the eigenvalues $\Lambda_{m,+}$.

Therefore the spectrum of the Liouvillian reads

$$\{\lambda_0 \equiv \Lambda_{0,+}, \lambda_1 \equiv \Lambda_{1,+}, \lambda_2 \equiv \Lambda_{-1,+}, \lambda_3 = AJ\}. \quad (3.66)$$

Assuming that the Liouvillian is diagonalizable, i.e., we are out of any Liouvillian Exceptional Point [259], it can be written as (3.61),

$$\tilde{\mathcal{L}} = \sum_{\nu=0}^3 \lambda_\nu |B_\nu)(B_\nu|, \quad (3.67)$$

where we denote $|B_\nu)$ the eigenvectors of the vectorized Liouvillian, which are vectors on the double Hilbert space $|B_\nu) \in \mathcal{H} \otimes \mathcal{H}$, or equivalently linear operators over the original Hilbert space $\hat{B}_\nu \in \mathcal{L}(\mathcal{H})$.

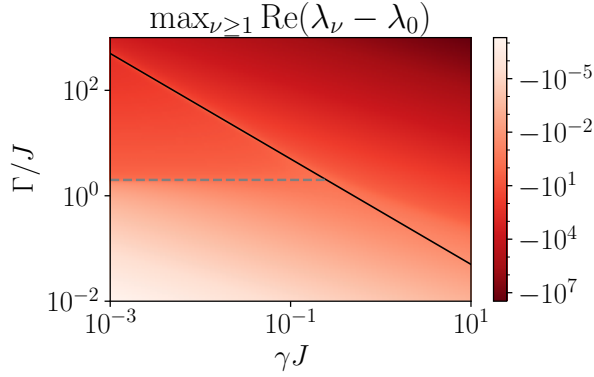


Figure 3.2. Maximum difference of the real part of $\lambda_\nu, \nu \geq 1$ with λ_0 . The difference is always negative for the displayed range of parameters. Therefore, λ_0 is always the eigenvalue with the largest real part. The transitions between the \mathcal{PT} u, \mathcal{PT} b, and NI phases are shown in the dashed and solid line for reference.

When $\gamma > 0, \Gamma > 0$ the eigenvalue with the largest real part is always λ_0 . This can be checked for a large range of parameters in Fig. 3.2 where the maximum difference $\max_{\nu \geq 1} \text{Re}(\lambda_\nu - \lambda_0)$ is always negative.

Figure 3.3 shows the position of the four eigenvalues in the complex plane for different values of the strength of the noise γ and the decay rate Γ . A first check is that always the eigenvalue with the largest real part is λ_0 as we have already argued. For weak decay rate (c1-4) the plot shows that the eigenvalues with the second largest real part are λ_1, λ_2 , which are complex conjugates. Lastly the eigenvalue with the smallest real part is λ_3 . In all of these, the imaginary part is close to $\text{Im}(\lambda_n) \approx 2$, much larger than the difference between real parts in (c1-3). This implies that in these regime the dynamics will show oscillations, which is a key property of the \mathcal{PT} symmetric phase. Note that we observe a similar positioning of the eigenvalues in (b3), and in (b1) and (b2) the pair λ_1, λ_2 are complex conjugates of each other, but they have the smallest real part. The reader should also note that (b3) is exactly in the line $\gamma = \gamma^*$ and thus the generator follows the

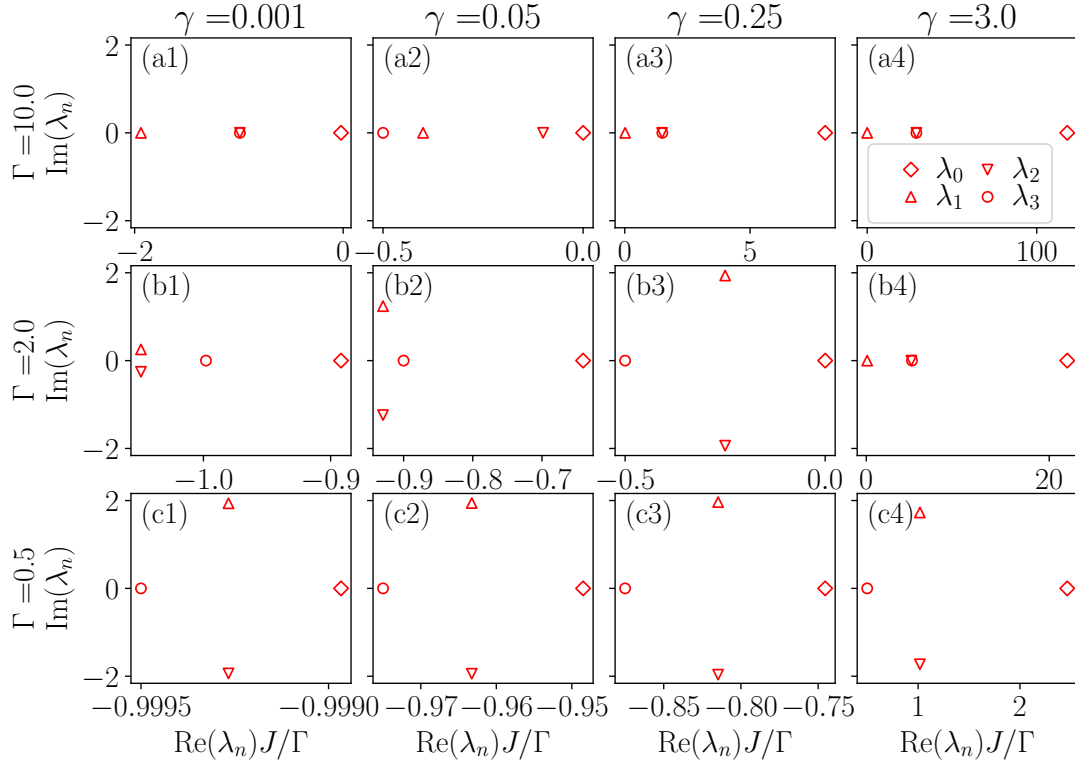


Figure 3.3. Spectrum of the SDQ Liouvillian for different locations in the phase diagram of the system. The parameters span the different phases: (a1) \mathcal{PT} broken, (c1-3) \mathcal{PT} unbroken, and (a3, a4, b4) Noise Induced; as well as the transitions between them: (b1,2) \mathcal{PT} breaking transition, (a2,b3) TD-TI transition and (c4) transition from mixed state to $|e\rangle$ state. Note that the x -axis has been rescaled by Γ/J .

standard GKSL master equation and has the eigenvalue with the largest real part equal to exactly zero. Note that this also happens in (a2) with the difference that in there the eigenvalues λ_1, λ_2 are not complex conjugates. In the cases (a1, 3, 4) and (b4) we see that the eigenvalues λ_2 and λ_3 are degenerate, and that λ_1 is the eigenvalue with the smallest real part.

We now investigate the two most relevant spectral properties of the SDQ Liouvillian which will determine the dynamics, namely the *dissipative gap* and the the maximum *oscillating frequency* $\max_\nu(\omega_\nu)$. These are shown in the phase diagrams of Fig. 3.4 (a) and (b) respectively. The dissipative gap is defined as

$$\Delta = \min_{\nu \geq 1} (\text{Re}(\lambda_0) - \text{Re}(\lambda_\nu)), \quad (3.68)$$

since, as we have already argued, λ_0 is the eigenvalue with the largest real part. This quantity encodes how fast the convergence to the steady state occurs, in particular the corrections to the steady state are suppressed by a factor $e^{-\Delta t}$, which implies a convergence to the steady state at times $t \sim \Delta^{-1}$. Unfortunately, to the best of our knowledge, there is

not a simple expression for the dissipative gap, and one has to resort to direct computation from the analytic expression of the eigenvalues (3.66).

Inspecting Fig. 3.4 (a) we observe the very wide range of values that this quantity can take, from 10^{-7} to 10^6 . The three different phases: \mathcal{PT} unbroken ($\mathcal{PT}u$), \mathcal{PT} broken ($\mathcal{PT}b$) and Noise Induced (NI) have very different behavior of this quantity. In the $\mathcal{PT}u$ phase the dissipative gap is very small, of $\mathcal{O}(10^{-7})$ to $\mathcal{O}(10^{-3})$, which implies a convergence to the steady state at very long times, and a small exponential decay on top of the oscillations observed in the $\mathcal{PT}u$ phase. As we will discuss in Sec.3.5, this residual exponential damping has been observed in the experimental setup, and a Stochastic Non-Hermitian Hamiltonian with white noise on the anti-hermitian part, i.e., the SDQ model here presented, can provide a quantitative explanation for this behavior.

The $\mathcal{PT}b$ phase has a larger dissipative gap, of $\mathcal{O}(1)$, which implies a faster convergence to the steady state than in the $\mathcal{PT}u$ phase. Interestingly, the dissipative gap stays relatively constant dep on the $\mathcal{PT}b$ phase. In the transition to the NI phase, at $\gamma = \gamma^*$, the dissipative gap diminishes, which means that the GKSL dynamics takes longer to reach the steady state. Lastly, in the NI phase, the dissipative gap is extremely large, and grows as we progressively go deeper in the NI phase, reaching values of $\mathcal{O}(10^6)$.

Figure 3.4 (b) shows the maximum value of the oscillating frequency. Recall that the oscillating frequency is defined as the imaginary part of the eigenvalues of the Liouvillian, defined as

$$\omega_\nu = \text{Im}(\lambda_\nu). \quad (3.69)$$

Since we know the exact expressions for the spectrum, we know that there can only be two eigenvalues with a non-zero oscillating frequency, i.e., λ_1, λ_2 , and they have opposing imaginary parts because they are complex conjugates of each other. Fig. 3.4 (b) shows that the $\mathcal{PT}u$ phase has a constant maximum oscillating frequency close to $\omega = 2$. This means that in this range of parameters the most important contribution is the oscillating frequency, and thus the dynamics shows the oscillations characteristic of the $\mathcal{PT}u$ phase of the noiseless model. These oscillations are attenuated by a very small oscillating gap, as discussed previously, which allows us to see the oscillations. This is not the situation in the $\mathcal{PT}b$ or NI phases, where the dissipative gap is larger and thus no oscillations will be seen, even if the eigenvalues of the Liouvillian have an imaginary component. Interestingly, in a small portion of the $\mathcal{PT}b$ and the NI phases the oscillating frequency does not vanish, this happens when $\gamma = \frac{1}{3\Gamma}$ and $\gamma = \frac{1}{\Gamma}$, which are respectively in the $\mathcal{PT}b$ and NI phases. This can be clearly seen in Fig. 3.4 (b) where the oscillating frequency is non-zero close to the dotted orange lines, representing the aforementioned power laws. Out of these power laws, the oscillating frequency of the Liouvillian eigenvalues vanishes. Interestingly, it also vanishes at the $\gamma = \gamma^*$ transition at large values of the decay rate $10 \lesssim \Gamma$, and does not vanish at small values $\Gamma \lesssim 10$, a difference clearly seen in Fig. 3.3 (b3) and (a2) which show a non-zero imaginary part, and a vanishing imaginary part, respectively. Lastly, the last boundary of the region with non-zero oscillating frequency happens at strong noises. Due to the double logarithmic scale, we can directly see that

this boundary is characterized by the power law $\gamma = 2J\Gamma^{-2}$. In the next section, we find this same power law.

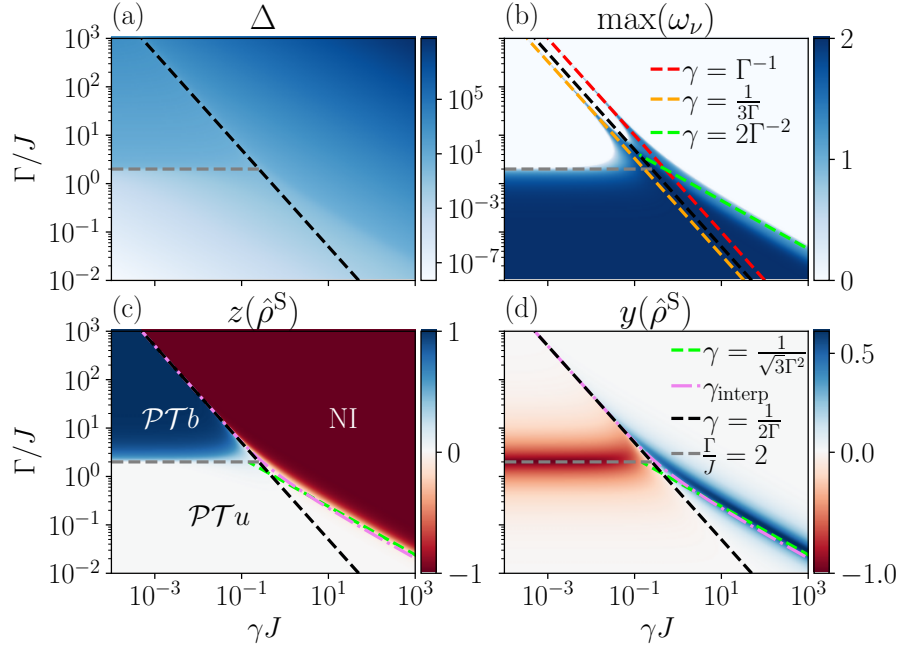


Figure 3.4. Spectral and steady-state phase diagrams: (a) dissipative gap Δ , (b) maximum imaginary part of the eigenvalues ω_ν , (c) z , and (d) y components of the Bloch vector for the stable steady state. The relevant parameters are the strength of the noise γ and the decay rate Γ . The transition to the noise-induced phase is at $\gamma^* = 1/(2\Gamma)$ (black). The transition from \mathcal{PT} broken to the \mathcal{PT} unbroken phase happens at $\Gamma/J = 2$ (gray dashed). In (b) the power laws $\gamma = 1/(3\Gamma)$ and $\gamma = 1/\Gamma$ are also shown (orange dotted). Figure adapted from [2].

Eigenvectors: Steady states

The steady state is described by the eigenvector $|B_0\rangle = (b_0^{(0)}, b_1^{(0)}, b_2^{(0)}, b_3^{(0)})^\top$ which is associated to the eigenvalue λ_0 . It can be computed from the system of equations

$$\begin{cases} +iJ(b_1^{(0)} - b_2^{(0)}) = \lambda_0 b_0^{(0)}, \\ +iJ(b_0^{(0)} - b_3^{(0)}) = (\lambda_0 - AJ)b_1^{(0)}, \\ -iJ(b_0^{(0)} - b_3^{(0)}) = (\lambda_0 - AJ)b_2^{(0)}, \\ -iJ(b_1^{(0)} - b_2^{(0)}) = (\lambda_0 - BJ)b_3^{(0)}. \end{cases} \quad (3.70)$$

Taking the ratio between the second and third equations, we find

$$b_1^{(0)} = -b_2^{(0)}. \quad (3.71)$$

Given that we know that for the relevant range of parameters $\lambda_0 > A$, and thus $\lambda_0 - A \neq 0$. From the first equation, we now find

$$b_1^{(0)} = -i \frac{\lambda_0}{2J} b_0^{(0)},$$

which, substituting in the second one, gives

$$b_3^{(0)} = b_0^{(0)} \left(1 + \frac{\lambda_0(\lambda_0 - AJ)}{2J^2} \right).$$

We now choose $b_0^{(0)}$ such that, for real λ_0 , the eigenvector has trace unity when written as a matrix

$$|B_0\rangle = \frac{1}{2 + \lambda_0 \frac{\lambda_0 - AJ}{2J^2}} \begin{pmatrix} 1 \\ -\frac{i}{2J}\lambda_0 \\ \frac{i}{2J}\lambda_0 \\ 1 + \lambda_0 \frac{\lambda_0 - AJ}{2J^2} \end{pmatrix}, \quad (3.72)$$

or equivalently in matrix form

$$\hat{B}_0 = \frac{1}{4J^2 + \lambda_0(\lambda_0 - AJ)} \begin{pmatrix} 2J^2 & -iJ\lambda_0 \\ +iJ\lambda_0 & 2J^2 + \lambda_0(\lambda_0 - AJ) \end{pmatrix} = \hat{\rho}^s. \quad (3.73)$$

We will characterize this steady state by its coordinates in the Bloch sphere. The z coordinate reads

$$z(\hat{\rho}^s) = -\frac{\lambda_0(\lambda_0 - AJ)}{4J^2 + \lambda_0(\lambda_0 - AJ)}, \quad (3.74)$$

characterizing the population imbalance in the state. This quantity is shown in Fig. 3.4 (c), where we see three different behaviors defining the $\mathcal{PT}u$, $\mathcal{PT}b$, and NI phases. The $\mathcal{PT}u$ phase has z coordinate equal to zero, this is because the steady state is close to the maximally mixed state. The convergence to this steady state is dictated by the dissipative gap Δ discussed previously, which implies that the convergence to the steady state happens at very long times. Therefore, the dynamics converges to the steady state with very lightly damped oscillations. For this reason, we name this phase \mathcal{PT} unbroken, for its similarity to the \mathcal{PT} unbroken phase of the noiseless model. The $\mathcal{PT}b$ phase shows a value of z close to unity. This means that the steady state is close to the $|f\rangle$ state. This phase has also been observed in the noiseless Dissipative Qubit, the decay rate is large compared to the hopping $\Gamma/J > 2$ which makes the population of the $|e\rangle$ state decay, and J is not able to counteract it, thus the stable steady state is $|f\rangle$. Lastly, we observe the NI phase, in which the z coordinate goes to $z \approx -1$. This means that for strong enough noise, in particular $\gamma > \gamma^*$, the steady state becomes $|e\rangle$, which was the state that originally had losses. This is a noise-induced transition [260] to stability, reminiscent of

the one discussed in the previous chapter [1]. Note that, interestingly, the transition from \mathcal{PT}_b to NI follows perfectly well the $\gamma = \gamma^*$ line (black solid), but the transition from \mathcal{PT}_u to NI at larger noise has some corrections and the transition happens for a slightly higher value of Γ than expected, also there are corrections to the power law $\gamma = \frac{1}{2\Gamma}$. The double logarithmic scale allows to see that the transition from the \mathcal{PT}_u phase to the NI phase happens at a different power law given by $\gamma = \frac{J}{\sqrt{3}\Gamma^2}$ (green dashed line), note the different proportionality constant to the boundary of the non-zero oscillating frequency. This implies that the region $\gamma > \gamma^*$, which we have so far referred to as NI, has a richer structure, showing a steady state with Bloch coordinate z very close to zero (also y is close to zero, so the state is close to the maximally mixed state) when $1/(2\Gamma) < \gamma < \frac{J}{\sqrt{3}\Gamma^2}$. We now provide a justification for this power law. We begin by taking the asymptotic expansion for strong noise of the eigenvalue with the largest real part, which reads

$$\lambda_0 \sim 4\gamma\Gamma^2 - 2\Gamma - \frac{2J^2}{3\gamma\Gamma^2} + \mathcal{O}(\gamma^{-2}). \quad (3.75)$$

Taking only the first order term and substituting in the expression for the z coordinate gives

$$z(\hat{\rho}^s) \sim \frac{-1}{1 + \frac{J^2}{\gamma\Gamma^2(3\gamma\Gamma^2 - \Gamma)}} \sim \frac{-1}{1 + \frac{J^2}{3\gamma^2\Gamma^4}}, \quad (3.76)$$

where in the last step we discarded terms of lower order in γ . Now we assume that $\gamma \gg 1$ so that $J^2/(3\gamma^2\Gamma^4) \ll 1$ and the expression admits the Taylor expansion

$$z(\hat{\rho}^s) \sim -1 + \frac{J^2}{3\gamma^2\Gamma^4} + \mathcal{O}(\gamma^{-3}). \quad (3.77)$$

We want to find the edge of the $z(\hat{\rho}^s) = 0$ region, which is equivalent to setting the previous expression to zero

$$\frac{J^2}{3\gamma_N^2\Gamma^4} = 1 \Rightarrow \gamma_N = \frac{J}{\sqrt{3}\Gamma^2}. \quad (3.78)$$

This expression agrees with the boundary observed in Fig. 3.4 (c). Note that there is a region that interpolates between the $\gamma^* = \frac{1}{2\Gamma}$ and the $\gamma_N = \frac{J}{\sqrt{3}\Gamma^2}$ power laws. This means that the transition to $z = -1$ close to $\gamma J = 0.25$ is slightly above the two power laws.

A function that approximately interpolates between the two power laws can be derived. In order to do this, we take the expansion of λ_0 (3.75) discarding terms of order $\mathcal{O}(\gamma^{-2})$. Substituting in the expression for the z coordinate yields

$$z(\hat{\rho}^s) \sim -1 + \frac{18\gamma^2\Gamma^4J^2}{3\gamma\Gamma^3(\gamma\Gamma(3\Gamma^2(2\gamma\Gamma - 1)(3\gamma\Gamma - 1) - J^2) + 3J^2) + 2J^4}, \quad (3.79)$$

which, when equated to zero, factorizes in the simple form

$$(3\gamma\Gamma^3(2\gamma\Gamma - 1) - J^2) \cdot (3\gamma\Gamma^3(3\gamma\Gamma - 1) - 2J^2) = 0, \quad (3.80)$$

which has four solutions

$$\gamma = \frac{\Gamma^3 \pm \sqrt{8\Gamma^4J^2 + \Gamma^6}}{6\Gamma^4}, \quad (3.81)$$

$$\gamma = \frac{3\Gamma^3 \pm \sqrt{3(8\Gamma^4J^2 + 3\Gamma^6)}}{12\Gamma^4}. \quad (3.82)$$

From all these solutions, the one that correctly reproduces the expected power law $\gamma = 1/(2\Gamma)$ at large Γ is

$$\gamma_{\text{interp}} = \frac{3\Gamma^3 + \sqrt{3(8\Gamma^4J^2 + 3\Gamma^6)}}{12\Gamma^4}, \quad (3.83)$$

and also reproduces the $\gamma = J/(\sqrt{3}\Gamma^2)$

This expression is shown in Fig. 3.4 (c,d) (violet dash-dotted line). We see that it correctly reproduces the large Γ behavior but slightly underestimates the transition⁵ to the NI phase from the $\mathcal{PT}\text{b}$ phase. Apart from the slight offset, the curve seems to correctly characterize the shape of the transition region from the $\mathcal{PT}\text{u}$ to the NI phases. Also note that it captures quite well the region where y starts to be large and positive (see Fig. 3.4 (d)).

Before continuing, let us discuss how to “move” in this phase diagram. When we change J at a fixed value of Γ and γ we will follow a diagonal parallel to the transition line $\gamma = \gamma^*$, in particular increasing J will take us down and to the right while decreasing J will take us to the left and up. Note that since it is parallel, we cannot go into the noise-induced phase by changing the hopping strength J . The only possibility to go in the NI phase by changing J is to start in the part of the $\mathcal{PT}\text{u}$ phase which has $\gamma > \gamma^*$ (the white zone over the black solid line), and since this transition no longer follows the same power law but the alternative one $\gamma = J\Gamma^{-2}$, it can be crossed by decreasing J . The other two possibilities to move in the phase diagram are to change the decay rate Γ at fixed J and γ , which moves vertically, or to change the noise strength γ at fixed Γ and J , which moves horizontally. Since changing the strength of the noise seems to be quite challenging, we think that changing the decay rate Γ is probably the most feasible way of observing the three phases.

The y component reads

$$y(\hat{\rho}^s) = \frac{2\lambda_0 J}{4J^2 + \lambda_0(\lambda_0 - AJ)}, \quad (3.84)$$

⁵We stress that here we use the notion of *transition* between phases as simply referring to going between different *regimes* with different steady state properties. A more careful study of the nature of the transitions is carried out in Sec. 3.3.4.

characterizing the imaginary part of the coherences in the $\hat{\sigma}_z$ basis. Note that since λ_0 is real, the coherence $\propto -i\lambda_0$ is purely imaginary and thus the x coordinate of the steady state vanishes. Figure 3.4 shows the y Bloch coordinate of the stable steady state as a function of the dimensionless noise strength γJ and the dimensionless decay rate Γ/J . We see that deep in the three phases, $\mathcal{PT}\text{u,b}$ and NI, the y coordinate of the stable steady state vanishes, meaning that the state is almost diagonal in the $\hat{\sigma}_z$ basis. However, in the transitions between the phases, the y coordinate is non-zero. Particularly, in the \mathcal{PT} breaking transition, the state gets close to the left side of the Bloch sphere with $y \approx -1$, i.e., the $|-y\rangle$ state, a feature already experimentally observed [80]. Note that the y value remains close to $y \approx -1$ for different values of the strength of the noise, not too close to the transition to the NI phase $\gamma = \gamma^*$. Close to the transition, the stable steady state has a small but non-zero coherence. The sign of this quantity sharply changes when we have $\gamma > \gamma^*$, and we observe that in the transition from $\mathcal{PT}\text{u}$ to NI, the state acquires a positive y component. However, this component is not as large as in the \mathcal{PT} breaking transition, only reaching $y \approx 0.5$. Interestingly, the region with largest y component is around the transition $\gamma = \Gamma^{-2}$, and closely follows that power law.

We now compute the remaining eigenstates. Consider first the case of λ_1 and λ_2 , let $m = 1, 2$, therefore the system of equations reads

$$\begin{cases} +i(b_1^{(m)} - b_2^{(m)}) = \lambda_m b_0^{(m)}, \\ +i(b_0^{(m)} - b_3^{(m)}) = (\lambda_m - A)b_1^{(m)}, \\ -i(b_0^{(m)} - b_3^{(m)}) = (\lambda_m - A)b_2^{(m)}, \\ -i(b_1^{(m)} - b_2^{(m)}) = (\lambda_m - B)b_3^{(m)}. \end{cases} \quad (3.85)$$

To compute the largest eigenvector, we assumed that $\lambda_0 \neq A$; this is not necessarily the case anymore. Summing the first and the last equations, we find

$$\lambda_m(b_0^{(m)} + b_3^{(m)}) = Bb_3^{(m)}, \quad (3.86)$$

from where we can find a relation between $b_0^{(m)}$ and $b_3^{(m)}$

$$b_3^{(m)} = \frac{\lambda_m}{B - \lambda_m} b_0^{(m)}, \quad (3.87)$$

where we have assumed that $\lambda_m < B$, a reasonable assumption for $\lambda_{1,2}$. Summing the second and third equation we find $(\lambda_m - A)(b_1^{(m)} + b_2^{(m)}) = 0$ which gives $b_1^{(m)} = -b_2^{(m)}$. Note that if $\lambda_m = A$, the condition is already fulfilled without the need for the components of the eigenvector to be of opposite sign. However, in the case $\lambda_m = A$, the argument that we use in the next paragraph for λ_3 applies, and we find that $|B_m\rangle = |B_3\rangle$. Under the condition $\lambda_m \neq A$ we thus find that

$$2ib_1^{(m)} = \lambda_m b_0^{(m)} \quad (3.88)$$

and thus

$$|B_m) = \frac{BJ - \lambda_m}{BJ} \begin{pmatrix} 1 \\ -i\frac{\lambda_m}{2J} \\ +i\frac{\lambda_m}{2J} \\ \frac{\lambda_m}{BJ - \lambda_m} \end{pmatrix}, \quad (3.89)$$

where this choice ensures that $|B_m)$ is traceful.

Lastly, consider the case of $\lambda_3 = A$, therefore the system of equations reads

$$\begin{cases} +i(b_1^{(3)} - b_2^{(3)}) = Ab_0^{(3)}, \\ +i(b_0^{(3)} - b_3^{(3)}) = 0, \\ -i(b_0^{(3)} - b_3^{(3)}) = 0, \\ -i(b_1^{(3)} - b_2^{(3)}) = (A - B)b_3^{(3)}. \end{cases} \quad (3.90)$$

From the second and third equations, we find $b_0^{(3)} = b_3^{(3)}$. Summing the first and last, we find

$$(2A - B)b_0^{(3)} = 0,$$

which implies that $b_0^{(3)} = 0$. Therefore, the only remaining part is $b_1^{(3)} = b_2^{(3)}$, which can be set to unity, and the eigenvector is simply

$$|B_3) = \begin{pmatrix} 0 \\ 1 \\ 1 \\ 0 \end{pmatrix}, \quad \hat{B}_3 = \begin{pmatrix} 0 & 1 \\ 1 & 0 \end{pmatrix} = \hat{\sigma}_x. \quad (3.91)$$

Therefore, this eigenmatrix only has off-diagonal elements and cannot be a physical density matrix by itself.

Liouvillian Exceptional Points of the SDQ

One of the most interesting features of non-Hermitian matrices is the appearance of Exceptional Points (EPs). These are interesting from many points of view, perhaps the most interesting one is that the system shows an enhanced sensitivity close to an exceptional point [59]. When these exceptional points happen in a Liouvillian generator, they are called *Liouvillian Exceptional Point* (LEP). In Sec. 3.2.6, we already introduced the concept of LEPs and studied their effect in the dynamics, particularly in the steady states and the approach to steady states. In here, we study the LEPs of the antidephasing Liouvillian of the SDQ. At an exceptional point, the eigenvalues and eigenvectors of the matrix coalesce, and typically, a real difference of eigenvalues becomes imaginary. For this reason, the maximum non-orthogonality of eigenstates, i.e., $\max_{\mu \neq \nu} |\langle \hat{B}_\mu, \hat{B}_\nu \rangle|^2$, showcases the appearance of a LEP. Figure 3.5 shows the behavior of this quantity along

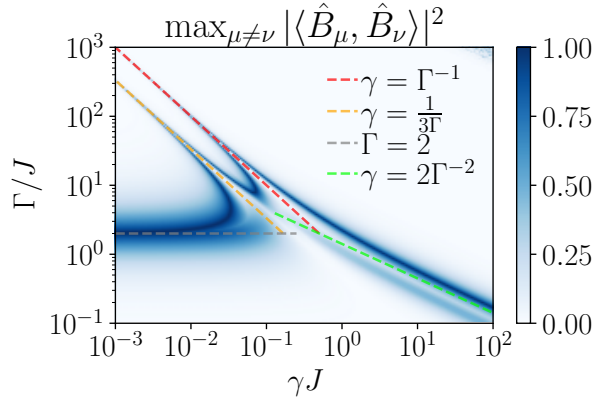


Figure 3.5. Maximum non-orthogonality between eigenstates of the antidephasing Liouvillian.

the phase diagram. For very small noise, there are five **LEPs**, one at $\Gamma/J = 2$, two around $\Gamma = 1/(3\gamma)$, one slightly below and one slightly above the power law, and other two at $\Gamma = 1/\gamma$, again, slightly below and above the power law. All of these **LEPs** are of order two, for non-zero strength of the noise, except for $\Gamma/J = 2$, which is of order four, as we shall see now.

As the strength of the noise is increased, the LEP at $\Gamma/J = 2$ shifts to a higher value of the decay rate, and eventually converges with the one at $\Gamma = \frac{1}{3\gamma} - \epsilon$ at a strength of the noise $\gamma J \approx 0.03$. After this there are 3 LEP's, the LEP at $\Gamma = \frac{1}{3\gamma} + \epsilon$ and the one at $\Gamma = \gamma^{-1} - \epsilon$ converge at $\gamma J \approx 0.1$. After this, there is only a single LEP. Furthermore, this LEP now occurs at a different power law $\gamma \sim 2\Gamma^{-2}$. Note that this boundary exactly agrees with the boundary describing the region having a non-zero oscillating frequency in Fig. 3.4 (b). This is not a coincidence since around an exceptional point, the eigenvalues change behavior; i.e., if the difference between eigenvalues is real below the EP, it becomes imaginary above and vice versa. Therefore, Fig. 3.4 (b) makes sure that there is a spectral degeneracy at the LEP, and Fig. 3.5 indicates coalescence of the eigenstates.

Figure 3.6 (left) shows the second maximum of the non-orthogonality between eigenvectors. We see that the second maximum is only close to 1 around $\Gamma/J = 2$, and it is close to zero otherwise, except on a power law $\gamma \sim \Gamma^{-2}$, also present in Fig. 3.5, where it is close to 0.5. Lastly, Fig. 3.6 (right) shows the third maximum value of the non-orthogonality, which is only non-zero close to $\Gamma/J = 2$, and furthermore it is much narrower than the second maximum around this point. This analysis indicates that the LEP's at $\gamma = \frac{1}{3\Gamma} \pm \epsilon$, and $\gamma = \frac{1}{\Gamma} \pm \epsilon$ are of order 2, with only two eigenvectors coalescing, but the LEP at $\Gamma/J = 2$ is of order 4 with 4 eigenvectors coalescing.

Figure 3.7 shows the maximum and second maximum value of the non-orthogonality as a function of the inverse dimensionless decay rate J/Γ . A similar quantity $|\langle +|-\rangle|$, where $|\pm\rangle$ are the eigenstates of the DQ, was measured experimentally in [80] and surprisingly, the data shows qualitatively similar behavior to the second maximum value of the overlap

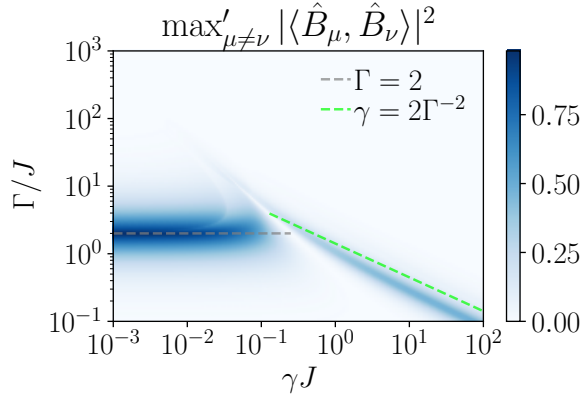


Figure 3.6. Second maximum (left) and third maximum (right) of the non-orthogonality between eigenstates of the antidephasing Liouvillian.

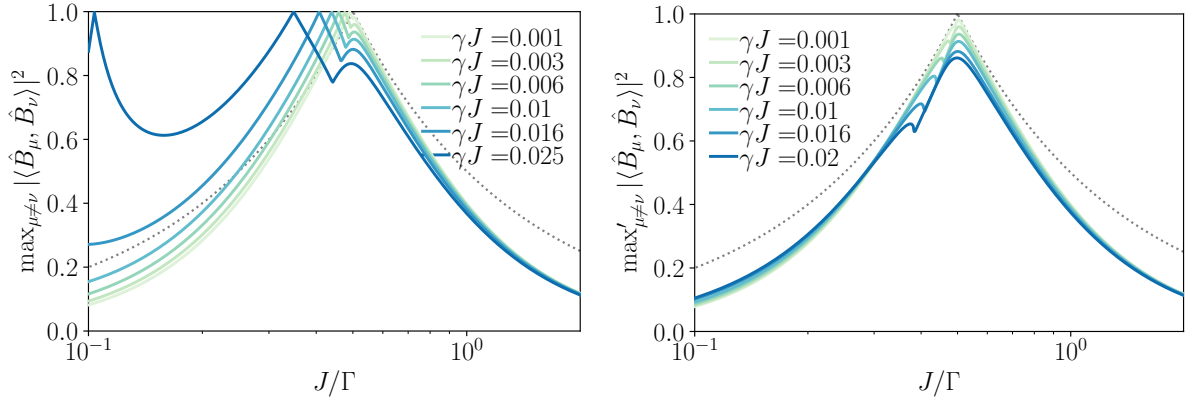


Figure 3.7. Maximum (left) and second maximum (right) value of the non-orthogonality as a function of the inverse decay rate J/Γ around the LEP $\Gamma/J = 2$. The dotted curve represents $\min(\frac{\Gamma}{2J}, \frac{2J}{\Gamma})$.

between eigenstates of the antidephasing Liouvillian, in particular a similar dip to the one seen in Fig. 3.7 (right) below $J/\Gamma = 1/2$, was observed in the data.

3.3.3 Bloch sphere dynamics

The dynamics generated by the antidephasing master equation can be written for the three coordinates of the Bloch sphere x, y, z . Introducing the Bloch decomposition of the density matrix $\hat{\rho} = \frac{1}{2}(\hat{1} + \mathbf{r} \cdot \hat{\sigma})$ and using the (anti)commutation properties of the Pauli

matrices $\{\hat{\sigma}_i, \hat{\sigma}_j\} = 2\delta_{ij}\hat{\mathbb{1}}$, $[\hat{\sigma}_i, \hat{\sigma}_j] = 2i\epsilon_{ijk}\hat{\sigma}_k$ we find

$$\begin{aligned}\dot{\rho} &= J(y\hat{\sigma}_z - z\hat{\sigma}_y) - (\Gamma - \gamma\Gamma^2)(\hat{\rho} - \frac{1}{2}\hat{\sigma}_z - \frac{1}{2}z\hat{\mathbb{1}}) + \gamma\Gamma^2(1-z)\frac{\hat{\mathbb{1}} - \hat{\sigma}_z}{2} \\ &\quad + (\Gamma - 2\gamma\Gamma^2)(1-z)\hat{\rho}\end{aligned}\quad (3.92)$$

$$\begin{aligned}&= J(y\hat{\sigma}_z - z\hat{\sigma}_y) - \left(\gamma\Gamma^2\frac{x}{2}\Gamma(1-2\gamma\Gamma)\frac{x}{2}z\right)\hat{\sigma}_x \\ &\quad - \left(\gamma\Gamma^2\frac{y}{2} + \Gamma(1-2\gamma\Gamma)\frac{y}{2}z\right)\hat{\sigma}_y + \left(\frac{\Gamma}{2}(1-2\gamma\Gamma) - \frac{z}{2}(2\gamma\Gamma^2 + z\Gamma(1-2\gamma\Gamma))\right)\hat{\sigma}_z.\end{aligned}\quad (3.93)$$

Note that the only nonlinearity comes from the second line of the first equation, and that the terms in the identity vanish since the nonlinear antidephasing dynamics is TP. Using the fact that the Pauli matrices and the identity $\{\hat{\mathbb{1}}, \hat{\sigma}\}$ form a basis of the Hilbert space of operators, the operator equation can be written as a system of coupled nonlinear differential equations for the Bloch coordinates as

$$\begin{cases} \dot{x} = -(\gamma\Gamma^2 + z\Gamma(1-2\gamma\Gamma))x, \\ \dot{y} = -2Jz - (\gamma\Gamma^2 + z\Gamma(1-2\gamma\Gamma))y, \\ \dot{z} = 2Jy - \Gamma(1-2\gamma\Gamma)(z^2 - 1). \end{cases}\quad (3.94)$$

We see that the equation for the coordinate x is linear in x ; this means that choosing $x = 0$ ensures that the x coordinate does not evolve and lets us simplify our analysis to a cross-section of the Bloch sphere, with just the y, z plane. This is equivalent to the observation made before that $\hat{\rho}^s = \hat{B}_0$ had purely imaginary coherences, and thus vanishing x coordinate. The equation for the y coordinate involves a term in J coupling it to the z coordinate, a term $-\gamma\Gamma^2y$ describing a decay of the y coordinate and a nonlinear term $-z\Gamma(1-2\gamma\Gamma)y$ which is negative if $\gamma < \gamma^*$ and $z > 0$ and positive if $\gamma > \gamma^*$ and $z < 0$. This nonlinear term describes a decay or a growth of y which depends on the z value. Lastly, the equation of motion for z has a linear term in J coupling it to the equation for y and a term proportional to $z^2 - 1$, which has a negative coefficient if $\gamma < \gamma^*$ and a positive coefficient if $\gamma > \gamma^*$.

The dynamics generated by this system is illustrated in Fig. 3.8 where the streamlines of the vector field are shown for different values of the non-hermiticity and the strength of the noise. Furthermore, the analytically computed stable steady state is indicated with a red diamond.

When the strength of the noise is very weak (cf. Figs. 3.8 (a1,b1,c1)), we observe a behavior close to the behavior of the Dissipative qubit. When the strength of the NH drive is small (c1), the dissipative qubit is in the $\mathcal{PT}\text{u}$ phase, and thus we see that the dynamics generate oscillations. From the previous analysis, we know that these oscillations can be seen because in the $\mathcal{PT}\text{u}$ phase, the maximum oscillating frequency is non-zero, while the dissipative gap is very small. Unlike the noiseless system, these oscillations are not centered around the center of the Bloch sphere but are slightly shifted towards the left, i.e., a negative value of y . From the phase diagram analysis, we predicted this behavior by observing that Fig. 3.4 (d) is not exactly zero if we are in the proximity of the \mathcal{PT} breaking transition. Exactly at \mathcal{PT} -braking transition (b1), the dynamics shows orbits similar to the ones before, but the center of the orbits has shifted towards the left-most

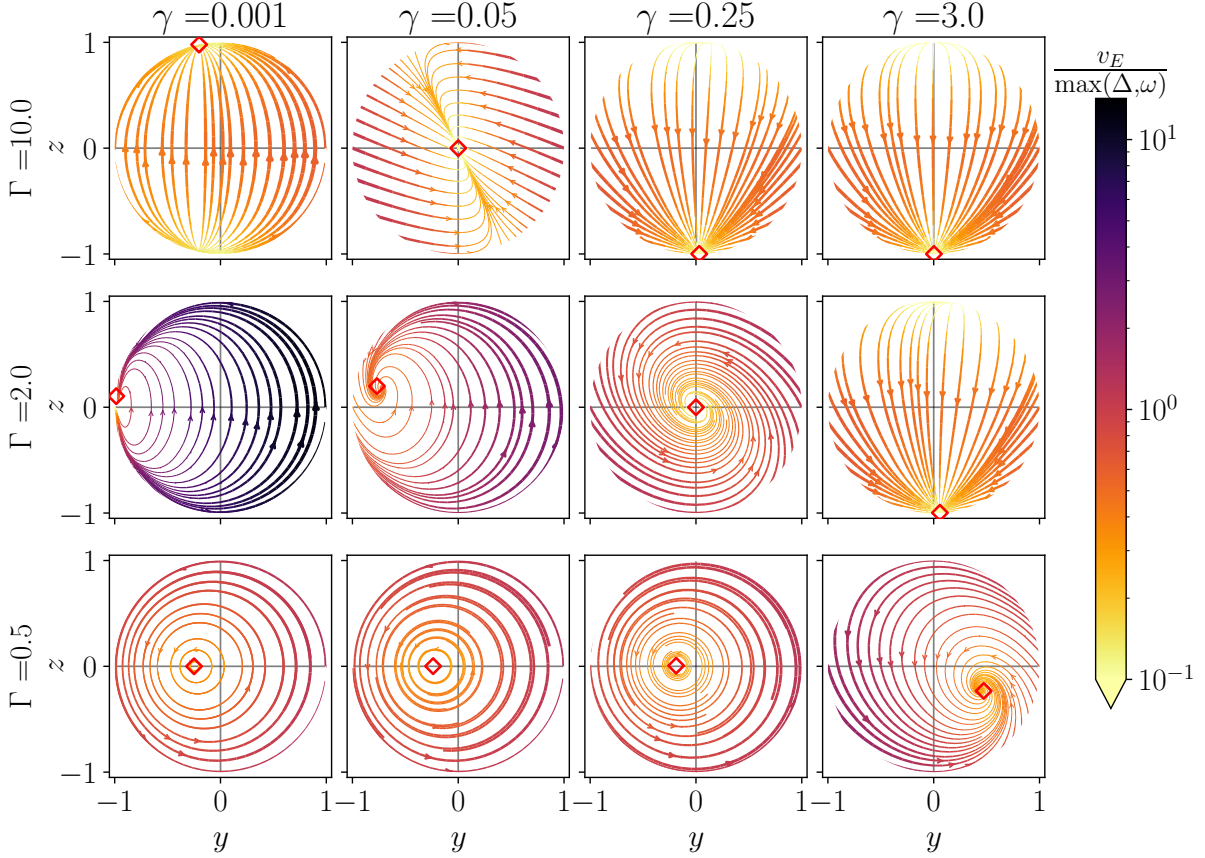


Figure 3.8. Streamlines of the vector fields in the cross-section of the Bloch sphere with $x = 0$. The parameters span the different phases: (a1) \mathcal{PT} broken, (c1-3) \mathcal{PT} unbroken, and (a3, a4, b4) Noise Induced; as well as the transitions between them: (b1,2) \mathcal{PT} breaking transition, (a2,b3) TD-TI transition and (c4) transition from mixed state to $|e\rangle$ state. The analytical steady state (3.72) is shown as the red diamond. The color and linewidth represent the Euclidean speed (3.95), divided by the maximum of the two main frequency units: the dissipative gap Δ and the maximum imaginary part of the eigenvalues $\omega = \max_{\nu}(\text{Im}(\lambda_{\nu}))$.

part of the Bloch sphere with $y \approx -1$, as expected from Fig. 3.4 (d). Lastly, when the strength of the decay rate is strong (a1), we see a convergence to a state very close to the $|f\rangle$ state. This is well-known to be the \mathcal{PT} broken phase of the model, where the non-Hermiticity completely kills all the population of the $|e\rangle$ state and thus the steady state is the $|f\rangle$ state. Interestingly, here there is a small but non-zero y component which moves the steady state slightly to the left, i.e., a small but negative y .

Now we consider a slightly stronger noise (cf. Figs. 3.8 (a2,b2,c2)). The dynamics for weak non-Hermiticity (c2) is quite similar to the one seen before (c1) with one difference. In here, it is more apparent that the oscillations are damped. This happens because the dissipative gap is larger than it was in (c1). This convergence to the steady state was also present in (c1), but since the convergence happened at extremely long times, the

trajectories looked as if they were closed. At the \mathcal{PT} -breaking transition of the noiseless model, we observe an oscillatory convergence to the steady state, which is now close to the west of the Bloch sphere with a small z component. Figure (a2) shows the behavior exactly at the transition from \mathcal{PT} broken to the Noise Induced (NI) phase, i.e., exactly at $\gamma = \gamma^*$. At this transition point, the dynamics is CPTP and the antidephasing master equation reduces to the standard GKSL master equation. Interestingly, the steady state is the maximally mixed state in the center of the Bloch sphere. This happens because exactly at the transition point the dynamics is generated by a Lindbladian (3.50) which obeys the property

$$\mathcal{L}[\hat{1}] = -iJ[\hat{\sigma}_x, \hat{1}] - \Gamma[\hat{\Pi}, [\hat{\Pi}, \hat{1}]] = 0,$$

which implies that the maximally mixed state, or infinite temperature Gibbs state $\hat{\rho} = \hat{1}/N$, is the steady state of the dynamics. The convergence happens in an interesting way, from Fig. 3.3 (a2), we know that the oscillating frequency is zero, but from the previous discussion on the purity, we know that at the $\gamma = \gamma^*$ transition, the purity remains constant at first order in the z axis. For this reason, the dynamics is perpendicular to the z axis, giving a state with the same purity, which is related to the radius on the Bloch sphere. Interestingly, the convergence to the maximally mixed state happens through a tilted axis.

Considering a stronger noise $\gamma = 0.25$ we find that for a small decay rate $\Gamma = 0.5$ Fig. 3.8 (c3) the behavior is qualitatively similar to Fig. 3.8 (c1) and Fig. 3.8 (c2), with a larger dissipative gap and thus faster damping on the oscillations. When $\Gamma = 2$ we are exactly at both the transitions, \mathcal{PT} breaking and $\gamma = \gamma^*$. Since the master equation reduces to **GKSL**, we converge to the maximally mixed state in the center of the Bloch sphere. This convergence happens reasonably fast with $\Delta \approx 0.25$, but this convergence is slow enough to see the oscillatory convergence, which happens because Fig. 3.3 (b3) has a non-zero oscillating frequency. Again, as in (a2), note that the streamlines are perpendicular to the z axis, since we know that at the transition $\gamma = \gamma^*$ all the Bloch sphere decreases purity, except for the z axis, which stays with constant purity. When the decay rate is large $\Gamma = 10$, we are in the NI phase, and we see a convergence to the $|e\rangle$ state. Note that now there is a small but non-zero positive component of y since we are over the transition line $\gamma > \gamma^*$. The reader should also note the difference in the trajectories converging to the stable steady state in this phase and in the \mathcal{PT} b phase, which had trajectories following the surface of the sphere, and then trajectories closely resembling an ellipse inside of the sphere. In the NI phase, this convergence does not follow ellipses and instead seems to happen more abruptly.

Considering a large noise $\gamma = 3$ and a small decay rate $\Gamma = 0.5$ the system is in the transition from the \mathcal{PT} u to the NI phase, which we know from the steady state analysis that happens with a positive value of the y coordinate (cf. Fig. 3.4 (d)). Furthermore, in this case, the convergence to the steady state is also oscillatory since the maximum oscillating frequency is non-zero (cf. Fig. 3.4 (b)). For large values of the decay rate $\Gamma = 2, 10$ we are in the NI phase, and we observe a convergence to the $|e\rangle$ state as expected.

The last piece of information contained in Fig. 3.8 is the speed of the trajectories, which is represented in the color and in the width of the streamlines. We simply took the Euclidean speed

$$v_E := \sqrt{(\dot{y})^2 + (\dot{z})^2}. \quad (3.95)$$

The spectral analysis of the dynamics indicated that there are two main quantities responsible for the speed at which the dynamics happen: the dissipative gap and the oscillating frequency. Here, to compare the speed throughout the whole phase diagram of parameters, we take the speed and divide it by the maximum of the two quantities: the dissipative gap and the maximum oscillating frequency. Interestingly, almost all the speed of the dynamics is well understood in terms of one of the two components, because the dynamics is around $v_E / \max(\Delta, \omega) \sim 1$. However, there is one speed that is not well explained by any of these quantities. Figure 3.8 (b1), exactly at the \mathcal{PT} breaking transition, has a speed that is one order of magnitude larger than any of these two quantities. Therefore, the speed of the dynamics at the \mathcal{PT} breaking transition remains to be explained; it is probably related to the difference in convergence to the steady state. We think that the cause for this is the structure of the eigenvalues in Fig. 3.3 (b1), which has the conjugate eigenvalues as the ones with the smallest real part. Maybe in that case λ_3 is not relevant to the dynamics and the relevant dissipative gap has to be defined as the difference with the real part of the complex conjugate eigenvalues.

Polar coordinates: Nullclines

The equations for the Bloch coordinates can be transformed to spherical coordinates simply by using the transformation between the coordinates

$$x = r \sin \theta \cos \phi, \quad y = r \sin \theta \sin \phi, \quad z = r \cos \theta,$$

and the chain rule, we can obtain the following system of equations

$$\begin{cases} \dot{r} = \Gamma ((2\gamma\Gamma - 1)(r^2 - 1) \cos \theta - \gamma\Gamma r \sin^2 \theta), \\ \dot{\theta} = -\frac{\Gamma \sin \theta}{r} (1 - 2\gamma\Gamma + \gamma\Gamma r \cos \theta) - 2J \sin \phi, \\ \dot{\phi} = -2J \cos \phi \cot \theta. \end{cases} \quad (3.96)$$

Note that the equation of motion for r is very similar to the equation for the derivative of the purity (3.58). This is because the purity is related to the radius by $P_t = (1 + r_t^2)/2$ and thus its derivative is $\dot{P}_t = r_t \dot{r}_t$. In a similar way to the x, y, z case, starting with $\phi = \pi/2$ ensures that the ϕ coordinate does not evolve, and thus we can effectively reduce the system of equations to

$$\begin{cases} \dot{r} = \Gamma ((2\gamma\Gamma - 1)(r^2 - 1) \cos \theta - \gamma\Gamma r \sin^2 \theta), \\ \dot{\theta} = -\frac{\Gamma \sin \theta}{r} (1 - 2\gamma\Gamma + \gamma\Gamma r \cos \theta) - 2J. \end{cases} \quad (3.97)$$

The analysis of the steady states previously done from the spectral properties of the Liouvillian can also be made from the equations of motion of the Bloch coordinates. In the study of nonlinear dynamics [156] the *nullclines* of a system of equations $\dot{\mathbf{x}} = \mathbf{f}(\mathbf{x})$ are defined as the curves where the derivative of each of the coordinates vanishes, i.e., for the coordinate x_j the nullcline is the curve \mathbf{x}^{N_j} which makes the equation vanish $f_j(\mathbf{x}^{N_j}) = 0$. The steady states of the system then live in the intersections of the nullclines.

Radial nullclines: State purification

The nullcline for the radial coordinate can be found as

$$r_{\theta}^{N_r} = \frac{\gamma\Gamma \sin^2 \theta \mp \sqrt{4(1-2\gamma\Gamma)^2 \cos^2 \theta + \gamma^2\Gamma^2 \sin^4 \theta}}{(4\gamma\Gamma - 2) \cos \theta}. \quad (3.98)$$

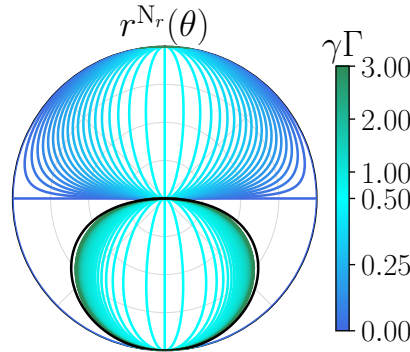


Figure 3.9. Nullclines of the radial coordinate.

Note that this equation only depends on the dimensionless product $\gamma\Gamma$; in particular, there is no dependence on J . Furthermore, this equation characterizes the white region in Fig. 3.1, i.e., the region with vanishing derivative of the purity, which separates the regions that purify from the regions whose purity decreases. Figure 3.9 shows the radial nullclines for different values of $\gamma\Gamma$. For $\gamma = 0$, we see that (3.98) reduces to unity. Therefore, the surface of the Bloch sphere does not lose purity, i.e., the radius states constant, and pure states remain pure, as is well-known to happen for a deterministic NH Hamiltonian. However, by inspecting the differential equation

$$\dot{r} = -\Gamma(r^2 - 1) \cos \theta,$$

we see that there is another way of making this function vanish and that is choosing $\theta = \pm\pi/2$. This extra line is shown in Fig. 3.9, and corresponds to the dynamics being exactly perpendicular to the y axis and thus keeping r constant at first order in time.

Considering $0 < \gamma\Gamma < 1/2$, we see that the nullclines progressively shrink from covering half of the Bloch sphere (dark blue) to a narrow area around the upper half of the z axis (cyan). Exactly at the transition $\gamma\Gamma = 1/2$, we see that (3.98) is ill-defined, so resorting

to the original equation of motion, we find

$$\dot{r} = -\gamma\Gamma^2 r \sin^2 \theta,$$

which vanishes for $r = 0$ or for $\theta = 0, \pi$. This gives the nullcline to be exactly the z axis. From the previous dynamical analysis, we know that exactly at this transition, the dynamics is [CPTP](#), the maximally mixed state is a steady state, and the dynamics is perpendicular to the z axis, thus keeping the r coordinate constant. When $\gamma\Gamma > 1/2$, the nullclines shift to the southern hemisphere of the Bloch ball (cyan to green lines). This was known from the previous analysis of the derivative of the purity.

By checking (3.98), we see that we have two nullclines corresponding to the two possible values of \mp . The most important nullcline is the one with $-$, since it is the one that generates most of the curves in Fig. 3.9. However, the nullcline with $+$ contributes to the southern hemisphere of the circle at $\gamma\Gamma = 0$, to the north pole for $\gamma\Gamma > 1/2$, and to the south pole for $\gamma\Gamma < 1/2$. These two points have each an unstable steady state, because no matter if the stable steady state is $|f\rangle$ in the $\mathcal{PT}\text{b}$ phase, if the dynamics start with $|\psi_0\rangle = |e\rangle$ there will not be any way of reaching $|f\rangle$. However, the moment that $|\psi_0\rangle$ has even the smallest contribution of $|f\rangle$, the dynamics will take us there.

If we take the limit $\gamma\Gamma \rightarrow \infty$ we find the nullcline

$$r_\theta^{\text{Nr}} = \frac{1 - \cos(2\theta) - 2\sqrt{16\cos^2\theta + \sin^4\theta}}{8\cos\theta}, \quad (3.99)$$

which is also shown in Fig. 3.9 (black solid line). We see that the convergence happens quickly with $\gamma\Gamma = 3$ being very close to the limiting curve.

The radial nullclines enclose the area of the cross-section of the Bloch sphere with states that purify. We can compute this area as

$$A_p = \frac{1}{2} \int_0^\pi r_\theta^2 d\theta, \quad (3.100)$$

where r_θ is given by eq. (3.98). This can be understood in the following way: the area of a section with angle θ of a circle with radius r is $\frac{\theta}{2\pi}\pi r^2$. Summing many small intervals $d\theta$ of a changing radius r_θ gives the previous formula.

The integral does not admit a closed form, and we have to resort to numerical integration. The results are shown in Fig. 3.10 (left), which shows the portion of the area of the Bloch sphere's cross section that purifies. When $\gamma\Gamma = 0$ exactly half of the Bloch sphere purifies, but this area quickly shrinks, and when $\gamma\Gamma = 1/2$ the dynamics is given by the [GKSL](#) master equation, and the portion of purifying states completely vanishes. For stronger noise, the portion of the Bloch sphere that purifies grows, until it saturates at a value of

$$A_p \rightarrow 0.3095\pi,$$

when $\gamma\Gamma \rightarrow \infty$. Which means that in the infinitely strong noise limit, around 31% of the Bloch sphere purifies. Even if the integral does not admit a closed form, Figure 3.10

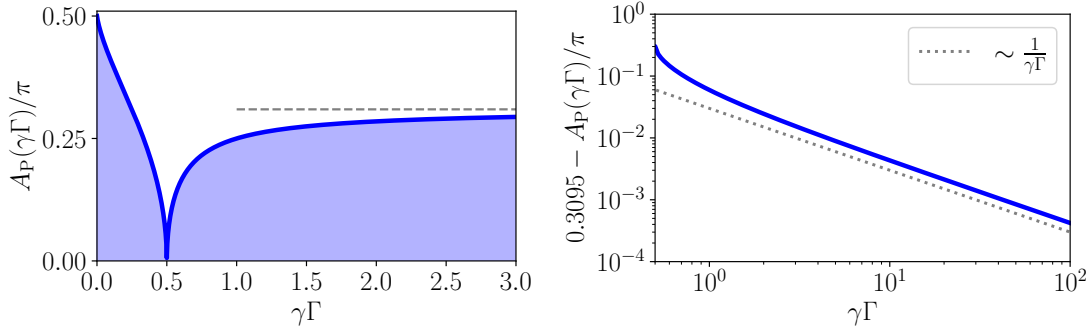


Figure 3.10. Area of the purifying region of the Bloch sphere (left) in units of the area of the cross section of the Bloch sphere π as a function of the dimensionless product $\gamma\Gamma$ (blue solid line). The numerical limiting value 0.3095 is also shown (gray dashed line). Difference between the limiting value and the area of the Bloch sphere (right) in a log-log scale. The power law $\sim 1/(\gamma\Gamma)$ is also shown (gray dotted line).

(right) shows that the convergence to the steady state value happens with a power law $\frac{1}{\gamma\Gamma}$.

Angular nullclines

In a similar way, we can compute the nullcline associated with the angular coordinate. The expression simply reads

$$r_\theta^{N_\theta} = \frac{\Gamma(2\gamma\Gamma - 1) \sin \theta}{2J + \gamma\Gamma^2 \cos \theta \sin \theta}. \quad (3.101)$$

Note that this equation does depend on J , and so do the steady states of the system. Figure 3.11 shows the angular nullclines for different values of J (blue) as well as the radial nullcline (red). The radial nullclines represent physically where the vector field in the Bloch sphere is perpendicular to the radial unit vector, and the angular nullclines where the vector field is perpendicular to the angular unit vector. The steady states are thus in the intersection of both. Note that interestingly, the nullclines do not only cross at one point, but in two. One of these is the stable steady state or attractor of the dynamics, and the other is the maximally mixed state. However, this is an unstable fixed point; if the dynamics starts slightly away from the maximally mixed state, it will go to the stable steady state predicted by the spectral analysis. This stable steady state is also shown in the figure (blue circles), which we see agrees perfectly with one of the crossing points of the nullclines. When $\gamma\Gamma < 1/2$, therefore the unstable steady state is close to the $|e\rangle$ state for small J , which corresponds to the radial nullcline (3.98) in the + branch.

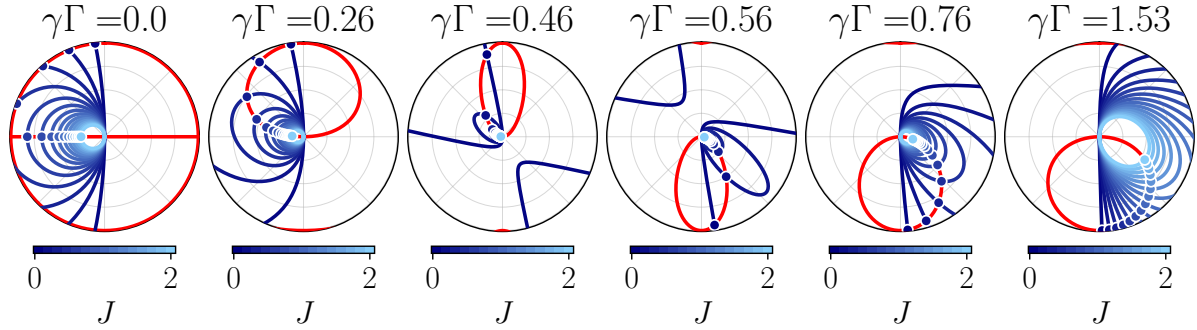


Figure 3.11. Angular nullclines (blue) for different values of J (colorbar) with the radial nullclines (red) for increasing values of $\gamma\Gamma$ (left to right). Different stable steady states computed from the eigenvector analysis of the system (blue dots). The smallest value of J considered is $J = 0.05$, and there are 15 evenly spaced values up to $J = 2$.

Let us now investigate the behavior of the angular nullclines. When $\gamma\Gamma = 0$, we see that the angular nullcline reduces to

$$r_\theta^{N_\theta} = -\frac{\Gamma}{2J} \sin \theta,$$

which describes a circle of radius $\Gamma/(4J)$ centered at $r = \Gamma/(4J)$, $\theta = -\pi/2$. We see that this gives an arc of a big circle which does not close inside the Bloch ball when $\Gamma/J > 2$, i.e., the \mathcal{PT} broken phase, and a circle completely inside the Bloch sphere when $\Gamma/J < 2$, i.e., the \mathcal{PT} unbroken phase. The steady state analysis, and the crossing points of the nullclines give the steady states to be on the surface of the Bloch ball when $\Gamma/J > 2$ and on the $\theta = -\pi/2$ line with $r = \Gamma/(2J)$ when $\Gamma/J < 2$. In the noiseless case, it is known that at the EP the steady state is the $| -y \rangle$ state, which was even observed experimentally [80]. This does not happen abruptly, but as Γ decreases, we see that the steady state gets closer and closer to the equator. In the \mathcal{PT} u phase, the steady state from this analysis is inside the Bloch sphere, but it takes an infinite time to reach the steady state due to the oscillations coming from the \mathcal{PT} symmetry not showing any decay.

When $\gamma\Gamma$ is small (see $\gamma\Gamma = 0, 0.26$) the radial coordinate is negative⁶ meaning that the angular nullclines live of the western hemisphere of the Bloch ball. We see that the nullclines deform slightly, taking a shape similar to an ellipse, and tilting slightly upwards. One could think that the angular nullclines always live of the western hemisphere when $\gamma\Gamma < 1/2$ but this is not the case since $\sin \theta \cos \theta$ is negative for $\theta \in (\pi/2, \pi)$, therefore if $2J - \gamma\Gamma^2/2 < 0$ is negative we can have the behavior shown for $\gamma\Gamma = 0.46$ where the angular nullcline has a component in the $\theta \in [\pi/2, \pi]$ quadrant. When we cross the $\gamma\Gamma > 1/2$, the shape of the nullclines is similar but flips, with most of the angular nullclines being in the $\theta \in [\pi/2, \pi]$ quadrant. The ellipses of the nullclines widen progressively as

⁶Due to the spherical coordinates chosen $\theta \in [0, \pi]$ so a negative radial coordinate corresponds to an angle outside that range

we increase $\gamma\Gamma$ until they cover most of the eastern hemisphere of the Bloch ball for large $\gamma\Gamma$. This change in behavior of the angular nullclines is what gives the change in the y coordinate of the steady state around the $\gamma = \gamma^*$ transition.

3.3.4 Transitions between the different phases of the model

The formal definition of a *phase transition* requires a thermodynamic limit; for this reason, although the SDQ phase diagram (cf. Fig. 3.4) shows different *phases* with markedly characteristic behavior, and changing the parameters, we can observe *transitions between the phases*, we will not refer to these as phase transitions in the strict sense. Even if we avoid using such terminology in here, we study the transitions more in depth, in particular, in a similar spirit to the study of phase transitions, we ask whether the transitions in the SDQ model are *continuous* or *discontinuous*. We will take as the “*order parameter*” describing the different phases $z(\hat{\rho}^S)$ which has three different values for the different phases $z = 0$ ($\mathcal{PT}u$), $z = +1$ ($\mathcal{PT}b$) and $z = -1$ (NI).

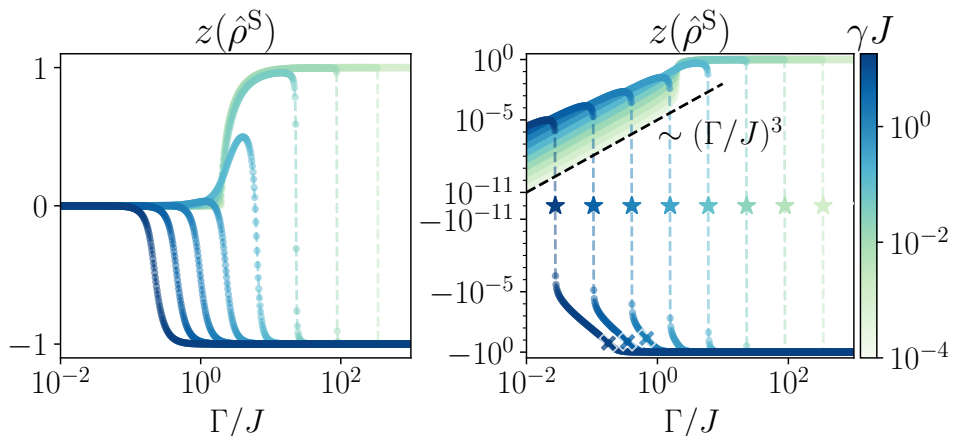


Figure 3.12. z coordinate in the Bloch sphere as a function of the dimensionless decay rate Γ/J for different values of the strength of the noise γJ . The plots are shown on a linear-log scale (left) and a symmetric logarithmic⁷-log (right). The plot shows the power law at small decay rate $(\Gamma/J)^3$ (dashed black)

Figure 3.12 shows the z coordinate of the steady state as a function of the dimensionless decay rate Γ/J in two scales: linear-log (left) and symmetric logarithmic⁷-log (right) for different values of the strength of the noise γJ . Let us analyze first the lin-log case: For very weak noise the z coordinate goes from zero to $+1$, when the noise is increased we observe a transition to the $z = -1$ after the $z = +1$ phase, this transition may look discontinuous, but it is not since as we consider more and more points closer to the transition the transition becomes smooth. A case in which the transition is not continuous will be discussed in the forthcoming section. As we increase the strength

⁷The symmetric log scale uses a linear threshold, in this case $\epsilon_{\text{thres}} = 10^{-11}$ such that the scale between $[-\epsilon_{\text{thres}}, \epsilon_{\text{thres}}]$ is linear.

of the noise, the transition becomes smoother, and we stop seeing the $\mathcal{PT}\text{b}$ phase with $z = +1$, transitioning directly to the NI phase with $z = -1$.

The plot with the symmetric logarithmic scale (right) provides further insight into this behavior. We see that for finite noise γJ the z coordinate starts growing with a power law $z \sim \Gamma^3/J^3$, whose prefactor increases with γJ , then at $\Gamma/J = 2$ the small noise curves go towards $z = +1$ in the $\mathcal{PT}\text{b}$ phase, and then transition to the NI phase $z = -1$ at $\Gamma = 1/(2\gamma)$ (stars). For the stronger noise cases, particularly when $1/(2\gamma J) < 2$, we see that the system transitions directly to the NI phase, however it does so by first growing with the power law $z \sim \Gamma^3$, then exactly at $\Gamma = 1/(2\gamma)$, because we see the perfect agreement with the star symbols, the z coordinate vanishes, and for bigger values of the decay rate the z coordinate is negative. Note that for very strong noise γJ there is a second power law implying that z first becomes slightly negative, and then decreases as⁸ $z \sim -(\Gamma/J)^\alpha$ until it reaches $z = -1$. Note that a value close to $z = -1$ takes a while to be reached, with the second power-law in the phase diagram Fig. 3.4 (c) $\Gamma = \sqrt{J}/\sqrt{\sqrt{3}\gamma}$ (crosses) characterizing the onset of the $z \approx -1$ region.

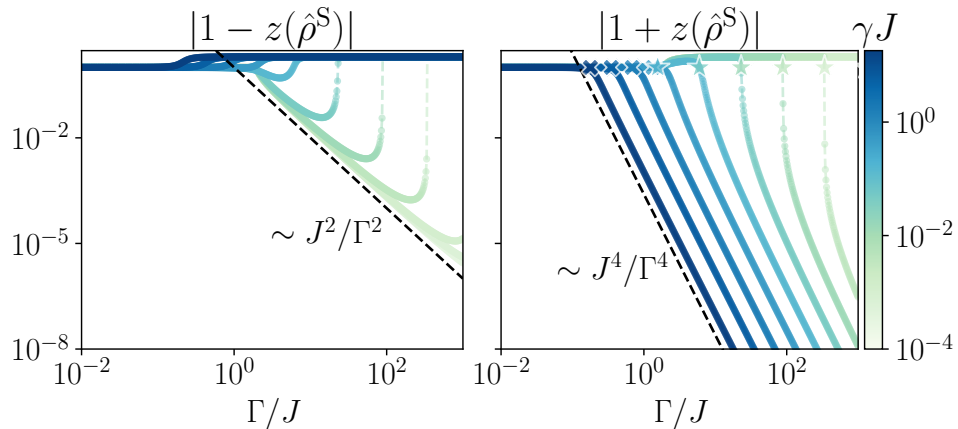


Figure 3.13. Convergence to the $\mathcal{PT}\text{b}$ $z = +1$ (left) and NI $z = -1$ (right) phases as a function of the dimensionless decay rate Γ/J for different strengths of the noise γJ .

Figure 3.13 shows the rate at which the system converges to the $\mathcal{PT}\text{b}$ (left) and NI (right) phases. In particular we look at the difference $d_{z,+1} = |z(\hat{\rho}^S) - 1|$ for the $\mathcal{PT}\text{b}$ phase (left), which shows that for the noise strengths γJ for which the $\mathcal{PT}\text{b}$ is present, i.e., $\gamma J < 1/4$, the z coordinate approaches 1 with an inverse quadratic power law $d_{z,+1} \sim J^2\Gamma^{-2}$, before slowing down and transitioning to the NI phase at $\Gamma = 1/(2\gamma)$.

To study the convergence to the NI phase (right), we introduce the difference $d_{z,-1} = |z(\hat{\rho}^S) + 1|$. For the weak noises in which a $\mathcal{PT}\text{b}$ phase is present, the difference fastly decreases at the NI transition $\Gamma = 1/(2\gamma)$ (stars) and acquires a power law behavior at bigger values of the decay rate. As we consider stronger noise the system directly transitions to the inverse quartic power law $d_{z,-1} \sim J^4\Gamma^{-4}$ and the starting value of the

⁸This power seems to be in the range $\alpha \in [4, 5]$ with $\alpha \approx 4.5$ from numerical inspection.

transition agrees with $\Gamma = \sqrt{J}/\sqrt{\sqrt{3}\gamma}$ (crosses). The inverse quartic power law implies a much faster convergence to the limiting value when we enter the NI phase.

A non-analytic transition

For all the values of the parameters studied before the transitions between the different phases seem to be smooth, by this we mean that considering values of Γ/J very close to the transition point between any two phases, e.g. the order parameter z goes continuously between $z = +1$ and $z = -1$ when transitioning from the $\mathcal{PT}\text{b}$ to NI phases. There is one exception to this behavior, which appears in the case $J = 0$, which does not follow naturally from the previous discussion since J was taken as the unit of frequency.

In this case, the antidephasing Liouvillian reads

$$\tilde{\mathcal{L}}_{\text{SDQ}} = \begin{pmatrix} 0 & 0 & 0 & 0 \\ 0 & \Gamma(\gamma\Gamma - 1) & 0 & 0 \\ 0 & 0 & \Gamma(\gamma\Gamma - 1) & 0 \\ 0 & 0 & 0 & 2\Gamma(2\gamma\Gamma - 1) \end{pmatrix}. \quad (3.102)$$

This matrix is trivially diagonal with eigenvalues

$$\{0, \Gamma(\gamma\Gamma - 1), \Gamma(\gamma\Gamma - 1), 2\Gamma(2\gamma\Gamma - 1)\},$$

and eigenvectors given by the vectors of the canonical basis

$$\left\{ \begin{pmatrix} 1 \\ 0 \\ 0 \\ 0 \end{pmatrix}, \begin{pmatrix} 0 \\ 1 \\ 0 \\ 0 \end{pmatrix}, \begin{pmatrix} 0 \\ 0 \\ 1 \\ 0 \end{pmatrix}, \begin{pmatrix} 0 \\ 0 \\ 0 \\ 1 \end{pmatrix} \right\}.$$

Note that when understood as vectorized density matrices the first and fourth eigenvectors are physical, representing the states $|f\rangle\langle f|$ and $|e\rangle\langle e|$, respectively, while the second and third eigenvector are unphysical since they have zero trace and are not positive semidefinite.

The parameter Γ may be taken as the unit of frequency, and the only free parameter is the dimensionless product $\gamma\Gamma$. The structure of eigenvalues is as follows:

- When $\gamma\Gamma \in (0, \frac{1}{3})$, the zero eigenvalue is the largest one, the pair of eigenvalues $\gamma\Gamma - 1$ is the second largest and $2(2\gamma\Gamma - 1)$ is the smallest eigenvalue.
- When $\gamma\Gamma = \frac{1}{3}$ the zero eigenvalue is the largest one but the pair $\gamma\Gamma - 1$ and $2(2\gamma\Gamma - 1)$ are triply degenerate.
- When $\gamma\Gamma \in (\frac{1}{3}, \frac{1}{2})$ the largest eigenvalue is zero, $2(2\gamma\Gamma - 1)$ is the second largest and the pair $\gamma\Gamma - 1$ are the smallest eigenvalues.

- When $\gamma\Gamma = \frac{1}{2}$ at this point, the zero eigenvalue and $2(2\gamma\Gamma - 1)$ are degenerate and are the largest eigenvalues, while the pair $\gamma\Gamma - 1$ are the smallest eigenvalues.
- When $\gamma\Gamma \in (\frac{1}{2}, 1)$ $2(2\gamma\Gamma - 1)$ is the largest eigenvalue, zero is the second largest, and $\gamma\Gamma - 1$ are the smallest.
- When $\gamma\Gamma = 1$, the smallest eigenvalue is triply degenerate between the zero eigenvalue and $\gamma\Gamma - 1$.
- When $\gamma\Gamma > 1$ $2(2\gamma\Gamma - 1)$ is the largest eigenvalue, the doubly degenerate eigenvalue $\gamma\Gamma - 1$ is the second largest, and zero is the smallest eigenvalue.

Note then that when $\gamma\Gamma = 1/2$ we have a non-analytic transition, if $\gamma\Gamma < 1/2$, no matter how close the parameter is to $1/2$, the stable steady state is $|f\rangle$ and if $\gamma\Gamma > 1/2$ the stable steady state is $|e\rangle$. The transition is discontinuous in the order parameter $z(\hat{\rho}^s)$, which abruptly changes from $+1$ to -1 , and no perturbation theory in $\gamma\Gamma - 1/2$ can explain this behavior. The dissipative gap close to this point $\gamma\Gamma \in (\frac{1}{3}, 1)$ is $\Delta = |2(2\gamma\Gamma - 1)|$ and it characterizes the time-scale $t \sim \Delta^{-1}$ at which the stable steady state is reached. At $\gamma\Gamma = 1/2$ we have a dissipative gap closing, another feature reminiscent of phase transitions, and any linear combination of the two eigenvectors, i.e., any diagonal matrix of the form $\rho_{ee}|e\rangle\langle e| + \rho_{ff}|f\rangle\langle f|$, is a steady state. In particular the maximally mixed state $\rho_{ee} = \rho_{ff} = 1/2$ is a steady state, a feature which we already expected since at $\gamma\Gamma = 1/2$ the dynamics is known to obey a standard GKSL master equation with the property $\mathcal{L}[\hat{1}] = 0$. Both of the phases shown at $J = 0$ give exactly the \mathcal{PT} b and NI behavior⁹, although the transition becomes smooth at finite values of J , and a small gap is opened at the avoided crossing of the eigenvalues. Note that the points in which the eigenvalues become degenerate are *not* exceptional points because the eigenvectors do not coalesce; instead, they are the so-called *diabolical points* [261] due to their double cone or *diabolo* shaped energy surface.

Interestingly, the two parameters at which the second largest eigenvalue becomes triply degenerate give the power laws $\gamma = 1/(3\Gamma)$ and $\gamma = 1/\Gamma$ at which the oscillating frequency is non-zero outside of the \mathcal{PT} u phase. Note that this observation does not explain the non-zero oscillating frequency since all the eigenvalues are purely real. However, a perturbative expansion in small J may explain how the eigenvalues acquire an imaginary part here.

Lastly, the $J = 0$ limit provides an analytical explanation for the presence of the noise-induced phase when $\gamma\Gamma > 1/2$, in which the stable steady state is $|e\rangle$. In this case, the eigenvalues and especially the eigenvectors are much simpler to analyze and understand. In the next section, we provide an alternative physical explanation for the preference of the $|e\rangle$ state over the $|f\rangle$ state.

⁹No \mathcal{PT} u phase can ever be observed for $J = 0$ since the hopping J can be understood as “counteracting” the decay rate and giving an overall real spectrum.

A physical reason for the Noise-Induced Phase for $J = 0$

When the hopping between the two levels vanishes, $J = 0$, the stochastic Hamiltonian describing the evolution of the system

$$d\hat{H} = -i\Gamma\hat{\Pi}dt - i\Gamma\sqrt{2\gamma}\hat{\Pi}dW_t = \begin{pmatrix} 0 & 0 \\ 0 & -i\Gamma(dt + \sqrt{2\gamma}dW_t) \end{pmatrix}, \quad (3.103)$$

where, as before, we have introduced the projector over the $|e\rangle$ state $\hat{\Pi} = |e\rangle\langle e|$. The evolution of this system is generated by the propagator $e^{-id\hat{H}}$ and we can study the effect it has on components over $|e\rangle$ and $|f\rangle$, i.e., we evolve for a small period of time and look at what is the effect that this has over the two components of the state. For the component over $|e\rangle$ this is

$$\langle e|\psi_{dt}\rangle = \frac{\langle e|e^{-id\hat{H}}|\psi_0\rangle}{\|e^{-id\hat{H}}|\psi_0\rangle\|} = \frac{\langle e|\psi_0\rangle (1 - \sqrt{2\gamma}\Gamma dW_t + \Gamma(\gamma\Gamma - 1)dt)}{\sqrt{1 + 2\Gamma|\langle\psi_0|e\rangle|^2((2\gamma\Gamma - 1)dt - \sqrt{2\gamma}dW_t)}}, \quad (3.104)$$

and for the component over $|f\rangle$

$$\langle f|\psi_{dt}\rangle = \frac{\langle f|e^{-id\hat{H}}|\psi_0\rangle}{\|e^{-id\hat{H}}|\psi_0\rangle\|} = \frac{\langle f|\psi_0\rangle}{\sqrt{1 + 2\Gamma|\langle\psi_0|e\rangle|^2((2\gamma\Gamma - 1)dt - \sqrt{2\gamma}dW_t)}}. \quad (3.105)$$

Note that the renormalization affects equally both of the coordinates, even if it depends only on the projection of $|\psi_0\rangle$ over the $|e\rangle$ state. A simple way to compare these two quantities and determine where the dynamics prefers to go is to look at the ratio between the two, assuming that the initial state is pure and that it has support over both states $\langle e|\psi_0\rangle, \langle f|\psi_0\rangle \neq 0$ the ratio reads

$$\frac{\langle e|\psi_{dt}\rangle}{\langle f|\psi_{dt}\rangle} = \frac{\langle e|\psi_0\rangle}{\langle f|\psi_0\rangle} (1 - \sqrt{2\gamma}\Gamma dW_t + \Gamma(\gamma\Gamma - 1)dt). \quad (3.106)$$

In the noiseless limit $\gamma \rightarrow 0$, we recover the standard non-Hermitian results

$$\frac{\langle e|\psi_{dt}\rangle}{\langle f|\psi_{dt}\rangle} = \frac{\langle e|\psi_0\rangle}{\langle f|\psi_0\rangle} (1 - \Gamma dt), \quad (3.107)$$

which means that we are inhibiting the component over the state $|e\rangle$ due to losses, and thus the stable steady state (or attractor) of the dynamics is $|f\rangle$. This is still the case when the noise γ is weak, since the term $\gamma\Gamma - 1 < 0$. When we consider the strong noise limit $\gamma \gg 1$, the $|e\rangle$ state is favored

$$\frac{\langle e|\psi_{dt}\rangle}{\langle f|\psi_{dt}\rangle} \approx \frac{\langle e|\psi_0\rangle}{\langle f|\psi_0\rangle} (1 + \gamma\Gamma^2 dt - \sqrt{2\gamma}\Gamma dW_t), \quad (3.108)$$

and thus, the attractor of the dynamics becomes the $|e\rangle$ state; however, note that the stochastic term dW_t gives subleading $\mathcal{O}(\sqrt{\gamma})$ terms, which do not need to be positive or negative. On average $\mathbb{E}\left(\frac{\langle e|\psi_{dt}\rangle}{\langle f|\psi_{dt}\rangle}\right)$ this transition $\langle e|\psi_{dt}\rangle = \langle f|\psi_{dt}\rangle$ happens exactly when

$$\gamma\Gamma - 1 = 0, \Rightarrow \gamma = \frac{1}{\Gamma}. \quad (3.109)$$

Interestingly, even if we know that $\gamma = \Gamma^{-1}$ is in the NI phase, it is not the transition point, which we know is at $\gamma = 1/(2\Gamma)$. This means that when $\gamma > \Gamma^{-1}$, the dynamics prefers to go to the $|e\rangle$ state because the projection over the $|e\rangle$ state grows in time faster than the projection over the $|f\rangle$ state. But in the range $1/(2\Gamma) < \gamma < 1/\Gamma$ this is not the case, the dynamics still inhibits the $|e\rangle$ state compared to the $|f\rangle$ state.

The reason for the NI phase in this range does not come from the numerator but rather the denominator of the expression, and thus cannot be seen by studying the ratio between the two components. One problem in understanding the behavior of these expressions is the presence in the denominator of a stochastic contribution. This problem is similar in spirit to the problem found when imposing trace preservation, which led us to take the average over the noise first, and only then impose TP or renormalize. If we do so here, we find

$$\frac{\mathbb{E}(\langle e|e^{-id\hat{H}}|\psi_0\rangle)}{\mathbb{E}(\|e^{-id\hat{H}}|\psi_0\rangle\|)} = \frac{\langle e|\psi_0\rangle (1 + \Gamma(\gamma\Gamma - 1)dt)}{\sqrt{1 + 2\Gamma|\langle\psi_0|e\rangle|^2((2\gamma\Gamma - 1)dt)}}, \quad (3.110)$$

$$\frac{\mathbb{E}(\langle f|e^{-id\hat{H}}|\psi_0\rangle)}{\mathbb{E}(\|e^{-id\hat{H}}|\psi_0\rangle\|)} = \frac{\langle f|\psi_0\rangle}{\sqrt{1 + 2\Gamma|\langle\psi_0|e\rangle|^2((2\gamma\Gamma - 1)dt)}}. \quad (3.111)$$

Inspecting these functions, we see that $\langle e|\psi_0\rangle$ sets the starting values and the functional shape, but neither of these is the most important for us. What is the most important feature is whether the functions grow or decrease at first order in time (since anyhow dt is infinitesimal). We see a change as a function of the parameters, when $\gamma\Gamma < 1/2$ the projection over $|f\rangle$ grows and the projection over $|e\rangle$ decreases, when, $1/2 < \gamma\Gamma < 1$ both of the projections decrease. It thus remains to be understood how the NI phase appears in this regime of parameters; it may be through the effect of the hopping J , which we did not take into account here.

3.3.5 Dynamics of the SDQ

Up to now, we have analyzed the spectral and eigenvector properties of the antidephasing Liouvillian and the steady-state features of the equations of motion for the Bloch coordinates. Our main focus so far has been finding the steady states of the dynamics happening for different parameters. We found that apart from the $\mathcal{PT}u$ and \mathcal{PT} b-like phases, there exists a third phase which is Noise Induced, and which has the unstable state $|e\rangle$ as a steady state. Now we will turn to fully simulating the dynamics of the SDQ. To this end we will numerically solve the nonlinear system of equations for the Bloch

coordinates y_t , z_t . We will use a standard Runge-Kutta algorithm of 4th order, which we compare to other approaches at the end of this section.

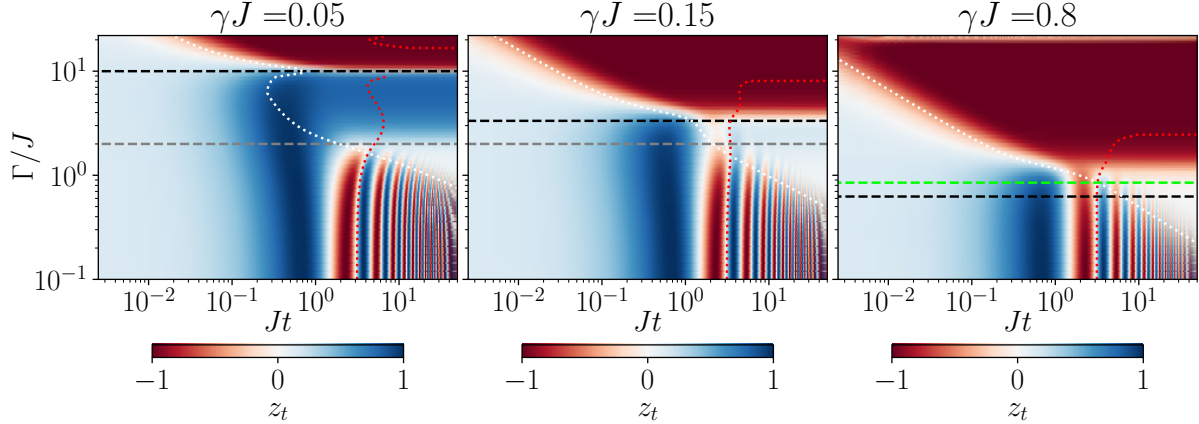


Figure 3.14. Dynamics of the Bloch z coordinate for different values of the decay rate Γ/J and the noise strength $\gamma J = 0.05, 0.15, 0.8$ (left to right). The initial value of the coordinates are $x_0 = 0$, $y_0 = \sin \theta_0$, $z_0 = \cos \theta_0$ and $\theta_0 = 1.43$. The time axis has a time-step of $J\Delta t = 0.0025$. The dotted lines correspond to the inverse dissipative gap $t \sim \Delta^{-1}$ (white dotted) and to the period of oscillation $T = 2\pi/\omega$ (red dotted). We also show the values of Γ/J at which the transitions between the different phases happen: the \mathcal{PT} u to \mathcal{PT} b transition at $\Gamma/J = 2$ (gray dashed horizontal line), the \mathcal{PT} b to NI transition at $\Gamma = 1/(2\gamma)$ (black dashed) and the \mathcal{PT} u to NI transition at $\Gamma = \sqrt{J/(\sqrt{3}\gamma)}$ (green dashed). Note that $\gamma J = 0.8$ is still not in the second power law region, and this is why the transition happens for a larger value of Γ/J .

We first study the evolution of the z_t coordinate. In Fig. 3.14 we show the time evolution of z_t for different values of Γ/J (vertical axis) and three different strengths of the noise $\gamma J = 0.05, 0.15, 0.5$. For weak noise $\gamma J = 0.05$, the system is in the \mathcal{PT} u-like phase for low Γ/J , and we see the characteristic oscillations of this phase. The oscillation period agrees perfectly with $2\pi/\omega$ (red dotted line), where ω is the maximum oscillating frequency of the SDQ. We see that after the time scale dictated by the gap $t \sim \Delta^{-1}$ (white line), the oscillations in the z coordinate vanish and give a vanishing z Bloch coordinate. Note that the period of the oscillating slightly increases when Γ/J gets close to the original \mathcal{PT} breaking transition of the model. Increasing the decay rate Γ/J in the range $2 < \Gamma/J < 10$ gives the behavior expected from the \mathcal{PT} b phase, after the inverse dissipative gap, the system converges to the $|f\rangle$ state, i.e., $z_t \approx 1$. The oscillating frequency does not completely vanish in this case, because we are in the part of the \mathcal{PT} b phase with a nonzero value of ω (note the minima of $2\pi/\omega$ at $\gamma = 1/(3\Gamma)$). However, since $\Delta \gg \omega$, the exponential decay dominates and the oscillations are not seen. At $\Gamma/J = 10$, we are exactly at the $\gamma = \gamma^*$ transition, the dynamics is CPTP, and the convergence happens to the maximally mixed state, but with a larger time-scale, indicating a smaller dissipative gap. Lastly, when the decay rate is large $\Gamma/J > 10$, we see that the system

is fully in the NI phase, with a convergence to the $|e\rangle$ state, $z \approx -1$, in a very fast time scale $Jt \approx 10^{-2}$. Note that even in this phase, the oscillating frequency is non-zero at $\gamma = 1/\Gamma$, but the dynamics has long stabilized before the oscillation could be seen.

The behavior is similar with a slightly stronger noise $\gamma J = 0.15$, particularly for both the $\mathcal{PT}u$ and NI phases, which show damped oscillations and fast exponential convergence, respectively. However, in this case since the limits of the $\mathcal{PT}b$ phase are close $1/(2\gamma) = 3.33\dots$, the dynamics does not converge to the $|f\rangle$ state but rather get a very small $z \approx 0$ coordinate, after the inverse dissipative gap. When we consider larger values of the noise $\gamma J = 0.8$ we see that there is no $\mathcal{PT}b$ phase, as expected, and the transition to $z = -1$ phase happens with the second power law $\gamma = J\Gamma^{-2}$ (green dashed line). The convergence to the steady state is perfectly characterized by the inverse dissipative gap. Also note that the oscillation period stays constant as Γ/J changes because the oscillation frequency only vanishes well in the NI phase, in particular $\gamma = 2J\Gamma^{-2}$.

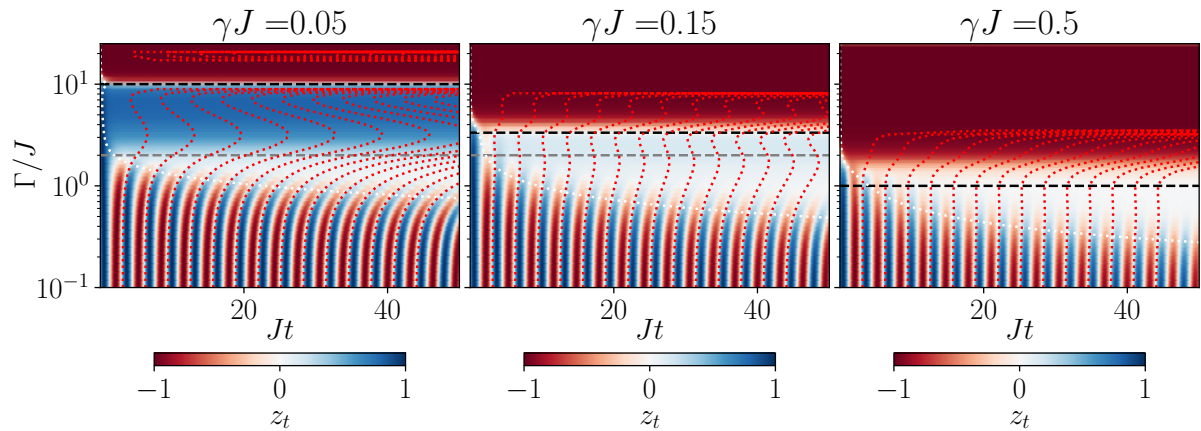


Figure 3.15. Dynamics of the Bloch z coordinate with linear scale on the time axis. Parameters as in Fig. 3.14.

The reader may note that the oscillations of the $\mathcal{PT}u$ phase look strange when plotted in logscale for very large Jt . Figure 3.15 shows the same quantity as before, but in a linear scale on the time axis. This shows that indeed the oscillations are perfectly explained by the multiples of the oscillation period $2\pi n/\omega$ (red dotted lines) and that for the weaker noises $\gamma J = 0.05, 0.15$, the period clearly grows as we approach the \mathcal{PT} breaking transition.

Figure 3.16 shows the evolution of the y coordinate of the Bloch sphere. At weak noise (left), we observe oscillations, as expected from the $\mathcal{PT}u$ phase, and a convergence to a state with a small but negative y coordinate after the inverse dissipative gap. At the \mathcal{PT} breaking transition, the dynamics show convergence to a steady state with $y \approx -1$. In the rest of the $\mathcal{PT}b$ phase, the steady state has a negative y component (also seen for slightly stronger noise $\gamma J = 0.15$) but exactly at the $\gamma = \gamma^*$ transition this changes and the steady state acquires a small but positive y component. This y component vanishes as we go inside the NI phase. For strong noise $\gamma J = 0.8$, there is no $\mathcal{PT}b$ phase, and the y coordinate becomes positive in the NI transition, and vanishes as we progressively

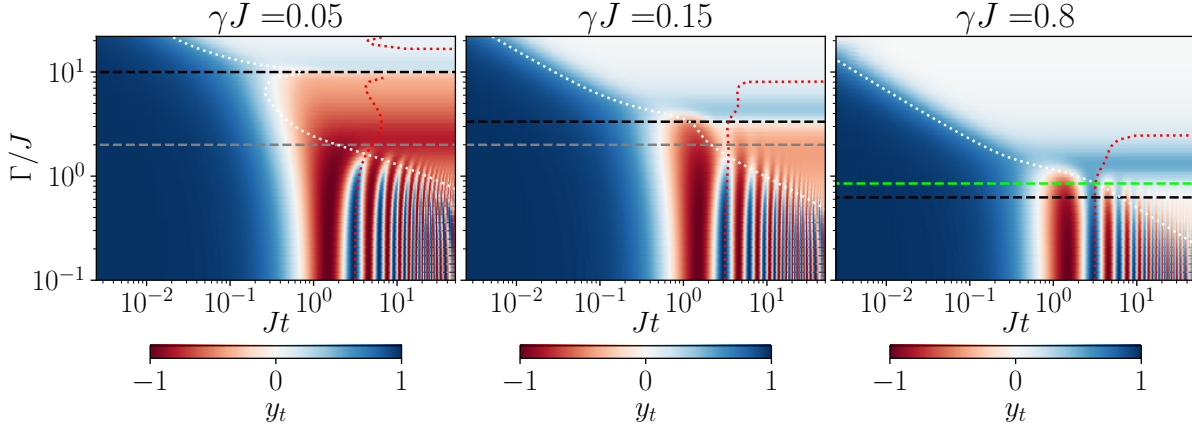


Figure 3.16. Dynamics of the Bloch y coordinate. Parameters as in Fig. 3.14.

enter the NI phase. Note that even the second power law $\Gamma = 1/\sqrt{\sqrt{3}\gamma}$ underestimates the point at which we enter the NI phase, because $\gamma J = 0.8$ is in the interpolating region between the two power laws.

Comparison of different numerical approaches

The 4th order Runge-Kutta algorithm finds the numerical solution to a system of differential equations $\dot{\mathbf{r}} = \mathbf{f}(\mathbf{r}, t)$ subject to the initial condition \mathbf{r}_0 . Taking a timestep Δt , the numerical solution to the system of equations reads

$$\mathbf{r}_{n+1} = \mathbf{r}_n + \frac{\Delta t}{6}(\mathbf{k}_1 + 2\mathbf{k}_2 + 2\mathbf{k}_3 + \mathbf{k}_4), \quad t_{n+1} = t_n + \Delta t, \quad (3.112)$$

where the auxiliary variables are defined as

$$\mathbf{k}_1 = \mathbf{f}(\mathbf{r}_n, t_n), \quad (3.113a)$$

$$\mathbf{k}_2 = \mathbf{f}\left(\mathbf{r}_n + \frac{\mathbf{k}_1}{2}\Delta t, t_n + \frac{\Delta t}{2}\right), \quad (3.113b)$$

$$\mathbf{k}_3 = \mathbf{f}\left(\mathbf{r}_n + \frac{\mathbf{k}_2}{2}\Delta t, t_n + \frac{\Delta t}{2}\right), \quad (3.113c)$$

$$\mathbf{k}_4 = \mathbf{f}(\mathbf{r}_n + \mathbf{k}_3\Delta t, t_n + \Delta t). \quad (3.113d)$$

Since any quantum state of a qubit is fully characterized by its Bloch coordinates (x, y, z) and the coordinates follow a system of ordinary differential equations this method gives the solution for the dynamics.

A more general approach, which is practical for quantum systems with small Hilbert space dimension, is the following. We first vectorize the Liouvillian using the Choi-Jamiolkowski isomorphism (in our case this is given by (3.46)), i.e., we find \mathcal{L}_{vec} as a $N^2 \times N^2$ matrix acting on vectors which represents density operators. Given the vectorized Liouvillian,

we can compute the evolution generated by that Liouvillian by Trotterizing the time evolution as

$$e^{\mathcal{L}_{\text{vec}}t} = e^{\mathcal{L}_{\text{vec}}\Delta t} \dots e^{\mathcal{L}_{\text{vec}}\Delta t} = (e^{\mathcal{L}\Delta t})^{N_t}, \quad (3.114)$$

where $t = \Delta t N_t$. Note that this identity is exact since \mathcal{L}_{vec} is time independent and trivially commutes with itself at different times. Therefore given an initial state $\hat{\rho}_0 \rightarrow |\rho_0\rangle$ we can compute the infinitesimal propagator $e^{\mathcal{L}\Delta t}$ and the time evolution of the state follows as

$$|\rho_t\rangle = \frac{(e^{\mathcal{L}\Delta t})^{N_t} |\rho_0\rangle}{(\hat{1}|(e^{\mathcal{L}\Delta t})^{N_t} |\rho_0\rangle)}, \quad (3.115)$$

where we have used the identity $\text{Tr}(\hat{\rho}_t) = \text{Tr}(\hat{1}\hat{\rho}_t) = (\hat{1}|\rho_t)$, where the Euclidean inner product of vectorized operators $(A|B) = \sum_{n,m} A_{nm}^* B_{nm} = \text{Tr}(\hat{A}^\dagger \hat{B})$ is the same as the Hilbert-Schmidt inner product for operators.

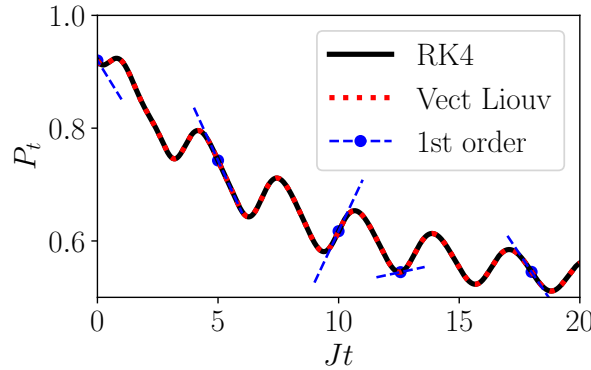


Figure 3.17. Evolution of the purity computed in two different ways: using a 4th order Runge-Kutta integrator on the Bloch coordinates dynamics (black solid line), and using the vectorized Liouvillian (red dotted line). As a further check, we compare with the 1st order purity evolution (3.58) (blue dashed lines). The parameters for the simulation are $\gamma = 0.5, \Gamma = 0.5$ and the initial (mixed) state has Bloch components $\mathbf{r} = (0.2, 0.8, 0.4)$. The absolute value of the difference between the two solutions is of order 10^{-11} with a timestep $J\Delta t = 0.004$.

Figure 3.17 shows a comparison between these two methods: Runge-Kutta (black) and the Trotterized evolution of the Liouvillian (dotted red), for solving the evolution of the purity of the SDQ model. We see perfect agreement between the two curves; indeed, the maximum difference between the purity in both of them is $\max_t |P_t^{(\text{RK4})} - P_t^{(\text{Liouv})}| = \mathcal{O}(10^{-11})$. Furthermore, the evolution of the purity agrees well with the first order approximation for the purity at different times given by the $\partial_t P_t$ equation for the SDQ (3.58). In practice, we choose to solve the dynamics numerically using the Runge-Kutta method since the vectorized Liouvillian is computationally harder since we have to compute the matrix exponential of a 4×4 matrix and then compute N_t matrix products.

3.3.6 Approach to steady states

We now want to study how the convergence to the stable steady state $\hat{\rho}^s$ happens. In order to do this, we will study the behavior of the Uhlmann fidelity $F(\hat{\rho}_t, \hat{\rho}^s)$ between the time-evolved state and the stable steady state. The fidelity gives a natural “distance” between two given states, cf. Sec. 1.1. The Uhlmann fidelity [15, 262] between two general mixed states $F(\hat{\rho}, \hat{\sigma})$ reads

$$F(\hat{\rho}, \hat{\sigma}) = \text{Tr} \left(\sqrt{\sqrt{\hat{\rho}} \hat{\sigma} \sqrt{\hat{\rho}}} \right)^2. \quad (3.116)$$

This expression is cumbersome since it involves many matrix square roots. However, when $\hat{\rho}$ and $\hat{\sigma}$ are two states of a qubit, there is a simpler expression due to Jozsa [16] and Hubner [263] which reads

$$F(\hat{\rho}, \hat{\sigma}) = \text{Tr}(\hat{\rho}\hat{\sigma}) + 2\sqrt{\det \hat{\rho} \det \hat{\sigma}}. \quad (3.117)$$

For different values of the parameters of the SDQ, we have found different phases, characterized by different steady states and a different route to the steady state. We want to characterize the convergence to the steady state in a unified way in all phases. For this reason, we study the fidelity between the time-evolved state and the stable steady state to which the dynamics converges $F_t^s := F(\hat{\rho}_t, \rho^s)$ for the given parameters $\gamma J, \Gamma/J$.

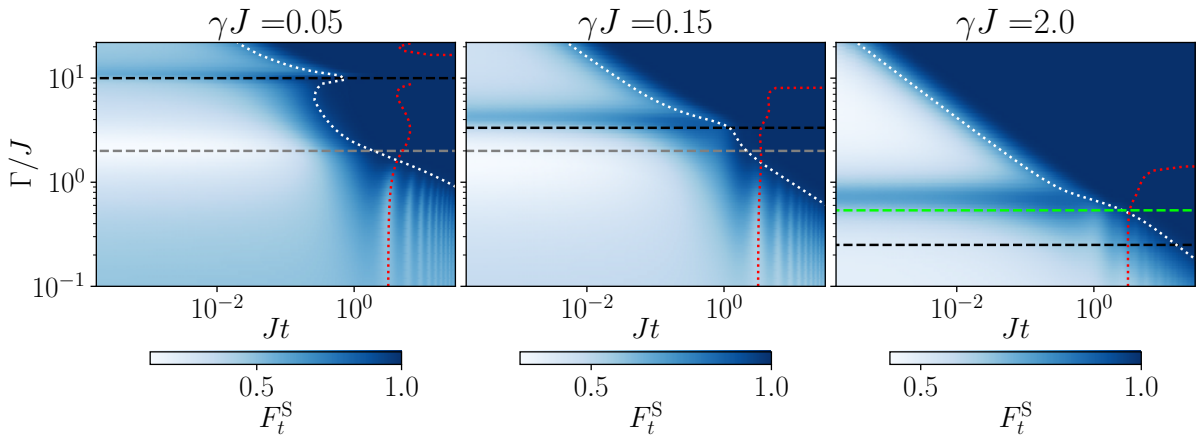


Figure 3.18. Fidelity between the time-evolved state and the stable steady state as a function of the loss parameter Γ and time for noise strengths $\gamma J = 0.05, 0.15, 2$. The transitions are shown between the \mathcal{PT}_u to \mathcal{PT}_b phases $\Gamma/J = 2$ (gray dashed) and \mathcal{PT}_b to NI phases $\Gamma = 1/(2\gamma)$ (black dashed) and \mathcal{PT}_u to NI phases $\Gamma = 1/\sqrt{3\gamma}$. The time-scales of the inverse dissipative gap Δ^{-1} (white dotted) and the oscillation period $2\pi/\omega$ (red dotted) are also shown. The simulation solves the system of equations for the Bloch coordinates using the Runge-Kutta method.

Figure 3.18 shows the evolution of the fidelity F_t^s as a function of time and the decay rate Γ/J , which, as we discussed previously, seems to be a feasible parameter to change on the experimental setup, at least more than the strength of the noise. We first show a weak noise case $\gamma J = 0.05$, in which we see that in the $\mathcal{PT}\text{u}$ phase the convergence to the steady state is oscillatory, and after the inverse dissipative gap the dynamics converges to the stable steady state, which we know is close to the center of the Bloch ball, i.e., a mixed state. Note that the period of the oscillations is perfectly characterized by $2\pi/\omega$. The $\mathcal{PT}\text{b}$ has a faster convergence towards the stable steady state, which does not allow for seeing the oscillations since $\Delta^{-1} \ll 2\pi/\omega$. In the transition to the NI phase, the dissipative gap decreases, and thus the time for stabilization increases, although the fidelity between the time-evolved state and the maximally mixed state, the stable steady state when $\gamma = \gamma^*$, is larger than for the rest of the decay rates. This means that Lindblad dynamics happen in a way that keeps the state closer to the steady state than the rest of the SDQ dynamics. Lastly, the convergence in the NI phase is very fast, much faster than in any of the other phases.

The behavior for slightly stronger noise $\gamma J = 0.15$ is similar, with oscillatory convergence in the $\mathcal{PT}\text{u}$ phase, very fast convergence in the NI phase. However, for this value, the dissipative gap does not decrease much around the $\gamma = \gamma^*$ transition. This means that the dissipation time-scale $t = \Delta^{-1}$ does not have a peak around $\gamma = \gamma^*$. However, the fidelity is bigger for this transition, which, interestingly, happens slightly over $\gamma = \gamma^*$. When we consider strong noise $\gamma J = 2$, there is no $\mathcal{PT}\text{b}$ phase; we transition directly from $\mathcal{PT}\text{u}$ to NI. We see that $\gamma = \gamma^*$ largely underestimates the decay rate at which the transition happens, and even γ_N underestimates this value, although it is much closer, because the noise strength is not strong enough to be in the region where the second power law fits well, but rather in the interpolating region between both power laws.

3.4 Single trajectory dynamics

3.4.1 General Equation of motion

If we first make sure that all single trajectories, i.e., realizations of the noise $\xi_t^{(j)}$, represent normalized trajectories, the dynamics will in general be different. This can be obtained by modifying the SME (3.3) to obtain a nonlinear SME given by

$$\begin{aligned} d\hat{\rho}_t = & \left(\tilde{\mathcal{L}}_{\hat{H}_R, \hat{H}_I, \hat{\mathbf{L}}}^{\text{AD}}[\hat{\rho}_t] - \text{Tr}(\tilde{\mathcal{L}}_{\hat{H}_R, \hat{H}_I, \hat{\mathbf{L}}}^{\text{AD}}[\hat{\rho}_t])\hat{\rho}_t \right) dt \\ & + \sum_{n=1}^{N_C} \left(\tilde{\mathcal{M}}_{\hat{L}_n}[\hat{\rho}_t] - \text{Tr}(\tilde{\mathcal{M}}_{\hat{L}_n}[\hat{\rho}_t])\hat{\rho}_t \right) dW_t^{(n)}, \end{aligned} \quad (3.118)$$

which if we average over the noise $\hat{\rho}_t = \mathbb{E}(\hat{\rho}_t)$ yields

$$\partial_t \hat{\rho}_t = \tilde{\mathcal{L}}_{\hat{H}_R, \hat{H}_I, \hat{\mathbf{L}}}^{\text{AD}}[\hat{\rho}_t] - \mathbb{E} \left(\text{Tr}(\tilde{\mathcal{L}}_{\hat{H}_R, \hat{H}_I, \hat{\mathbf{L}}}^{\text{AD}}[\hat{\rho}_t])\hat{\rho}_t \right). \quad (3.119)$$

As previously discussed, this master equation is not closed; the evolution of the first moment $\hat{\rho}_t$ depends on the second moment $\mathbb{E}(\hat{\rho}_t^2)$, and the one for the second depends on the third and the fourth, and so on, leading to a hierarchy of equations. For this reason, when dealing analytically with the average over the noise, we did not follow this approach. However, since this is actually the protocol that describes properly single trajectories, we will now focus on the properties of the nonlinear SME (3.118).

The SDE for the purity can be obtained from $d\text{Tr}(\hat{\rho}^2) = 2\text{Tr}(\hat{\rho}d\hat{\rho}) + \text{Tr}(d\hat{\rho}d\hat{\rho})$, which gives

$$\begin{aligned} dP_t = & \left\{ 2\text{Tr}(\tilde{\mathcal{L}}[\hat{\rho}_t]\hat{\rho}_t) - 2\text{Tr}(\hat{\rho}_t^2)\text{Tr}(\tilde{\mathcal{L}}[\hat{\rho}_t]) \right. \\ & + \sum_{n=1}^{N_c} \left(\text{Tr}(\tilde{\mathcal{M}}_n[\hat{\rho}_t]^2) - \text{Tr}(\tilde{\mathcal{M}}_n[\hat{\rho}_t])^2\text{Tr}(\hat{\rho}_t^2) \right) \Big\} dt \\ & + 2 \sum_{n=1}^{N_c} \left(\text{Tr}(\tilde{\mathcal{M}}_n[\hat{\rho}_t]\hat{\rho}_t) - \text{Tr}(\tilde{\mathcal{M}}_n[\hat{\rho}_t])\text{Tr}(\hat{\rho}_t^2) \right) dW_t^{(n)}, \end{aligned} \quad (3.120)$$

where we omitted the $\hat{H}_R, \hat{H}_I \dots$ dependence on the Liouvillian and introduced $\tilde{\mathcal{M}}_{\hat{L}_n} \equiv \tilde{\mathcal{M}}_n$. Now we assume that the state $\hat{\rho}_t$ is pure, so we find

$$\begin{aligned} dP_t = & \left\{ 2\text{Tr}(\tilde{\mathcal{L}}[\hat{\rho}_t]\hat{\rho}_t) - 2\text{Tr}(\tilde{\mathcal{L}}[\hat{\rho}_t]) \right. \\ & + \sum_{n=1}^{N_c} \left(\text{Tr}(\tilde{\mathcal{M}}_n[\hat{\rho}_t]^2) - \text{Tr}(\tilde{\mathcal{M}}_n[\hat{\rho}_t])^2 \right) \Big\} dt \\ & + 2 \sum_{n=1}^{N_c} \left(\text{Tr}(\tilde{\mathcal{M}}_n[\hat{\rho}_t]\hat{\rho}_t) - \text{Tr}(\tilde{\mathcal{M}}_n[\hat{\rho}_t]) \right) dW_t^{(n)}. \end{aligned} \quad (3.121)$$

Consider a generic superoperator $\mathcal{S}[\bullet] = \hat{S}^{(l)} \bullet + \bullet \hat{S}^{(r)} + \sum_n \hat{J}_n^{(l)} \bullet \hat{J}_n^{(r)}$, it is easy to check that for this superoperator

$$\text{Tr}(\mathcal{S}[|\psi\rangle\langle\psi|]|\psi\rangle\langle\psi|) - \text{Tr}(\mathcal{S}[|\psi\rangle\langle\psi|]) = \sum_n \left(\langle \hat{J}_n^{(l)} \rangle_\psi \langle \hat{J}_n^{(r)} \rangle_\psi - \langle \hat{J}_n^{(r)} \hat{J}_n^{(l)} \rangle_\psi \right).$$

Since the superoperator in the stochastic term $dW_t^{(n)}$ does not have jump terms, it vanishes, and we are left with an ordinary differential equation for the purity

$$\begin{aligned} dP_t = & \sum_{n=1}^{N_c} \gamma_n \left\{ 4\langle \hat{L}_n \rangle_\psi^2 - 4\langle \hat{L}_n^2 \rangle_\psi + 2\text{Tr}(\{\hat{L}_n, |\psi\rangle\langle\psi|\}^2) - 2\text{Tr}(\{\hat{L}_n, |\psi\rangle\langle\psi|\})^2 \right\} dt \\ = & \sum_{n=1}^{N_c} \gamma_n \left(4\cancel{\langle \hat{L}_n \rangle_\psi^2} - 4\cancel{\langle \hat{L}_n^2 \rangle_\psi} + 4\cancel{\langle \hat{L}_n \rangle_\psi^2} + 4\cancel{\langle \hat{L}_n^2 \rangle_\psi} - 8\cancel{\langle \hat{L}_n \rangle_\psi^2} \right) dt \\ dP_t = & 0. \end{aligned} \quad (3.122)$$

Therefore, the SME keeps pure states pure at single trajectories. This was expected since Non-Hermitian Hamiltonians keep the rank of states constant [264], which in particular implies that a pure state remains pure. This result holds for arbitrary time-dependent NH Hamiltonians.

3.4.2 Single trajectory dynamics of the SDQ

The single trajectory dynamics of the SDQ poses the perfect playground to study the validity of the analytical results obtained in the rest of the chapter, since in experiments such as [80] there is, in principle, access to single realizations of the noise. For this reason, we also studied the single trajectory dynamics in [7]. The nonlinear stochastic master equation for the SDQ reads

$$\begin{aligned} d\hat{\rho}_t = & \left(-iJ[\hat{\sigma}_x, \hat{\rho}_t] - \Gamma\{\hat{\Pi}, \hat{\rho}_t\} + \gamma\Gamma^2\{\hat{\Pi}, \{\hat{\Pi}, \hat{\rho}_t\}\} + (2\Gamma - 4\gamma\Gamma^2)\text{Tr}(\hat{\Pi}\hat{\rho}_t\hat{\Pi})\hat{\rho}_t \right) dt \\ & - \left(\sqrt{2\gamma}\Gamma\{\hat{\Pi}, \hat{\rho}_t\} - 2\sqrt{2\gamma_n}\Gamma\text{Tr}(\hat{\Pi}\hat{\rho}_t)\hat{\rho}_t \right) dW_t. \end{aligned} \quad (3.123)$$

We now introduce the single trajectory Bloch coordinates $\hat{\rho}_t = \frac{1}{2}(\hat{\mathbb{1}} + \mathbf{r} \cdot \hat{\boldsymbol{\sigma}})$ where $\mathbf{r} = (\mathfrak{x}, \mathfrak{y}, \mathfrak{z})$ and $\hat{\boldsymbol{\sigma}} = (\hat{\sigma}_x, \hat{\sigma}_y, \hat{\sigma}_z)$. The antidephasing SME can then be written equivalently as

$$\begin{cases} d\mathfrak{x} = (-(\gamma\Gamma^2 + \mathfrak{z}\Gamma(1 - 2\gamma\Gamma))\mathfrak{x}) dt - \sqrt{2\gamma}\Gamma\mathfrak{x}\mathfrak{z} dW_t, \\ d\mathfrak{y} = (-2J\mathfrak{z} - (\gamma\Gamma^2 + \mathfrak{z}\Gamma(1 - 2\gamma\Gamma))\mathfrak{y}) dt - \sqrt{2\gamma}\Gamma\mathfrak{y}\mathfrak{z} dW_t, \\ d\mathfrak{z} = (2J\mathfrak{y} - \Gamma(1 - 2\gamma\Gamma)(\mathfrak{z}^2 - 1)) dt - \sqrt{2\gamma}\Gamma(\mathfrak{z}^2 - 1) dW_t. \end{cases} \quad (3.124)$$

The first equation is linear in \mathfrak{x} , which implies that starting from $\mathfrak{x} = 0$ ensures that this coordinate is stationary in time. Using the Itô lemma, the $\mathfrak{y}, \mathfrak{z}$ coordinates can be equivalently expressed in terms of the polar coordinates $\mathfrak{y} = r \sin \theta$, $\mathfrak{z} = r \cos \theta$ as

$$\begin{cases} dr(\mathfrak{y}, \mathfrak{z}) = \partial_{\mathfrak{y}}r(\mathfrak{y}, \mathfrak{z})d\mathfrak{y} + \partial_{\mathfrak{z}}r(\mathfrak{y}, \mathfrak{z})d\mathfrak{z} + \frac{1}{2}\frac{\partial^2r(\mathfrak{y}, \mathfrak{z})}{\partial\mathfrak{y}^2}d\mathfrak{y}^2 + \frac{1}{2}\frac{\partial^2r(\mathfrak{y}, \mathfrak{z})}{\partial\mathfrak{z}^2}d\mathfrak{z}^2 + \frac{\partial^2r(\mathfrak{y}, \mathfrak{z})}{\partial\mathfrak{y}\partial\mathfrak{z}}d\mathfrak{y}d\mathfrak{z}, \\ d\theta(\mathfrak{y}, \mathfrak{z}) = \partial_{\mathfrak{y}}\theta(\mathfrak{y}, \mathfrak{z})d\mathfrak{y} + \partial_{\mathfrak{z}}\theta(\mathfrak{y}, \mathfrak{z})d\mathfrak{z} + \frac{1}{2}\frac{\partial^2\theta(\mathfrak{y}, \mathfrak{z})}{\partial\mathfrak{y}^2}d\mathfrak{y}^2 + \frac{1}{2}\frac{\partial^2\theta(\mathfrak{y}, \mathfrak{z})}{\partial\mathfrak{z}^2}d\mathfrak{z}^2 + \frac{\partial^2\theta(\mathfrak{y}, \mathfrak{z})}{\partial\mathfrak{y}\partial\mathfrak{z}}d\mathfrak{y}d\mathfrak{z}, \end{cases}$$

which simplify to

$$\begin{cases} dr = \frac{\Gamma(r^2 - 1)(r(2\gamma\Gamma - 1)\cos(\theta) - \gamma\Gamma\sin^2(\theta))}{r} dt - \sqrt{2\gamma}\Gamma(r^2 - 1)\cos(\theta)dW_t, \\ d\theta = -\frac{\sqrt{2\gamma}\Gamma\sin(\theta)}{r} dW_t - \left(\frac{\Gamma\sin(\theta)(\gamma\Gamma(3r^2 - 2)\cos(\theta) - 2\gamma\Gamma r + r)}{r^2} + 2J \right) dt. \end{cases}$$

If the dynamics starts from a pure state $r = 1$, we find that the radial coordinate does not evolve in time $dr = 0$, as we proved generally in the previous section, since pure states remain pure. In this case, the dynamics is completely determined by a single SDE for the

angle θ in the Bloch sphere

$$d\theta = -\sqrt{2\gamma}\Gamma \sin(\theta)dW_t - (2J + \Gamma(1 - 2\gamma\Gamma + \gamma\Gamma \cos(\theta)) \sin(\theta)) dt. \quad (3.125)$$

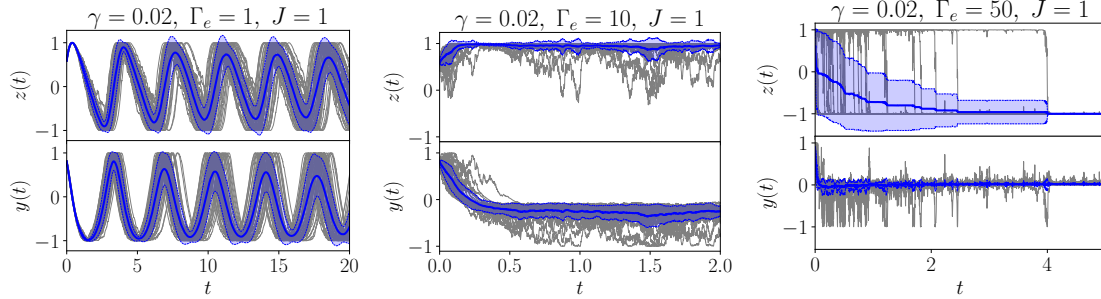


Figure 3.19. Different instances of single trajectory dynamics in the $\mathcal{PT}u$ (left), $\mathcal{PT}b$ (center), and NI (right) phases. The plots show the time evolution of the Bloch coordinates \mathfrak{z}_t and \mathfrak{y}_t (gray lines) as well as their average $z_t = \mathbb{E}(\mathfrak{z}_t)$, $y_t = \mathbb{E}(\mathfrak{y}_t)$ (blue line) and their standard deviation (shaded blue area). There are $N_{av} = 50$ realizations of each trajectory, and each time array has 2000 time-steps. The parameters are $\gamma J = 0.02$ and $\Gamma/J = 1, 10, 50$. The initial state has parameters $r_0 = 1$, $\theta_0 = 0.9438\text{rad}$.

Figure 3.19 shows the time evolution of the Bloch coordinates for three different choices of parameters in the $\mathcal{PT}u$, $\mathcal{PT}b$, and NI phases. The $\mathcal{PT}u$ dynamics show the characteristic oscillations, which as was observed experimentally are not perfectly sinusoidal but each period is slightly asymmetric [80], the $\mathcal{PT}b$ phase converges to the $|f\rangle$ state with $z = +1$, $y \approx 0$, keeping some fluctuations around this value, and the NI phase converges fast to the $|e\rangle$ state $z = -1$, $y = 0$. Interestingly, the single trajectories show that in the limit of large Γ the trajectories behave similar to Poissonian quantum jumps, and in the NI phase there are no fluctuations at long times in the z_t value.

Figure 3.20 shows the evolution of the average of single trajectories, which shows a good agreement with the similar plots in Figs. 3.14, 3.16 (left) although here the dynamics was solved for a shorter overall time. We see that the $\mathcal{PT}u$ phase shows oscillations at the frequency predicted by the spectral analysis (red dotted line). In the $\mathcal{PT}b$ phase, the dynamics converges close to $z \approx +1$, although here the dynamics shows more fluctuations, which we already saw in Fig. 3.19 (center). Lastly, the NI phase is very clearly observed, the dynamics converges fast to $z = -1$ and $y = 0$, and it shows very little fluctuations around this value. The transitions between the three phases occur at the predicted value $\Gamma/J = 2$ (gray dotted) and $\gamma\Gamma = 1$ (black line).

Figure 3.21 shows the phase diagrams of the Bloch coordinates for the steady state obtained numerically. Except for the $\mathcal{PT}u$ phase for very small decay rate, which is not sampled reliably, the phase diagrams show good agreement with what we expect from the values obtained analytically. To check this, we compute the *remainder* as the difference

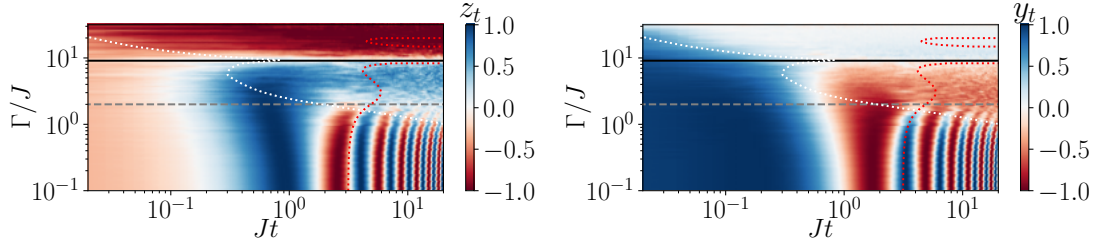


Figure 3.20. Plot of the evolution of the average Bloch coordinates $z_t = \mathbb{E}(\mathfrak{z}_t)$ (left) and $y_t = \mathbb{E}(\mathfrak{y}_t)$ (right) for a fixed value of the noise-strength $\gamma J = 0.055$ as a function of time and the decay rate Γ/J .

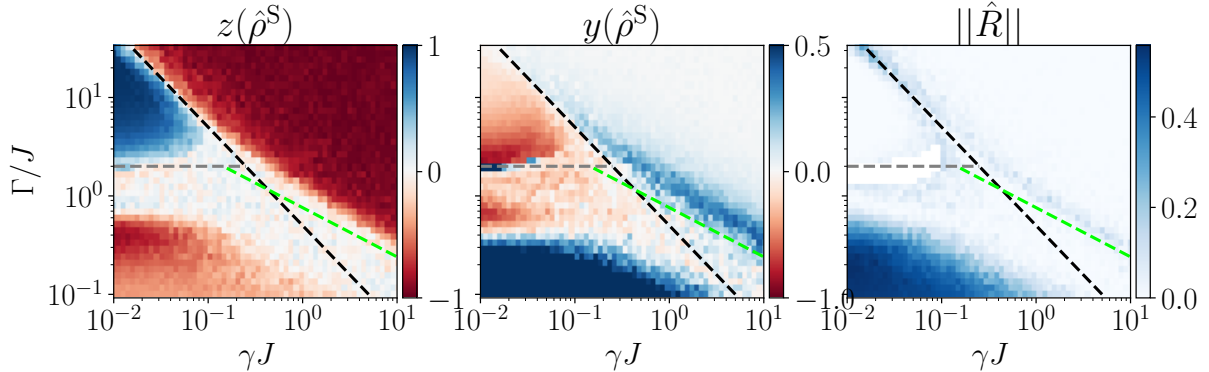


Figure 3.21. Single trajectory steady state phase diagrams for the Stochastic Dissipative Qubit. Each data point shows the last slice of the time evolution of trajectories where the time array has 300 time-steps and the final time is $t_{\text{fin}} = 10/\Delta$. This means that the evolution is more reliable for the NI and $\mathcal{PT}\text{b}$ phases since the $\mathcal{PT}\text{u}$ phase shows oscillations which need not be well sampled through this approach.

between the single trajectory and the average result

$$\hat{R} = \mathbb{E}(\hat{\rho}_t) - \hat{\rho}_t^{(\text{av})}, \quad (3.126)$$

whose Hilbert-Schmidt norm follows as

$$\|\hat{R}\|^2 = \text{Tr}(\hat{R}^\dagger \hat{R}) = \frac{(z^{(\text{st})} - z^{(\text{av})})^2 + (y^{(\text{st})} - y^{(\text{av})})^2}{2}, \quad (3.127)$$

which is shown in Fig. 3.21 (right) and shows that, except for the region deep in the $\mathcal{PT}\text{u}$ phase, the solution obtained from averaging single trajectories and from first averaging and then renormalizing, agrees quite well, and is mostly largest at the transitions, which happen at slightly different values for the two approaches.

3.4.3 Noise-Induced phase in No-Pump dynamics

One conceptual problem with including white noise on a quantum non-Hermitian Hamiltonian is that since ξ_t has support over the whole real line, the Hamiltonian

$$\hat{H}_t = \hat{H}_0 - i\hat{L}(1 + \sqrt{2\gamma}\xi_t), \quad (3.128)$$

is not guaranteed to have a negative imaginary part, since $1 + \sqrt{2\gamma}\xi_t$ can always be negative. This could provide a simple explanation for the emergence of the NI phase, since the times when $1 + \sqrt{2\gamma}\xi_t < 0$, the noise can be understood as pumping population in one of the states. In here, we develop a formalism that prohibits the existence of these pumps, and we show that the NI phase still happens without them.

For this reason, we impose the constraint $1 + \sqrt{2\gamma}\xi_t \geq 0$, which “cuts off” part of the tail of the distribution. To have it symmetric, we also get rid of the right tail of the distribution. Therefore we introduce an associated stochastic process ζ_t which is Gaussian in the range $[-\frac{1}{\sqrt{2\gamma}}, \frac{1}{\sqrt{2\gamma}}]$, and zero outside of that range.

How to deal with truncated Gaussian noise?

The Itō rule comes from the property

$$\int_{-\infty}^{\infty} \xi^2 \mathfrak{P}(\xi) d\xi = t, \quad (3.129)$$

where $\mathfrak{P}(\xi) = \frac{1}{\sqrt{2\pi t}} e^{-\xi^2/(2t)}$ is a normal distribution. Now, the truncated Gaussian stochastic process ζ has a probability distribution $\mathfrak{P}(\zeta)$ given by

$$\mathfrak{P}(\zeta) = \frac{1}{\operatorname{erf}((2\sqrt{\gamma t})^{-1})\sqrt{2\pi t}} e^{-\frac{\zeta^2}{2t}},$$

which ensures that $\int_{-1/\sqrt{2\gamma}}^{1/\sqrt{2\gamma}} \mathfrak{P}(\zeta) d\zeta = 1$. Clearly, when $\gamma \rightarrow 0$, the cutoffs diverge and we recover the normal distribution. Now, the analogous result that leads to Itō’s rule is

$$\int_{-\Lambda}^{\Lambda} \zeta^2 \mathfrak{P}(\zeta) d\zeta = t \left(1 - \frac{e^{-\frac{1}{4\gamma t}}}{\operatorname{erf}(\frac{1}{2\sqrt{\gamma t}})\sqrt{\pi\gamma t}} \right), \quad (3.130)$$

where we introduced the cutoff $\Lambda = (\sqrt{2\gamma})^{-1}$. From this expression, we see that when $\epsilon = \gamma t \ll 1$, we recover the linear dependence. This shows that considering small noise γ and small times dt , the stochastic process ζ_t , and its Itō version $dV_t := \zeta_t dt$ also have a non-zero value of dV_t^2 , but it is not necessarily equal to dt .

Numerically solving a truncated Gaussian SDE

To simulate the no-pump dynamics, we choose a very simple Euler-Maruyama integrator and adapt it for our purposes. The SDE is

$$dY = a(Y)dt + b(Y)dV_t + c(Y)dV_t^2, \quad (3.131)$$

where following the previous analysis, we keep the terms dV_t^2 , since they are non-zero, but do not enforce them to be equal to dt . The numerical solution is given by

$$Y_n = Y_{n-1} + a(Y_{n-1})\Delta t + b(Y_{n-1})\Delta V_n + c(Y_{n-1})\Delta V_n^2, \quad (3.132)$$

where ΔV_n is sampled from a truncated Gaussian with variance Δt , zero average, and cutoffs given by Λ . The SDE that we are simulating is obtained by re-expressing the angle SDE without assuming that $dV^2 = dt$, i.e.,

$$d\theta = -(2J + \Gamma \sin \theta)dt - \sqrt{2\gamma}\Gamma \sin \theta dV_t + \gamma\Gamma^2 \sin \theta (2 - \cos \theta)dV_t^2. \quad (3.133)$$

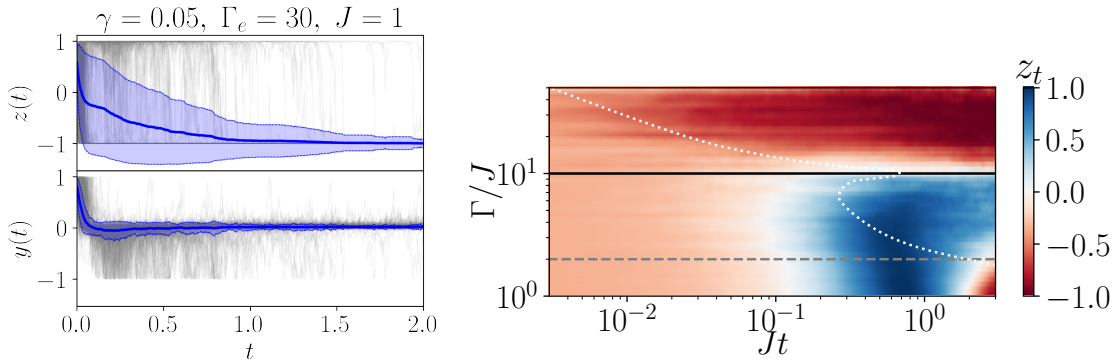


Figure 3.22. No pump dynamics of the SDQ. The figure shows single trajectories in the NI phase (left) and the behavior of the average for a fixed noise strength $\gamma J = 0.05$.

Figure 3.22 shows the evolution of the Bloch coordinates (left). We observe a clear convergence to $z = -1$, from where we can already conclude that the NI phase is still present when we enforce no pump dynamics. Fig. 3.22 (right) shows the average evolution of the z_t coordinate for different values of the decay rate, and we observe that the transition from the PTb to NI phase is similar to the one obtained before, and that the NI phase, also when no pumps are present, shows little fluctuations around its steady state value. This analysis shows that the pumps are not the physical reason behind the NI phase, we however found out that if the terms dV_t^2 were removed, no NI phase could be found, and we can thus conclude that the property of Itô's process which makes dV_t^2 non-zero, causes the existence of the NI phase.

3.4.4 Justifying Trace Preservation at average level

The formalism that leads to a closed antidephasing master equation for the average density matrix assumes that we first average and then impose trace preservation, i.e., we are using $\frac{\mathbb{E}(\tilde{\rho}_t)}{\mathbb{E}(\text{Tr}(\tilde{\rho}_t))}$ as an approximation of $\mathbb{E}\left(\frac{\tilde{\rho}_t}{\text{Tr}(\tilde{\rho}_t)}\right)$ which is the physical one happening in the lab, since the trajectories remain pure, normalized states. One could shift the focus, and consider certain physical situations where we have access to the average of the unnormalized DM $\mathbb{E}(\tilde{\rho}_t)$, such as for example with an ensemble of systems which may or may not have decayed, such as is done in certain quantum optical realizations of NH Hamiltonians [265], in which we do not have access to the normalized single trajectory dynamics. However, the recent experiments [80, 85] have access to single trajectories and thus when averaging over realizations they have access to $\mathbb{E}\left(\frac{\tilde{\rho}_t}{\text{Tr}(\tilde{\rho}_t)}\right)$. A similar issue is encountered in the spectral form factor at finite temperature which requires the computation of an “annealed” average [124, 126] $\langle|Z_{\beta+it}|^2\rangle/\langle Z_{\beta}^2\rangle$ as an approximation of $\langle|Z_{\beta+it}|^2/Z_{\beta}^2\rangle$. In this case, it is known that in the limit $\beta \rightarrow 0$ the approximation becomes exact. For the types of averages that we have here, the validity of this approximation is not known, and thus, we develop a formal treatment of this approximation in this section.

Let us take the argument in [266] and extend it to our case with density matrices. We begin by writing the density matrix as its noise average plus a perturbation

$$\tilde{\rho} = \mathbb{E}(\tilde{\rho}) + \delta\tilde{\rho} \equiv \tilde{\rho} + \delta\tilde{\rho}, \quad \text{Tr}(\tilde{\rho}) = \mathbb{E}(\text{Tr}(\tilde{\rho})) + \text{Tr}(\delta\tilde{\rho}). \quad (3.134)$$

By construction, these objects obey

$$\mathbb{E}(\delta\tilde{\rho}) = 0, \quad \mathbb{E}(\text{Tr}(\delta\tilde{\rho})) = 0$$

Noticing that now $\mathbb{E}(\tilde{\rho}) \equiv \tilde{\rho}$, $\mathbb{E}(\text{Tr}(\tilde{\rho})) = \text{Tr}(\tilde{\rho})$ are *not* random variables anymore, and they can come out of the expectation value, the relevant expectation value can be written as

$$\begin{aligned} \mathbb{E}\left(\frac{\tilde{\rho}}{\text{Tr}(\tilde{\rho})}\right) &= \mathbb{E}\left(\frac{\tilde{\rho} + \delta\tilde{\rho}}{\text{Tr}(\tilde{\rho}) + \text{Tr}(\delta\tilde{\rho})}\right) \\ &= \frac{\tilde{\rho}}{\text{Tr}(\tilde{\rho})}\mathbb{E}\left(\frac{1}{1 + \frac{\text{Tr}(\delta\tilde{\rho})}{\text{Tr}(\tilde{\rho})}}\right) + \frac{\mathbb{1}}{\text{Tr}(\tilde{\rho})}\mathbb{E}\left(\frac{\delta\tilde{\rho}}{1 + \frac{\text{Tr}(\delta\tilde{\rho})}{\text{Tr}(\tilde{\rho})}}\right). \end{aligned} \quad (3.135)$$

Which, assuming the trace of the perturbation to be small compared to the trace of the average $|\text{Tr}(\delta\tilde{\rho})/\text{Tr}(\tilde{\rho})| \leq 1$, can be expanded in power series giving

$$\mathbb{E}\left(\frac{\tilde{\rho}}{\text{Tr}(\tilde{\rho})}\right) = \frac{\tilde{\rho}}{\text{Tr}(\tilde{\rho})} + \frac{\tilde{\rho}}{\text{Tr}(\tilde{\rho})} \sum_{n=2}^{\infty} (-1)^n \frac{\mathbb{E}(\text{Tr}(\delta\tilde{\rho})^n)}{\text{Tr}(\tilde{\rho})^n} + \sum_{n=1}^{\infty} (-1)^n \frac{\mathbb{E}(\delta\tilde{\rho} \text{Tr}(\delta\tilde{\rho})^n)}{\text{Tr}(\tilde{\rho})^{n+1}}, \quad (3.136)$$

where we have used the properties of zero averages to cancel some of the terms. Now what remains to be found is how small the correction term is; for this, we assume that

the corrections $\delta\tilde{\varrho}$ are in some sense small. For the trace, this means

$$|\mathrm{Tr}(\delta\tilde{\varrho})| \ll \mathrm{Tr}(\tilde{\varrho}), \quad \epsilon := \frac{|\mathrm{Tr}(\delta\tilde{\varrho})|}{\mathrm{Tr}(\tilde{\varrho})} \ll 1.$$

For the operator itself, we have to introduce the matrix norm

$$\|\delta\tilde{\varrho}\| \ll \|\tilde{\varrho}\|, \quad \delta := \frac{\|\delta\tilde{\varrho}\|}{\|\tilde{\varrho}\|} \ll 1.$$

Furthermore, since $\tilde{\varrho} \geq 0$ is positive semidefinite¹⁰ $\|\tilde{\varrho}\| \leq \mathrm{Tr}(\tilde{\varrho})$. The remainder $\hat{R} := \mathbb{E}\left(\frac{\hat{\varrho}_t}{\mathrm{Tr}(\hat{\varrho}_t)}\right) - \frac{\tilde{\varrho}_t}{\mathrm{Tr}(\tilde{\varrho}_t)}$ reads

$$\hat{R} := \frac{\tilde{\varrho}}{\mathrm{Tr}(\tilde{\varrho})} \sum_{n=2}^{\infty} (-1)^n \frac{\mathbb{E}(\mathrm{Tr}(\delta\tilde{\varrho})^n)}{\mathrm{Tr}(\tilde{\varrho})^n} + \sum_{n=1}^{\infty} (-1)^n \frac{\mathbb{E}(\delta\tilde{\varrho} \mathrm{Tr}(\delta\tilde{\varrho})^n)}{\mathrm{Tr}(\tilde{\varrho})^{n+1}}. \quad (3.137)$$

By virtue of sub-additivity of the matrix norm, the norm of this quantity can be upper-bounded as

$$\|\hat{R}\| \leq \frac{\|\tilde{\varrho}\|}{\mathrm{Tr}(\tilde{\varrho})} \left(\sum_{n=2}^{\infty} \frac{\mathbb{E}(|\mathrm{Tr}(\delta\tilde{\varrho})^n|)}{\mathrm{Tr}(\tilde{\varrho})^n} + \sum_{n=1}^{\infty} \frac{\mathbb{E}\left(\frac{\|\delta\tilde{\varrho}\|}{\|\tilde{\varrho}\|} |\mathrm{Tr}(\delta\tilde{\varrho})^n|\right)}{\mathrm{Tr}(\tilde{\varrho})^n} \right), \quad (3.138)$$

which using $\|\tilde{\varrho}\| \leq \mathrm{Tr}(\tilde{\varrho})$ yields

$$\|\hat{R}\| \leq \left(\sum_{n=2}^{\infty} \frac{\mathbb{E}(|\mathrm{Tr}(\delta\tilde{\varrho})^n|)}{\mathrm{Tr}(\tilde{\varrho})^n} + \sum_{n=1}^{\infty} \frac{\mathbb{E}\left(\frac{\|\delta\tilde{\varrho}\|}{\|\tilde{\varrho}\|} |\mathrm{Tr}(\delta\tilde{\varrho})^n|\right)}{\mathrm{Tr}(\tilde{\varrho})^n} \right). \quad (3.139)$$

Focusing only on the lowest order contribution, the first term is ϵ^2 and the second is $\epsilon\delta$; therefore, the remainder is upper bounded by a term of order

$$\|\hat{R}\| \lesssim \epsilon^2 + \epsilon\delta \quad (3.140)$$

which already gives an argument that the remainder is small. If we do not use the subadditivity property, we may be able to find a better bound. The lowest order terms of the remainder can be written as

$$\hat{R}' = \frac{1}{\mathrm{Tr}(\tilde{\varrho})^2} \mathbb{E} \left((\tilde{\varrho} \mathrm{Tr}(\delta\tilde{\varrho}) - \mathrm{Tr}(\tilde{\varrho})\delta\tilde{\varrho}) \frac{\mathrm{Tr}(\delta\tilde{\varrho})}{\mathrm{Tr}(\tilde{\varrho})} \right).$$

¹⁰We did not specify here the norm that we choose, however from a practical point of view we are interested in either the operator norm $\|\hat{A}\|_{\mathrm{op}}^2 = \max_n \lambda_n$ or the Hilbert-Schmidt or Frobenius norm $\|\hat{A}\|_{\mathrm{HS}}^2 = \mathrm{Tr}(\hat{A}^\dagger \hat{A})$. For a positive semidefinite operator, both of these norms fulfill this property since $\max_n \lambda_n \leq \sum_n \lambda_n$ and $\sum_n \lambda_n^2 \leq (\sum_n \lambda_n)^2$ for $\lambda_n \geq 0$.

This shows that the remainder's lowest order terms are traceless $\text{Tr}(\hat{R}') = 0$, even without the noise average. These terms have opposite signs, and using the subadditivity property removes these signs; thus, the bound derived using this property may be worse.

It is also possible to show that taking the Hilbert Schmidt norm of this remainder (3.126), it can be expressed as the difference of Bloch coordinates for a qubit (3.127). In Fig. 3.21, we show that, except for the lower left corner for which the integrator is not well-suited, the norm of the difference between the two averages is small for the steady states.

3.5 Experimental results

We first review several possible platforms in which a realization of the Stochastic Dissipative Qubit could be feasible; then we turn to analyze data from the residual decay rate of the Dissipative Qubit [80], for which the SDQ provides a model for the effect of the noise.

3.5.1 Possible experimental implementations of the Stochastic Dissipative Qubit

Superconducting circuit realization of the Non-Hermitian Qubit

The first purely quantum experimental realization of a Non-Hermitian Hamiltonian was done by Naghiloo *et al.* [80]. In their experimental setup, they leverage superconducting circuits to engineer a NH Hamiltonian, in particular the Dissipative Qubit. We now review the basics of the experimental setup and some of their observations, particularly the most relevant ones for the aim of this chapter.

The setup uses a transmon circuit, which is made from two Josephson Junctions in a SQUID geometry, with a capacitor connected in parallel. The transmon has several energy levels which can be addressed individually with a microwave pulse, in particular, the energy levels that will be used are $\{|g\rangle, |e\rangle, |f\rangle\}$. The spacing between these energy levels is tuned by applying a magnetic flux Φ through the SQUID loop, and the coupling between two of them $J(|e\rangle\langle f| + |f\rangle\langle e|)$ is obtained by a “*coherent resonant drive of variable amplitude and detuning*” [80].

The transmon is embedded in a 3D cavity, which introduces dissipation in the system modelled by the standard GKSL master equation. In particular, the interaction between the transmon and the fundamental mode of the cavity gives a state-dependent shift of the cavity frequency, which can be probed with a microwave tone, and then the phase-shift is detected through homodyne measurement with a Josephson parametric amplifier [80]. The idea to build the Dissipative Qubit is to consider the sub-manifold of states $\{|e\rangle, |f\rangle\}$ as the qubit system, and $|g\rangle$ as a stable ground state, effectively acting as a continuum, outside of the qubit states. Each of the energy levels $|e\rangle, |f\rangle$ has an associated decay rate Γ_e, Γ_f , the effective description as a NH Hamiltonian is only valid when $\Gamma_e \gg \Gamma_f$ so that the decay rate of the $|f\rangle$ state can be disregarded. Furthermore, the cavity has an

impedance mismatch element that allows tuning the density of states of the cavity. By changing the magnetic flux the frequency of the transition between $|g\rangle$ and $|e\rangle$ can be tuned to one of the regions where the cavity density of states is enhanced, thus giving a larger decay rate γ_e , so that the condition $\Gamma_e \gg \Gamma_f$ can be fulfilled [80]. The transition $|e\rangle \rightarrow |g\rangle$ is continuously monitored and trajectories showing a quantum jump are discarded to obtain the effective NH Hamiltonian.

The ideal behavior of the Dissipative Qubit has two phases corresponding to \mathcal{PT} unbroken, with real energy difference, and the \mathcal{PT} broken, with imaginary energy difference. These two phases give purely oscillatory and purely decaying dynamics, respectively. However, the experiments show that in the \mathcal{PT} unbroken phase, there is a residual damping term Γ_R . In one of the experiments, it is estimated to be $\zeta_R = 0.6\mu\text{s}^{-1}$, too large to be explained by the small decay rate Γ_f . The authors thus conclude that this finite decay rate is associated to “charge and flux noise” [80]. The magnetic flux is used to set the $|g\rangle$ to $|e\rangle$ transition frequency in one of the regions with high density of states, therefore noise in the flux translates to noise in the anti-hermitian part of the Dissipative Qubit, therefore the real experiment may be modelled by the Stochastic Dissipative Qubit introduced here. One of the reasons for this is that the SDQ has a \mathcal{PT} u-like phase in which the dissipative gap is non-zero. This will be investigated in detail in Sec. 3.5, which gives supporting evidence of the SDQ correctly reproducing the observed residual decay for a particular value of the strength of the noise γ .

Trapped Ion realization

A recent alternative realization of a Non-Hermitian Hamiltonian, particularly the Dissipative Qubit, has been recently reported. In here, the platform used is a *trapped ion* [235]. The basic setup uses a single $^{40}\text{Ca}^+$ ion in a linear Paul trap [267]. The setup considers four relevant energy levels $\{| \uparrow \rangle, | \downarrow \rangle, | A \rangle, | g \rangle\}$ where the qubit levels $| \uparrow \rangle = | m = +5/2 \rangle, | \downarrow \rangle = | m = +3/2 \rangle$ live in the meta-stable $D_{5/2}$ manifold, the auxiliary level $| A \rangle$ lives in the $P_{3/2}$ manifold and the ground state $| g \rangle$ lives in the $S_{1/2}$ manifold. Firstly, a Rabi drive $J\sigma_x = J| \uparrow \rangle \langle \downarrow | + \text{h.c.}$ is introduced through resonant radio frequency pulses at the qubit frequency [235]. The $| \downarrow \rangle$ state is coupled to the auxiliary state $| A \rangle$ using π -polarized light with pulse-strength J_A implementing the second drive $J_A| \downarrow \rangle \langle A | + \text{h.c.}$. The population in the $| A \rangle$ state fastly decays to $| g \rangle$ through spontaneous emission 93.5% of the time, which is described by a GKSL dissipator with jump operator $\sqrt{\Gamma_g}| g \rangle \langle A |$. When $\Gamma_g \gg J_A$ the auxiliary level can be adiabatically eliminated [268] and post-selection of the quantum jumps gives the anti-hermitian term in the Hamiltonian as $i\Gamma_{\text{TI}}\sigma_z = i\Gamma_{\text{TI}}(| \uparrow \rangle \langle \uparrow | - | \downarrow \rangle \langle \downarrow |)$, where the decay rate is $\Gamma_{\text{TI}} = J_A^2/\Gamma_g \ll \Gamma_g$.

One advantage of this experimental setup is that the decay rate depends on a quantity that can in principle be tuned, such as the pulse strength J_A , and thus it could be possible to modulate it in a noisy way $J_A(1 + \sqrt{2\gamma}\xi_t)$ which could provide a way to experimentally manipulate the strength of the noise γ . One limitation of this experimental platform is that the $| A \rangle$ level decays back to the $D_{5/2}$ manifold 5.87% of the times [235] which effectively limits the time that the NH descriptor is valid to $t \sim 2\pi/|\sqrt{J^2 - \Gamma_{\text{TI}}^2}|$. Experimentally, this means that only a couple or one Rabi oscillations can be seen before

the description breaks down. However, our main result, the presence of the NI phase, happens very fast, much faster than the Rabi oscillations since $\Delta \gg \omega$ in the NI phase. This means that it should be possible to observe the NI phase, i.e., convergence to the $|\downarrow\rangle$ state, in this experimental platform.

3.5.2 Modelling noise in the Dissipative Qubit

The antidephasing dynamics of the Stochastic Dissipative Qubit naturally lead to an exponential decay, i.e., a nonzero dissipative gap, caused by the presence of noise, even in the \mathcal{PT} -unbroken-like region, as we already discussed in Fig. 3.4 (a). The explicit expression of the dissipative gap is quite cumbersome, however, in the large J limit it is simplifies to

$$\lim_{J \rightarrow \infty} \Delta(\gamma_N J, \frac{\Gamma}{J}) J = \frac{\gamma_N \Gamma^2}{2}, \quad (3.141)$$

where the factors of J make sure that this quantity has dimensions of frequency. And the large J limit ensures that the dynamics is in the \mathcal{PT} u phase, considering that the noise is not too large, in particular $\gamma < 1/(2\Gamma)$.

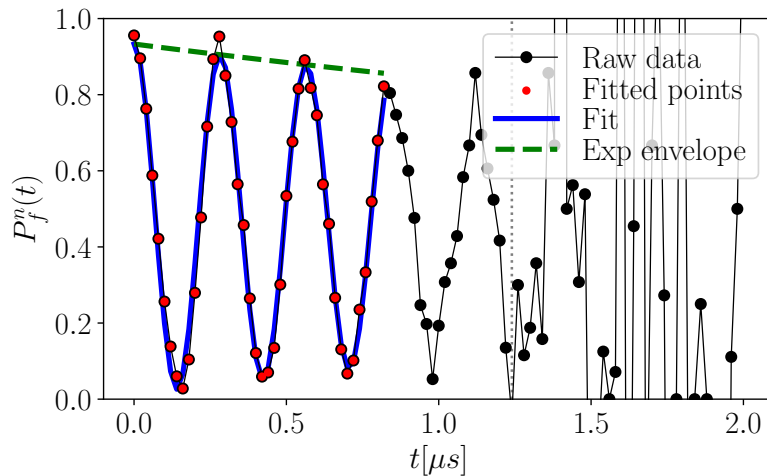


Figure 3.23. Fitting strategy for the experimental data in the \mathcal{PT} -symmetric phase. Normalized population $P_f^n(t)$ of the $|f\rangle$ state (black circles) for the full range of times, at some point the results become very noisy, so we only fit the first data points (red circles). The data in that range is fitted to the damped exponential $f_{\Gamma_R, b, c, \omega}(t)$ (blue line), which also naturally describes the exponential envelope $ce^{-\Gamma_R t} + b$ (3.142) (green dashed line).

The main observation that cannot be explained in the framework of the Dissipative Qubit is the presence of the residual damping rate estimated to be in one case $\zeta_R = 0.6 \mu\text{s}^{-1}$. Using the simplified expression for the dissipative gap at large J , we can easily extract the value of the strength of noise $\gamma_N = \frac{2\zeta_R}{\Gamma^2}$ needed to explain the residual decay rate. Using

the experimental parameter, $\Gamma = 6.7/2\mu s^{-1}$, we find that $\gamma_N = 0.107\mu s$ matches, at large J , the value $\Gamma_0 = 0.6\mu s^{-1}$.

The value for the residual decay rate is, however, not as simple as the value $\zeta_R = 0.6\mu s^{-1}$. We will devote this section to a more careful exploration of this residual damping from an analysis of the data for the evolution of the DQ in *Naghiloo et al.* [80]. Figure 3.23 presents the evolution of the normalized population of the $|f\rangle$ state $P_f^n(t)$ in time in the \mathcal{PT} unbroken phase of the DQ. We observe the characteristic oscillations from the real spectrum associated with \mathcal{PT} symmetric systems. However, careful observation shows that this evolution has a small exponential envelope, which makes the oscillations progressively decay. This is the *residual decay rate* that cannot be explained in the deterministic non-Hermitian framework. We will fit the experimental data to a damped exponential

$$f_{\Gamma_R, b, c, \omega}(t) = ce^{-\Gamma_R t} \cos(\omega t) + b. \quad (3.142)$$

Algorithm 1 Fitting strategy of Experimental Populations

```

1: for  $J \in J_{\text{arr}}$  do
2:   for  $t \in t_{\text{arr}}$  do
3:     if  $P_f^n(t) > 1$  or  $P_f^n(t) < 0$  then
4:       Append  $t$  to  $t_{\text{out}}$ 
5:     else
6:        $t_{\text{out}} = \max t_{\text{arr}}$ 
7:     end if
8:   end for
9:   Set  $t_{\text{phys}} = \min t_{\text{out}}$ 
10:  Fit  $P_f^n(t)$  to  $f_{\Gamma_R, b, c, \omega}(t)$  (3.142) in the range  $t \in [0, t_{\text{phys}-20}]$ 
11: end for

```

There is, however, one problem when dealing with the real data: some of the populations are out of the range where the populations are physical $0 \leq P_f^n(t) \leq 1$, e.g., see $t > 1.5\mu s$ in Fig. 3.23. To deal with this, we developed Algorithm 1 to decide the range of times kept for the fit. The idea is to compute the minimum time at which the normalized population is out of the physical range t_{phys} , and fit the evolution in the range before this time, where we set the offset 20 sites before t_{phys} in the array.

Figure 3.24 shows the results for the residual decay rate extracted from the experimental data (circles with errorbar), the dissipative gap as function of the qubit coupling J for different values of the noise γ_N (solid lines), the noiseless results (dashed black) and the single value $\zeta_R = 0.6\mu s^{-1}$ in [80] (dotted gray). Let us first comment on the experimental data. We see that the extracted values are not too far from the estimated value $\zeta_R = 0.6\mu s^{-1}$. However, they are not constant. In particular, they are lower than ζ_R in the \mathcal{PT} -symmetric phase, and far from the theoretical noiseless prediction (dashed black) in the \mathcal{PT} -broken region. The dissipative gap reduces to the noiseless result when the

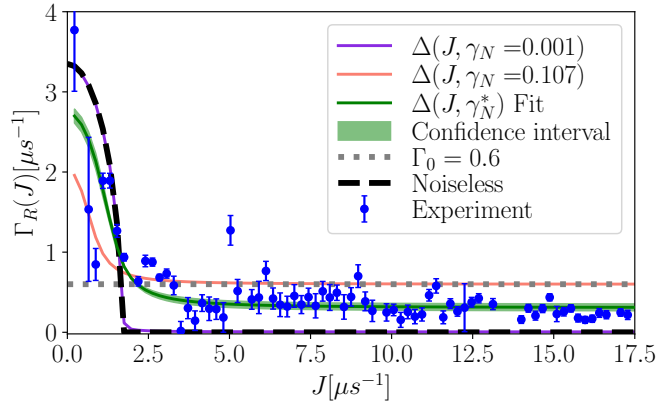


Figure 3.24. Residual damping as a function of the hopping strength J fitted from experimental data (blue points). The noiseless result ($\gamma_N = 0$, dashed black line) expected from a NH Hamiltonian $\text{Im}(\sqrt{4J^2 - (\gamma_e/2)^2})$ differs from the constant value argued in the paper $\Gamma_0 = 0.6\mu\text{s}^{-1}$ (gray dotted line). However, adding noise leads to a better match with the data. The solid lines represent the dissipative gap of the SDQ model at (i) very small noise ($\gamma_N = 0.001$ purple), (ii) at a noise level that reproduces the $\Gamma_0 = 0.6\mu\text{s}^{-1}$, given by $\gamma_N = 2\Gamma_0/\Gamma_e^2$, and (iii) lastly the fitted value to the experimental data which gives $\gamma_N^* \approx (0.055 \pm 0.004)\mu\text{s}$. The 95% confidence interval of $\pm 2\sigma$ in this parameter is also shown (shaded green region).

strength of the noise is very small (purple line), with the only caveat that the exceptional point is smoothed due to the fact that at very small, but non-zero, noise strength the exceptional point is not present. The dissipative gap at the value of the strength of the noise estimated from ζ_R is seen to fastly converge to ζ_R (pink solid line).

Given the exact expression for the dissipative gap, it is possible to fit the experimental results for Γ_R . Through a least-square minimization, we find an estimate for the strength of the flux noise in the experimental setup $\gamma_N^* \approx 0.055 \pm 0.004\mu\text{s}$, which is shown (green solid line) to model reasonably well the residual decay rate in Fig. 3.24. Even when a $\pm 2\sigma$ deviation of the optimal value of the strength of the noise is considered, the results stay very close to the prediction (green dashed region).

Hermitian vs Anti-hermitian noise

We can extend our model to a case where we have both Hermitian and anti-Hermitian noise in the Hamiltonian

$$\hat{H}_t = \hat{H}_{\text{R}} - i\hat{H}_{\text{I}} + \sqrt{2\gamma_{\text{R}}}\hat{L}_{\text{R}}\xi_t^{\text{R}} - i\sqrt{2\gamma_{\text{I}}}\hat{L}_{\text{I}}\xi_t^{\text{I}}, \quad (3.143)$$

where the classical white real and imaginary noise are uncorrelated $\mathbb{E}(\xi_t^\alpha) = 0$, $\mathbb{E}(\xi_t^\alpha \xi_{t'}^{\alpha'}) = \delta_{\alpha,\alpha'} \delta(t - t')$ with $\alpha \in \{\text{R, I}\}$. In this case, the nonlinear master equation reads

$$\begin{aligned}\partial_t \hat{\rho}_t = & -i[\hat{H}_\text{R}, \hat{\rho}_t] - \{\hat{H}_\text{I}, \hat{\rho}_t\} - \gamma_\text{R}[\hat{L}_\text{R}, [\hat{L}_\text{R}, \hat{\rho}_t]] + \gamma_\text{I}\{\hat{L}_\text{I}, \{\hat{L}_\text{I}, \hat{\rho}_t\}\} \\ & + 2\text{Tr}(\hat{H}_\text{I}\hat{\rho}_t)\hat{\rho}_t - 4\gamma_\text{I}\text{Tr}(\hat{L}_\text{I}^2\hat{\rho}_t)\hat{\rho}_t,\end{aligned}\quad (3.144)$$

which has both a dephasing and an antidephasing contribution. The non-TP Liouvillian for this master equation has exactly the same form as (3.61), with the only difference that the constants are slightly modified to include both the real and imaginary noises

$$A = \Gamma((\gamma_\text{I} - \gamma_\text{R})\Gamma - 1), \quad B = 2\Gamma(2\gamma_\text{I}\Gamma - 1).$$

As expected, the real noise only appears in A since this is the one modelling the decay of the coherence ρ_{ef} , and does not affect the populations ρ_{ee}, ρ_{ff} .

This means that we can directly use the formulas for the eigenvalues and the dissipative gap, only slightly modifying the A, B constants. We consider three possible models, fitting the strengths of the noise to the experimental data, and we find

- *Both noises:*

$$\gamma_\text{I} = (0.046 \pm 0.004)\mu\text{s}, \quad \gamma_\text{R} = (0.010 \pm 0.003)\mu\text{s}.$$

- *Antidephasing*, i.e., only anti-Hermitian noise:

$$\gamma_\text{I} = (0.055 \pm 0.004)\mu\text{s}.$$

- *Dephasing*, i.e., only Hermitian noise:

$$\gamma_\text{R} = (0.028 \pm 0.003)\mu\text{s}.$$

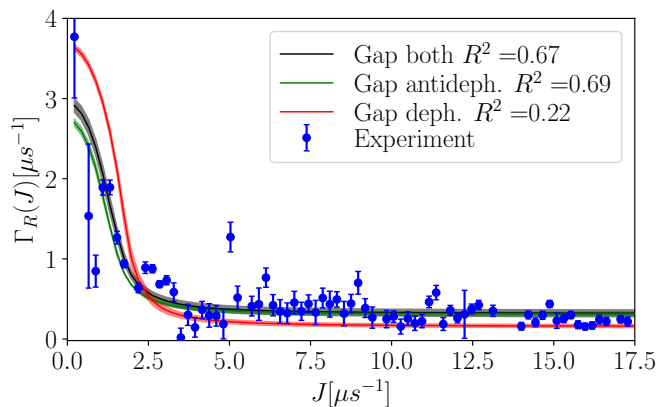


Figure 3.25. Comparison between real and imaginary noise models for the residual decay rate of the dissipative qubit as a function of the hopping J .

Figure 3.25 compares the three possible models, with their respective R^2 value showing a better fit for R^2 closer to 1. We find that the antidephasing model provides the best model, with the largest R^2 , and the model with both noises closely follows with a similar value for R^2 . This model with both noises fits a higher value for γ_i than for γ_R , almost 5 times larger. The dephasing model performs quite poorly, with a much smaller value of R^2 , from which we can claim that the anti-Hermitian noise has a more important effect on the residual decay rate than its hermitian counterpart. Further work in this line necessarily involves introducing an indicator for the goodness of the fit, which is well-suited for non-linear fits, and a further data analysis to test whether the outlier data is really needed.

These results provide the first physical application of the formalism developed in this chapter. They show that the SDQ can correctly reproduce the residual exponential decay in the \mathcal{PT} symmetric phase of the dissipative qubit, and give a tool to determine the strength of the noise in a physical setup. The fact that the residual exponential decay is not consistent with the ζ_R value provided in [80] does not pose a problem, since it was extracted from a different experiment, namely changing the detuning Δ , done at a different time. We expect that the strength of the noise in our model greatly depends on the specific conditions of the experiment, such as temperature.

Note that here we do not claim that this provides an experimental validation of our theory or of our model; to do that, a more careful experiment should be done. We think that observing the NI phase could provide a strong experimental confirmation of the theory here developed. The aim of this section is thus to showcase that our theory has predictive power beyond the current theoretical understanding of Non-Hermitian Hamiltonians.

3.6 Discussion

3.6.1 Comparison to other dynamics

The original formal approach to OQS theory considered mostly CPTP maps [29, 30]. In recent years, refined experiments have managed to implement post-selection [80] and a variety of different CPTD maps [84, 269]. This has been motivated by a variety of master equation generating different CPTD situations, such as the *hybrid Liouvillian* [252]. Furthermore, considering a biased ensemble of trajectories, where we assign different weights or probabilities to different trajectories, allows us to even create CPTI maps [240, 270], which appear in the context of *tilted Liouvillians* or *generalized master equations* [271], whose classical limit is described by the *Lebowitz-Spohn* operator [272].

The dynamics generated by the anti-dephasing master equation presented here is more general than these approaches, but it can reduce to them in proper limits. We believe this could be of interest to provide different ways of engineering antidephasing dynamics and for this reason we provide the map between the equations.

The *hybrid Liouvillian* describes a situation in which the experimentalist makes post-selection on a given quantum jump, but the detector has a finite efficiency $\eta \in [0, 1]$ at

detecting the quantum jumps. Consider, for now, a single decoherence channel

$$\tilde{\mathcal{L}}_{\hat{H}_0, \mu, q, \hat{A}}^{\text{hyb}}[\bullet] = -i[\hat{H}_0, \bullet] + \mu(q\hat{A} \bullet \hat{A}^\dagger - \frac{1}{2}\{\hat{A}^\dagger \hat{A}, \bullet\}), \quad (3.145)$$

which nicely interpolates between Non-Hermitian evolution when the detector is totally efficient $q = 1 - \eta = 0$ and Lindblad dynamics when the detector is totally inefficient $q = 1 - \eta = 1$. This hybrid Liouvillian only has a physical interpretation in terms of post-selected trajectories when $q \in [0, 1]$. The dynamics is always trace-decreasing when $q \in [0, 1)$ and trace-preserving for $q = 1$.

Let us consider the simple case of antidephasing used in the SDQ in which $\hat{L} \propto \hat{\Pi}$ when $\hat{\Pi}$ is a projector, i.e., $\hat{\Pi}^2 = \hat{\Pi}$. The antidephasing Liouvillian then reads

$$\tilde{\mathcal{L}}_{\hat{H}_R, \Gamma\hat{\Pi}, \sqrt{\gamma}\Gamma\hat{\Pi}}^{\text{AD}}[\bullet] = -i[\hat{H}_R, \bullet] + 2\gamma\Gamma^2\hat{\Pi} \bullet \hat{\Pi} - \Gamma(1 - \gamma\Gamma)\{\hat{\Pi}, \bullet\}. \quad (3.146)$$

Note that this equation is valid for any d -dimensional quantum system and not necessarily a qubit. The two equations are the same when we impose the conditions

$$\hat{H}_0 = \hat{H}_R, \quad (3.147a)$$

$$\mu q\hat{A} \bullet \hat{A}^\dagger = 2\gamma\Gamma^2\hat{\Pi} \bullet \hat{\Pi}, \quad (3.147b)$$

$$\frac{1}{2}\mu\hat{A}^\dagger\hat{A} = \Gamma(1 - \gamma\Gamma)\hat{\Pi}^2. \quad (3.147c)$$

This mapping is only valid when $\Gamma(1 - \gamma\Gamma) \geq 0$, i.e., we need to impose $\gamma\Gamma \leq 1$. Both conditions can be satisfied by setting $\hat{A} = \hat{\Pi}$ and

$$q = \frac{\gamma\Gamma}{1 - \gamma\Gamma}, \quad \mu = 2\Gamma(1 - \gamma\Gamma). \quad (3.148)$$

Note that the restriction $0 \leq q \leq 1$ imposes a further constraint on $\gamma\Gamma$, which has to be smaller than $\gamma\Gamma \leq 1/2$ so that $q \leq 1$. Therefore

$$\tilde{\mathcal{L}}_{\hat{H}_R, \Gamma\hat{\Pi}, \sqrt{\gamma}\Gamma\hat{\Pi}}^{\text{AD}} = \tilde{\mathcal{L}}_{\hat{H}_R, \Gamma(1 - \gamma\Gamma), \frac{\gamma\Gamma}{1 - \gamma\Gamma}, \hat{\Pi}}^{\text{hyb}}, \quad \gamma \leq \frac{1}{2\Gamma}. \quad (3.149)$$

Interestingly the mapping to the hybrid Liouvillian is only valid outside of the NI phase, which means that by using post-selection of quantum jumps we cannot observe the NI phase.

This mapping is also valid in the case of many noise channels which on the gybrid Liouvillian would be characterized by the set of decay rates $\{\mu_k\}_{k=1}^{N_c}$, the set of parameters quantifying how much of each jump is kept $\{q_k\}_{k=1}^{N_c}$ and the set of jump operators \hat{A}_k . The antidephasing master equation with jump operators proportional to a set of projectors is characterized by the set of decay rates $\{\gamma_k\}_{k=1}^{N_c}$, and the jump operators $\hat{L}_k = \Gamma_k\hat{\Pi}_k$.

Therefore setting

$$q_k = \frac{\gamma_k \Gamma_k}{1 - \gamma_k \Gamma_k}, \quad \mu_k = 2\Gamma_k(1 - \gamma_k \Gamma_k), \quad \hat{A}_k = \hat{\Pi}_k, \quad (3.150)$$

under the extra condition $\gamma_k \Gamma_k \leq 1/2$ gives a mapping between the antidephasing and hybrid Liouvillians with an arbitrary number of channels.

Another commonly considered master equation beyond GKSL form involves the *tilted Liouvillian*. This generator describes the dynamics of a biased ensemble of trajectories and, in its simplest form, reads

$$\tilde{\mathcal{L}}_{\hat{H}_0, \mu, s}[\bullet] = -i[\hat{H}, \bullet] + \mu(e^{-s}\hat{L} \bullet \hat{L}^\dagger - \frac{1}{2}\{\hat{L}^\dagger \hat{L}, \bullet\}). \quad (3.151)$$

This generator describes the dynamics of the biased ensemble of trajectories $\tilde{\rho}_s(t) = \sum_{K=0}^{\infty} \tilde{\rho}^{(K)}(t) e^{-sK}$, where $\tilde{\rho}^{(K)}$ represents the density matrix of the dynamics with K events after time t , i.e., jumps with operator \hat{L} . The variable s represents the conjugate field to K . The dynamics generated by this equation is not trace-preserving if $s \neq 0$, if $s < 0$ the system is in the *active* phase, in which the trajectories with jumps are favored, and the dynamics is trace-increasing, and if $s > 0$ the system is in the *passive* phase with less jumps than usual, and the dynamics is trace-decreasing [270]. A similar calculation gives

$$e^{-s} = \frac{\gamma\Gamma}{1 - \gamma\Gamma}, \quad \mu = 2\Gamma(1 - \gamma\Gamma), \quad (3.152)$$

which does not have the restriction $e^{-s} \leq 1$ and thus the mapping is valid for as long as $\gamma\Gamma \leq 1$, the argument naturally extends to the case of many channels. This mapping covers a bit of the NI phase of the SDQ, which means that in principle it should be possible to observe some features of the NI phase, like the convergence to the unstable state $|e\rangle$, by biasing quantum trajectories. However, one possible problem with this connection is that the approach in tilted Liouvillians typically uses the quantum Doob transform to map a non-CPTP map to a CPTP map, instead of using a nonlinear equation as we do.

Note that although the antidephasing Liouvillian is “more general” in the sense that it does not need to fulfill the constraint $\gamma_k \Gamma_k \leq 1/2 \forall k$ for the hybrid Liouvillian or $\gamma_k \Gamma_k \leq 1 \forall k$ for the tilted Liouvillian, and can describe a larger range of parameters, the hybrid and tilted Liouvillians account for possibly not hermitian jumps, which is a feature not present for antidephasing dynamics.

3.6.2 What did we learn in this chapter?

In this chapter, we have provided a general theory for the dynamics of Stochastic Non-Hermitian Hamiltonians. We started by writing a generic Stochastic Master Equation for the dynamics of the unnormalized density matrix $\tilde{\rho}_t$. Remarkably, this equation differs from other standard Stochastic Master equations since the drift term possesses an exotic

dissipator. We term this new dissipator the *anti-dephasing Liouvillian* since it is composed of a double anti-commutator, and it is not of GKSL form. The dynamics generated by the antidephasing Liouvillian are not trace preserving, and thus not physical by themselves, so we introduced a nonlinear term to make the dynamics physical. The choice of when to impose trace preservation can lead to several different equations, in here we first focused on describing the average dynamics of the master equation, so we took the choice of first averaging over the noise to find a non-TP master equation, which now does not depend explicitly on the noise, and impose TP to the average dynamics finding the *nonlinear antidephasing master equation*. This is the main result of our general theory; this master equation describes the average evolution of the density matrix under general white noise fluctuations in the anti-hermitian part of a non-Hermitian Hamiltonian. It describes an entirely new form of dissipative quantum dynamics, which allows for certain interesting phenomena illustrated afterwards.

After deriving the nonlinear master equation, we analyze the gauge transformations that leave the master equation invariant. In particular, we find that: a shift of the deterministic anti-hermitian part leaves the ME invariant, but not the Liouvillian; orthogonal transformations of the jump operators leave the antidephasing Liouvillian invariant, and a shift of the jump operators leaves the Liouvillian invariant when properly cancelled in the antihermitian deterministic part. To show the possibilities opened by the antidephasing dynamics, we compute an equation of motion for the evolution of the purity, which reduces to the known results for a dephasing channel and quantum brownian motion for a pure state, and involves out-of-time-order terms [1]. Furthermore, we characterized the steady states, with special focus on the *stable steady state* of the dynamics, in terms of the Liouvillian eigendecomposition. For a diagonalizable Liouvillian, i.e., without Liouvillian Exceptional Points [251], the stable steady states live in the subspace spanned by the eigenvectors whose eigenvalues have the largest real part. In particular, the convergence towards this steady state is characterized by the dissipative gap, characterizing the exponential damping of the contribution of the states living in the eigenspace with the second largest real part, and the oscillating eigenfrequencies characterizing how each of these contributions oscillates. When the system displays a Liouvillian Exceptional Point, we found that the evolution acquires an extra polynomial of time, which can change the convergence to the steady states and the steady states themselves.

To illustrate the general theory, we considered an experimentally realizable model, a stochastic version of the Dissipative Qubit [80]. We can directly find the antidephasing master equation for this system, as well as explicitly write the evolution for the purity for all the different states in the Bloch ball. The expression for the purity shows a change in behavior when $\gamma < \gamma^*$, with purifying states in the northern hemisphere, and $\gamma > \gamma^*$, with purifying states in the southern hemisphere. The spectrum of the Liouvillian can be exactly computed, which gives all the spectral information needed to understand the convergence to steady states in this model, the dissipative gap Δ , and the oscillating frequency ω .

The SDQ model shows three different phases: In the $\mathcal{PT}u$ phase the dissipative gap is very small and the oscillating frequency is large, which explains the oscillations seen in the

dynamics of this phase; in the \mathcal{PT} b phase the dissipative gap is larger and the oscillating frequency vanishes except for the line $\gamma = 1/(3\Gamma)$; and the NI phase has a very large gap and no oscillating frequency, except for $\gamma = 1/\Gamma$ and the transition from the \mathcal{PT} u to NI. Even if a non-zero oscillating frequency is present for a small part of these regions (\mathcal{PT} b and NI), the dissipative gap is larger and thus the dynamics has converged before there is a chance to see the oscillations.

The phases of the SDQ are better characterized in terms of the stable steady state properties, which follow from the properties of the eigenvector with the largest real part of the eigenvalue. The stable steady state analysis yields the main properties of the three phases: the \mathcal{PT} u shows oscillatory convergence at very long times (very small dissipative gap) to a mixed steady state close to the center of the Bloch ball, the \mathcal{PT} b phase converges to the $|f\rangle$ state and the NI phase converges to the $|e\rangle$ state, the one that has losses in the NH Hamiltonian. The stable steady states at the transitions between the phases can also be characterized: At the \mathcal{PT} u to \mathcal{PT} b transition $\Gamma/J = 2$, the state approaches $| -y \rangle$, a feature already observed in the experiment [80], at the \mathcal{PT} u to NI transition $\gamma = J/(\sqrt{3}\Gamma^2)$ the stable steady state acquires a positive y coordinate, and at the \mathcal{PT} b to NI transition $\gamma = 1/(2\Gamma)$ the stable steady state is the maximally mixed state $\hat{\rho}^s = \hat{1}/N$. Furthermore, the eigenstates of the Liouvillian can also tell us where the antidephasing Liouvillian has an Exceptional Point. We found that there can be up to 5 different LEP's in this model, two around each of the power laws $\gamma = 1/\Gamma$ and $\gamma = 1/(3\Gamma)$, all of order 2, which have a non-zero oscillating frequency, and one at $\Gamma/J = 2$, of order 4. Furthermore, the non-orthogonality of the eigenstates of the Liouvillian around the LEP $\Gamma/J = 2$ shows similar behavior to the experimental data in [80].

The dynamics of the qubit can be equivalently recast in terms of the Bloch coordinates. These provide a tool to explore the dynamics of the Bloch sphere as a vector field in the Bloch ball, and agree with the steady states predicted from the spectral analysis. In particular, the nullclines of the vector field and their intersections characterize the stable and unstable steady states of the evolution. Furthermore, from these expressions, we can compute how much of the Bloch ball is purified.

We have also studied the transitions between the different phases of the model. For finite J , all these transitions are continuous, meaning that, by zooming in on the transition point, the analogous quantity to the order parameter, i.e., the z coordinate in our case, passes through every single value. We could also compute the power law with which we converge to the $z = +1$ in the \mathcal{PT} b phase and to $z = -1$ in the NI phase; these power laws are, respectively, an inverse quadratic and an inverse quartic function of the dimensionless decay rate Γ/J . Considering the limit $J = 0$, the system shows a discontinuous transition at $\gamma\Gamma = 1/2$; it also provides a simpler understanding of the steady states, which discontinuously change from $|f\rangle$ below the transition to $|e\rangle$ over the transition. This limit also provides an explanation of why the dynamics prefers to go to $|e\rangle$ instead of $|f\rangle$; however, this analysis does not explain the full extent of the NI phase, only providing a physical reason for it when $\gamma > \Gamma^{-1}$.

The dynamics of the SDQ shows that the predictions from the spectral and steady state analysis are correct, and that the dissipative gap and oscillating frequency correctly predict the main time-scales of the dynamics.

We also considered the dynamics renormalized at single trajectories, where we showed that pure states remain pure under this dynamics and provided a justification for the validity of the approach followed in the first section of the chapter. The single-trajectory dynamics agree with the predictions from the average formalism, and extending this analysis, we can show that the noise-induced phase does not arise from the pumps.

Once the dynamics of the SDQ were fully understood, we considered the experimental implementation of our results. We first review two possible physical approaches to realize the Dissipative Qubit in the lab [80, 235]. After this, we show that the SDQ can correctly reproduce the residual decay rate observed in the \mathcal{PT} symmetric phase of the Dissipative Qubit in [80], and provide a method to find the noise strength in the experimental setup. We finished the chapter by providing the regions in which the antidephasing Liouvillian for the SDQ can be mapped to the *hybrid* and *tilted* Liouvillian.

3.6.3 Open Questions

We now state and discuss several directions for further research:

- One possible direction of study involves the study of the spectral statistics and the distribution of the eigenvalues $\lambda_n(t)$ of the stochastic non-Hermitian Hamiltonian $(\hat{H}_R + i\hat{H}_I + i\sum_{n=1}^{N_c} \xi_t^{(n)} \hat{L}_n) |n_t\rangle = \lambda_n(t) |n_t\rangle$. When N_c is extensive we expect their distribution to follow some of the distributions for complex random matrices, but in the intermediate regime with a few but not too many sources of noise, the spectrum shows very interesting behavior already for simple cases, such as point gaps [64, 65] and strange shapes of its distribution. One possible direction in this line is to extend the topological classification of non-hermitian Hamiltonians [65, 66] to stochastic Hamiltonians.
- One disadvantage of the formalism developed in this chapter is that we take a non-hermitian Hamiltonian as our starting point, and add noise to it. A possible direction would be to consider how post-selection behaves when one of the decay rates is fluctuating. In this line, it may be useful to consider the truncated noise case, cf. Sec. 3.4.3, since enforcing the decay rate of a certain channel $\mu_t = \Gamma(1 + \sqrt{2\gamma}\zeta_t) \geq 0$ ensures that the master equation is Markovian and does not run into the conceptual issues posed by non-Markovian unravelings [257]. This would make the notion of success rate in stochastic non-Hermitian dynamics clear.
- We observed that noise opens up state preparation to many different steady states. We leveraged this in the qubit case to prepare non-stabilizer or *magic* steady states [7], but the extension to more complicated many-body systems and highly entangled states remains an exciting venue for further research.
- One of the most counterintuitive results that we found in this chapter is the appearance of the noise-induced phase, where the system stabilizes to the lossy state due to

the action of the noise. We already ruled out the possibility of this phase happening due to the pumps, cf. Sec. 3.4.3, we now understand that it happens because of the property of Itō processes that $dW_t^2 \neq 0$, but a simple intuitive explanation for the appearance of this state remains to be found.

- From a practical point of view, a comparison between all the possible different approaches to explain the decay in the NH qubit, namely: open dissipative qubit [269], hybrid Liouvillian [252], anti-Hermitian noise [2] and Hermitian noise, is needed to determine what are the most important sources of noise in the experimental setup.
- Comparing with the dynamics generated by the tilted Liouvillian, we find that in this context they make their dynamics physical through a *quantum Doob transform* [240, 241, 270, 273] while we make them physical simply by renormalization. What is the difference between these two approaches, can the Doob transform provide a linear alternative to renormalization?
- A line of research which connects with the theory developed in Chap. 2 is to study a variant of the SOV, particularly that where the operator is the density matrix, for stochastic non-Hermitian dynamics.
- A more formal line of research involves the study of the properties of the eigenvectors and eigenvalues of a non-TP generator, continuing with what we found in Sec. 3.2.6.
- The single trajectory dynamics for strong noise and decay rate show a behavior reminiscent of quantum spikes [274, 275], see Fig. 3.19. Can we prove that these are spikes? For this, we need to locate first the regimes of parameters with many “pre-spikes” so that we can study whether they fulfill the statistical properties of spikes.
- Another intriguing direction is to study the behavior of the evolution when there is a Liouvillian exceptional point, where the dynamics seem to change much and cannot be described by the dissipative gap. In a similar line, it would be interesting to provide an extensive characterization of the effective dissipative gap introduced in Eq. (3.34).
- Lastly, a direction of study which could connect to quantum computing is to leverage this approach to model the stability to perturbations of imaginary time evolution algorithms [276] and to study their general computational power [277].

Results of Chapter 3

- We derived the nonlinear antidephasing master equation in the general setup (3.9)

$$\partial_t \hat{\rho}_t = -i[\hat{H}_R, \hat{\rho}_t] - \{\hat{H}_I - \langle \hat{H}_I \rangle, \hat{\rho}_t\} + \gamma \{\hat{L}, \{\hat{L}, \hat{\rho}_t\}\} - 4\gamma \langle \hat{L}^2 \rangle \hat{\rho}_t,$$

and applied it to the case of the SDQ (3.48)

$$\partial_t \hat{\rho}_t = -iJ[\hat{\sigma}_x, \hat{\rho}_t] - \Gamma(1 - \gamma\Gamma)\{\hat{\Pi}, \hat{\rho}_t\} + 2\gamma\Gamma^2\hat{\Pi}\hat{\rho}_t\hat{\Pi} + 2\Gamma(1 - 2\gamma\Gamma)\langle \hat{\Pi} \rangle \hat{\rho}_t$$

- We derived the equation of motion for the purity in the generic case (3.25)

$$\dot{P}_t = 4\text{Tr} \left(\hat{H}_1(\hat{\rho}_t P_t - \hat{\rho}_t^2) \right) + 4\gamma \left(\text{Tr}(\hat{L}^2 \hat{\rho}_t^2) + \text{Tr}(\hat{L}\hat{\rho}_t \hat{L}\hat{\rho}_t) - 2\langle \hat{L}^2 \rangle P_t \right)$$

and in the SDQ case (3.58)

$$\partial_t P_t = \Gamma r_t \left((2\gamma\Gamma - 1)(r_t^2 - 1) \cos(\theta_t) - \gamma\Gamma r_t \sin^2(\theta_t) \right).$$

- We computed analytically the spectrum of the SDQ exactly (3.66). This gives analytically the dissipative gap Δ governing exponential decay, and the oscillating frequency ω of the SDQ.
- We find that the steady state of the SDQ has three possible phases: $\mathcal{PT}u$, $\mathcal{PT}b$, and NI, characterized by $z \approx 0$, $z \approx 1$, $z \approx -1$, respectively. The Exact expression (3.74) is given by

$$z(\hat{\rho}^s) = -\frac{\lambda_0(\lambda_0 - AJ)}{4J^2 + \lambda_0(\lambda_0 - AJ)}$$

- The Stochastic Dissipative Qubit in the Noise Induced phase converges to the lossy $|e\rangle$ state, which is stabilized by the action of the noise. See Fig. 3.4
- We characterized the Liouvillian Exceptional Points of the SDQ antidephasing Liouvillian. See Figures 3.5, 3.6.
- Characterized transitions between different phases, all are continuous, see Fig. 3.12, except for the one at $J = 0$, which is discontinuous, cf. Sec. 3.3.4
- We checked that single trajectory dynamics show good agreement with the average dynamics, cf. Sec. 3.4. Furthermore, the NI phase is also present when we restrict to no pump dynamics.
- We showed that the SDQ model can correctly model the residual decay rate in the experimental realization of the Dissipative Qubit, see Fig. 3.24.

Chapter 4

Decomposing the spectral form factor

Abstract

- In this chapter, we will be concerned with understanding the role that each k -th neighbor level spacing has on the universal shape of the [SFF](#). To this end, we will introduce the k -th neighbor Spectral Form Factor $S_t^{(k)}$.
- We will compute analytical expressions for the k -th neighbor Spectral Form Factors ([knSFFs](#)) for the basic ensembles of quantum chaos theory, i.e., Gaussian Random Matrices, and Poisson. We will compute both exact and approximate expressions, which will show better numerical stability. Furthermore, throughout the chapter, we will use a physical many-body system, the *disordered XXZ* spin chain, to compare our results with a system that transitions from chaos to integrability.
- We will first compute some properties of individual [knSFF](#)'s, such as their minimum and maximum time, as well as the deepest [knSFF](#). Both of these properties show markedly different behavior between Poisson and [RMT](#), which implies that they may be used as a signature for Quantum Chaos. For this reason, we study them along the transition from chaos to integrability.
- We will focus next on the properties of sums of [knSFF](#)'s and what they can tell us about the universal ramp of the [SFF](#). To this end, we first study the *partial SFF* which only has neighbors up to range K . We study the time-scale of the onset of the ramp, characterized by either the Thouless or the dip time, as a function of the maximum range of neighbors. Interestingly, we find that all neighbors are needed to explain the full extent of the ramp, but the very short-range and the very long-range ones have a greater impact on its length.
- Another striking property that we find is that when we only consider [knSFF](#)'s with even or odd k , the two behave very differently. Almost all of the ramp is built by the even neighbors, while the biggest contribution of the odds is to cancel a resonance.

The goal of this chapter is to provide a decomposition of the spectral form factor ([SFF](#)), which highlights its relation to all the different k -th nearest neighbors level spacing distributions of its spectrum. To this end, we isolate the contribution from the k -th nearest

neighbors to the **SFF**. This quantity will be computed analytically for the different ensembles of Random Matrices. We will study their properties and use this construction to build the full **SFF** progressively, and thus distinguish the role of each spectral range in its universal shape.

4.1 Introduction

4.1.1 A story for the results

Imagine that a thousand people are asked to place a small stone in a line, and we compare two different situations:

1. The first group of people will place a stone somewhere on the line, we annotate where they placed it, and then remove it before the next participant places the stone,
2. The second group of people will place the stone, and we will keep the stone in the line. The position of the previous stones thus affects the position that a given participant will choose, and probably the next stone will be placed in one of the gaps of the previous stones.

Group 1 is generating positions in a random¹ and independent way. By independent, we mean that the position chosen for one of the stones does *not* depend on the position of the previous stones, and it does not affect the position of the future stones. Group 2, on the other hand, is also generating a random pattern, but now this pattern is *not* independent; we say it is *correlated*, since the position of one stone depends on the previous stones, and will affect the future stones.

We now see the configuration of the stones by the two groups, not knowing which one is which, and we want to determine which group is independent and which is correlated. A first option is to measure all the distances between adjacent stones and count how many of these are between 0 and 0.1, between 0.1 and 0.2, and so on. This is what statisticians call a *histogram*, and for this particular case, we call it the spacing distribution. When the positions are independent, we expect many gaps with a small distance, and a smaller number of gaps with a smaller distance between adjacent stones. When the positions are correlated, we expect very few small gaps, more gaps at an intermediate distance, and few gaps at a very long distance. The key question for us here is “*what model reproduces these distributions?*”, especially in the case where the positions are correlated. Interestingly, many correlated patterns can be described in an easy way through what we call a *random matrix*. Remember that a matrix is nothing but a table of numbers, and here we choose each of these numbers randomly. Interestingly, when we compute a thing called the *eigenvalues*² of this random matrix, they are correlated, and their distribution explains many correlated patterns, such as the thought experiment with the stones.

¹Let us assume that this is a random uniform process, although it is known that humans are notoriously bad at generating random uniform patterns.

²From a geometric point of view, a matrix can be understood as a transformation over vectors, a vector is an arrow of a certain length pointing in a certain direction. A matrix transforms a vector into a new one, for example, it can rotate it by 45°. You can think of it as stretching, contracting, and

Although we do not know that an experiment like this one was realized, and we doubt that it would even be interesting to do so, there are many examples arising in nature of random patterns that show the correlations of a random matrix. These examples include: the times of arrival of buses in Cuernavaca (Mexico) [278], a city which had a structureless bus system with autonomous bus drivers, this made each bus driver “space out” from the other; the distances between parked cars [279, 280], between birds perched on a power line [281], or even between the nests of birds of prey [282]. In the quantum world, these examples are far from anecdotal; they are so common that they are used to distinguish whether a quantum system shows chaos or not. In this framework, *chaotic* quantum systems have energy levels that are correlated in the way predicted by a random matrix, like Group 2 of the thought experiment, while *non-chaotic* systems present energy levels that behave independently, like Group 1. This characterization applies to systems as different as heavy nuclei, such as that of uranium, quantum systems such as the building blocks of quantum computers, or even models related to black holes. These examples show that correlated random patterns are ubiquitous in nature, especially in the quantum world, and thus it is very important to characterize and understand them.

In developing a more careful study of these systems, we can take several different approaches; let us mention here two particularly relevant ones:

- We can investigate the distribution of distances between stones with a given number of stones between them, for example, the distribution of distances between two stones with five stones between them. These objects are called the *k-th nearest neighbors level spacing* distributions. We can compute each of these distributions and compare with what we expect for independent and correlated positions. However, to do this accurately, we have to keep track of all the positions of the stones, which may be hard to do in a real experiment, and compare many of these distributions.
- Another possibility is to assign a musical note to every stone, where the note’s pitch is given by its position in the line, with the smallest positions having a low pitch and the highest positions having a high pitch. These musical notes can be understood as an arrow rotating on a circle at different speeds of rotation. We then combine all the notes and look at the length squared of the combined arrow as time passes, which physically corresponds to the amplitude, i.e., the loudness, of the sound. This quantity is what we call the *Spectral Form Factor* and shows a big distinction between the two cases. At the beginning, the arrows point in a similar direction, so their sum is big, and thus the sound is very loud. Still, as time passes, if the positions are independent, the frequencies have no relation to each other. They simply cancel out, leading to a constant value at long times, which we call the *plateau*, so we hear that the signal dims out and stays around a constant value that we hear as noise. However, if the positions are correlated, the story is quite different. We see that the sum of the frequencies first decreases and then increases. This part is called the *ramp*, before saturating to the plateau. This means that the sound dims out much

twisting a rubber band. Most of the directions of this rubber band will get twisted, but a few ones do not; they just get stretched or contracted, but do not change direction. These directions are what we call the *eigenvectors* of the matrix, and the *eigenvalues* are a number that tells you how much they get stretched or contracted.

more and then increases until it reaches the plateau. The presence of the ramp is an indicator of correlations in the positions and can help distinguish between the two situations. This measure is easier to compare; we just need to “hear” or look at the signal and see if it increases, and it is also more robust to missing data.

What we do in this chapter is to combine these two approaches: we decompose the spectral form factor according to the spectral distance, i.e., we isolate the contribution coming from stones which have one, two, or three . . . neighbors in between. And especially, we compute how each of them will “sound” when we assign musical notes to the positions; in a sense, each of these corresponds to a different harmonic. As a result, we get a more detailed understanding of the spectral form factor. Using this new construction, we then study how the ramp is built progressively as we consider neighbors further and further apart in the line. For example, we see the sound that the SFF would have if we only included the first, second, and third neighbors, and so on. By doing this, we find one of the main results of this chapter: we see that the neighbor ranges that have the biggest effect on the length of the ramp in the spectral form factor are the very short range and the very long range, those going almost from end to end of the line.

4.1.2 Why do we decompose the SFF?

The spectral form factor’s characteristic shape for a chaotic system: decay, correlation hole, linear ramp, and plateau, makes it a very appealing quantity to use as a signature of quantum chaos. The [BGS](#) conjecture states that quantum chaotic systems have the spectral statistics of random matrices. This conjecture was developed in systems with a well-defined semiclassical limit, such that by *quantum chaotic* systems, what is meant is a quantum system with a chaotic semiclassical limit [110]. However, in recent times, this conjecture is usually applied, and surprisingly still works in many situations, to quantum systems without a well-defined semiclassical limit, such as spin chains.

There has been great effort in trying to prove the [BGS](#) conjecture, much of it through the lens of the [SFF](#). In the semiclassical limit, the linear ramp is proven using *periodic orbit theory* [283, 284] by Berry [118]. However for systems with time reversal symmetry the [SFF](#) has logarithmic corrections for Random Matrices, the first of these corrections was derived for chaotic systems by Sieber and Richter [134, 285], and the remaining corrections were proven by Müller *et al.* [135, 286, 287]. In the many-body case, there was a recent breakthrough by Kos *et al.* [136] which could prove the linear ramp and quadratic correction for a kicked Ising spin chain with no semiclassical limit, as well as introduced a minimal model of many-body quantum chaos [288–290].

Our motivation in this chapter is different; we stay mostly on the [RMT](#) side of the [BGS](#) conjecture and unveil the structure of the [SFF](#). In particular, we focus on writing the [SFF](#) in terms of the k -th neighbor level spacing distributions. It has been argued in the literature that one can take a Wigner-surmise-like expression for them. The kn SFFs that we study throughout the chapter represent a decomposition of the [SFF](#) which highlights the role of the spectral distance. This is of great relevance because it is widely known that long-range spectral measures of quantum chaos stop agreeing with the predictions

from **RMT**. This phenomenon is known as *RMT universality breaking*. With the tools we develop here, we are able to test the regimes in which this universality breaking is particularly apparent, which quantities are more sensitive to it, and which are less. One of the main results of the chapter is that very long-range spacings, albeit highly *non-universal*, are key to explain the full extent of the ramp of the **SFF**. This highlights that there are quantities which are not very sensitive to the breakdown of **RMT** universality. The study of chaos generally involves two different types of quantities: those that characterize short-range spectral correlations, and those that characterize long-range energy correlations. Although the long-range measures can capture some short-range correlations in certain limits, e.g., number variance with $L \approx 1$, the two are quite different in their definitions. This creates a division between the two limits, where the simple quantities, like the level-spacing distribution or the spacing ratios, are studied for a wide variety of problems due to their simplicity, while the long-range measures, which are usually more delicate, are less investigated. A noteworthy exception to this is the spectral form factor, since its characteristic shape and simple definition make it appealing to compute in many different systems. The k -th neighbor level spacing distribution offers a conceptually simple interpolation between the short-range and long-range spectral measures, where the parameter is simply the neighbor range k . Our formalism introduces the **knSFF** as the time evolution associated with the k -th neighbor level spacing (**knLS**), thus interpolating more naturally between short and long-range spectral correlations, only now measured in time, instead of in frequency space.

4.2 A Wigner-surmise for the k -th neighbor level spacing distribution

Random Matrices play a defining role in the theory of quantum chaos, cf. Sec. 1.7. In particular, the BGS conjecture states that the spectral correlations of quantum systems with a chaotic classical limit will follow the predictions from RMT. When spectral correlations are studied, the most common is to study the nearest-neighbor Level Spacing (nnLS) distribution $\mathfrak{P}(s)$, which measures correlations between neighboring energies in the spectrum. However, it is important to note that correlations extend all over the spectrum. In here, we want to study long-range correlations in the spectrum, which are encoded in the joint probability density of eigenvalues of a Gaussian Random Matrix, given exactly by

$$\rho_\beta(E_1, \dots, E_N) = C \prod_{1 \leq i < j \leq N} |E_i - E_j|^\beta e^{-A \sum_{i=1}^N E_i^2}, \quad (4.1)$$

where β is the Dyson index distinguishing Orthogonal $\beta = 1$, Unitary $\beta = 2$ and Symplectic $\beta = 4$ symmetry classes (cf. Sec. 1.6.1, the product of the differences of the energies is called the *Vandermonde* determinant, the constant A sets the energy scale, while the constant C ensures normalization of the distribution but will not be relevant in our study.

In what follows, we will sometimes denote $\mathbf{E} = (E_1, \dots, E_N)$ the vector of all eigenvalues of the random matrix.

A key feature of a Random Matrix is that its eigenvalues are correlated. To characterize the correlations all over the spectrum $\{E_n\}_{n=1}^N$, we can define the *k-th neighbor level spacing* (knLS)

$$s_n^{(k)} := E_{n+k} - E_n, \quad (4.2)$$

which characterizes the difference between any energy level E_n and its k -th neighbor E_{n+k} . We want to study the knLS distribution, which can be obtained from the Joint probability distribution simply as

$$\begin{aligned} \mathfrak{P}_\beta^{(k)}(s) &= \int_{-\infty}^{\infty} dE_1 \int_{E_1}^{\infty} dE_2 \cdots \int_{E_k}^{\infty} dE_N \rho_\beta(E_1, \dots, E_N) \\ &\times \frac{1}{N-k} \sum_{n=1}^{N-k} \delta[s - (E_{k+n} - E_n)]. \end{aligned} \quad (4.3)$$

Note that this expression averages over all possible levels in the spectrum that have a k -th neighbor. This expression can be obtained by generalizing the nnLS distribution of a 3×3 random matrix [116, 291], which has two nearest neighbor level spacings that are averaged.

The exact analytical computation of the knLS distribution for a general matrix dimension and a general neighbor distance k is unknown. There is a generalization of the Wigner surmise which provides a good approximation [292, 293]

$$\mathfrak{P}_\beta^{(k)}(s) \approx C_\alpha s^\alpha e^{-A_\alpha s^2}. \quad (4.4)$$

The parameter α depends on the spectral distance k and the ensemble index β through

$$\alpha = \frac{k(k+1)}{2} \beta + k - 1. \quad (4.5)$$

The power law and the functional form of α were derived analytically in [293] and the appendix of [6]. Furthermore, in [6] we argue that this power can be corrected using the exact variance of the knLS distribution which is known analytically for random matrices. This correction introduces logarithmic corrections in the power and its asymptotic expansion is $\alpha \sim \frac{\pi^2 \beta k^2}{4 \ln(k)}$ at large k [6]. The values of A_α and C_α are

$$A_\alpha = \left[\frac{\Gamma\left(\frac{\alpha}{2} + 1\right)}{k \Gamma\left(\frac{\alpha+1}{2}\right)} \right]^2, \quad C_\alpha = \frac{2}{\Gamma\left(\frac{\alpha+1}{2}\right)} \left[\frac{\Gamma\left(\frac{\alpha}{2} + 1\right)}{k \Gamma\left(\frac{\alpha+1}{2}\right)} \right]^{\alpha+1}. \quad (4.6)$$

While the k -th neighbor level spacing for Poissonian random matrices follows the distribution

$$\mathfrak{P}_0^{(k)}(s) = \frac{1}{(k-1)!} s^{k-1} e^{-s}. \quad (4.7)$$

4.2.1 Validity of the generalized Wigner-like surmise

Let us now comment on the validity and history of derivations of a Wigner-like surmise for the $knLS$ distribution. The first derivation of such an expression that we are aware of is by Engel *et al.* [294], which assumes an ansatz like the Brody distribution [295] and leaves the power law α as a free parameter. Abul-Magd *et al.* [296] found the power α that we will use here through a small s expansion, the Wigner-like surmise then follows by assuming Gaussian behavior at large s . There are formal expressions for the $knLS$ by Mehta [103] (the $E_\beta(n, S)$ functions) which are nonetheless not explicit and thus would not allow us to perform the same kind of computations that we do in this chapter, nonetheless several connections between different neighbor ranges k and ensembles β were proven by Forrester [297]. Using approximate, but closed, expressions is typical in the physics literature since even the Wigner surmise for nearest neighbor level spacings is well-known to be an approximation for $N > 2$, to which corrections can be computed in the $N \rightarrow \infty$ limit [101]. Rao proposed a first-principle derivation of the Wigner-like surmise [293], but since the spectrum $\{E_i\}$ is not ordered $E_{i+k} - E_i$ is not guaranteed to be a k -th neighbor level spacing and thus the arguments used are not valid. In the Appendix of [6] we introduce a formal derivation which does not suffer from this issue; it does however, lead to an integral over a large dimensional simplex, which cannot be computed analytically, so we find the Wigner-like surmise, with the previously predicted power α [296], under a certain assumption to the behavior of the simplicial integral, and thus only as an approximation. This expression was generalized to two dimensions in [298] and to spacing ratios in [299]. Interestingly, this last article observes that the power α does not apply for large k . This is also something that we observed in our analysis [6], in which we proposed to correct the power to $\tilde{\alpha}$ so that the value of the variance of the $knLS$ distribution agrees with its known value analytically [6, 98, 300], this leads to the corrected power [6]

$$\tilde{\alpha} = \frac{\pi^2 \beta k^2}{2(\pi^2 \beta c_\beta + 2 \ln k)} - \frac{3}{4} + \mathcal{O}(k^{-2}), \quad (4.8)$$

where the constant is given by

$$c_\beta = \begin{cases} \frac{4}{\pi} - 1 & \beta = 1, \\ \frac{3\pi}{8} - 1 & \beta = 2, \\ \frac{45\pi}{128} - 1 & \beta = 4. \end{cases}$$

We found that comparing the $knLS$ distributions, this corrected power fits much better the numerical data, both for random matrices and for the chaotic phase of disordered

XXZ [6]. However, in the rest of the chapter, we will always use the value of the power α as in (4.5), since surprisingly for the **SFF** analysis it gives better results than some of the corrected versions $\tilde{\alpha}$. This seems to suggest that a more accurate expression for the **knLS** does not have to imply more accurate expressions for the **SFF** analysis, which is an observation that requires further study. However, most of our formulas depend on α as a parameter, so they allow us to modify $\alpha(\beta, k)$ to any function, and there may be some choice of the function which provides a more accurate **SFF** results than (4.5).

4.3 The k -th neighbor SFF

The *Spectral Form Factor* at infinite temperature is defined from the spectrum of the system $\{E_i\}_{i=1}^N$ as

$$\mathfrak{S}_t := \frac{1}{N^2} \sum_{i,j=1}^N e^{-i(E_i - E_j)t}. \quad (4.9)$$

Other customary definitions of this quantity involve a finite temperature T or other filtering functions $g(E_i)$, cf. Sec. 1.9. Here, however, we stay with the definition at infinite temperature since it will be the simplest to analyze. As it is apparent from its definition, the SFF depends on *all* the energy differences in the system $\{E_i - E_j\}_{i,j=1}^N$. The SFF is a real quantity, an expression in which this is manifestly clear reads

$$\mathfrak{S}_t = \frac{1}{N} + \frac{2}{N^2} \sum_{i>j} \cos((E_i - E_j)t). \quad (4.10)$$

This expression can be decomposed according to all the different spectral distances k , which is characterized by the k -th neighbor Level spacing $s_i^{(k)} = E_{i+k} - E_i$. In this spirit, we can define the k -th neighbor Spectral Form Factor (**knSFF**) as the contribution from the **knLS**'s with a fixed spectral range k , $\{s_i^{(k)}\}_{i=1}^{N-k}$ to the whole SFF

$$\mathfrak{S}_t^{(k)} := \frac{2}{N^2} \sum_{i=1}^{N-k} \cos(s_i^{(k)} t), \quad (4.11)$$

which, when summed over all the different spectral distances k , gives the full SFF, as expected

$$\mathfrak{S}_t = \frac{1}{N} + \sum_{k=1}^{N-1} \mathfrak{S}_t^{(k)}. \quad (4.12)$$

4.3.1 The ensemble averaged *knSFF*

The SFF is not *self-averaging* [127], which means that it shows oscillations due to *quantum noise*, which do not cancel each other. For this reason, it is customary to take an additional average. There are many possible averages that can be taken; the most common ones are

- Average over an ensemble of matrices. In the context of random matrix theory, this is the most natural since the RMT ensembles are very well-known and taking an average over them is easy. This average will be denoted $\mathbb{E}_\beta(\bullet) \equiv \mathbb{E}_{\mathbf{E} \sim \rho_\beta(\mathbf{E})}(\bullet)$, where β is the Dyson index characterizing the symmetry of the ensemble over which we average.
- Average over disorder given by some parameter in the Hamiltonian of the system. For the case of disordered XXZ, the disorder is in the parameters $\mathbf{h} = (h_1, \dots, h_L)$, which physically represents an onsite random magnetic field. This average will be denoted by $\mathbb{E}_W(\bullet) \equiv \mathbb{E}_{\mathbf{h} \sim \mathcal{U}(-\frac{W}{2}, \frac{W}{2})}(\bullet)$, where W determines the width of possible values that the disorder takes
- If there is no ensemble of matrices or a parameter to represent disorder the average can be performed by doing some time-averaging, i.e. over a window time Δt the SFF is averaged as $\mathbb{E}_{\Delta t}(\bullet) = \frac{1}{\Delta t} \int_{t-\Delta t/2}^{t+\Delta t/2} \bullet dt$, we will however not need the time-averaging in this chapter, a discussion on this average and other averages found by different filtering functions $g(E_i)$ can be found in [131].

In here, we will focus mostly on the first two averages. Therefore, the SFF averaged over a RMT ensemble can be expressed in terms of the ensemble-averaged *knSFF* as

$$S_t = \frac{1}{N} + \sum_{k=1}^{N-1} \mathbb{E}_\beta(\mathfrak{S}_t^{(k)}), \quad (4.13)$$

where the *ensemble average knSFF*, or simply *knSFF* from now on can be computed as

$$S_t^{(k)} = \mathbb{E}_\beta(\mathfrak{S}_t^{(k)}) = \frac{2}{N^2} \sum_{i=1}^{N-k} \int d^N \mathbf{E} \rho(\mathbf{E}) \cos(s_i^{(k)} t), \quad (4.14)$$

where we assume the array of energies $\mathbf{E} = (E_1, \dots, E_N)$ to be ordered $E_j \geq E_i$ if $j \geq i$, and thus the measure of this integral is a short-hand notation for

$$\int d^N \mathbf{E} \rho(\mathbf{E}) \equiv \int_{-\infty}^{\infty} dE_1 \int_{E_1}^{\infty} dE_2 \cdots \int_{E_{N-1}}^{\infty} dE_N \rho(E_1, \dots, E_N). \quad (4.15)$$

Dealing with the exact ensemble average of the *knSFF* is still a hard task. For this, we will consider the following assumption:

We consider that the energy spacing $s_i^{(k)} = E_{i+k} - E_i$ is independent of the energy level E_i . This implies that the k -th neighbor level spacing has the same distribution all throughout the spectrum. This is, of course, not true because of the density of states of the spectrum, which will have regions with more levels and regions with fewer levels. It is, however,

customary in studies of spectral statistics to *unfold* the spectrum such that the density of states is flat, and the statistics of the spacings in different parts of the spectrum can be studied jointly. Under these conditions, $s_i^{(k)} \rightarrow s_1^{(k)}$ and the sum gives a $(N - k)$ factor.

Under this assumption, and considering the *knLS* distribution to be well approximated by the Wigner surmise (4.4) the *knSFF* is given by

$$S_t^{(k)} \approx \frac{2(N - k)}{N^2} \int_0^\infty ds^{(k)} \mathfrak{P}^{(k)}(s^{(k)}) \cos(s^{(k)}t) \equiv C_N^{(k)} f_t^{(k)}, \quad (4.16)$$

where we have introduced the function $f_t^{(k)}$ as the Fourier transform of the *knLS* distribution and the constant $C_N^{(k)}$

$$f_t^{(k)} := \int ds \mathfrak{P}^{(k)}(s) \cos(st), \quad (4.17a)$$

$$C_N^{(k)} := \frac{2(N - k)}{N^2}. \quad (4.17b)$$

General Autocorrelation functions

Interestingly, this approach can be extended to a general autocorrelation function such as

$$\mathfrak{C}_t \equiv \frac{\text{Tr}(\hat{O}\hat{O}_t)}{\text{Tr}(\hat{O}^2)} = \frac{1}{\mathfrak{N}^2} \sum_{i,j=1}^N |O_{ij}|^2 \cos[(E_i - E_j)t], \quad (4.18)$$

where the normalization factor is simply given by $\mathfrak{N}^2 = \sum_{i,j=1}^N |O_{ij}|^2$. The time evolution can be re-expressed in terms of different neighbor ranges k as

$$\mathfrak{C}_t = \frac{1}{\mathfrak{N}^2} \sum_{i=1}^N |O_{ii}|^2 + \frac{2}{N^2} \sum_{k=1}^{N-1} \sum_{i=1}^{N-k} |O_{i,i+k}|^2 \cos(s_i^{(k)}t). \quad (4.19)$$

The ensemble average of this quantity is

$$\mathbb{E}_\beta(\mathfrak{C}_t) = \frac{1}{\mathfrak{N}^2} \sum_{i=1}^N |O_{ii}|^2 + \sum_{k=1}^{N-1} \mathbb{E}_\beta(\mathfrak{C}_t^{(k)}), \quad (4.20)$$

where the contribution from k -th neighbors in the spectrum has the same time dependence as for the *knSFF* but with a different prefactor

$$\mathbb{E}_\beta(\mathfrak{C}_t^{(k)}) = O_N^{(k)} f_t^{(k)}. \quad (4.21)$$

where the coefficient is given by $O_N^{(k)} = \frac{2}{\mathfrak{N}^2} \sum_{i=1}^{N-k} |O_{i,i+k}|^2$. The autocorrelation functions and their connection to the *knSFF* will play a role in Sec. 4.6 where we introduce a dissipative protocol to measure the k -th neighbor SFF. For this reason we focus on au-

tocorrelation functions, but note that under the substitution $|O_{ij}|^2 \leftrightarrow A_{ij}B_{ji}$ it is also possible to obtain a more general two point correlation function $\text{Tr}(\hat{A}_t \hat{B})/\text{Tr}(\hat{A} \hat{B})$.

4.3.2 *knSFF for Gaussian Random Matrices*

We now turn to compute the time-dependent functions $f_t^{(k)}$ which characterize the evolution of the *knSFFs*. Introducing the series expansion of the cosine function in (4.17a), we find

$$f_t^{(k)} \equiv \int_0^\infty ds \mathfrak{P}_\beta^{(k)}(s) \sum_{n=0}^\infty \frac{(-1)^n}{(2n)!} s^{2n} t^{2n}. \quad (4.22)$$

The integrals of the even powers of the spacing give

$$\int_0^\infty ds s^{2n} \mathfrak{P}_\beta^{(k)}(s) = C_\alpha \int_0^\infty ds s^{2n} s^\alpha e^{-A_\alpha s^2} = \frac{\Gamma(\frac{\alpha+1}{2} + n)}{\Gamma(\frac{\alpha+1}{2})} \frac{1}{A_\alpha^n}, \quad (4.23)$$

where the result follows from the integral

$$\int_0^\infty s^z e^{-As^2} ds = \frac{1}{2} \int_0^\infty x^{\frac{z-1}{2}} e^{-Ax} dx = \frac{1}{2} \Gamma\left(\frac{z+1}{2}\right) A^{-\frac{z+1}{2}}.$$

The ratio of Gamma functions is also called *Pochhammer symbol* $(a)_n = a(a+1)\dots(a+n-1) = \Gamma(a+n)/\Gamma(a)$. Therefore, the $f_t^{(k)}$ function is determined by the series

$$f_t^{(k)} = \sum_{n=0}^\infty \frac{\Gamma(\frac{\alpha+1}{2} + n)}{\Gamma(\frac{\alpha+1}{2})(2n)!} \left(-\frac{t^2}{A_\alpha}\right)^n, \quad (4.24)$$

which converges to a *hypergeometric function*

$$f_t^{(k)} = {}_1F_1\left(\frac{\alpha+1}{2}; \frac{1}{2}; -\frac{t^2}{4A_\alpha}\right) \quad (4.25a)$$

$$= e^{-\frac{t^2}{4A_\alpha}} {}_1F_1\left(-\frac{\alpha}{2}; \frac{1}{2}; \frac{t^2}{4A_\alpha}\right). \quad (4.25b)$$

It is now convenient to introduce a frequency ω_k in terms of the A_α constant as

$$\omega_k^2 := \frac{\alpha}{2A_\alpha}, \quad (4.26)$$

This frequency sets the inverse time-scale for oscillations of this function. Furthermore, it can be written in terms of a *Laguerre function*

$$f_t^{(k)} = \sqrt{\frac{\pi\alpha}{2}} \frac{k}{\omega_k} e^{-\frac{\omega_k^2 t^2}{2\alpha}} L_{\frac{\alpha}{2}}^{-\frac{1}{2}}\left(\frac{\omega_k^2 t^2}{2\alpha}\right). \quad (4.27)$$

The Laguerre function $L_\mu^a(z)$ is an extension of the generalized Laguerre polynomial $L_m^a(z)$ for non-integer $\mu \notin \mathbb{N}$ [301] and $a > -1$, it is defined by the series

$$L_\mu^a(z) = \sum_{k=0}^{\infty} \binom{\mu + a}{\mu - k} \frac{(-z)^k}{k!} = \sum_{k=0}^{\infty} \frac{\Gamma(\mu + a + 1)}{\Gamma(\mu - k + 1)\Gamma(a + k + 1)} \frac{(-z)^k}{k!}. \quad (4.28)$$

This expression naturally reduces to a finite sum given by the generalized Laguerre Polynomial when $\mu \in \mathbb{N}$

$$L_m^a(z) = \sum_{k=0}^m \binom{m + a}{m - k} \frac{(-z)^k}{k!}. \quad (4.29)$$

Laguerre polynomials are numerically easy to deal with, but the Laguerre functions pose a greater challenge due to the infinite sum. This means that in practice, when the arguments of the function are large and non-integer, the numerical evaluation fails. For this reason we introduce the large n expansions of the Laguerre functions³:

$$\begin{aligned} L_n^a(x) = & \frac{n^{a/2-1/4}}{\sqrt{\pi}x^{a/2+1/4}} e^{x/2} \left[\cos(\theta_{a,n}(x)) (1 + \mathcal{O}(n^{-1})) \right. \\ & \left. + \sin(\theta_{a,n}(x)) \left(\frac{b_a(x)}{\sqrt{n}} + \mathcal{O}(n^{-1}) \right) \right] \end{aligned} \quad (4.30)$$

where the auxiliary functions are defined as

$$\theta_{a,n}(x) := 2\sqrt{nx} - a\frac{\pi}{2} - \frac{\pi}{4}, \quad (4.31a)$$

$$b_a(x) := \frac{4x^2 - 12a^2 - 24ax - 24x + 3}{48\sqrt{x}}. \quad (4.31b)$$

Note that in the case relevant for us $a = -1/2$, $n = \alpha/2$ and $x = \omega_k^2 t^2 / (2\alpha)$ the function in the trigonometric functions simplifies greatly $\theta_{-1/2, \alpha/2}(x) = \omega_k t$ and the second function reduces to $b_{-1/2}(x) = \frac{\sqrt{x}}{12}(x - 3)$. This yields the approximation for the Laguerre functions appearing in the expansion of the knSFF

$$L_{\alpha/2}^{-1/2} \left(\frac{\omega_k^2 t^2}{2\alpha} \right) \approx \sqrt{\frac{2}{\pi\alpha}} e^{\frac{\omega_k^2 t^2}{4\alpha}} \left[\cos(\omega_k t) + \sqrt{\frac{2}{\alpha}} b_{-1/2} \left(\frac{\omega_k^2 t^2}{2\alpha} \right) \sin(\omega_k t) \right]. \quad (4.32)$$

This approximation neglects terms of order $\mathcal{O}(\alpha^{-1})$. When plugging this expression back into the expression for $f_t^{(k)}$, we have a prefactor k/ω_k which also needs to be approximated to the same order. If we expand all the terms explicitly, we find

$$\frac{k}{\omega_k} = \frac{1}{\sqrt{\alpha/2}} \frac{\Gamma(\alpha/2 + 1)}{\Gamma(\alpha/2 + 1/2)} = 1 + \mathcal{O}(\alpha^{-1}). \quad (4.33)$$

³See Digital Library of Mathematical Functions <https://dlmf.nist.gov/18.15#iv>

All these approximations lead to an expression of the kn SFF function $f_t^{(k)}$ of the form

$$f_t^{(k)} = e^{-\frac{\omega_k^2 t^2}{4\alpha}} \left[\cos(\omega_k t) + \sqrt{\frac{2}{\alpha}} b_{-\frac{1}{2}} \left(\frac{\omega_k^2 t^2}{2\alpha} \right) \sin(\omega_k t) \right] + \mathcal{O}(\alpha^{-1}). \quad (4.34)$$

Note that we do not expand terms involving time in large α , since we only assume $\alpha \gg 1$, but we impose no condition on the relation between $\omega_k^2 t^2$ and 2α , since it would render our approximation valid only for a certain window of times. The frequency ω_k can be expanded a large k as

$$\omega_k \approx k - \frac{1}{2\beta k} + \mathcal{O}(k^{-2}), \quad (4.35)$$

which physically means that the kn SFFs linearly increases their frequency as we consider further and further apart neighbors k .

Let us now make several remarks on the nature of $f_t^{(k)}$ in (4.34):

1. The initial value of the function is equal to unity $f_{t=0}^{(k)} = 1$,
2. For long times $t \rightarrow \infty$ the gaussian envelope $e^{-\omega^2 t^2/(4\alpha)}$ makes the function vanish $\lim_{t \rightarrow \infty} f_t^{(k)} = 0$,
3. The sine and cosine terms oscillate at the same frequency ω_k , which scales linearly with k at large k ,
4. The prefactor multiplying the cosine is simply the Gaussian envelope. For the sine term, there is an extra prefactor, which is time-dependent and less relevant for large k since it is of order $\mathcal{O}(k^{-1})$. This prefactor is more important for large t , since it vanishes identically at $t = 0$. This can be easily understood since small k terms are more significant at long times.
5. Let us compute the number of oscillations in the standard deviation of the envelope. For this, we compute the ratio between the width of the envelope $\tau_k^{(\text{env})} = \sqrt{2\alpha}/\omega_k$ and the period of the oscillations $T_k = 2\pi/\omega_k$ to be

$$\frac{\tau_k^{(\text{env})}}{T_k} = \frac{\sqrt{2\alpha}}{2\pi} \sim \frac{\sqrt{\beta}}{2\pi} k. \quad (4.36)$$

This means that the number of oscillations per width of the envelope grows linearly with k , which is apparent from Figure 4.1. Furthermore, it also grows as we consider a RMT ensemble with a larger value of the Dyson parameter β .

6. If the distribution of kn LS was a pure Gaussian function centered at $s^{(k)} = k$ the kn SFF would only involve a Gaussian envelope and the cosine term, i.e. $f_t^{(k)} = e^{-k^2 t^2/(4\alpha)} \cos(kt)$, since the Fourier transform of a Gaussian is another Gaussian. This implies that the sine contribution comes directly from the non-Gaussianity of the k^n LS distribution.

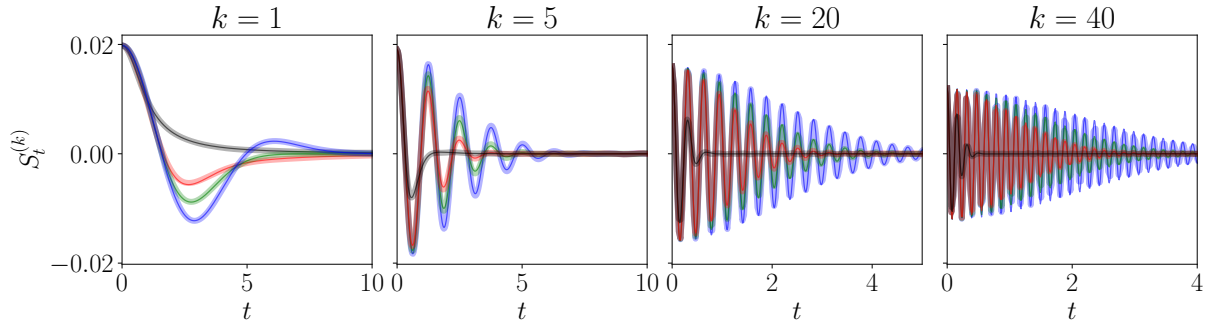


Figure 4.1. Time evolution of the $kn\text{SFF}$ for Poisson (black), GOE (red), GUE (green) and GSE (blue) for different spectral neighbors, $k = 1, 5, 20, 40$ in systems of dimension $N = 100$. The plots for $k = 5, 20, 40$ show analytical results (thin lines) from (4.39) and (4.37), while for $k = 1$ we show the exact expression (4.27), and numerical results for random matrices averaged over $N_{\text{av}} = 1000$ realizations (thick transparent lines). While we do not expect the approximation (4.37) to be good for small k , it works already quite well for GSE and $k = 1$ and less so for GUE and GOE, in that order. Note the different scales in the time axis, chosen to better represent the increasing number of oscillations with the spectral neighbor k , see Eq. (4.36). Figure adapted from [3].

The approximation to order $\mathcal{O}(\alpha^{-1})$ of the $kn\text{SFF}$ then is given by

$$S_t^{(k)} \approx \frac{2(N-k)}{N^2} e^{-\frac{\omega_k^2 t^2}{4\alpha}} \left[\cos(\omega_k t) + \frac{1}{12\alpha} \omega_k t \left(\frac{\omega_k^2 t^2}{2\alpha} - 3 \right) \sin(\omega_k t) \right]. \quad (4.37)$$

Figure 4.1 shows the comparison of the analytical approximation with the numerical simulation of Random Matrices. In particular, the plots for $k \geq 5$ show very good agreement with the approximate expression. While $k = 1$ uses the exact form of the $kn\text{SFF}$, which shows very good agreement with the numerical computation of the $kn\text{SFF}$

4.3.3 $kn\text{SFF}$ for the Poisson ensemble

The $kn\text{LS}$ distribution for Poisson (4.7) is given by a power-law, with a smaller power than the corresponding RMT distribution, multiplied by a decaying exponential, instead

of a Gaussian. The $f_t^{(k)}$ function for Poisson is then given by

$$\begin{aligned}
f_t^{(k)} &= \int_0^\infty \mathfrak{P}_0^{(k)}(s) \cos(st) ds = \frac{1}{(k-1)!} \int_0^\infty s^{k-1} e^{-s} \cos(st) ds \\
&= \frac{1}{2(k-1)!} \int_0^\infty s^{k-1} e^{-(1-it)s} ds + \text{c.c.} = \frac{\Gamma(k)}{(k-1)!} \frac{1}{2(1-it)^k} + \text{c.c.} \\
&= \frac{1}{2(1-it)^k} + \frac{1}{2(1+it)^k} = \frac{(\sqrt{1+t^2})^k (e^{ik \arctan(t)} + e^{-ik \arctan(t)})}{2(1+t^2)^k} \\
&= \frac{\cos(k \arctan(t))}{(1+t^2)^{\frac{k}{2}}},
\end{aligned} \tag{4.38}$$

where c.c. denotes the complex conjugate, and we used the definition of the Euler's Gamma function $\Gamma(z) = \int_0^\infty x^{z-1} e^{-x} dx$, its connection to the factorial $\Gamma(n) = (n-1)!$ for $n \in \mathbb{N}$, and lastly expressed it in terms of manifestly real quantities using the polar decomposition of the complex number $1+it = \sqrt{1+t^2} e^{i \arctan(t)}$

The kn SFF for the Poisson ensemble has a Lorentzian envelope to a power $k/2$, which grows as we consider neighbors further apart, multiplied by the cosine of the inverse tangent function multiplied by k . Introducing the prefactor $C_N^{(k)}$ accounting for the number of k -th spacings and the normalization of the SFF, we find the kn SFF for the Poisson ensemble to be given exactly by

$$S_t^{(k)} = \frac{2(N-k)}{N^2} \frac{\cos(k \arctan t)}{(1+t^2)^{\frac{k}{2}}}. \tag{4.39}$$

Figure 4.1 shows the kn SFF for the Poisson ensemble for different spectral ranges $k = 1, 5, 20, 40$ in black and compares it to numerical realizations of uncorrelated levels (thick transparent black lines). Compared to the random matrix case, we observe that Poisson has:

- The $k = 1$ kn SFF shows no dip, simply a monotonic decay towards zero. This is due to the fact that the nnLS of Poisson does not vanish at $s = 0$, but rather it is maximal at $s = 0$.
- For neighbors further apart $k \geq 2$ in the spectrum, the kn SFF of Poisson does show a dip, and even oscillations, arising from the small s behavior $\mathfrak{P}_0^{(k)}(s) \sim s^{k-1}$. Furthermore, note that the oscillations show the same frequency as for RMT since the average oscillation frequency is set by the average level spacing $\mathbb{E}_{0,\beta}(s^{(k)}) = k$ in both Poisson and RMT.
- The Lorentzian envelope $1/(1+t^2)^{k/2}$ attenuates the oscillations very fast, much faster than the Gaussian envelope. Note that this is not a feature of the Lorentzian nature of the envelope, which would typically have heavier tails than a Gaussian, but of the high power $k/2$. For this reason, we do not see a faster convergence to zero for $k = 1$, but only for larger spectral ranges.

4.3.4 Comparison with the disordered XXZ spin chain

A typical example of a many-body system showing a transition between chaos and integrability is the *disordered XXZ spin chain*. This system has been extensively studied in the context of many-body localization [130, 302, 303] and is described by the Hamiltonian

$$\hat{H}_{\text{dXXZ}} = \sum_{n=1}^L (\hat{\sigma}_n^x \hat{\sigma}_{n+1}^x + \hat{\sigma}_n^y \hat{\sigma}_{n+1}^y + J_z \hat{\sigma}_n^z \hat{\sigma}_{n+1}^z + h_n \hat{\sigma}_n^z), \quad (4.40)$$

where $h_n \sim \mathcal{U}_{[-\frac{W}{2}, \frac{W}{2}]}$ corresponds to random local disorder, representing physically an onsite magnetic field, with a strength of the uniform disorder W . When $W = 0$, the model is integrable through the Bethe ansatz. At small but non-zero values of the disorder, the system is chaotic, following RMT statistics, thus obeying the BGS conjecture. As W increases, the spectrum becomes integrable following Poisson statistics, which has spurred interest in this phase as potentially being a Many-Body Localized phase, in which the eigenvectors become localized. We will not investigate eigenstate properties in this thesis, nor investigate in depth the physics of the *transition* or *crossover* from chaotic to integrable statistics. See [302, 304, 305] for reviews on the topic, and [306, 307] for formal mathematical work towards a proof of many-body localization.

The kn SFFs are computed for the disordered XXZ spin chain of length L in the following way:

- We generate the random on-site magnetic field $\mathbf{h} = (h_1, \dots, h_L)$ where $h_n \sim \mathcal{U}_{[-\frac{W}{2}, \frac{W}{2}]}$ with a fixed value of the width of the disorder W . We set the parameter $J_z = 2.21$ and impose periodic boundary conditions.
- We compute \hat{H}_{dXXZ} for that realization of the noise. We want to restrict our analysis to the zero magnetization sector, i.e., the subspace with the same number of spins up as spins down, which has dimension $d = \binom{L}{L/2}$. For a spin chain of length $L = 16$ spins, the dimension of this subspace is $d = 12,870$
- We diagonalize the Hamiltonian and find the set of energies of the system $\{E_n\}_{n=1}^d$. In practice, the states close to the ground state or the highest excited state will not follow the random matrix prediction, so we restrict the $N \equiv N_{en} = 200$ energy levels around the densest part of the spectrum.
- We perform a numerical unfolding of the energies, as described in Sec. 1.6.2, to remove the dependence on the density of states $\rho(E)$. This gives the set of unfolded energies $\{e_n | e_n = \bar{\eta}(E_n)\}_{n=1}^{N_{en}}$.
- From the set of unfolded energies, we compute the set of all the kn LS $\{s_n^{(k)} | s_n^{(k)} = e_{n+k} - e_n\}_{n=1}^{N-k}$. From this we compute the kn SFF $\mathfrak{S}_t^{(k)}$.
- Lastly, we perform an average over different realizations of the local disorder \mathbf{h}_n to find the disorder-averaged kn SFF for the XXZ model

$$S_t^{(k)} = \mathbb{E}_W(\mathfrak{S}_t^{(k)}). \quad (4.41)$$

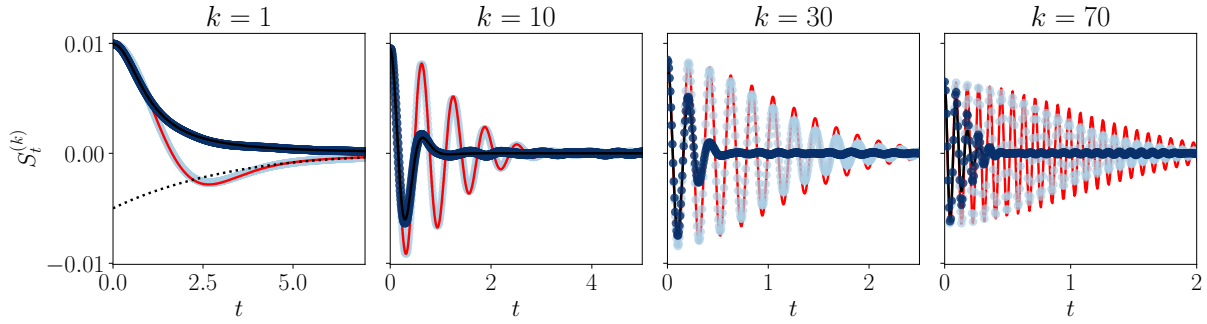


Figure 4.2. *k*-th neighbor Spectral Form Factor for the disordered XXZ spin chain for different neighbor levels $k = 1, 10, 30, 70$ in the chaotic ($W = 1$, light blue dots) and the integrable ($W = 20$, dark blue dots) phases along with the Poissonian (black line) and GOE (red line) curves. The disordered XXZ model has $J_z = 2.21$ and PBC. The deviation between the integrable phase and the Poissonian results is apparent starting from $k = 10$, and increases for larger k . Note that the oscillations differ only in their amplitude, not in their frequency. We emphasize the different scales on the time axis. Figure adapted from [3].

In Figure 4.2 we compare the GOE and Poisson kn SFFs for different spectral ranges $k = 1, 10, 30, 70$ to the kn SFFs computed numerically for the disordered XXZ spin chain in the chaotic $W = 1$ and integrable $W = 20$ regimes. We observe very good agreement between the small $k = 1, 10$ numerical results and the GOE and Poisson limit. However, when we study longer range spectral ranges $k = 30, 70$, we observe deviations from GOE and Poisson. These deviations happen particularly in the width of the kn SFF envelope, since the frequency of the oscillations agrees well with Poisson and RMT. This is a well-known occurrence in studies of long-range spectral correlations, which is known as the *breakdown of RMT universality*. In systems with a semiclassical limit, it can be understood from short periodic orbits, which do not follow the universal behavior [135, 287], but in the many-body setting, we think it still lacks a clear explanation. Interestingly, after the analytical kn SFF from Poisson has converged to zero, the numerical computation still shows some small amplitude oscillations.

4.4 Properties of the k -th neighbor SFF

We now focus on studying some of the properties of the kn SFFs. In particular, we first focus on computing the minimum and minimum-time of each kn SFF, we then explore the neighbor range k^* with the deepest kn SFF, and finally, we show that the kn SFF is also *not* a self-averaging quantity.

4.4.1 Minimum and minimum time

In here, we find analytical expressions for the minimum value attained by the kn SFF $S_{t_m}^{(k)}$ and the time at which this minimum is reached $t_m(k)$ for Random Matrices and Poisson.

Random Matrices

In principle, it would be possible to compute the minimum time $t_m(k)$ by minimizing either the exact (4.25) or approximate (4.37) expression. This is, however, quite challenging in practice. For this reason, we take the approximation (4.37) and realize that for short times the sine term is attenuated by a polynomial, which vanishes at $t = 0$; therefore, most of the contribution at short times comes from the cosine term. We also know that for large k , the oscillations are much faster than the envelope, so that we can assume that the Gaussian envelope is effectively constant.

From this argument, we easily find that the minimum of the cosine term appears when $\omega_k t_m(k) = \pi$, which gives

$$t_m(k) \approx \frac{\pi}{\omega_k} \stackrel{(4.35)}{\sim} \frac{\pi}{k}. \quad (4.42)$$

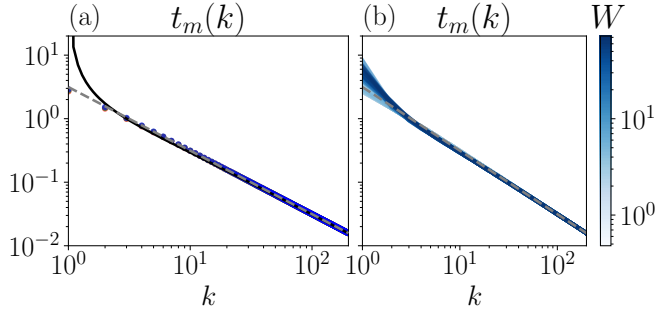


Figure 4.3. Minimum time as a function of the neighbor degree for (a) ideal ensembles: Poisson (black), GOE (red), GUE (green) and GSE (blue) computed numerically from the unfolded spectrum along with the approximate expression (4.42) (dashed grey). (b) Results for the XXZ spin chain for different values of the disorder (blue colorscale) along with the analytical result $t_m(k) = \pi/k$ (dashed gray). Figure adapted from [3].

So we find that the minimum times decay inversely proportional to the neighbor range k , and, interestingly, does not depend on the symmetry of the ensemble β . This is shown in Fig. 4.3 (a) which shows that the numerical minimum time for the three RMT ensembles is very similar, except for $k = 1$, and that it follows the approximate expression (4.42), which clearly shows a power law $t_m \sim k^{-1}$ decay (see inset). Note that for $k = 1$ the approximate expression is not valid. Furthermore, for small k , the period of the

oscillations is comparable to the characteristic time-scale of the envelope and thus the Gaussian envelope contributes to the time at which the minimum occurs.

Let us now evaluate the minimum value attained by the *knSFF* $S_{t_m}^{(k)}$, we substitute $\omega_k t_m = \pi$ and find

$$S_{t_m}^{(k)} = -\frac{2(N-k)}{N^2} e^{-\frac{\pi^2}{4\alpha}}. \quad (4.43)$$

The approximate expression for the *knSFF* is known to not hold for small k , there is however a minimal change to the expression of α , dropping the -1 factor, which gives the expression

$$S_{t_m}^{(k)} \sim -\frac{2(N-k)}{N^2} e^{-\frac{\pi^2}{2k(\beta k + \beta + 2)}}, \quad (4.44)$$

which reproduces the RMT results well for the full range of k , and for all the ensembles. Figure 4.4 (left) shows the minimum value of the *knSFF* $\min(S_t^{(k)}) \equiv S_{t_m}^{(k)}$ obtained numerically (transparent solid lines) and from the analytical expression (4.44) (dashed lines) showcasing the agreement between the two. We see that the three ensembles show different minima for small k , with the minima of GSE being the deepest, GUE the second deepest, and GOE the shallowest. Interestingly, after $k \gtrsim 10$ the three ensembles show equally deep *knSFFs*, a feature which can also be observed in Fig. 4.1. The reason behind this is that the function $-\frac{\pi^2}{2k(\beta k + \beta + 2)} \sim -\frac{\pi^2}{2\beta k^2}$ quickly converges to zero for large k , giving a value of the exponential close to unity, and the only contribution is that of the prefactor $-2(N-k)/N^2$ accounting for the number of *knLS* $N-k$.

This modification can be justified in the following way. If we evaluate the exact expression for the *knSFF* (4.25) $f_t^{(1)} =_1 F_1(\frac{\beta+1}{2}, \frac{1}{2}, -\frac{\omega_1^2 t^2}{2\beta})$ for $k=1$ where the approximated expression does not hold, the minimum does not happen at $\omega_1 t_m = \pi$ but rather for a smaller value $\omega_1 t_m < \pi$. This value can be found numerically to be

$$\begin{cases} \omega_1 t_m \approx 2.124, & S_{t_m}^{(1)} \approx -0.285 \quad \text{for } \beta = 1, \\ \omega_1 t_m \approx 2.449, & S_{t_m}^{(1)} \approx -0.446 \quad \text{for } \beta = 2, \\ \omega_1 t_m \approx 2.711, & S_{t_m}^{(1)} \approx -0.618 \quad \text{for } \beta = 4, \end{cases} \quad (4.45)$$

and evaluating (4.44) for $k=1$ gives

$$S_{t_m}^{(1)} \approx \begin{cases} -0.291 & \text{for } \beta = 1, \\ -0.439 & \text{for } \beta = 2, \\ -0.610 & \text{for } \beta = 4, \end{cases} \quad (4.46)$$

which provides a much better approximation for $k=1$, and thus corrects the behavior for small k . The large k behavior is guaranteed to work since the difference between α and $\alpha+1$ vanishes for large k .

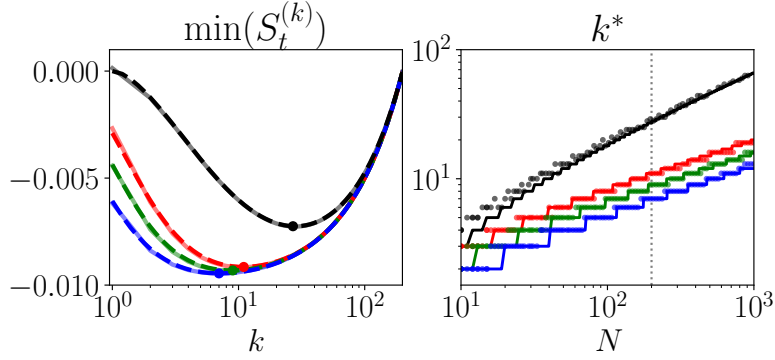


Figure 4.4. (left) **Minimum value of $kn\text{SFF } S_t^{(k)}$ as a function of the spectral distance k .** Approximate analytical results (dashed lines) for the RMT ensembles (4.44) and Poisson distribution (4.48), and numerical results (solid lines). Colors are as in Fig. 4.1, i.e., Poisson (black), GOE (red), GUE (green), and GSE (blue). The numerical results are obtained from matrices of dimension $N = 200$ and averaged over $N_{\text{av}} = 2000$ elements of the ensemble. Note that the function at large k is linear, even if the choice of logarithmic scale in the k axis does not allow a simple visualization. (right) **Scaling of the deepest neighbor k^*** as a function of the system size N computed numerically for RMT and Poisson ensembles (circles) and the analytical approximations (4.53) and (4.58) rounded to the nearest integer (lines). Numerical results are averaged over $N_{\text{av}} = 200$ matrices. We show a guide for the eye at $N = 200$ (gray dotted line), which agrees with the values of k^* used in Figure 4.6 for the Poissonian and GOE endpoints of W . Figure adapted from [3].

Poisson ensemble

In order to find the minimum time of the $kn\text{SFF}$ in the Poisson ensemble, we begin by differentiating the explicit expression (4.38) in terms of $(1 - it)^{-k}$ and setting it to zero to find

$$\begin{aligned} \partial_t f_t^{(k)} &= \frac{ik}{(1 + t^2)^{k+1}} \left((1 - it)^{k+1} - (1 + it)^{k+1} \right) = 0, \\ &(\sqrt{1 + t^2})^{k+1} e^{i(k+1) \arctan(t)} = (\sqrt{1 + t^2})^{k+1} e^{-i(k+1) \arctan(t)}. \end{aligned}$$

There are many values of t that solve this equation, which give all the relative maxima and minima of the $kn\text{SFF}$. If we set the argument of the exponential to zero, we find the first relative maxima at $t = 0$; if we set it to π , we find the first relative minimum—which is the absolute minimum since the Lorentzian envelope is monotonously decreasing for $t \in (0, \infty)$. Therefore we find the condition $(k + 1) \arctan(t_m(k)) = \pi$ which leads to

$$t_m(k) = \tan \left(\frac{\pi}{1 + k} \right). \quad (4.47)$$

Note that this expression diverges at $k = 1$ because the $k = 1$ knSFF for Poisson does not have a minimum and simply decreases monotonically towards zero; this is a consequence of the nnLS distribution for Poisson not vanishing at the origin $\mathfrak{P}_0^{(1)}(s = 0) = 1$ [120]. When k becomes large the argument $\pi/(k+1)$ becomes small and thus $t_m(k) \sim \frac{\pi}{k+1} \sim \frac{\pi}{k}$, i.e. the minimum time shows the same asymptotic value as Random Matrices. This suggests that the minimum time of the knSFF does not distinguish between chaos and integrability for $k \geq 2$, but rather shows an almost (except for $k = 1$) constant behavior in the transition from chaos to integrability, as will be discussed in the following section. Figure 4.3 (left) shows the behavior of the minimum time computed analytically for Poisson (black solid line), which shows a divergence for $k = 1$, but quickly converges, at $k = 2$, to the results from the other random matrix ensembles.

Given the analytical value of the minimum time $t_m(k)$ it is easy to compute the minimum value of the knSFF $S_{t_m}^{(k)}$, which yields

$$S_{t_m}^{(k)} = \frac{2(N-k)}{N^2} \cos^k \left(\frac{\pi}{1+k} \right) \cos \left(\frac{k\pi}{k+1} \right), \quad (4.48)$$

where the term with the k -th power is obtained from the Lorentzian envelope using the identity $1 + \tan^2(x) = \cos^{-2}(x)$. Figure 4.4 (left) shows the comparison between the analytical expression (4.48) and numerical realizations of the Poisson ensemble. We see that the depth of the first knSFF is zero, since it has no dip. Interestingly, the knSFF for the Poisson ensemble can be quite deep, deeper than $k = 1$ for GOE and GUE, for example. This is an effect coming purely from the fact that when we have many levels in between two levels, they acquire a considerable level repulsion, even if the individual levels are uncorrelated. It is also interesting to note that the minimum of the knSFF for Poisson also converges to the linear expression $-2(N-k)/N^2$; this regime stems from the fact that there is a small number of knLS's for large k . Note that this transition happens at larger values of k , $k \gtrsim 30$, which comes from the fact that $\cos(\frac{k\pi}{k+1}) \cos^k(\frac{\pi}{k+1}) \sim -1 + \frac{\pi^2}{2k} + \mathcal{O}(k^{-2})$ converges to -1 with a power $\sim k^{-1}$ instead of the power $\sim k^{-2}$ found for Random Matrices.

From this analysis, an argument as to why the Poisson ensemble shows no correlation hole readily follows. Figure 4.5 shows the minimum value attained by each knSFF for Poisson in the interval in which they show a minimum at finite time $k \in [2, 3, \dots, N-1]$. We show that none of these minima $S_{t_m}^{(k)}$ is deep enough to compensate the first knSFF which has no dip, i.e. $\nexists k$ such that $S_{t_m}^{(k)} + S_{t_m}^{(1)} < 0$.

XXZ spin chain

We now turn to discuss how the minimum of the knSFF and its minimum time show up in the disordered XXZ spin chain, which is well known to show a transition from chaos to integrability as the strength of the disorder W increases. Figure 4.3 (right) shows the minimum time as a function of k for different values of the disorder strength W . We see that in the integrable phase, large W (dark blue), the first spacing shows a larger

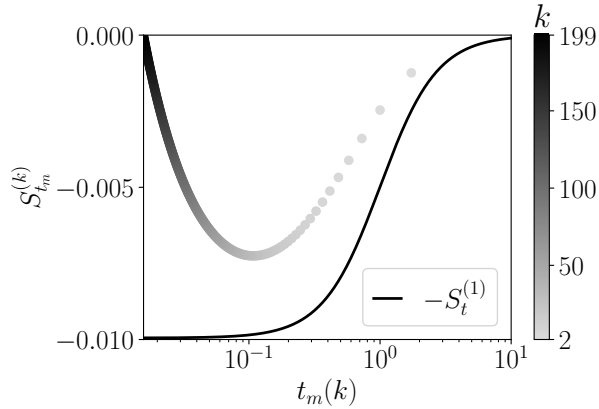


Figure 4.5. Justification for lack of correlation hole in the Poisson ensemble. The image shows the minimum value $S_{t_m}^{(k)}$ at the minimum time $t_m(k)$ (circles) for the spectral range in the interval $k \in [2, 3, \dots, N - 1]$ obtained analytically where $N = 200$. The plot also shows the first kn SFF for Poisson with a minus $-S_t^{(k=1)}$. This highlights that no kn SFF is deep enough to compensate for the value of the $S_t^{(1)}$, which does not show a dip.

minimum time, but it quickly converges to the $\sim \pi/k$ behavior. The chaotic phase, small W (light blue), follows the prediction from the first spacing quite well.

Figure 4.6 (left) shows the minimum of the kn SFF as a function of k for different values of the disorder. This quantity shows a different behavior in the chaotic or integrable phases, given respectively by GOE (red dashed line) and Poisson (black dashed line). We observe a transition between the two regimes as the strength of the disorder W is increased. Remarkably, the numerical results for XXZ in both phases show very good agreement with GOE and Poisson, respectively. This is due to two main reasons:

- The minimum of the kn SFF happens at very short times $t_m \sim \frac{\pi}{k}$ which for large k are $t_m \ll 1$. As we previously discussed, deviations from RMT happen in the envelope of the kn SFF, and at short times, the envelope has not had time to change much.
- The second reason is that the breakdown of RMT universality happens for long-range spacings, with $k \ll 1$. However, for very long-range spacings, the behavior of the minimum as a function of k is dominated by the prefactor $2(N - k)/N^2$ coming from the finite number of spacings. Therefore, even if deviations from universality could be seen in quantities relating to the minimum of $f_t^{(k)}$, this prefactor hides their effect.

4.4.2 Deepest kn SFF

We now investigate the spectral distance k^* at which the kn SFF shows the deepest minimum. For small k , considering neighbors further away, i.e., increasing k increases the depth of the kn SFF, but at large k , increasing k has the opposite effect, it decreases the

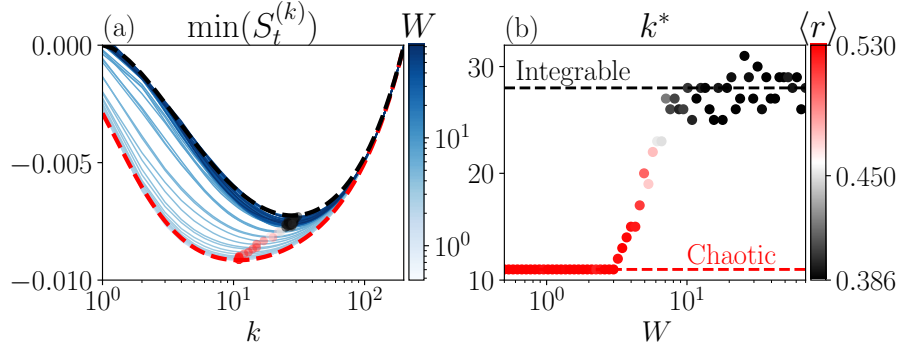


Figure 4.6. (a) Minimum of the $kn\text{SFF}$ as a function of the neighbor degree k , the colored dots mark the deepest $kn\text{SFF}$, (b) deepest k -th neighbors SFF k^* as a function of the disorder strength, the colorscale marks the $\langle r \rangle$ parameter [115]. The values of k^* for GOE and Poisson are $k^* = 11$ and $k^* = 28$ respectively, which can be obtained from the expansions for k^* (4.53), (4.58) respectively, with $N = 200$, which is the energy window size. Figure adapted from [3].

depth of the $kn\text{SFF}$. The spectral distance k^* marks the transition between these regimes: shorter-range neighbors $k < k^*$ increase the depth as k grows, and longer-range neighbors $k > k^*$ decrease the depth as k grows.

Random Matrices

To compute the k^* with the deepest $kn\text{SFF}$ we differentiate expression (4.44) to find

$$\frac{\partial S_{t_m}^{(k)}}{\partial k} = \frac{e^{-\frac{\pi^2}{2k(\beta k + \beta + 2)}} (2k^2(\beta k + \beta + 2)^2 + \pi^2(2\beta k + \beta + 2)(k - N))}{k^2 N^2 (\beta k + \beta + 2)^2}, \quad (4.49)$$

where the minimum k^* will be given by the condition

$$2k^{*2}(\beta k^* + \beta + 2)^2 + \pi^2(2\beta k^* + \beta + 2)(k^* - N) = 0, \quad (4.50)$$

Now let us consider the following limit $N \gg k \gg 1$ in which k is large, but much smaller than the number of levels N . This *mesoscopic* regime of k is indeed the relevant one in which the minimum happens, as can be seen from Fig. 4.4. The large k limit $k \gg 1$ allows us to perform the approximation

$$\frac{2\beta k + \beta + 2}{\beta k + \beta + 2} \sim 2 + \mathcal{O}(k^{-1}).$$

On the other hand, since the number of levels is much larger than the neighbor range $N \gg k$, we can approximate $k - N \approx -N(1 + \mathcal{O}(k/N))$. In the mesoscopic regime of k ,

the deepest k^* can be found from the solutions of

$$k^{*2}(2 + \beta + \beta k^*) = N\pi^2. \quad (4.51)$$

This polynomial has one real root, given by the analytical expression

$$k^* = -\frac{\beta + 2}{3\beta} + \frac{\sqrt[3]{2}(\beta + 2)^2}{3\beta \sqrt[3]{\sqrt{g_{\beta,N}^2 - 4(\beta + 2)^6} + g_{\beta,N}}} + \frac{\sqrt[3]{\sqrt{g_{\beta,N}^2 - 4(\beta + 2)^6} + g_{\beta,N}}}{3\sqrt[3]{2}\beta}, \quad (4.52)$$

where the auxiliary function $g_{\beta,N}$ is defined as

$$g_{\beta,N} := -2\beta^3 - 12\beta^2 - 24\beta + 27\pi^2\beta^2N - 16.$$

This expression is quite cumbersome and does not bring any physical insight. For this reason, taking a large N expansion, we can find the asymptotic behavior

$$k^* \sim \mathcal{C}_{\frac{1}{3}}N^{\frac{1}{3}} + \mathcal{C}_0 + \mathcal{C}_{-\frac{1}{3}}N^{-\frac{1}{3}} + \mathcal{O}(N^{-\frac{2}{3}}), \quad (4.53)$$

where the coefficients are given by

$$\mathcal{C}_{\frac{1}{3}} = \left(\frac{\pi^2}{\beta}\right)^{\frac{1}{3}}, \quad \mathcal{C}_0 = -\frac{\beta + 2}{3\beta}, \quad \mathcal{C}_{-\frac{1}{3}} = \frac{(2 + \beta)^2 - 3\beta\pi^2}{9\beta^{\frac{5}{3}}\pi^{\frac{2}{3}}}.$$

Therefore, we have found that the deepest knSFF for Random Matrices scales as the cube root of the system's dimension N . Figure 4.4 shows (right) shows the analytical expression obtained from (4.53) where we plot the nearest integer $\text{nint}(k^*)$ since $k^* \in \mathbb{N}$. This result is then compared to the numerical result (dots) obtained numerically from Random Matrices. We observe a slight deviation between the analytical prediction and the numerical value for small N , which is to be expected due to the large N expansion. Otherwise, the cube root function seems to fit quite well the behavior of k^* , especially for large N . This figure also shows that for a fixed N the neighbor range with the deepest knSFF, k^* , increases as we decrease β , i.e. $k_{\text{GSE}}^* < k_{\text{GUE}}^* < k_{\text{GOE}}^*$.

Poisson ensemble

Let us consider again the mesoscopic limit in which $1 \ll k \ll N$, expanding the knSFF for the Poisson ensemble in large k leads to the expression

$$S_{t_m}^{(k)} = -\frac{2(N - k)}{N^2} \left(1 - \frac{\pi^2}{2k} + \frac{4\pi^2 + \pi^4}{8k^2} + \mathcal{O}(k^{-3})\right), \quad (4.54)$$

whose minimum is given by the real solutions of the cubic equation

$$8k^3 - \pi^2 k (4N + \pi^2 + 4) + 2\pi^2 (4 + \pi^2) N = 0, \quad (4.55)$$

given by

$$k^* = \frac{\sqrt[3]{\sqrt{4g_{0,N}^3 + h_{0,N}^2} + h_{0,N}}}{24\sqrt[3]{2}} - \frac{g_{0,N}}{12 \cdot 2^{2/3} \sqrt[3]{\sqrt{4g_{0,N}^3 + h_{0,N}^2} + h_{0,N}}}, \quad (4.56)$$

which depends on the auxiliary functions

$$g_{0,N} := -96\pi^2 N - 24\pi^4 - 96\pi^2, \quad (4.57a)$$

$$h_{0,N} := -(3456\pi^4 + 13824\pi^2)N. \quad (4.57b)$$

The exact solution is again quite involved and cumbersome; however, taking the large N limit, we find

$$k_0^* \sim \frac{\pi}{\sqrt{2}} N^{\frac{1}{2}} - \left(1 + \frac{\pi^2}{4}\right) + \mathcal{O}(N^{-\frac{1}{2}}). \quad (4.58)$$

Therefore, the deepest $knSFF$ scales faster than for the Gaussian ensembles, in particular for the Poisson ensemble, it scales as the square root of the dimension of the system. This can be observed in Fig. 4.4 (right), where we see that the deepest k^* is much larger for Poisson than for the RMT ensembles. We can also observe good agreement between the numerical results and the predicted growth at large N .

XXZ spin chain: Transition from chaos to integrability

The value of k^* shows a markedly different behavior in Poisson and RMT ensembles and thus can be used to probe the transition between chaos and integrability. In a similar way to the average level spacing ratio $\langle r \rangle$ [115] [cf. Sec. 1.8.1], k^* is a scalar indicator of the transition between chaos and integrability. Restricting to a system of size $N = 200$, the predicted values of k^* from (4.53) and (4.58) are $k_{\text{GOE}}^* = 11$ and $k_{\text{P}}^* = 28$. Figure 4.6 (b) shows the transition between these two values as we increase the strength of the noise W , we observe that the chaotic phase agrees very well with the analytical prediction (red dashed line), at $W = 3$ we start to see k^* growing, notably this deviation happens at a smaller value of W than for the average spacing ratio $\langle r \rangle$ (colorscale) which still remains close to the chaotic value until $W \approx 5$. This implies that the transition from chaos to integrability is not as sharp when using this indicator. When $W \gtrsim 8$, the system is in the integrable phase. This phase has a larger deviation of the numerical data around k_{P}^* , which may come from the shallower minimum, making the determination of the deepest $knSFF$ less precise, cf. Fig. 4.6 (a).

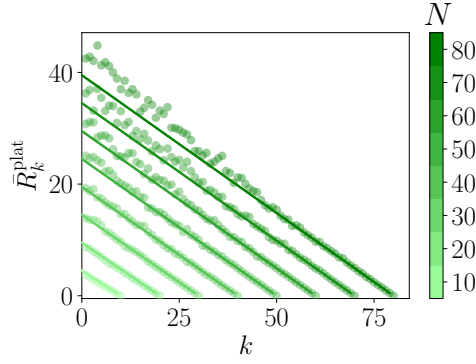


Figure 4.7. Relative variance of the plateau of the $kn\text{SFF}$ as a function of the neighbor degree k , for GUE random matrices of dimension N (colorscale). The results are averaged over $N_{\text{av}} = 1000$ ensemble realizations and $\bar{R}_k^{\text{plat}} := \frac{1}{T} \int_{t_p}^{t_p+T} R_k(\tau) d\tau$ is the time averaged relative variance on the plateau. Solid lines correspond to (4.61). Figure adapted from [3].

4.4.3 The $kn\text{SFF}$ is not self-averaging

The SFF is well-known to *not* be self-averaging [127]. This property refers to the oscillations present in the SFF that do not vanish as we take larger and larger system sizes N . In this section, we study whether or not the $kn\text{SFF}$ s are self-averaging, and we find that they are not, which was to be expected since if they were self-averaging, the full SFF, a mere sum of them, would also be self-averaging.

A given physical quantity is *self-averaging* if its relative variance decreases as the system size N is increased. In here we follow Schiulaz *et al.* [308] and define the relative variance $R_k(t)$ of the $kn\text{SFF}$ $\mathfrak{S}_t^{(k)}$ as

$$R_k(t) := \frac{\mathbb{E}_\beta((\mathfrak{S}_t^{(k)} + c_N)^2) - \mathbb{E}_\beta(\mathfrak{S}_t^{(k)} + c_N)^2}{\mathbb{E}_\beta(\mathfrak{S}_t^{(k)} + c_N)^2}, \quad (4.59)$$

where $c_N = \frac{1}{N(N-1)}$ is the value of the plateau divided equally between all the $N-1$ possible neighbor ranges. We have added this value to ensure that the average of the $kn\text{SFF}$ is non-zero $\mathbb{E}_\beta(\mathfrak{S}_t + c_N) > 0$, and thus the ratio is well-defined. The time regime in which the lack of self-averaging of the SFF is particularly apparent is the plateau; for this reason, we introduce the time-averaged relative variance in the plateau as

$$\bar{R}_k^{\text{plat}} := \frac{1}{T} \int_{t_p}^{t_p+T} R_k(\tau) d\tau. \quad (4.60)$$

Figure 4.7 shows the relative variance of the plateau for each $kn\text{SFF}$ as a function of k for GUE ensembles of different dimensions N . We observe that the relative variance

decreases approximately linearly with k following the scaling law

$$\bar{R}_k^{\text{plat}} = (N - k) \frac{N - 1}{2N}. \quad (4.61)$$

This equation shows that the kn SFF are *not* self-averaging since increasing the dimension of the system N increases linearly the relative variance of the plateau, which means that quantum noise shows up in the individual kn SFFs $\mathfrak{S}_t^{(k)}$ and thus they need to be averaged, as we have done in the rest of the chapter.

In this analysis, there is a paradoxical effect; we “guessed” the scaling law (4.61) from the numerical data. If, however, we try to compute it analytically, we find a different scaling that does not agree with the numerical results. If t is in the plateau $\mathbb{E}_\beta(\mathfrak{S}_t^{(k)}) = 0$, therefore the Relative variance simplifies to

$$\begin{aligned} R_k(t \geq t_p) &= N^2(N - 1)^2 \left(\mathbb{E}_\beta(\mathfrak{S}_t^{(k)})^2 + \frac{1}{N^2(N - 1)^2} - \frac{1}{N^2(N - 1)^2} \right), \\ &= N^2(N - 1)^2 \mathbb{E}_\beta(\mathfrak{S}_t^{(k)})^2. \end{aligned} \quad (4.62)$$

Now, assuming that all spacings behave equally, which they should since we unfolded the spectrum, we can write $\mathfrak{S}_t^{(k)} = \frac{2(N - k)}{N^2} \cos(st)$. At this point, we can either compute the ensemble average analytically as

$$\begin{aligned} \mathbb{E}_\beta(\mathfrak{S}_t^{(k)})^2 &= \left(\frac{2(N - k)}{N^2} \right)^2 \int_0^\infty \cos^2(st) \mathfrak{P}_\beta(s) ds \\ &= 2(N - k)^2 \frac{{}_1F_1\left(\frac{\alpha+1}{2}, \frac{1}{2}, -\frac{t^2}{4}\right) + 1}{N^4} \xrightarrow{t \rightarrow \infty} \frac{2(N - k)^2}{N^4}, \end{aligned} \quad (4.63)$$

or exchange the ensemble and time-average to compute

$$\frac{1}{T} \int_{t_r}^{t_r+T} d\tau \mathfrak{S}_t^{(k)2} = \left(\frac{2(N - k)}{N^2} \right)^2 \frac{1}{T} \int_{t_r}^{t_r+T} d\tau \cos^2(st) \xrightarrow{T \rightarrow \infty} \frac{2(N - k)^2}{N^4}, \quad (4.64)$$

where t_r is a reference time in the plateau $t_r > 2\pi$. Both approaches yield the time-averaged relative variance at the plateau to be given by

$$\bar{R}_k^{\text{plat}} = \frac{2(N - 1)^2(N - k)^2}{N^2}. \quad (4.65)$$

This scaling decays quadratically while the numerical results suggest a linear decay, implying an inconsistency between the numerical and analytical approaches, which requires further study to be solved.

4.5 Building the full SFF

In this section we consider how the formalism developed in the previous sections that introduced the *knSFF*, can help in explaining the behavior of the full SFF. In particular we study how each spectral range k affects the build-up of the correlation hole.

4.5.1 The partial SFF

The quantities studied in the previous section, i.e., the properties of single *knSFFs*, do not help in describing the features of the full SFF. This is because the SFF is the sum of many fastly oscillating functions, and its particular shape comes from cancellations of these oscillatory functions.

In order to overcome this obstacle, whilst keeping information of the k -th spectral range, we introduce the *partial K -neighbors SFF*, which considers only the first K neighbors $k \in [0, 1, \dots, K]$

$$S_{t,K} := \frac{1}{N} + \sum_{k=1}^K S_t^{(k)}. \quad (4.66)$$

Note that when $K \rightarrow N - 1$, the partial SFF recovers the standard SFF. We now turn to study how the ramp is built as we consider longer-range neighbors.

Time-scales of the Ramp: Dip and Thouless times

To characterize the extent of the ramp, the first requirement is to introduce a time-scale that determines the start of the ramp, without the need for human observation. In here we consider two different characteristic times, which we define and study below.

The general behavior of the SFF involves: decay, dip, ramp, and plateau. This behavior will also be present in the partial SFF. One may think of defining the *dip time* as the time at which the SFF reaches the absolute minimum. This is, however, not a good definition for the particular definition of the SFF used here, although it may work reasonably well at finite temperature or with a particular filter function, since the oscillations in the decay can reach smaller values than the dip. For this reason, we define the dip time for the partial K -neighbors SFF $S_{t,K}$ in the following way:

1. We first compute the set of relative maxima of the partial SFF

$$t_{\text{rel-max}}^{(K)} := \{t' \in \mathbb{R} \text{ such that } \dot{S}_{t,K}|_{t'} = 0, \ddot{S}_{t,K}|_{t'} < 0\}, \quad (4.67)$$

2. The dip time then is given by the absolute minimum of the SFF evaluated at the relative maxima, i.e., the dip time $t_{\text{dip}}^{(K)}$ fulfills

$$S_{t_{\text{dip}}^{(K)},K} = \min_{\tau \in t_{\text{rel-max}}^{(K)}} S_{\tau,K} \quad (4.68)$$

This definition is illustrated in Fig. 4.8 (bottom). The partial SFF shows some oscillations before the onset of the ramp, and, due to quantum noise, shows small fluctuations in the ramp. The relative maxima $t_{\text{rel-max}}$ are highlighted (dark green dots), and they show clearly an absolute minimum around the onset of the ramp (red line). This definition ensures that after the dip time $t > t_{\text{dip}}^{(K)}$ the relative maxima of the partial SFF grow, i.e., after the dip time the SFF grows on average, which can be taken as a definition of the beginning of the ramp.

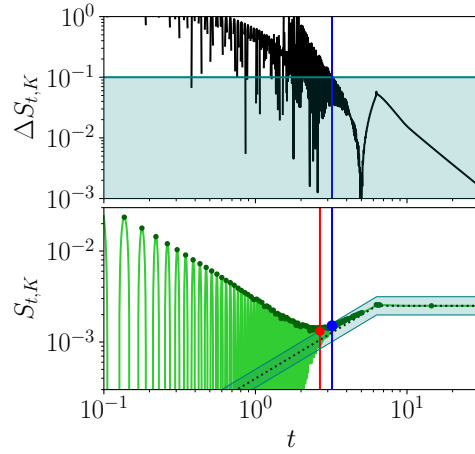


Figure 4.8. Visualization of the Thouless (blue) and dip (red) times for the partial SFF with $K = 150$, $N = 200$ for the GUE, constructed from the analytical expressions for the knSFF's derived in the main text. (top) Visualization of the logarithm of the ratio of SFF and the connected SFF $\Delta S_{t,K}$. The tolerance parameter $\epsilon = 0.1$ (turquoise horizontal line) and the Thouless time (blue vertical line). (bottom) Partial SFF for the GUE (light green solid line), along with the relative maxima (green circles), and the connected SFF (black dotted line). The shaded area shows the interval $[b_t 10^{-\epsilon}, b_t 10^{+\epsilon}]$ for visualization of the condition $\Delta S_{t,K} = \epsilon$. We stress that the defining condition of the Thouless time is more clearly seen in the behavior of $\Delta S_{t,K}$ and not in this area. Figure adapted from [3].

The second natural time-scale comes from the universality of the ramp of the SFF and is known as the *Thouless time*. This timescale was originally proposed in the single-particle context by *Edwards and Thouless* [309] and studied extensively for many-body spectral form factors by Šuntajs *et al.* [130], which is the definition that we will follow⁴. Let us begin by introducing the logarithmic ratio of the partial K neighbors SFF $S_{t,K}$ and the connected SFF b_t (see Sec. 1.9.2)

$$\Delta S_{t,K} = \left| \log_{10} \left(\frac{S_{t,K}}{b_t} \right) \right|. \quad (4.69)$$

⁴If $K < N - 1$, the partial SFF is not necessarily positive. This poses a problem for the smoothing of the SFF since it has very pronounced oscillations, which may become negative. For this reason, contrary to the approach in Ref. [130], we decide not to smooth the SFF through a time average.

The *Thouless time* $t_{\text{Th}}^{(K)}$ for the partial SFF is then defined as the time such that

$$\Delta S_{t_{\text{Th}}^{(K)}, K} = \epsilon, \quad \text{and} \quad \Delta S_{t, K} < \epsilon, \quad \forall t > t_{\text{Th}}^{(K)}. \quad (4.70)$$

This time thus characterizes the time after which the partial K SFF stays close—with a tolerance set by ϵ —to the connected universal SFF b_t . Figure 4.8 (top) shows the logarithmic ratio $\Delta S_{t, K}$ for the partial SFF for GUE with $K = 150$ neighbors, computed from the approximation of the kn SFFs. The Thouless time (blue vertical line) is defined as the time when the logarithmic ratio remains smaller than the tolerance parameter ϵ (horizontal turquoise line). This plot also showcases another interesting phenomena, the logarithmic ratio, although smaller than the tolerance ϵ , decreases in the ramp and has a relative maximum exactly at the Heisenberg time $t_p = 2\pi$, this relative maximum is not seen in the logarithmic ratio between the full SFF and the connected SFF $\Delta S_{t, N-1}$ (cf. Fig. 4.14 $\beta = 2$ bottom) which suggests that the neighbors $k > 150$ play a role in smoothing the transition from the ramp to the plateau. In the same figure we observe that the log ratio $\Delta S_{t, N-1}$ in the plateau for GUE fastly decreases and is $\Delta S_{t, N-1} < 10^{-5}$ at $t = 10$ which implies that the very long-range neighbors $k > 150$ also play a role in suppressing the oscillations of the full SFF in the plateau. Figure 4.8 (bottom) shows the connected SFF for GUE b_t^{GUE} (dotted black line), along with the interval $[b_t 10^{-\epsilon}, b_t 10^{+\epsilon}]$ intended to visualize the condition $\Delta S_{t, K} = \epsilon$.

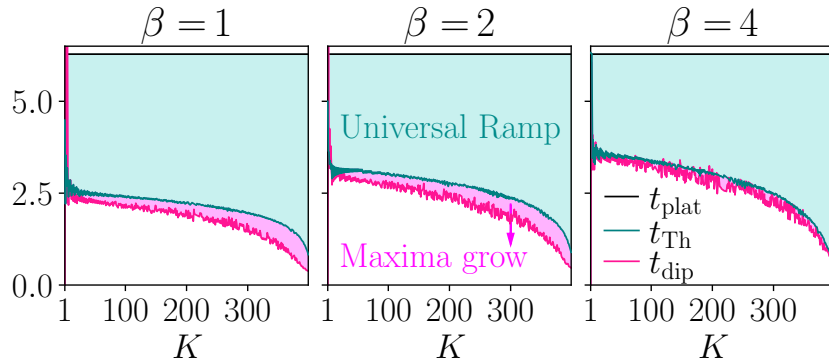


Figure 4.9. Time scales for the partial K -neighbors SFF. The plots show the dip (pink), Thouless (turquoise), and plateau $t_p = 2\pi$ (black) times as a function of the maximum number of neighbors K considered, for the three Gaussian ensembles. The shaded regions represent the part where the SFF grows in a non-universal way (pink) and where it grows with the universal ramp of the connected SFF (light blue). The results are computed with $N_{\text{en}} = 400$ from the analytical expressions of the SFF for Random Matrices (4.37). For the Thouless time, we used the partial SFF without smoothing, taking $\epsilon = 0.1$ for GOE and GUE and $\epsilon = 0.25$ for GSE. This choice is due to the challenge in building the full spike of the GSE from summing kn SFFs (cf. Sec. 4.5.3). Figure adapted from [3].

Figure 4.9 shows the *dip* (pink) and *Thouless* (turquoise) times, along with the Heisenberg time $t_p = 2\pi$ at which the plateau starts. These time-scales are computed for the partial

SFF and thus depend on the maximum number of neighbors K considered. When the time is larger than the dip time $t > t_{\text{dip}}$ the relative maxima grow (pink shaded area) but in a non-universal way, and when the time is larger than the Thouless time $t > t_{\text{Th}}$ the partial SFF follows the universal ramp of the connected SFF (turquoise shaded area), up to a tolerance of ϵ . Interestingly, in the case of RMT, we find that the dip time precedes the Thouless time, i.e., $t_{\text{dip}} < t_{\text{Th}} < t_{\text{plat}}$. The time-scale of the start of the ramp generally shows a fast decrease when K is small $K \lesssim 5$, because adding a new neighbor range affects drastically the start of the ramp, in whichever definition of its characteristic time. After this initial decay, we find that the decay slows down, i.e., adding one more neighbor range when K is already large, say $K = 100$, does not change much the start of the ramp. However, this is not the case when K is very large; in this regime, the decay speeds up for the further apart neighbors $K \gtrsim 350$, and we see that the very long-range neighbors are key to explaining the full extent of the ramp in the SFF.

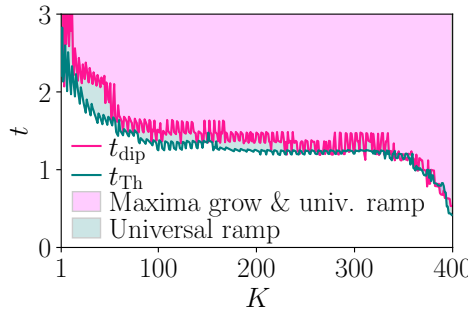


Figure 4.10. Thouless and dip times for the kn SFF as a function of the maximum neighbor range K for the XXZ model in the chaotic phase. The results use $\epsilon = 0.2$ [130] considering $N_{\text{en}} = 400$ energy levels and averaged over $N_{\text{av}} = 150$ realizations of the disorder. Figure adapted from [3].

Figure 4.10 shows the dip and Thouless times for the disordered XXZ spin chain in the chaotic phase $W = 1$. The qualitative results agree with the prediction from random matrices, considering the short-range $K \lesssim 50$ neighbors start to form the ramp. The extent of the ramp does not change, and actually stays flatter than in the RMT case, as we consider neighbors $100 \lesssim K \lesssim 300$, which means that these are not key to explain the extent of the ramp, and lastly considering the furthest apart neighbors $K \gtrsim 350$ decreases the starting time of the ramp. Therefore, we find that the neighbors who are more responsible for the full extent of the ramp are the short- and the very-long-range neighbors, and that the intermediate neighbors do not affect the ramp much. In the particular case of disordered XXZ, we see that actually the Thouless time precedes the dip time, contrary to what was observed in RMT, but since the definitions measure slightly different properties of the start of the ramp, i.e., when maxima start to grow and when the partial SFF is ϵ -close to the connected SFF, there is no general argument to say which one should happen first and it will depend on particular features of the underlying system.

4.5.2 Contribution from even and odd neighbors

One may wonder what the effect is of considering only even or odd values of k , i.e., a system with only the even or odd level spacings. The ensemble average of the *even* and *odd* knSFFs is given by

$$\mathbb{E}_\beta \left(\mathfrak{S}_t^{(\text{even})} \right) = \frac{1}{2N} + \sum_{k \text{ even}} \mathbb{E}_\beta \left(\mathfrak{S}_t^{(2k)} \right), \quad (4.71\text{a})$$

$$\mathbb{E}_\beta \left(\mathfrak{S}_t^{(\text{odd})} \right) = \frac{1}{2N} + \sum_{k \text{ odd}} \mathbb{E}_\beta \left(\mathfrak{S}_t^{(2k-1)} \right). \quad (4.71\text{b})$$

The reader should also note that the plateau value $1/N$ was split equally between both quantities.

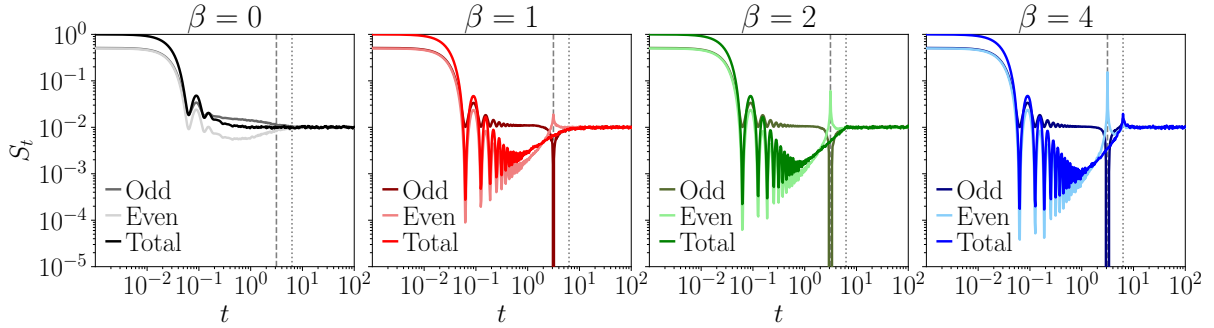


Figure 4.11. Odd vs even neighbor contributions to the SFF and their sum for Poisson, GOE, GUE and GSE; computed numerically from $N_{\text{av}} = 1000$ matrices of dimension $N = 100$. For visualization of the data in a log-log scale, an extra factor of $1/2N$ was added to the even and odd contributions. The even contributions construct a ‘resonance’ while the odd ones construct an ‘anti-resonance’. The vertical lines highlight the time at which the resonance and anti-resonance happen, $t^* = \pi$ (dashed gray), and at which the plateau starts for the Gaussian ensembles, $t_p = 2\pi$ (dotted gray). Figure adapted from [3].

Figure 4.11 shows the time evolution of the even and odd SFFs computed numerically for Poisson and the different RMT ensembles along with their sum, or *total* SFF. Inspecting these plots, we find an interesting phenomenon, the even neighbors build most of the ramp of the SFF, and then constructively interfere—showing a ‘*resonance*’—at $t = \pi$, in the middle of the ramp. The odd neighbors, however, stay almost constant during most of the ramp and only constructively interfere to build a negative peak—which we will call an ‘*anti-resonance*’—which exactly cancels the resonance in the even neighbors. The similarity between the even SFF in GOE and the total SFF in GSE is also noteworthy. Mehta and Dyson discovered that “*the probability distribution of a set of N alternate eigenvalues of a matrix in the orthogonal ensemble of order $2N$ is identical with the probability distribution of the set of all eigenvalues of a matrix in the symplectic ensemble of order N* ” [310]. This is exactly the reason why the even SFF in GOE is so similar to the full SFF

in GSE, up to the detail that since the connection is between $\text{GOE}(2k, 2N) \equiv \text{GSE}(k, N)$, the time at which the spike happens is $t = \pi$ for the even SFF of GOE and $t = 2\pi$ for GSE. This deep connection can be easily justified from the power $\alpha_{\beta, k}$ since the two power laws coincide for all k

$$\alpha_{1,2k} = k(2k + 1) + 2k - 1 = 2k(k + 1) + k - 1 = \alpha_{4,k}, \quad (4.72)$$

Therefore we can conclude that the emergence of the resonance is very similar to the emergence of the spike in GSE, in light of our formalism, we will propose an intuitive explanation for the spike in the next subsection.

The emergence of the resonance and antiresonance can be simply motivated from our analytical results

$$S_t^{(\text{even/odd})} = \frac{1}{2N} + \sum_{k \text{ even/odd}} C_N^{(k)} f_t^{(k)}. \quad (4.73)$$

If we take the large k approximation for the frequency of the oscillations $\omega_k \approx k$ and we discard the corrections to the cosine term the even and odd SFF's are, respectively, of the form $\sum_n \cos(2nt)$ and $\sum_n \cos((2n+1)t)$, when $t = \pi$ the terms of the form $\cos(2n\pi) = 1$, while the odd terms $\cos((2n+1)\pi) = -1$, which explains the observed resonance and anti-resonance. This simple argument does not explain, however, why most of the ramp is built from the even neighbors, nor why this anti-resonance appears in the middle of the ramp. To the best of our knowledge, these remain unanswered questions.

4.5.3 The full SFF

In the previous sections, we have studied how the different spectral distances k contributed to either individual k NSFFs or to their role in building progressively the ramp as more and more neighbors are considered. In here we consider the sum of all the k NSFFs, and study how well it reproduces the numerical and connected SFF.

Using the approximation for the k NSFFs, we can find an approximation to the total SFF as

$$S_t = \frac{1}{N} + \sum_{k=1}^{N-1} \frac{2(N-k)}{N^2} e^{-\frac{\omega_k^2 t^2}{4\alpha}} \left[\cos(\omega_k t) + \frac{\omega_k t}{12\alpha} \left(\frac{\omega_k^2 t^2}{2\alpha} - 3 \right) \sin(\omega_k t) \right]. \quad (4.74)$$

Figure 4.12 compares the analytical approximation to the full SFF (solid thin lines) given by (4.74) to the numerical simulation (thick transparent lines) to the connected SFF (dotted black lines). We see that, even without using any exact k NSFF, the analytical approximation works quite well and reproduces the expected behavior for the full SFF. In particular, the analytical approximation correctly reproduces the transition from the ramp to the plateau, with the characteristic smooth transition for GOE, the *kink* for GUE, and the *spike* for GSE. The plateau time is given by $\frac{t}{2\pi\bar{D}} = 1$ [121], where \bar{D} denotes the average density of states $\bar{D} = \int E D_E dE$ where $D_E := \frac{1}{N} \sum_{j=1}^N \delta(E - E_j)$. Therefore, given

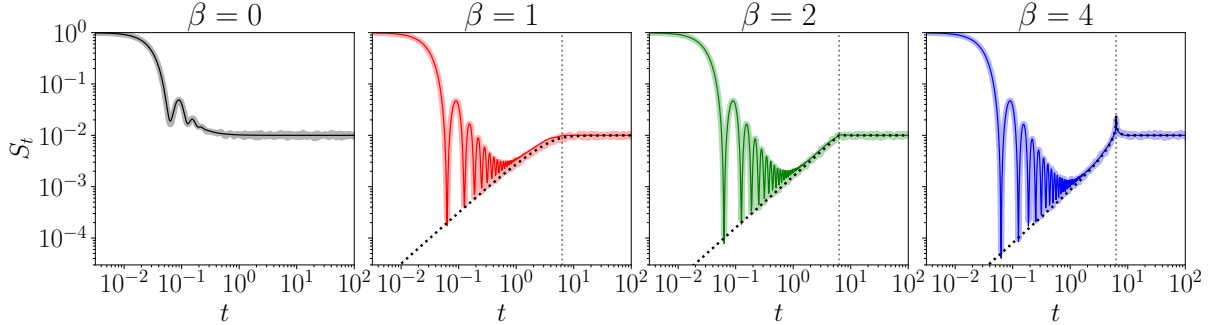


Figure 4.12. Spectral Form Factor for: Poisson (black), GOE (red), GUE (green) and GSE (blue) computed numerically (thick transparent line) and using the analytical results (thin solid line) given by (4.75) (black) and (4.74) (red, green, blue). The connected SFF for each of the ensembles, see Sec. 1.9.2, is also shown (black dotted line). The plots show results for random matrices with dimension $N = 100$ and the numerics have been averaged over $N_{\text{av}} = 1000$ matrices. The dotted gray line marks the start of the plateau at $t_p = 2\pi$. Figure adapted from [3].

that we have unfolded our spectrum, $\bar{D} = 1$, and the plateau time is $t_p = 2\pi$. Under careful observation of Fig. 4.12, we can see that the analytical approximation slightly overestimates the numerical results, which is more pronounced in the ramp for GOE. In the next subsection, we will characterize this deviation.

The exact SFF for Poisson reads

$$S_t^{(\text{Poisson})} = \frac{1}{N} + \sum_{k=1}^{N-1} \frac{2(N-k)}{N^2} \frac{\cos(k \arctan t)}{(1+t^2)^{k/2}}, \quad (4.75)$$

interestingly, this sum can be performed to yield

$$S_t^{(\text{Poisson})} = \frac{1}{N} + \frac{2}{N^2 t^2} - 2 \frac{t \sin(N \arctan(t)) + \cos(N \arctan(t))}{N^2 t^2 (t^2 + 1)^{N/2}}. \quad (4.76)$$

Let us comment on the role of the terms in the expression:

- $1/N$ sets the plateau value.
- $\frac{2}{N^2 t^2}$ ensures that the expression is positive in the short-time oscillations.
- The trigonometric functions give the oscillatory behavior. The fact that they contain the inverse tangent function does not modify much the behavior, especially for large N , since the first oscillation happens at $t = 2\pi/N$, which for large N is very small and the arctangent function admits the expansion $\arctan(x) = x + \mathcal{O}(x^3)$. Therefore, if we were to approximate $\arctan(t) \approx t$ in the argument of the trigonometric functions, the SFF still would look very similar.
- The cosine contribution dominates the oscillations.

- The contribution of the sine term is attenuated due to the fact that it is multiplied by a linear term t . Indeed the main contribution of the sine term is to ensure that $S_0^{(\text{Poisson})} = 1$, if that contribution is removed the starting value of the SFF is $(N + 2)/N$, i.e. the effect of the sine term is only apparent for small N .

Interestingly, since the cosines dominate the oscillations, the sine contribution can be discarded and the oscillations of the SFF for the Poisson ensemble are approximately bounded between the two functions

$$\frac{1}{N} + \frac{2}{N^2 t^2} \left(1 - \frac{1}{(t^2 + 1)^{\frac{N}{2}}} \right) \lesssim S_t \lesssim \frac{1}{N} + \frac{2}{N^2 t^2} \left(1 + \frac{1}{(t^2 + 1)^{\frac{N}{2}}} \right). \quad (4.77)$$

The kn SFF for Poisson shows a dip when $k > 1$, and it oscillates before converging to zero. However, as can be seen in Fig. 4.12 (left), these oscillations do not give a correlation hole and a ramp for the full SFF. The structure of the sum of kn SFFs for RMT (4.74) and for Poisson (4.75) is very different: the former has a Gaussian envelope while the latter has a Lorentzian envelope, the time parameter appears inside an inverse tangent function in Poisson, RMT has the extra contribution from the cosines. One natural question that then arises is *why does Poisson not show a correlation hole? Which is the most relevant feature to prevent the build-up of the correlation hole?*

As already argued before, the $\arctan(t)$ argument does not matter much, since the time is small, it may be simply approximated by a linear function. The difference between a Lorentzian envelope and a Gaussian envelope is also not the main reason for the difference because a Lorentzian will have a broader tail than a Gaussian with the same width, and thus the oscillations would be less suppressed. The main difference is that the Lorentzian in Poisson (4.75) appears to a power $k/2$; this gives an envelope with decreasing width as we increase k . If we are to manually change the envelope for a Gaussian with decreasing width, such as e^{-kt^2} or $e^{-k^2 t^2}$, the correlation hole is also not present. This ensures that the contribution from large k neighbors is attenuated and only contributes at very short times, which restricts their ability to interfere with building a ramp.

The behavior of the width of the envelope is very different for RMT. The width of the envelope $\tau^{(\text{env})}$ can be expanded at large k as

$$\begin{aligned} \tau^{(\text{env})} &= \frac{\sqrt{2\alpha}}{\omega_k} = 2\sqrt{A_\alpha} = 2 \frac{\Gamma(\frac{\alpha}{2} + 1)}{k \Gamma(\frac{\alpha+1}{2})}, \\ &= \sqrt{\beta} + \frac{2 + \beta}{2\sqrt{\beta}k} + \mathcal{O}(k^{-2}). \end{aligned} \quad (4.78)$$

We see that this width decays as $1/k$, but saturates to a constant $\sqrt{\beta}$ at large k . This means that long-range neighbors have an envelope wide enough so that they can interfere and build up the correlation hole. The characteristic time of the envelope is compared to

the plateau time in Fig. 4.13 (b) as $t_p/\tau^{(\text{env})}$. We see that at small k the growth is linear⁵, implying $\tau^{(\text{env})} \sim 1/k$, and it progressively saturates to a constant.

An intuitive argument for the appearance of the spike in GSE

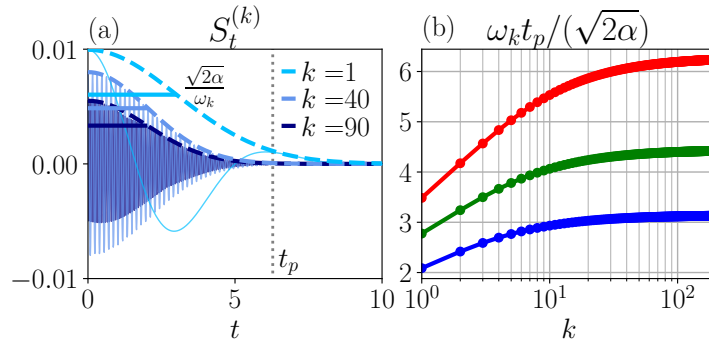


Figure 4.13. (a) $kn\text{SFF}$ for GSE for $k = 1, 40, 90$ (solid thin lines) and Gaussian envelope (dashed thick line), standard deviation of the Gaussian envelope $\sqrt{2\alpha}/\omega_k$ (solid horizontal lines) and plateau time $t_p = 2\pi$ (dotted gray line). (b) Ratio between the plateau time $t_p = 2\pi$ and the width of the Gaussian envelope $\sqrt{2\alpha}/\omega_k$ as a function of the neighbor degree k for the three Gaussian ensembles: GOE (red), GUE (green), and GSE (blue). Figure adapted from [3].

The study of the width of the envelope $\tau^{(\text{env})}$ can also help to explain the spike in GSE. The Gaussian Symplectic Ensemble is the one with the largest $\tau^{(\text{env})} \sim 2$, and this allows the existence of the spike. Figure 4.13 (a) shows several $kn\text{SFFs}$ for GSE. Interestingly, the first $kn\text{SFF}$, with $k = 1$, has a positive oscillation around t_p . Figure 4.13(b) shows the ratio $t_p/\tau^{(\text{env})}$, i.e., how many widths of the envelope fit in the plateau time, or in other words, how many standard deviations of the Gaussian are the plateau away. We see that for the GSE (blue), the plateau is two standard deviations at $k = 1$, and progressively grows to being $t_p/\tau^{(\text{env})} \sim 2\pi/\sqrt{\beta} = \pi$ standard deviations. This ensures that the $kn\text{SFFs}$ are not too attenuated and allows them to interfere in building the characteristic spike of GSE. For the GUE, the plateau is from slightly under three standard deviations to $\sqrt{2\pi} \approx 4.44$ standard deviations, which lets the $kn\text{SFFs}$ construct the kink, but prevents any further interference. Finally, GOE is the most attenuated of the Gaussian ensembles, which makes the transition from the ramp to the plateau smooth, as expected.

How well do the approximations reproduce the full SFF

We performed several approximations to achieve expressions for the $kn\text{SFFs}$. Here we study the validity of the full expression for the SFF as obtained from sums of approxi-

⁵Here there is a small subtlety since the x-axis is in logarithmic scale, for the purpose of visualizing a wider range of k , so strictly we cannot claim that linear in lin-log scale implies that the function grows linearly. When the same data is plotted in a linear scale, we still see the small k linear behavior.

mate kn SFFs (4.74). To this end, and following Suntajs *et al.* [130], we introduce the logarithmic distance $d(\bullet, \bullet)$ between two SFF's $S_t^{(1)}, S_t^{(2)}$ as

$$d(S_t^{(1)}, S_t^{(2)}) := \left| \log_{10} \left(\frac{S_t^{(1)}}{S_t^{(2)}} \right) \right|, \quad (4.79)$$

which is positive $d(\bullet, \bullet) \geq 0$ and vanishes if the two SFF's are equal at time t , i.e. $S_t^{(1)} = S_t^{(2)} \Rightarrow d(S_t^{(1)}, S_t^{(2)}) = 0$.

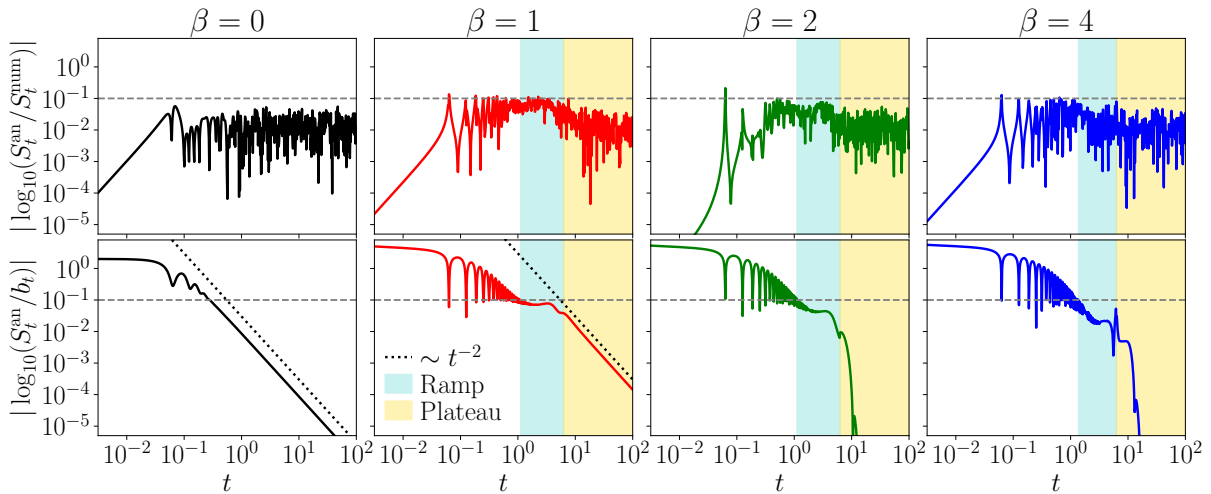


Figure 4.14. Comparisons of the approximate analytical SFF with numerical (top) and connected (bottom) SFF's for (left to right): Poisson, GOE, GUE and GSE. The dashed line marks the $\epsilon = 0.1$ difference between the two quantities. We observe that the difference with the numerics stays bounded by 0.1, i.e. a 10% difference between the two SFF's. The colored regions indicate the universal ramp (light blue), from the Thouless time to the Ehrenfest time, and the plateau (light yellow), after the Ehrenfest time. Figure adapted from [3].

Figure 4.14 (top) shows the comparison between the numerical SFF computed for random matrices and the analytical approximation (4.74) ($\beta \geq 1$) and the same comparison for numerical realizations of the Poisson ensemble with (4.75) ($\beta = 0$). For random matrices $\beta \geq 1$ we also highlight the ramp of the analytical approximation of the SFF $t_{\text{Th}} \geq t \geq t_p = 2\pi$ (light blue) as well as the plateau $t \geq t_p = 2\pi$ (light yellow). At $t = 0$ both SFF's start with $S_{t=0}^{(i)} = 1$, therefore their distance at short times is always very small for all the possible ensembles. Comparing to the numerical results implies that $S_t^{(\text{num})}$ has some numerical fluctuations, even if we perform an ensemble average. This causes the distance between the analytical and numerical SFF to show oscillations and to not vanish. The most interesting feature can be observed for the RMT ensembles, specially for GOE, where the analytical approximation slightly overestimates the ramp of the SFF (blue region). We see that this discrepancy is of around 10%. The distance remains bounded by $d \leq 0.1$ (gray dashed line), which justifies the validity of the approximations

performed in deriving the expressions for the *knSFF*. Lastly, it is noteworthy that we have not included any exact *knSFF* in the description, and that even without any of the special functions the analytical approximation captures well the behavior of the full SFF.

Figure 4.14 (bottom) shows the distance between the analytical approximation of the SFF and the connected SFF b_t . For Poisson we take $b_t^{\beta=0} = 1/N$, i.e. the plateau value, while for RMT we take the connected SFF (see Sec. 1.9.2). Note that at short times b_t is very small while $S_{t=0}^{(\text{an})} = 1$ which implies that the distance starts decaying from $d \approx 1$. It starts to decay, it shows the characteristic short-time oscillations of the infinite Temperature SFF, and fastly goes below $d \leq 0.1$. For Poisson it decreases monotonically after this first oscillations and decays with a power law $d \sim t^{-2}$, indicating fast convergence to the plateau. For GOE we see that during the ramp starts the distance does not decrease much, and remains constant, a feature coming from the overestimation of the analytical approximation of the ramp, and then starts to decrease before the plateau starts, and decreases again as $d \sim t^{-2}$ during the plateau. A similar behavior is observed for GUE and GSE, although the distance between the analytical approximation and the connected SFF decreases as we increase β , which ensures that the terms of $\mathcal{O}(\alpha^{-1})$ discarded are more negligible. For these two ensembles we observe a non-monotonic behavior in the transition from the ramp to the plateau, a feature probably arising from the difficulty of building exactly the kink or the spike from finitely many oscillatory function, after this the distance between the two vanishes very fast, much faster than the previous power law, in the plateau, indicating a much faster convergence to the $1/N$ value.

The non-monotonic *spiky* behavior observed in the transition from the ramp to the plateau in GSE implies that the value of ϵ should be chosen carefully to characterize the onset of the ramp, and not only the plateau, which would happen if a smaller value of ϵ was to be chosen.

4.5.4 What is the simplest form of the *knSFF* which gives rise to a ramp?

The purpose of the previous sections was to find exact and approximate expressions for the *knSFFs* of random matrices, this lead to the exact expressions (4.25) (4.27) and the approximation (4.37), find their properties, and show how one can build the SFF from summing more and more of these *knSFFs*. In this section, however, we take an orthogonal point of view and instead of focusing on an accurate description of the *knSFF* we want to find the simplest *knSFF* expression which can give rise to a ramp.

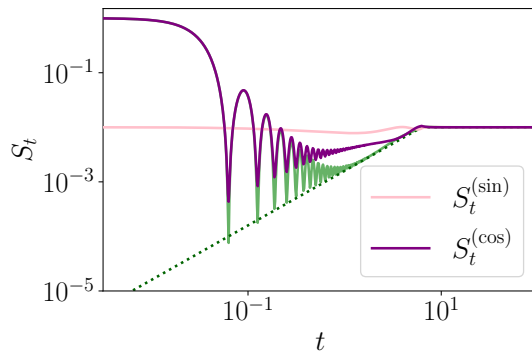


Figure 4.15. Cosine contribution (purple) and sine contribution (pink), full analytical SFF (green) obtained as the sum of the cosine and sine contributions. Lastly, we also show the connected SFF (dotted line) for the GUE ensemble. To show them on a log-log scale, all the contributions include the same plateau value $1/N$.

Only the cosine contributions do not give a linear ramp

We begin our analysis from the approximate analytical expression (4.37). We separate the cosine and sine contributions as

$$S_t^{(k,\cos)} = \frac{2(N-k)}{N^2} e^{-\frac{\omega_k^2 t^2}{4\alpha}} \cos(\omega_k t), \quad (4.80)$$

$$S_t^{(k,\sin)} = \frac{2(N-k)}{N^2} e^{-\frac{\omega_k^2 t^2}{4\alpha}} \frac{1}{12\alpha} \omega_k t \left(\frac{\omega_k^2 t^2}{2\alpha} - 3 \right) \sin(\omega_k t), \quad (4.81)$$

and compute the sum of all the contributions, such that $S_t^{(\cos)} = \sum_k S_t^{(k,\cos)}$, $S_t^{(\sin)} = \sum_k S_t^{(k,\sin)}$. Fig. 4.15 shows both of the contributions, we observe that the ramp generated by summing only the cosine terms (purple) is not linear, and does not agree with the full or connected SFF. This highlights the importance of the sine contribution, which arises from the non-gaussianity of the distribution, and without which the linear ramp cannot be built, we see that its biggest effect is at the start of the ramp, and right before the onset of the plateau.

Accounting for the non-gaussianity in a sum of cosines

We have just argued that the non-gaussianity is necessary to achieve the linear ramp of the SFF, however, there is a way to approximately include this contribution in the cosine such that the SFF can be understood as a Fourier transform. Let us begin by expanding the trigonometric functions in the approximation for the knSFF (4.37) to find

$$S_t^{(k)} \approx \frac{N-k}{N^2} e^{-\frac{\omega_k^2 t^2}{4\alpha}} \left(1 - i \frac{\omega_k t}{12\alpha} \left(\frac{\omega_k^2 t^2}{2\alpha} - 3 \right) \right) e^{i\omega_k t} + \text{c.c.} \quad (4.82)$$

The parenthesis can then be approximated by an exponential, which gives an approximation for the kn SFF as

$$S_t^{(k)} \approx 2 \frac{N-k}{N^2} e^{-\frac{\omega_k^2 t^2}{4\alpha}} \cos \left(\omega_k t + \frac{\omega_k t}{4\alpha} - \frac{\omega_k^3 t^3}{24\alpha^2} \right). \quad (4.83)$$

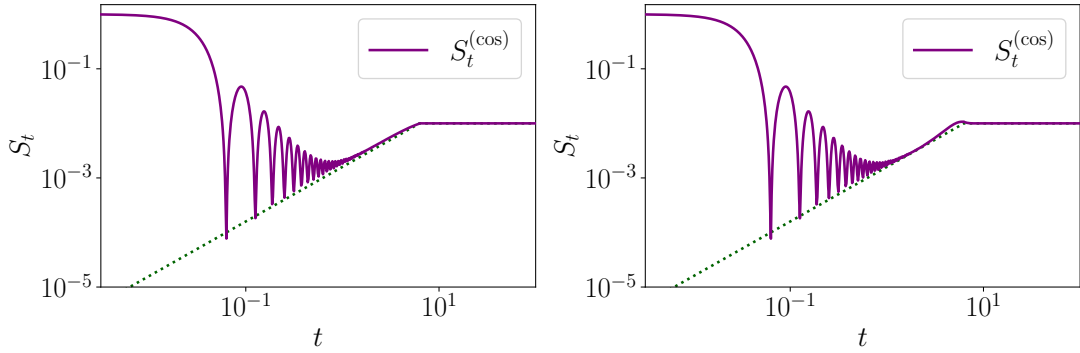


Figure 4.16. Full SFF obtained analytically as a sum of cosines with: full expression with cubic terms (4.83) (left) and modified frequency (4.84) (right) for GUE.

Figure 4.16 (left) shows the full SFF obtained analytically as a sum of only cosines contributions with this expression, we observe that the ramp we recover is linear and is very close to the universal value predicted by the connected SFF (dotted line). Therefore, it is possible to obtain a SFF with a linear ramp only from cosine contributions, but the cubic term is necessary for showing a linear ramp.

We can discard the $\mathcal{O}(t^3)$ term and we find that the kn SFF can be expressed simply as

$$S_t^{(k)} \approx 2 \frac{N-k}{N^2} e^{-\frac{\omega_k^2 t^2}{4\alpha}} \cos(\tilde{\omega}_k t), \quad (4.84)$$

where the modified frequency is simply $\tilde{\omega}_k = \omega_k(1 + \frac{1}{4\alpha})$. The advantage of this expression is that now the SFF can be expressed as a single discrete Fourier transform as

$$S_t = \frac{1}{N} + 2 \sum_{k=1}^{N-1} \frac{N-k}{N^2} e^{-\frac{\omega_k^2 t^2}{4\alpha}} \cos \left(\omega_k \left(1 + \frac{1}{4\alpha} \right) t \right). \quad (4.85)$$

Figure 4.16 (right) shows the full SFF obtained from this expression, we observe that it reproduces much better the full SFF than the one without the modified frequency, but worse than the expression with cubic terms, the biggest difference happens at around the onset of the plateau. From here we can conclude that the corrections to the frequency are those responsible for the starting part of the ramp, while the cubic contributions are those responsible for the transition from the ramp to the plateau.

Toy model: A system with correlations only to nearest-neighbors

The nearest neighbor level spacing distribution $\mathfrak{P}^{(1)}(s^{(1)})$ is an indicator of quantum chaos but is not enough to claim that the system is chaotic. This is in agreement with what we have studied in the previous part of this chapter, one needs to take into account the correlations at all possible spectral ranges k , to explain the full extent of the ramp of the SFF. In here, we build a toy model of a system which only contains correlations to nearest neighbors in energy, but not to the remaining neighbors, and compute the SFF of such system.

Recall that given two uncorrelated random variables x, y the probability distribution of their sum is given by their convolution, i.e. the second $k = 2$ level spacing $s^{(2)}$ would be $s^{(2)} \equiv s^{(1)} + s^{(1)}$. The level spacing distribution for $s^{(2)}$ can thus be computed as

$$\mathfrak{P}^{(2)}(s^{(2)}) = \mathfrak{P}^{(1)}(s^{(1)}) * \mathfrak{P}^{(1)}(s^{(1)}) = \int_0^{s^{(2)}} \mathfrak{P}^{(1)}(s) \mathfrak{P}^{(1)}(s^{(2)} - s) ds, \quad (4.86)$$

where $*$ denotes the convolution of two probability distributions and we have introduced in the integral the constraint that $s^{(1)}, s^{(2)} \geq 0$, which reduces the integration domain to $s \in [0, s^{(2)}]$. The *convolution theorem* states that the Fourier transform $\mathfrak{F}[\bullet]$ of a convolution is the product of the Fourier transforms, therefore the kn SFF for this toy model reads

$$\varsigma_t^{(k)} = \text{Re}(\mathfrak{F}[\mathfrak{P}^{(1)}]^k(t)), \quad (4.87)$$

where the Fourier transform of the nnLS distribution, $\mathfrak{F}[\mathfrak{P}^{(1)}](t)$, admits the exact expression

$$\varsigma_t^{(1)} = \mathfrak{F}[\mathfrak{P}^{(1)}] = {}_1F_1\left(\frac{\beta+1}{2}, \frac{1}{2}, -\frac{t^2}{4A_\beta}\right) - it {}_1F_1\left(\frac{\beta}{2}+1, \frac{3}{2}, -\frac{t^2}{4A_\beta}\right). \quad (4.88)$$

The full SFF can be built from the sum of the kn SFFs

$$\varsigma_t = \sum_k 2 \frac{N-k}{N^2} \text{Re}((\varsigma_t^{(1)})^k). \quad (4.89)$$

Figure 4.17 shows this expression (purple) and compares it with the numerical SFF for the GUE (green). We see that the uncorrelated SFF shows a correlation hole, which was to be expected since the probability distribution of all the spacings $P(s = E_n - E_m)$ vanishes at $s = 0$ [120], but does not show a linear ramp. Non-linear ramps have been observed in SFF's for integrable models, such as SYK₂ [311, 312], and thus cannot be used as a signature of chaos.

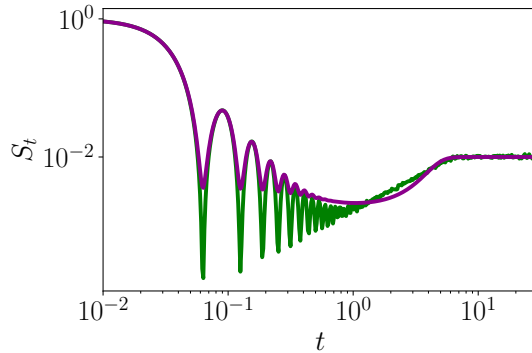


Figure 4.17. SFF computed numerically for the GUE (green) and for the toy model with energy correlations to nearest neighbors only ς_t (purple), Eq. (4.89). Figure adapted from [3].

4.6 A dissipative protocol to measure the $kn\text{SFF}$

The previous parts of this chapter have implicitly assumed that we had access to the spectrum of the system $\{E_j\}$ and that from there one can compute all the k -th neighbor level spacings and from the knowledge of the $kn\text{LS}$ find the $kn\text{SFF}$. This is indeed the approach that we have followed to compute numerically $kn\text{SFFs}$, but it is far from the approach that one would follow experimentally. Although originally the **SFF** was devised as a tool to measure chaos which would not be very affected by imperfect spectral data [119], there has been some recent efforts in trying to devise a quantum protocol to measure the **SFF** [313, 314] or closely related quantities [315] in experiments directly. This is especially challenging since measuring the **SFF** involves very long times, and a very faint signal, which is precisely what needs to be used to determine whether the system is integrable or chaotic. Even though these problems make it tough to measure, the first direct measurement of the **SFF** has been recently reported [316].

In here, in a similar spirit to [315], we consider a way of computing a related quantity to the $kn\text{SFF}$, in particular the k -th neighbor autocorrelation function $\mathfrak{C}_t^{(k)}$

$$\begin{aligned} \mathfrak{C}_t^{(k)} &= \frac{1}{\mathfrak{N}^2} \text{Tr}(\hat{O}^{(k)} \hat{O}_t^{(k)}) \\ &= \sum_i \frac{|O_{ii}|^2}{\mathfrak{N}^2} + \sum_{i=1}^{N-k} \frac{|O_{i+k,i}|^2}{\mathfrak{N}^2} \cos[(E_{k+i} - E_i)t], \end{aligned} \quad (4.90)$$

where \mathfrak{N} is simply a normalization factor. This autocorrelation function reduces exactly to the $kn\text{SFF}$ when $|O_{i+k,i}|^2 = |O_{j+k,j}|^2, \forall i, j$. If this is not the case it gives a different weight to each of the starting energies E_i , and gives a differently weighted average of the $kn\text{SFF}$.

It crucially depends on our ability to prepare such an operator $\hat{O}^{(k)}$. We propose a dissipative protocol to prepare such an operator as the long time limit of a certain evolution.

We consider the adjoint **GKSL** master equation with a single hermitian jump operator

$$\partial_t \hat{O}_t = i[\hat{H}_0, \hat{O}_t] - \gamma[\hat{L}, [\hat{L}, \hat{O}_t]]. \quad (4.91)$$

Furthermore, let us assume that \hat{L} and \hat{H}_0 commute $[\hat{H}_0, \hat{L}] = 0$ so that they share a common eigenbasis. In this case the solution of the adjoint master equation is simply

$$\hat{O}_t = \sum_{m,n} O_{mn} e^{-i(E_m - E_n)t - \gamma(l_m - l_n)^2 t} |m\rangle \langle n|. \quad (4.92)$$

Now consider that we could engineer a jump operator of the form

$$\hat{L} = \text{diag}(l_1, \dots, l_k, l_1, \dots, l_k, l_{2k+2}, \dots, l_N), \quad (4.93)$$

which has a repeated string of k eigenvalues l_1, \dots, l_k . If we do not consider the Hamiltonian evolution, or equivalently go to the interaction picture with respect to it the evolution up to time t_f is

$$\hat{O}_{t_f} = \sum_{m,n} O_{mn} e^{-\gamma(l_m - l_n)^2 t_f} |m\rangle \langle n|. \quad (4.94)$$

All off-diagonal elements decay exponentially fast with time, except for those in which $|m - n| = k$ and $m, n \in \{1, \dots, k\}$ which do not decay due to the structure of \hat{L} . Thus we see that the infinite time limit reads

$$\begin{aligned} \lim_{t_f \rightarrow \infty} \hat{O}_{t_f} &= \hat{O}^{(k)} = \sum_{i=1}^N \hat{O}_{ii} |i\rangle \langle i| + \sum_{i=1}^{2k} O_{i+k,i} |i+k\rangle \langle i| + \text{h.c.} \\ &= \begin{pmatrix} O_{11} & 0 & \dots & O_{1,k+1} & 0 & \dots \\ 0 & O_{22} & \dots & 0 & O_{2,k+2} & \dots \\ \vdots & \vdots & \ddots & & & \ddots \\ O_{k+1,1} & 0 & & O_{k+1,k+1} & & \\ 0 & O_{k+2,2} & & & O_{k+2,k+2} & \\ \vdots & \vdots & \ddots & & & \ddots \end{pmatrix}. \end{aligned} \quad (4.95)$$

This is intended to be a theoretical example to show that it is possible to devise a protocol to find a correlation function that encodes similar information to the k -nSFF. It is hard to conceive a physical mechanism to engineer a jump operator such as (4.93) in a realistic many-body system since it involves a highly structured decoherence-free subspace [202].

Another possible approach builds on the work of Joshi *et al.* [314]. In this work a **SFF** for a subsystem of a physical system was introduced, which introduces a certain dependence on the eigenstates on the **SFF**. Consider a bipartite Hilbert space $\mathcal{H} = \mathcal{H}_A \otimes \mathcal{H}_B$, if we could find a bipartition over which $\text{Tr}_B(\hat{\rho}_B(E_i)\hat{\rho}_B(E_j)) \propto \delta_{|i-j|,k}$ holds, where $\hat{\rho}_B(E_i) = \text{Tr}_A(|E_i\rangle \langle E_i|)$ is the reduced density matrix of subsystem B . If such a subsystem can be

found, then the randomized measurement protocol devised in [314] can be readily applied to measure the k -nSFF.

4.7 Conclusion

In this chapter, we have studied the role that each k -th neighbor level spacing plays in building the full **SFF**. In doing this, we have computed exact and approximate expressions for the k -th neighbor **SFF** for the different ensembles of random matrices and Poisson. This provides a simple decomposition of the **SFF** which highlights how each of the different long-range correlations shows up in the full **SFF**.

We then focused on understanding the properties of individual k -nSFF's, focusing first on the minimum and minimum time of the kn SFF. We find that the minimum time $t_m(k)$ does not distinguish Poisson and **RMT** if $k \geq 2$, in the same way it also does not distinguish the different phases of the disordered XXZ spin chain. This means that for all systems, whether chaotic or integrable, the kn SFF with $k \geq 2$ shows a dip whose time does not depend on the correlations of the ensemble, which have been removed through the unfolding. The minimum value of the kn SFF is markedly different in random matrix and Poisson ensembles. In a similar way, the deepest kn SFF k^* also shows different scaling which implies that it can be used to distinguish between chaotic and integrable systems. We used this to monitor the transition between chaos and integrability in the disordered XXZ model. In a similar way to the full **SFF**, the individual kn SFFs are *not* self-averaging.

We then turned to the study of properties of combinations of kn SFFs. We first introduced the partial K neighbors **SFF**, which considers a cutoff in the neighbor range. By studying the dip and Thouless times as a function of K , we concluded that the neighbors with the biggest effect in the length of the ramp are the short-range ($K \lesssim 5$ for **RMT** and $K \lesssim 50$ for disordered XXZ) and the very long-range ($K \gtrsim 350$ for **RMT** and $K \gtrsim 300$ for disordered XXZ). This conclusion is counterintuitive since we expect the very long-range correlations to not be universal. However, as we already discussed when studying the individual kn SFFs as in Fig. 4.2, the strength of the deviations from universality in the kn SFF depends on the time-scale, these are specially apparent in the envelope of the kn SFF, and at short times a correction to the width of the envelope has not had enough time to be very noticeable. This provides a possible explanation for this counterintuitive effect: at short times, even if the deviations from universality are big for very long-range spacings, these have not had enough time to have a big contribution that takes the **SFF** out of its universal ramp, and thus they still contribute to the universal ramp of the **SFF**. Another possible effect that could be taking part here is that when several long-range kn SFFs are combined, their non-universal contributions partially cancel each other, and thus we cannot observe the deviations from **RMT** universality in the full **SFF**.

We found that when the sum of even or odd neighbor ranges behaves in a strikingly different way. We find that the even neighbors build most of the ramp, and have a constructive interference in the center of the ramp at $t = \pi$. The contribution from the

odd neighbors is almost constant, and only cancels the constructive interference, yielding the linear ramp. This gives a ‘*resonance-antiresonance*’ behavior, which is characteristic of the **RMT** ensembles. Our analysis provides an intuitive explanation for the presence of the spike in the **GSE**. We computed the full **SFF** and compared it to numerical and analytical expressions for it, seeing that in the plateau regime our approach converges to the analytical expression.

We then study the simplest form of the *knSFF* that give rise to a ramp, trying to discern what are the features that give rise to a linear ramp. Instead we find several approaches that *do not* give a linear ramp, such as only taking the cosine term in the expression for the *knSFF*, or considering a toy model where there are only correlations to nearest neighbors. Lastly, we finish the chapter by introducing a dissipative protocol to measure a correlation function related to the *knSFF*.

4.7.1 Open questions

In light of the results of this chapter there are a number of possible directions for further research, let us name here a few:

- The analysis of *knSFFs* has been done so far at infinite temperature, extending to nonzero β , as introduced for the **SFF** in Sec. 1.9, would lead to the possibility of studying which spectral ranges contribute more to the almost-saturation of the universal bound in the inflection exponent $\eta \leq \pi/(2\beta)$ [4]. We already observed in the appendix of [4] that the effect of finite temperature is to wash out the longer-range *knSFFs*. The main obstacle in the analytical side for this research direction is that now the *knSFF* depends not only on the difference $E_{n+k} - E_n$ but also on the sum $E_{n+k} + E_n = s_n^{(k)} + 2E_n$.
- A very interesting direction of study is to extend the *knSFFs* to the dissipative or non-hermitian case, which on the random matrix side entails generalizing to ensembles such as Ginibre. In the non-unitary case most studies focus on short-range correlations [317] or the full **SFF** [131, 247, 318, 319]. The main obstacle in this line is that long-range spectral correlations between complex eigenvalues are more delicate to diagnose [320], which could be avoided by looking at correlations between singular values [66], particularly through their evolution in the singular form factor [321].
- Extending to more complicated random patterns which may be modelled through a wigner-like surmise with a modified exponent α is a promising direction of study, in which the insights from quantum chaos and random matrix theory could shed light on different physical phenomena. This direction was explored for point patterns in two dimensions in [322].
- Another possible direction is to propose corrections to the power α , as we did in [6], which could yield a more accurate expression for the *knSFFs* and clarify how patterns in the *knLS* manifest in the time evolution.

- Is it possible to achieve an operator of the form as $\hat{O}^{(k)}$, cf. sec. 4.6, through a variant of the Lanczos algorithm [5]?
- Lastly, we understood why certain **knSFFs** do *not* build a linear ramp, and what their role is in building the ramp of each of the spectral ranges. Still, it remains to be understood *why* the linear ramp of **RMT** arises from the expressions for the **knSFFs**, and which other possible expressions would build a linear ramp.

Recap of results of Chapter 4

- In the case of **RMT** we computed expressions for the **knSFF** analytically (4.25)

$$f_t^{(k)} = {}_1F_1\left(\frac{\alpha+1}{2}; \frac{1}{2}; -\frac{t^2}{4A_\alpha}\right),$$

and approximately (numerically more stable) (4.34)

$$S_t^{(k)} \approx \frac{2(N-k)}{N^2} e^{-\frac{\omega_k^2 t^2}{4\alpha}} \left[\cos(\omega_k t) + \frac{1}{12\alpha} \omega_k t \left(\frac{\omega_k^2 t^2}{2\alpha} - 3 \right) \sin(\omega_k t) \right].$$

The nature of each individual **knSFF** is clear from these expressions, which involve oscillatory functions multiplied by an envelope. In the case of Poisson, the exact expression we computed (4.38)

$$S_t^{(k)} = \frac{2(N-k)}{N^2} \frac{\cos(k \arctan t)}{(1+t^2)^{\frac{k}{2}}}.$$

This expression is numerically stable, since it is written in terms of ordinary functions, and thus we do not need to find approximations for it.

- The comparison between the analytical expressions for RMT and Poisson with the numerical expressions for the disordered XXZ spin chain in the two different phases, cf. Fig. 4.2, show that the deviations from universality happen specially in the width of the envelope of the **knSFF**, which is slightly narrower than **GOE** in the chaotic phase, and slightly wider than Poisson in the integrable phase.
- We computed an analytical expression for the minimum time for **RMT** (4.42)

$$t_m(k) \approx \frac{\pi}{k},$$

and for Poisson (4.47)

$$t_m(k) = \tan\left(\frac{\pi}{1+k}\right).$$

We find that this minimum time does not distinguish between chaos and integrability, except for $k = 1$, where Poisson shows no dip.

- We computed an analytical approximation for the minimum of each **knSFF** for RMT (4.44)

$$S_{t_m}^{(k)} \sim -\frac{2(N-k)}{N^2} e^{-\frac{\pi^2}{2k(\beta k + \beta + 2)}},$$

and for Poisson (4.48)

$$S_{t_m}^{(k)} = \frac{2(N-k)}{N^2} \cos^k \left(\frac{\pi}{1+k} \right) \cos \left(\frac{k\pi}{k+1} \right).$$

These can provide a simple justification for the lack of correlation hole in Poisson, since none of them is deep enough to compensate $S_t^{(1)}$, cf. Fig. 4.5.

- We also compute asymptotic expressions for the deepest **knSFF** k^* (4.53) for RMT

$$k_\beta^* \sim \sqrt[3]{\frac{\pi^2 N}{\beta}},$$

and for Poisson (4.58)

$$k_0^* \sim \sqrt{\frac{\pi^2 N}{2}}$$

These are markedly different for RMT and Poisson and thus can be used as a signature of the transition from chaos to integrability. We show them for the disordered XXZ spin chain in Fig. 4.6 along the chaos to integrability transition.

- We find that the **knSFF**, like the full SFF is not a *self-averaging* quantity, cf. Fig. 4.7.
- We introduce the partial SFF (4.66) with a limit in the range of the neighbors K . Introducing the dip and Thouless times of the partial SFF, we find that even if all neighbors are needed to explain the full extent of the ramp, the ones with the biggest effect are the very short-range and the very long-range. This is seen for RMT in Fig. 4.9 and for XXZ in Fig. 4.10.
- We find that when only the even or odd neighbors are considered, they show markedly different behavior for RMT. The even neighbors build most of the ramp while the odd only cancel the resonance of the even to give the ramp, cf. Fig. 4.11.
- We also show that the approximation for the **knSFF**'s works well in building the full **SFF**, cf. Figs. 4.12, 4.14.
- In terms of the **knSFF**'s, we can find a simple explanation for the appearance of the spike in **GSE**, cf. Fig. 4.13, which essentially appears because the envelope is wide enough to allow for a constructive interference of the **knSFF**'s.
- We construct a toy model in which there is only correlation to nearest neighbors, and we find that this system does not show a linear ramp in its SFF, cf. Fig. 4.17.

- Lastly, in Sec. 4.6 and in line with the other chapters of the thesis, we propose a dissipative protocol which could serve to measure a correlation function related to the knSFF.

Chapter 5

Discussion

This thesis has investigated the role of randomness in dissipative and chaotic quantum dynamics. Throughout the chapters, we have dealt with different aspects of randomness, broadly categorized as either noise, when randomness fluctuates in time, or randomness as a model for complex many-body dynamics, through the framework of *random matrix theory*. Another common methodological denominator of the thesis was going beyond the standard approach in the field, which allows us to provide more detailed descriptions of different phenomena. Here we discuss the main results of the thesis and their potential importance.

In this spirit, Chapter 2 focused on a noisy hamiltonian beyond the noise-average, introducing quantities such as the *stochastic operator variance* (SOV) and its higher moments and cumulants. For stochastic Hamiltonians, the unitarity of single trajectories simplifies greatly the computations, and shows that all the higher point moments evolve as given by the time evolution operator generated by the adjoint Lindbladian $\mathcal{E}_t^\dagger = e^{\mathcal{L}^\dagger t}$. The generalization to dynamics which are not unitary at single trajectories, such as continuous quantum measurements [42, 43, 77] or even *collapse theories* [225], promises a better understanding of the stability of stochastic quantum evolution, and its relation to the chaotic or integrable dynamics of the system. This direction may yield important practical and fundamental insights, since the SOV may characterize how “*error-resilient*” is a given operator, or provide a more refined quantity to explore in more stringent tests on the foundations of quantum mechanics [225].

In Sec. 2.3, we found that the product of two SOV fulfills a bound similar to the uncertainty relation. We found several versions of these inequalities, particularly state-dependent and state-independent. The main open question in this line is: how hard is it to measure the SOV? Perhaps it is enough to measure some of its expectation values. Following on this line, it may be very fruitful to explore the conditions for the saturation of the SOV uncertainty relations, the extra information contained in the operator versions of the bound, and how these could be used to derive limits on Open quantum dynamics, such as different quantum speed limits [222, 223].

In Sec. 2.6, we found a deep link between the SOV and dissipative OTOC’s. One potentially very important follow-up direction on this is to try to extend the universal bound on the Lyapunov exponent for the OTOC [128] to certain expectation values of the SOV. The main obstacle in this direction is that for a stochastic Hamiltonian, the connection holds to a *dissipative OTOC*, for which the Lyapunov regime is generally

hindered by dissipation. Extensions to more general dynamics which are not unitary at single trajectories, may bring different **OTOCs** which are not the dissipative one. A natural playground for this direction of study is the *Sachdev-Ye-Kitaev* model [137, 142, 323], which saturates the universal bound at low temperature, and its Brownian variant [324].

Chapter 3 goes beyond the standard approach in the theory of Non-Hermitian Hamiltonians, which assumes that the decay is constant, and studies the evolution of stochastic non-Hermitian Hamiltonians with noise in their decay. This leads to a novel master equation for the noise-average, which we name *antidephasing* since the dissipator is given by a double *anticommutator*. This dynamics shows markedly different behavior to the **GKSL** equation and to deterministic non-Hermitian Hamiltonians, which we show through the evolution of the purity. Furthermore, we characterize the steady states of the dynamics, and how the convergence happens, as dictated by the *dissipative gap*.

To further illustrate these dynamics, we consider the *stochastic dissipative qubit* (**SDQ**), an extension of a **NH** Hamiltonian recently realized experimentally [80, 85]. This system allows for a more in-depth analysis of the behavior of purity, which already showcases that purifying states have shifted from the northern hemisphere to the southern hemisphere. We also perform the full spectral analysis of the antidephasing Liouvillian analytically, from which we find the steady states and the dissipative gap. The steady state analysis shows that there are three different phases, the \mathcal{PT} unbroken in which the steady state is close to the maximally mixed state, the \mathcal{PT} broken in which the state is close to the excited state $|f\rangle$ and the noise induced (**NI**) phase in which the noise stabilizes the state $|e\rangle$, which originally had losses. This illustrates the power of the antidephasing approach and non-Hermitian dynamics for state preparation. Following on this analysis, we proposed a protocol [7] to prepare nonstabilizer or *magic* states as the steady states of the dynamics using non-Hermitian and stochastic non-Hermitian dynamics. The magic steady states are found where the Bloch y coordinate is non-zero in the \mathcal{PT} b phase close to the exceptional point or in the **NI** phase close to the transition to the \mathcal{PT} u phase. We checked that the properties of spectral and steady states describe the evolution of the density matrix dynamics well, and we also studied the evolution of single-trajectory dynamics. We also proved that the **NI** phase is present when we remove the pumps; therefore, a simple explanation for the appearance of this phase and the noise-induced stabilization is still lacking. Lastly, we used our formalism to model the residual decay rate observed in the \mathcal{PT} broken phase, cf. Sec. 3.5.

A natural extension of the ideas developed in Chaps. 2 and 3 is to study the **SOV** for a stochastic Non-Hermitian Hamiltonian. In this direction, one idea to simplify the analysis is to study the **SOV** for a density matrix $\mathbb{E}(\hat{\rho}_t^2) - \mathbb{E}(\hat{\rho}_t)^2$, since the dynamics is nonlinear in the density matrix, the Heisenberg and Schrödinger pictures are not equivalent, and the latter is more natural. If we start from a pure state $\hat{\rho}_0 = |\psi_0\rangle\langle\psi_0|$, since **NH** Hamiltonians keep pure states pure, the analysis can be mapped to the analysis of the average density matrix.

From a purely practical point of view, one of the most interesting open questions is: what is the *best* model to account for extra decay in non-Hermitian Hamiltonians? What

quantities should we study to test what the most important sources of noise are, and how should we take them into account in our description? There are many models, such as the open dissipative qubit [83], the hybrid Liouvillian [325], and here we introduce the *antidephasing* model [2], all of which attribute the source of extra decoherence to different phenomena. Hence, it begs to ask which of these models reproduces the dynamics better and which quantities we should look at to test this. Here, we made the first step in this direction by testing how well the anti-Hermitian noise models the residual exponential decay, and showed that it models it better than only real noise. However, a more thorough analysis and more data would be needed in order to find the best model.

In Chapter 4, we went beyond nearest-neighbor correlations between the energies of a random matrix and studied how each spectral range k contributes to the full ramp of the **SFF**. Our analysis provides a more detailed picture of spectral correlations, which naturally contains both short and long-range correlations, showing the dynamics they generate and their role in the spectral form factor. This detailed formalism allows us to find what properties are more sensitive to the breakdown of random matrix universality and which ones are less, e.g., the short-time behavior of the *knSFF* is not sensitive to the breakdown of universality since the deviations occur in the envelope. Building on this, we found our most counterintuitive result, namely that very long-range spectral correlations are key to explaining the full extent of the ramp in the **SFF**, although they are highly non-universal.

A possible research direction which would encompass many of the concepts of this thesis is to build a random matrix ensemble “in time” through a stochastic non-Hermitian Hamiltonian, in a similar spirit to the *Brownian GUE* studied in [326]. When we have $\mathcal{O}(N^2)$ sources of noise, acting in each of the operators $\hat{L}_{nm} = |n\rangle\langle m|$ we recover the **GUE** in time as $\{\hat{X}_t = \sum_{n,m} \xi_t^{(nm)} |n\rangle\langle m|, \hat{H}_t = (\hat{X}_t + \hat{X}_t^\dagger)/2\}$, where the only difference is that now there is a parameter t which lets us “*evolve through the ensemble*”. However, what is the behavior when we limit the sources of noise to a finite number $N_c \ll N^2$? How do we lose the **RMT** behavior as the number of sources of noise decreases? Do long-range correlations start to deviate from **RMT** before as happens in chaotic systems? If this is the case, what is the relation between the critical neighbor range¹ k_{crit} and the number of noise channels N_c ? Can we relate some of the spectral properties of the eigenvalues of the ensemble to *knLS* or the *knSFF*’s? Lastly, what is the role of the choice of operators in this model? This idea goes in the line of t -designs [327–329], these are random ensembles that reproduce the Haar random ensemble up to a certain moment, which have been investigated for stochastic Hamiltonians in [330].

This thesis has explored, scrutinized, and exploited the notion of randomness in the quantum world for several different problems. Far from being only a disruptive element that hinders quantum coherence, as is typically thought to be the case, we have showcased the power of randomness and noise in the quantum world. They provide a simple model for decoherence, which we characterized beyond the average through the *stochastic operator*

¹A general definition of the critical neighbor range could be the k_{crit} such that $\|f_{N_c}^{(k)} - f_{\text{RMT}}^{(k)}\| \leq \epsilon$ for $k \leq k_{\text{crit}}$ and $\|f_{N_c}^{(k)} - f_{\text{RMT}}^{(k)}\| > \epsilon$ for $k > k_{\text{crit}}$, where $f^{(k)}$ is a given function of the spectrum which depends only on k -th nearest neighbors and $\|\bullet\|$ is a certain norm.

variance [1]. We leveraged the noise to find novel *antidephasing* master equations which characterize the decoherence in the dissipative qubit and enlarge the possible steady states for state preparation [2, 7]. Lastly, randomness appears in the foundation of the theory of quantum chaos, through its connection to random matrix theory, and we provided a more detailed look at the long-range spectral correlations and their role in the spectral form factor [3].

Noise is ubiquitous in the real world around us and in the quantum realm. This thesis has showcased some of its power, and in a similar way to the idea of exploiting quantum properties for our advantage, noise, both in classical and quantum setups, may also be exploited for certain tasks [331].

Appendix A

Numerical solution of Stochastic Differential Equations

Here we briefly introduce some of the numerical algorithms used to solve Stochastic Differential Equations numerically. To fix the notation let the **SDE** be

$$d\mathbf{X}_t = \mathbf{a}(\mathbf{X}_t, t)dt + \mathbf{b}(\mathbf{X}_t, t)dW_t, \quad (\text{A.1})$$

we denote the initial condition $\mathbf{X}_0 = \mathbf{Y}_0$ and recursively construct the solution Y_n at time $t_n = n\Delta t$. \mathbf{X}_t denotes a possibly vector-like variable, and \mathbf{a} and \mathbf{b} are vector functions of it.

A.1 Euler-Maruyama

The Euler-Maruyama method is the simplest and least accurate, it is of order 0.5. It constructs the numerical solution recursively as

$$\mathbf{Y}_{n+1} = \mathbf{Y}_n + \mathbf{a}(\mathbf{Y}_n, t_n)\Delta t + \mathbf{b}(\mathbf{Y}_n, t_n)\Delta W_n, \quad (\text{A.2})$$

where $\Delta W_n \sim \mathcal{N}(0, \Delta t)$ is a normal random variable with variance Δt .

A.2 Stochastic Runge-Kutta

The stochastic Runge-Kutta method [332] is an *explicit order 1.0 strong scheme*. We compute recursively the solution as

$$\mathbf{Y}_{n+1} = \mathbf{Y}_n + \mathbf{a}_n \Delta t + \mathbf{b}_n \Delta W_n + \frac{1}{2\sqrt{\Delta t}} (\mathbf{b}(\mathbf{Y}_n) - \mathbf{b}_n)((\Delta W_n)^2 - \Delta t), \quad (\text{A.3})$$

where $\mathbf{Y}_n = \mathbf{Y}_n + \mathbf{a}_n \Delta t + \mathbf{b}_n \sqrt{\Delta t}$, $\mathbf{a}_n = \mathbf{a}(\mathbf{Y}_n)$, $\mathbf{b}_n = b(\mathbf{Y}_n)$, and $\Delta W_n = W_{n+1} - W_n$ are independent identically distributed normal random variables with zero average and variance Δt .

A.3 Kloeden-Platen

Another approach is the *explicit order 1.5 strong scheme* by Kloeden and Platen, see Chapt. 11.2 (eqs 2.1, 2.2, 2.3 page 378) of [332].

$$\begin{aligned}\mathbf{Y}_{n+1} = \mathbf{Y}_n + \mathbf{b}\Delta W + \frac{\mathbf{a}(\Upsilon_+) - \mathbf{a}(\Upsilon_-)}{2\sqrt{\Delta t}}\Delta Z + \frac{\mathbf{a}(\Upsilon_+) + 2\mathbf{a}_n + \mathbf{a}(\Upsilon_-)}{4}\Delta t \\ + \frac{\mathbf{b}(\Upsilon_+) - \mathbf{b}(\Upsilon_-)}{4\sqrt{\Delta t}}(\Delta W^2 - \Delta t) + \frac{\mathbf{b}(\Upsilon_+) - 2\mathbf{b}_n + \mathbf{b}(\Upsilon_-)}{2\Delta t}(\Delta W\Delta t - \Delta Z) \\ + \frac{\mathbf{b}(\Phi_+) - \mathbf{b}(\Phi_-) - \mathbf{b}(\Upsilon_+) + \mathbf{b}(\Upsilon_-)}{4\Delta t} \left(\frac{\Delta W^2}{3} - \Delta t \right) \Delta W,\end{aligned}$$

where $\mathbf{a}_n \equiv \mathbf{a}(\mathbf{Y}_n)$, $\mathbf{b}_n \equiv \mathbf{b}(\mathbf{Y}_n)$, Δt is the time step, the auxiliary variables are

$$\Upsilon_{\pm} = \mathbf{Y}_n + \mathbf{a}_n\Delta t \pm \mathbf{b}_n\sqrt{\Delta t}, \quad \Phi_{\pm} = \Upsilon_{\pm} \pm \mathbf{b}(\Upsilon_{\pm})\sqrt{\Delta t},$$

and the noises ΔW , ΔZ are found from the transformation (eq. 4.3 page 352)

$$\Delta W = U_1\sqrt{\Delta t}, \quad \Delta Z = \frac{\Delta t^{3/2}}{2}(U_1 + \frac{1}{\sqrt{3}}U_2),$$

where $U_1, U_2 \sim \mathcal{N}(0, 1)$ are i.i.d. normal random variables.

Bibliography

- [1] P. Martinez-Azcona, A. Kundu, A. del Campo, and A. Chenu, *Physical Review Letters* **131**, 160202 (2023), publisher: American Physical Society.
- [2] P. Martinez-Azcona, A. Kundu, A. Saxena, A. del Campo, and A. Chenu, *Physical Review Letters* **135**, 010402 (2025), publisher: American Physical Society.
- [3] P. Martinez-Azcona, R. Shir, and A. Chenu, *Physical Review B* **111**, 165108 (2025), publisher: American Physical Society.
- [4] P. Martinez-Azcona and A. Chenu, *Quantum* **6**, 852 (2022), publisher: Verein zur Förderung des Open Access Publizierens in den Quantenwissenschaften.
- [5] P. Nandy, A. S. Matsoukas-Roubeas, P. Martínez-Azcona, A. Dymarsky, and A. del Campo, *Physics Reports* **1125–1128**, 1–82 (2025).
- [6] R. Shir, P. Martinez-Azcona, and A. Chenu, “Surmise for random matrices’ level spacing distributions beyond nearest-neighbors,” (2025), arXiv:2504.20134 [quant-ph] .
- [7] P. Martinez-Azcona, M. Sarkis, A. Tkatchenko, and A. Chenu, “Magic steady state production: Non-hermitian and stochastic pathways,” (2025), arXiv:2507.08676 [quant-ph] .
- [8] W. H. Zurek, *Rev. Mod. Phys.* **75**, 715 (2003).
- [9] P. W. Anderson, *Science* **177**, 393 (1972), publisher: American Association for the Advancement of Science.
- [10] D. A. Lidar and T. A. Brun, eds., *Quantum Error Correction* (Cambridge University Press, Cambridge, 2013).
- [11] Z. Cai, R. Babbush, S. C. Benjamin, S. Endo, W. J. Huggins, Y. Li, J. R. McClean, and T. E. O’Brien, *Rev. Mod. Phys.* **95**, 045005 (2023).
- [12] R. P. Feynman, *QED: The strange theory of light and matter* (Princeton University Press, 2014).

- [13] M. A. Nielsen and I. L. Chuang, en “Quantum Computation and Quantum Information: 10th Anniversary Edition,” (2010), ISBN: 9780511976667 Publisher: Cambridge University Press.
- [14] M. M. Wilde, *Quantum Information Theory* (Cambridge University Press, Cambridge, 2013).
- [15] A. Uhlmann, *Reports on Mathematical Physics* **9**, 273 (1976).
- [16] R. Jozsa, *Journal of Modern Optics* **41**, 2315 (1994), publisher: Taylor & Francis eprint: <https://doi.org/10.1080/09500349414552171>.
- [17] H.-P. Breuer and F. Petruccione, *The theory of open quantum systems* (Oxford University Press on Demand, 2002).
- [18] A. Rivas and S. F. Huelga, *Open quantum systems*, Vol. 10 (Springer, 2012).
- [19] M. Stefanini, A. A. Ziolkowska, D. Budker, U. Poschinger, F. Schmidt-Kaler, A. Browaeys, A. Imamoglu, D. Chang, and J. Marino, “Is lindblad for me?” (2025), [arXiv:2506.22436 \[quant-ph\]](https://arxiv.org/abs/2506.22436) .
- [20] A. G. Redfield, *IBM Journal of Research and Development* **1**, 19 (1957).
- [21] A. G. Redfield, in *Advances in Magnetic and Optical Resonance*, Advances in Magnetic Resonance, Vol. 1, edited by J. S. Waugh (Academic Press, 1965) pp. 1–32.
- [22] R. Hartmann and W. T. Strunz, *Phys. Rev. A* **101**, 012103 (2020).
- [23] S. Nakajima, *Progress of Theoretical Physics* **20**, 948–959 (1958).
- [24] R. Zwanzig, *The Journal of Chemical Physics* **33**, 1338–1341 (1960).
- [25] C. Gonzalez-Ballester, *Quantum* **8**, 1454 (2024).
- [26] A. Smirne and B. Vacchini, *Phys. Rev. A* **82**, 022110 (2010).
- [27] Rivas, S. F. Huelga, and M. B. Plenio, *Reports on Progress in Physics* **77**, 094001 (2014), arXiv:1405.0303 [quant-ph].
- [28] L. Li, M. J. W. Hall, and H. M. Wiseman, *Physics Reports Concepts of quantum non-Markovianity: A hierarchy*, **759**, 1 (2018).
- [29] V. Gorini, A. Kossakowski, and E. C. G. Sudarshan, *J. Math. Phys.* **17**, 821 (1976).
- [30] G. Lindblad, *Communications in Mathematical Physics* **48**, 119 (1976).
- [31] I. Siemon, A. S. Holevo, and R. F. Werner, *Open Systems & Information Dynamics* (2017), [10.1142/S1230161217400157](https://doi.org/10.1142/S1230161217400157), publisher: World Scientific Publishing Company.

[32] I. Siemon, eng *Unbounded generators of dynamical semigroups*, DoctoralThesis, Hannover : Institutionelles Repozitorium der Leibniz Universität Hannover (2024).

[33] M.-D. Choi, *Linear Algebra and its Applications* **10**, 285 (1975).

[34] A. Jamiołkowski, *Reports on Math. Phys.* **3**, 275 (1972).

[35] A. A. Budini, *Physical Review A* **64**, 052110 (2001).

[36] A. A. Budini, *Phys. Rev. A* **63**, 012106 (2000).

[37] A. Chenu, M. Beau, J. Cao, and A. del Campo, *Physical Review Letters* **118**, 140403 (2017), publisher: American Physical Society.

[38] A. Kiely, *Europhysics Letters* **134**, 10001 (2021).

[39] C. W. Gardiner, *Handbook of stochastic methods*, Vol. 3 (springer Berlin, 1985).

[40] K. Jacobs, *Stochastic processes for physicists: understanding noisy systems* (Cambridge University Press, 2010).

[41] E. A. Novikov, *Sov. Phys. JETP* **20**, 1290 (1965).

[42] H. M. Wiseman and G. J. Milburn, *Quantum Measurement and Control* (Cambridge University Press, Cambridge, 2009).

[43] K. Jacobs, *Quantum Measurement Theory and its Applications* (Cambridge University Press, Cambridge, 2014).

[44] C. M. Bender and S. Boettcher, *Phys. Rev. Lett.* **80**, 5243 (1998).

[45] C. M. Bender, *Contemporary Physics* **46**, 277 (2005), arXiv:quant-ph/0501052.

[46] A. Mostafazadeh, *Journal of Mathematical Physics* **43**, 205 (2002), eprint: https://pubs.aip.org/aip/jmp/article-pdf/43/1/205/19019524/205_1_online.pdf.

[47] A. Mostafazadeh, *Journal of Mathematical Physics* **43**, 3944 (2002), arXiv:math-ph/0203005.

[48] A. Mostafazadeh, *Journal of Mathematical Physics* **43**, 2814 (2002).

[49] N. Hatano and D. R. Nelson, *Physical Review Letters* **77**, 570 (1996), publisher: American Physical Society.

[50] X. Zhang, Z. , Tian, L. , Ming-Hui, , and Y.-F. Chen, *Advances in Physics: X* **7**, 2109431 (2022), publisher: Taylor & Francis eprint: <https://doi.org/10.1080/23746149.2022.2109431>.

[51] J. T. Gohsrich, A. Banerjee, and F. K. Kunst, en “The non-Hermitian skin effect: A perspective,” (2025), arXiv:2410.23845 [quant-ph].

- [52] A. Ruschhaupt, F. Delgado, and J. G. Muga, *Journal of Physics A: Mathematical and General* **38**, L171 (2005).
- [53] R. El-Ganainy, K. G. Makris, D. N. Christodoulides, and Z. H. Musslimani, *Optics Letters* **32**, 2632 (2007), publisher: Optica Publishing Group.
- [54] A. Guo, G. J. Salamo, D. Duchesne, R. Morandotti, M. Volatier-Ravat, V. Aimez, G. A. Siviloglou, and D. N. Christodoulides, *Physical Review Letters* **103**, 093902 (2009), publisher: American Physical Society.
- [55] K. G. Makris, R. El-Ganainy, D. N. Christodoulides, and Z. H. Musslimani, *Physical Review Letters* **100**, 103904 (2008), publisher: American Physical Society.
- [56] C. E. Rüter, K. G. Makris, R. El-Ganainy, D. N. Christodoulides, M. Segev, and D. Kip, *Nature Physics* **6**, 192 (2010), number: 3 Publisher: Nature Publishing Group.
- [57] Y. Ashida, Z. Gong, and M. Ueda, *Advances in Physics* **69**, 249 (2020), arXiv:2006.01837 [cond-mat, physics:quant-ph].
- [58] Z. Lin, H. Ramezani, T. Eichelkraut, T. Kottos, H. Cao, and D. N. Christodoulides, *Physical Review Letters* **106**, 213901 (2011), publisher: American Physical Society.
- [59] J. Wiersig, *Physical Review Letters* **112**, 203901 (2014), publisher: American Physical Society.
- [60] J. Wiersig, *Physical Review A* **93**, 033809 (2016), publisher: American Physical Society.
- [61] W. Chen, Kaya Özdemir, G. Zhao, J. Wiersig, and L. Yang, *Nature* **548**, 192 (2017), publisher: Nature Publishing Group.
- [62] C. M. Bender, D. C. Brody, and M. P. Müller, *Physical Review Letters* **118**, 130201 (2017), publisher: American Physical Society.
- [63] A. Altland and M. R. Zirnbauer, *Physical Review B* **55**, 1142 (1997), publisher: American Physical Society.
- [64] Z. Gong, Y. Ashida, K. Kawabata, K. Takasan, S. Higashikawa, and M. Ueda, *Physical Review X* **8**, 031079 (2018).
- [65] K. Kawabata, K. Shiozaki, M. Ueda, and M. Sato, *Physical Review X* **9**, 041015 (2019), publisher: American Physical Society.
- [66] K. Kawabata, A. Kulkarni, J. Li, T. Numasawa, and S. Ryu, *PRX Quantum* **4**, 030328 (2023).

[67] F. Roccati, M. Bello, Z. Gong, M. Ueda, F. Ciccarello, A. Chenu, and A. Carollo, *Nature Communications* **15**, 2400 (2024), publisher: Nature Publishing Group.

[68] H. Feshbach, *Annals of Physics* **5**, 357 (1958).

[69] H. Feshbach, *Annals of Physics* **19**, 287 (1962).

[70] C. Cohen-Tannoudji, J. Dupont-Roc, and G. Grynberg, *enAtom—Photon Interactions: Basic Process and Applications*, 1st ed. (Wiley, 1998).

[71] J. G. Muga, J. P. Palao, B. Navarro, and I. L. Egusquiza, *Physics Reports* **395**, 357 (2004).

[72] J. Dalibard, Y. Castin, and K. Mølmer, *Physical Review Letters* **68**, 580 (1992).

[73] R. Dum, P. Zoller, and H. Ritsch, *Physical Review A* **45**, 4879 (1992), publisher: American Physical Society.

[74] M. B. Plenio and P. L. Knight, *Reviews of Modern Physics* **70**, 101 (1998), publisher: American Physical Society.

[75] H. J. Carmichael, *Statistical Methods in Quantum Optics 2*, Theoretical and Mathematical Physics (Springer, Berlin, Heidelberg, 2008).

[76] H. M. Wiseman, *Quantum and Semiclassical Optics: Journal of the European Optical Society Part B* **8**, 205 (1996).

[77] K. Jacobs and D. A. Steck, *Contemporary Physics* **47**, 279 (2006), arXiv:quant-ph/0611067.

[78] K. W. Murch, S. J. Weber, C. Macklin, and I. Siddiqi, *Nature* **502**, 211 (2013), number: 7470 Publisher: Nature Publishing Group.

[79] S. J. Weber, A. Chantasri, J. Dressel, A. N. Jordan, K. W. Murch, and I. Siddiqi, *Nature* **511**, 570 (2014), publisher: Nature Publishing Group.

[80] M. Naghiloo, M. Abbasi, Y. N. Joglekar, and K. W. Murch, *Nature Physics* **15**, 1232 (2019), number: 12 Publisher: Nature Publishing Group.

[81] M. Abbasi, W. Chen, M. Naghiloo, Y. N. Joglekar, and K. W. Murch, *Phys. Rev. Lett.* **128**, 160401 (2022).

[82] S. Erdamar, M. Abbasi, B. Ha, W. Chen, J. Muldoon, Y. Joglekar, and K. W. Murch, *Phys. Rev. Res.* **6**, L022013 (2024).

[83] W. Chen, M. Abbasi, B. Ha, S. Erdamar, Y. N. Joglekar, and K. W. Murch, *Phys. Rev. Lett.* **128**, 110402 (2022).

[84] W. Chen, M. Abbasi, Y. N. Joglekar, and K. W. Murch, *Physical Review Letters* **127**, 140504 (2021), arXiv:2103.06274 [cond-mat, physics:quant-ph].

[85] A. Quinn, J. Metzner, J. E. Muldoon, I. D. Moore, S. Brudney, S. Das, D. T. C. Allcock, and Y. N. Joglekar, “Observing super-quantum correlations across the exceptional point in a single, two-level trapped ion,” (2023), arXiv:2304.12413 [quant-ph].

[86] C. Emary, N. Lambert, and F. Nori, *Reports on Progress in Physics* **77**, 016001 (2013), publisher: IOP Publishing.

[87] R. Wakefield, A. Laing, and Y. N. Joglekar, *Applied Physics Letters* **124**, 201103 (2024), https://pubs.aip.org/aip/apl/article-pdf/doi/10.1063/5.0206393/19949810/201103_1_5.0206393.pdf.

[88] I. L. Paiva, A. Te’eni, B. Y. Peled, E. Cohen, and Y. Aharonov, *Communications Physics* **5**, 1 (2022), publisher: Nature Publishing Group.

[89] F. Roccati, G. M. Palma, F. Bagarello, and F. Ciccarello, *Open Systems & Information Dynamics* **29**, 2250004 (2022), arXiv:2201.05367 [quant-ph].

[90] D. C. Brody, *Journal of Physics A: Mathematical and Theoretical* **47**, 035305 (2014), arXiv:1308.2609 [math-ph, physics:quant-ph].

[91] N. Bohr, *The London, Edinburgh, and Dublin Philosophical Magazine and Journal of Science* **26**, 1 (1913), publisher: Taylor & Francis eprint: <https://doi.org/10.1080/14786441308634955>.

[92] D. C. Brody and E.-M. Graefe, *Physical Review Letters* **109**, 230405 (2012), publisher: American Physical Society.

[93] N. Hörnedal, O. A. Prośniak, A. del Campo, and A. Chenu, *Quantum* **9**, 1729 (2025).

[94] M. Naghiloo, en “Introduction to Experimental Quantum Measurement with Superconducting Qubits,” (2019), arXiv:1904.09291 [quant-ph].

[95] N. Bohr, *Nature* **137**, 344 (1936), publisher: Nature Publishing Group.

[96] E. P. Wigner, *Conference on Neutron Physics by Time of Flight* (1956), p. 59.

[97] E. P. Wigner, *SIAM Review* **9**, 1 (1967).

[98] T. A. Brody, J. Flores, J. B. French, P. Mello, A. Pandey, and S. S. Wong, *Reviews of Modern Physics* **53**, 385 (1981).

[99] T. Guhr, A. Mueller-Groeling, and H. A. Weidenmueller, *Physics Reports* **299**, 189 (1998), arXiv:cond-mat/9707301.

- [100] M. L. Mehta, *Random matrices* (Elsevier, 2004).
- [101] F. Haake, *Quantum Signatures of Chaos* (Springer Berlin Heidelberg, 2010).
- [102] F. J. Dyson, *Journal of Mathematical Physics* **3**, 1199–1215 (1962).
- [103] M. L. Mehta, *Random matrices* (Elsevier, 2004).
- [104] E. P. Wigner, *Mathematical Proceedings of the Cambridge Philosophical Society* **47**, 790–798 (1951).
- [105] S. Wimberger, *Nonlinear dynamics and quantum chaos*, Vol. 10 (Springer, 2014).
- [106] E. P. Wigner, *The Annals of Mathematics* **67**, 325 (1958).
- [107] C. L. Bertrand and A. M. García-García, *Physical Review B* **94**, 144201 (2016).
- [108] M. V. Berry and M. Tabor, *Proceedings of the Royal Society of London. A. Mathematical and Physical Sciences* **356**, 375 (1977), publisher: The Royal Society London.
- [109] J.-S. Caux and J. Mossel, *Journal of Statistical Mechanics: Theory and Experiment* **2011**, P02023 (2011).
- [110] O. Bohigas, M. J. Giannoni, and C. Schmit, *Physical Review Letters* **52**, 1 (1984).
- [111] H.-J. Stöckmann and J. Stein, *Phys. Rev. Lett.* **64**, 2215 (1990).
- [112] H.-J. Stöckmann, *Quantum Chaos: An Introduction* (Cambridge University Press, Cambridge, 1999).
- [113] F. Haake, M. Kuś, and R. Scharf, *Zeitschrift für Physik B Condensed Matter* **65**, 381 (1987).
- [114] V. Oganesyan and D. A. Huse, *Physical Review B* **75**, 155111 (2007), publisher: American Physical Society.
- [115] Y. Y. Atas, E. Bogomolny, O. Giraud, and G. Roux, *Physical Review Letters* **110**, 084101 (2013), publisher: American Physical Society.
- [116] Y. Y. Atas, E. Bogomolny, O. Giraud, P. Vivo, and E. Vivo, *Journal of Physics A: Mathematical and Theoretical* **46**, 355204 (2013), publisher: IOP Publishing.
- [117] F. J. Dyson and M. L. Mehta, *Journal of Mathematical Physics* **4**, 701 (1963).
- [118] M. V. Berry, *Proceedings of the Royal Society of London. A. Mathematical and Physical Sciences* **400**, 229 (1985), <https://royalsocietypublishing.org/doi/pdf/10.1098/rspa.1985.0078>.
- [119] L. Leviandier, M. Lombardi, R. Jost, and J. P. Pique, *Physical Review Letters* **56**, 2449 (1986), publisher: American Physical Society.

- [120] J. Wilkie and P. Brumer, *Physical Review Letters* **67**, 1185 (1991), publisher: American Physical Society.
- [121] Y. Alhassid and R. D. Levine, *Physical Review A* **46**, 4650 (1992), publisher: American Physical Society.
- [122] J.-Z. Ma, *Journal of the Physical Society of Japan* **64**, 4059 (1995), publisher: The Physical Society of Japan.
- [123] J. S. Cotler, G. Gur-Ari, M. Hanada, J. Polchinski, P. Saad, S. H. Shenker, D. Stanford, A. Streicher, and M. Tezuka, *Journal of High Energy Physics* **2017**, 118 (2017).
- [124] J. Cotler, N. Hunter-Jones, J. Liu, and B. Yoshida, *Journal of High Energy Physics* **2017**, 48 (2017).
- [125] A. Chenu, I. L. Egusquiza, J. Molina-Vilaplana, and A. del Campo, *Scientific Reports* **8**, 12634 (2018).
- [126] A. Chenu, J. Molina-Vilaplana, and A. d. Campo, *Quantum* **3**, 127 (2019), publisher: Verein zur Förderung des Open Access Publizierens in den Quantenwissenschaften.
- [127] R. E. Prange, *Physical Review Letters* **78**, 2280 (1997), publisher: American Physical Society.
- [128] J. Maldacena, S. H. Shenker, and D. Stanford, *Journal of High Energy Physics* **2016**, 106 (2016), arXiv:1503.01409 [cond-mat, physics:hep-th, physics:nlin, physics:quant-ph].
- [129] A. del Campo, J. Molina-Vilaplana, and J. Sonner, *Physical Review D* **95**, 126008 (2017), publisher: American Physical Society.
- [130] J. Šuntajs, J. Bonča, T. Prosen, and L. Vidmar, *Physical Review E* **102**, 062144 (2020), publisher: American Physical Society.
- [131] A. S. Matsoukas-Roubeas, M. Beau, L. F. Santos, and A. del Campo, *Physical Review A* **108**, 062201 (2023), publisher: American Physical Society.
- [132] Z. Xu, A. Chenu, T. Prosen, and A. del Campo, *Physical Review B* **103**, 064309 (2021).
- [133] F. Haake, *Quantum signatures of chaos* (Springer, 1991).
- [134] M. Sieber and K. Richter, *Physica Scripta* **2001**, 128 (2001), publisher: IOP Publishing.
- [135] S. Müller, S. Heusler, P. Braun, F. Haake, and A. Altland, *Phys. Rev. E* **72**, 046207 (2005).

- [136] P. Kos, M. Ljubotina, and T. c. v. Prosen, *Phys. Rev. X* **8**, 021062 (2018).
- [137] A. Kitaev, in *Talk given at the Fundamental Physics Prize Symposium*, Vol. 10 (2014) p. 33.
- [138] A. Kitaev, Kavli Institute for Theoretical Physics, Santa Barbara USA (2015).
- [139] I. Garcia-Mata, R. Jalabert, and D. Wisniacki, *Scholarpedia* **18**, 55237 (2023).
- [140] A. I. Larkin and Y. N. Ovchinnikov, *Soviet Journal of Experimental and Theoretical Physics* **28**, 1200 (1969).
- [141] S. Sachdev and J. Ye, *Phys. Rev. Lett.* **70**, 3339 (1993).
- [142] J. Maldacena and D. Stanford, *Physical Review D* **94**, 106002 (2016).
- [143] B. Kobrin, Z. Yang, G. D. Kahanamoku-Meyer, C. T. Olund, J. E. Moore, D. Stanford, and N. Y. Yao, *Physical Review Letters* **126**, 030602 (2021).
- [144] E. H. Lieb and D. W. Robinson, *Communications in Mathematical Physics* **28**, 251–257 (1972).
- [145] S. Xu and B. Swingle, *Physical Review X* **9**, 031048 (2019).
- [146] S. Xu and B. Swingle, *Nature Physics* **16**, 199–204 (2019).
- [147] S. Xu and B. Swingle, *PRX Quantum* **5**, 010201 (2024).
- [148] B. Swingle, *Nature Physics* **14**, 988 (2018), publisher: Nature Publishing Group.
- [149] D. E. Parker, X. Cao, A. Avdoshkin, T. Scaffidi, and E. Altman, *Physical Review X* **9**, 041017 (2019), publisher: American Physical Society.
- [150] J. S. Cotler, D. Ding, and G. R. Penington, *Annals of Physics* **396**, 318–333 (2018).
- [151] T. Xu, T. Scaffidi, and X. Cao, *Physical Review Letters* **124**, 140602 (2020).
- [152] E. B. Rozenbaum, S. Ganeshan, and V. Galitski, *Phys. Rev. Lett.* **118**, 086801 (2017).
- [153] E. B. Rozenbaum, L. A. Bunimovich, and V. Galitski, *Phys. Rev. Lett.* **125**, 014101 (2020).
- [154] S. Pilatowsky-Cameo, J. Chávez-Carlos, M. A. Bastarrachea-Magnani, P. Stránský, S. Lerma-Hernández, L. F. Santos, and J. G. Hirsch, *Physical Review E* **101**, 010202 (2020).
- [155] N. Dowling, P. Kos, and K. Modi, *Phys. Rev. Lett.* **131**, 180403 (2023).
- [156] S. H. Strogatz, *Nonlinear Dynamics and Chaos: With Applications to Physics, Biology, Chemistry and Engineering* (Westview, 2000).

[157] R. L. Devaney, *An Introduction to Chaotic Dynamical Systems* (Chapman and Hall/CRC, 2021).

[158] J. Banks, J. Brooks, G. Cairns, G. Davis, and P. Stacey, *The American Mathematical Monthly* **99**, 332–334 (1992).

[159] D. Chowdhury and B. Swingle, *Phys. Rev. D* **96**, 065005 (2017).

[160] N. Tsuji, T. Shitara, and M. Ueda, *Physical Review E* **98**, 012216 (2018).

[161] Y. Liao and V. Galitski, *Phys. Rev. B* **98**, 205124 (2018).

[162] A. Romero-Bermúdez, K. Schalm, and V. Scopelliti, *Journal of High Energy Physics* **2019** (2019), 10.1007/jhep07(2019)107.

[163] S. Sahu and B. Swingle, *Phys. Rev. B* **102**, 184303 (2020).

[164] Y. Sekino and L. Susskind, *Journal of High Energy Physics* **2008**, 065 (2008), arXiv:0808.2096 [hep-th, physics:quant-ph].

[165] A. Vikram and V. Galitski, *Phys. Rev. Lett.* **132**, 040402 (2024).

[166] J. Kurchan, *J. Stat. Phys.* **171**, 965 (2018).

[167] S. Pappalardi and J. Kurchan, *SciPost Physics* **13**, 006 (2022).

[168] N. Tsuji, T. Shitara, and M. Ueda, *Physical Review E* **97**, 012101 (2018).

[169] S. Pappalardi, L. Foini, and J. Kurchan, *SciPost Physics* **12**, 130 (2022).

[170] S. V. Syzranov, A. V. Gorshkov, and V. Galitski, *Physical Review B* **97**, 161114 (2018), arXiv:1704.08442 [cond-mat, physics:quant-ph].

[171] P. Zanardi and N. Anand, *Physical Review A* **103**, 062214 (2021).

[172] Y.-L. Zhang, Y. Huang, and X. Chen, *Physical Review B* **99**, 014303 (2019), publisher: American Physical Society.

[173] T. Schuster and N. Y. Yao, *Phys. Rev. Lett.* **131**, 160402 (2023).

[174] K. Richter, J. Diego Urbina, and S. Tomsovic, *Journal of Physics A: Mathematical and Theoretical* **55**, 453001 (2022).

[175] J. Preskill, *Quantum* **2**, 79 (2018), publisher: Verein zur Förderung des Open Access Publizierens in den Quantenwissenschaften.

[176] K. Bharti, A. Cervera-Lierta, T. H. Kyaw, T. Haug, S. Alperin-Lea, A. Anand, M. Degroote, H. Heimonen, J. S. Kottmann, T. Menke, W.-K. Mok, S. Sim, L.-C. Kwek, and A. Aspuru-Guzik, *Reviews of Modern Physics* **94**, 015004 (2022).

[177] K. Mølmer, Y. Castin, and J. Dalibard, *JOSA B* **10**, 524 (1993), publisher: Optica Publishing Group.

[178] H. Carmichael, *An Open Systems Approach to Quantum Optics*, Lecture Notes in Physics Monographs, Vol. 18 (Springer Berlin Heidelberg, Berlin, Heidelberg, 1993) chapter 9.

[179] H. J. Carmichael, *Statistical Methods in Quantum Optics 1* (Springer Berlin Heidelberg, 1999).

[180] E. N. Lorenz, *Journal of the Atmospheric Sciences* **20**, 130 (1963), publisher: American Meteorological Society Section: Journal of the Atmospheric Sciences.

[181] M. Schrauth, F. Dusel, Y. Thurn, F. Goth, D. Herdt, and J. S. E. Portela, “hyper-tiling,” (2023).

[182] S. Gammelmark, B. Julsgaard, and K. Mølmer, *Physical Review Letters* **111**, 160401 (2013), publisher: American Physical Society.

[183] P. Warszawski, H. M. Wiseman, and A. C. Doherty, *Physical Review A* **102**, 042210 (2020).

[184] R. Bhatia, *Positive Definite Matrices* (Princeton University Press, 2009).

[185] R. V. Kadison, *The Annals of Mathematics* **56**, 494 (1952).

[186] N. Anand and P. Zanardi, *Quantum* **6**, 746 (2022), publisher: Verein zur Förderung des Open Access Publizierens in den Quantenwissenschaften.

[187] W. Heisenberg, *Zeitschrift für Physik* **43**, 172 (1927).

[188] R. Bhatia and C. Davis, *Communications in Mathematical Physics* **215**, 239 (2000).

[189] H. P. Robertson, *Physical Review* **34**, 163 (1929), publisher: American Physical Society.

[190] E. Schrödinger, *Zum heisenbergschen unschärfeprinzip* (Akademie der Wissenschaften, 1930).

[191] T. Ando, *Linear Algebra and its Applications* **26**, 203 (1979).

[192] M.-D. Choi, *Journal of Operator Theory* **4**, 271 (1980), publisher: Theta Foundation.

[193] L. Dupays, I. L. Egusquiza, A. del Campo, and A. Chenu, *Phys. Rev. Res.* **2**, 033178 (2020).

[194] F. J. Gómez-Ruiz, J. J. Mayo, and A. del Campo, *Phys. Rev. Lett.* **124**, 240602 (2020).

[195] S. Pappalardi and J. Kurchan, *Entropy* **25**, 246 (2023).

[196] F. Verstraete, M. M. Wolf, and J. Ignacio Cirac, *Nature Physics* **5**, 633 (2009), publisher: Nature Publishing Group.

[197] J. T. Barreiro, M. Müller, P. Schindler, D. Nigg, T. Monz, M. Chwalla, M. Hennrich, C. F. Roos, P. Zoller, and R. Blatt, *Nature* **470**, 486 (2011), publisher: Nature Publishing Group.

[198] V. V. Albert and L. Jiang, *Physical Review A* **89**, 022118 (2014), arXiv:1310.1523 [cond-mat, physics:quant-ph].

[199] V. V. Albert, *en “Lindbladians with multiple steady states: theory and applications,”* (2018), arXiv:1802.00010 [cond-mat, physics:math-ph, physics:quant-ph].

[200] B. Baumgartner and H. Narnhofer, *Journal of Physics A: Mathematical and Theoretical* **41**, 395303 (2008).

[201] B. Buča and T. Prosen, *New Journal of Physics* **14**, 073007 (2012), publisher: IOP Publishing.

[202] D. A. Lidar, I. L. Chuang, and K. B. Whaley, *Physical Review Letters* **81**, 2594 (1998), publisher: American Physical Society.

[203] C. Gardiner and P. Zoller, *Quantum Noise: A Handbook of Markovian and Non-Markovian Quantum Stochastic Methods with Applications to Quantum Optics* (Springer Science & Business Media, 2004).

[204] R. L. Hudson and K. R. Parthasarathy, *Communications in Mathematical Physics* **93**, 301–323 (1984).

[205] R. J. Lewis-Swan, A. Safavi-Naini, J. J. Bollinger, and A. M. Rey, *Nature Communications* **10**, 1581 (2019), number: 1 Publisher: Nature Publishing Group.

[206] K. Hashimoto, K. Murata, and R. Yoshii, *Journal of High Energy Physics* **2017**, 138 (2017), arXiv:1703.09435 [cond-mat, physics:hep-th, physics:nlin, physics:quant-ph].

[207] B. Swingle and N. Yunger Halpern, *Physical Review A* **97**, 062113 (2018).

[208] H. J. Lipkin, N. Meshkov, and A. J. Glick, *Nuclear Physics* **62**, 188 (1965).

[209] S. Pappalardi, A. Russomanno, B. Žunkovič, F. Iemini, A. Silva, and R. Fazio, *Physical Review B* **98**, 134303 (2018).

[210] R. Islam, E. E. Edwards, K. Kim, S. Korenblit, C. Noh, H. Carmichael, G.-D. Lin, L.-M. Duan, C.-C. Joseph Wang, J. K. Freericks, and C. Monroe, *Nature Communications* **2**, 377 (2011).

[211] Z. Li, S. Colombo, C. Shu, G. Velez, S. Pilatowsky-Cameo, R. Schmied, S. Choi, M. Lukin, E. Pedrozo-Peña, and V. Vuletić, *Science* **380**, 1381–1384 (2023).

[212] A. M. Jayannavar and N. Kumar, *Physical Review Letters* **48**, 553 (1982), publisher: American Physical Society.

[213] P. D. Hislop, K. Kirkpatrick, S. Olla, and J. Schenker, *Journal of Mathematical Physics* **60**, 083303 (2019).

[214] A. Perelomov, *Generalized coherent states and their applications* (Springer Science & Business Media, 2012) chapter 4.

[215] I. L. Egusquiza, L. J. Garay, and J. M. Raya, *Physical Review A* **59**, 3236 (1999), arXiv:quant-ph/9811009.

[216] N. G. Van Kampen, *Physics Reports* **24**, 171 (1976).

[217] N. G. V. Kampen, *Stochastic Processes in Physics and Chemistry* (Elsevier, 1992) chapter XVI.

[218] P. Kapitza, in *Collected Papers of P.L. Kapitza*, edited by D. Ter haar (Pergamon, 1965) pp. 714–725.

[219] P. Kapitza, in *Collected Papers of P.L. Kapitza*, edited by D. Ter haar (Pergamon, 1965) pp. 726–737.

[220] R. Citro, E. G. Dalla Torre, L. D’Alessio, A. Polkovnikov, M. Babadi, T. Oka, and E. Demler, *Annals of Physics* **360**, 694 (2015).

[221] N. Defenu, A. Lerose, and S. Pappalardi, *Physics Reports Out-of-equilibrium dynamics of quantum many-body systems with long-range interactions*, **1074**, 1 (2024).

[222] A. del Campo, I. L. Egusquiza, M. B. Plenio, and S. F. Huelga, *Phys. Rev. Lett.* **110**, 050403 (2013).

[223] R. Hamazaki, *en“Limits to Fluctuation Dynamics,”* (2023), arXiv:2309.07301 [cond-mat, physics:quant-ph].

[224] H.-Y. Huang, R. Kueng, and J. Preskill, *Nature Physics* **16**, 1050–1057 (2020).

[225] M. Carlesso, S. Donadi, L. Ferialdi, M. Paternostro, H. Ulbricht, and A. Bassi, *Nature Physics* **18**, 243–250 (2022).

[226] J. Oppenheim, *Phys. Rev. X* **13**, 041040 (2023).

[227] C. Gerry and P. Knight, *Introductory Quantum Optics* (Cambridge University Press, Cambridge, 2004).

[228] S. Bravyi and A. Kitaev, *Physical Review A* **71**, 022316 (2005), arXiv:quant-ph/0403025.

[229] A. Nahum, J. Ruhman, S. Vijay, and J. Haah, *Phys. Rev. X* **7**, 031016 (2017).

[230] M. P. Fisher, V. Khemani, A. Nahum, and S. Vijay, *Annual Review of Condensed Matter Physics* **14**, 335 (2023).

[231] F. Schmolke and E. Lutz, *Physical Review Letters* **129**, 250601 (2022), arXiv:2206.02456 [cond-mat, physics:quant-ph].

[232] F. Schmolke and E. Lutz, *Physical Review Letters* **132**, 010402 (2024), arXiv:2306.12986 [cond-mat, physics:quant-ph].

[233] C. M. Bender, P. E. Dorey, C. Dunning, A. Fring, D. W. Hook, H. F. Jones, S. Kuzhel, G. Lévai, and R. Tateo, *enPT Symmetry: In Quantum and Classical Physics* (WORLD SCIENTIFIC (EUROPE), 2019).

[234] C. M. Bender and S. Boettcher, *Physical Review Letters* **80**, 5243 (1998), publisher: American Physical Society.

[235] A. Quinn, J. Metzner, J. E. Muldoon, I. D. Moore, S. Brudney, S. Das, D. T. C. Allcock, and Y. N. Joglekar, en “Observing super-quantum correlations across the exceptional point in a single, two-level trapped ion,” (2023), arXiv:2304.12413 [quant-ph].

[236] S. H. Strogatz, *Nonlinear Dynamics and Chaos: With Applications to Physics, Biology, Chemistry, and Engineering*, 2nd ed. (CRC Press, Boca Raton, 2019).

[237] D. Burgarth, P. Facchi, G. Garnero, H. Nakazato, S. Pascazio, and K. Yuasa, *Open Systems & Information Dynamics* **24**, 1750001 (2017), arXiv:1609.01476 [math-ph, physics:quant-ph].

[238] B. Gu and I. Franco, *The Journal of Chemical Physics* **151**, 014109 (2019).

[239] K. Kawasaki, *Journal of Physics A: Mathematical, Nuclear and General* **6**, 1289 (1973).

[240] F. Carollo, J. P. Garrahan, I. Lesanovsky, and C. Pérez-Espigares, *Phys. Rev. A* **98**, 010103 (2018).

[241] F. Carollo, R. L. Jack, and J. P. Garrahan, *Physical Review Letters* **122**, 130605 (2019), arXiv:1811.04969 [cond-mat, physics:quant-ph].

[242] F. Carollo, J. P. Garrahan, and R. L. Jack, *Journal of Statistical Physics* **184** (2021), 10.1007/s10955-021-02799-x.

[243] G. T. Landi, M. J. Kewming, M. T. Mitchison, and P. P. Potts, *PRX Quantum* **5**, 020201 (2024).

[244] D. A. Lidar, en “Lecture Notes on the Theory of Open Quantum Systems,” (2020), arXiv:1902.00967 [quant-ph].

[245] M. R. Geller, *Advanced Quantum Technologies* **6**, 2200156 (2023), eprint: <https://onlinelibrary.wiley.com/doi/pdf/10.1002/qute.202200156>.

[246] D. C. Brody and E.-M. Graefe, *Phys. Rev. Lett.* **109**, 230405 (2012).

[247] Z. Xu, L. P. García-Pintos, A. Chenu, and A. del Campo, *Physical Review Letters* **122**, 014103 (2019), arXiv:1810.02319 [cond-mat, physics:hep-th, physics:quant-ph].

[248] M. Beau, J. Kiukas, I. L. Egusquiza, and A. del Campo, *Phys. Rev. Lett.* **119**, 130401 (2017).

[249] D. Shemesh, *Linear Algebra and its Applications* **62**, 11 (1984).

[250] A. Jamiołkowski and G. Pastuszak, *Linear and Multilinear Algebra* **63**, 314 (2015), publisher: Taylor & Francis eprint: <https://doi.org/10.1080/03081087.2013.865734>.

[251] F. Minganti, A. Miranowicz, R. W. Chhajlany, and F. Nori, *Physical Review A* **100**, 062131 (2019), publisher: American Physical Society.

[252] F. Minganti, A. Miranowicz, R. W. Chhajlany, I. I. Arkhipov, and F. Nori, *Physical Review A* **101**, 062112 (2020), arXiv:2002.11620 [quant-ph].

[253] M. Naghiloo, D. Tan, P. Harrington, J. Alonso, E. Lutz, A. Romito, and K. Murch, *Physical Review Letters* **124**, 110604 (2020).

[254] L. Diósi, N. Gisin, and W. T. Strunz, *Phys. Rev. A* **58**, 1699 (1998).

[255] J. Gambetta, T. Askerud, and H. M. Wiseman, *Phys. Rev. A* **69**, 052104 (2004).

[256] L. Diósi, *Phys. Rev. Lett.* **100**, 080401 (2008).

[257] H. M. Wiseman and J. M. Gambetta, *Phys. Rev. Lett.* **101**, 140401 (2008).

[258] R. Nickalls, *The Math. Gazette* **77**, 354–359 (1993).

[259] F. Minganti, A. Miranowicz, R. W. Chhajlany, and F. Nori, *Phys. Rev. A* **100**, 062131 (2019).

[260] W. Horsthemke and R. LaFever, *Noise-Induced Transitions*, Springer Series in Synergetics, Vol. 15 (Springer Berlin Heidelberg, 2006).

[261] M. V. Berry and M. Wilkinson, *Proceedings of the Royal Society of London. A. Mathematical and Physical Sciences* **392**, 15 (1997), publisher: Royal Society.

[262] D. Bures, *Transactions of the American Mathematical Society* **135**, 199 (1969).

[263] M. Hübner, *Physics Letters A* **163**, 239 (1992).

[264] N. Hörnedal, O. A. Prośniak, A. d. Campo, and A. Chenu, “A geometrical description of non-Hermitian dynamics: speed limits in finite rank density operators,” (2024), arXiv:2405.13913 [quant-ph].

[265] M. O. Scully and M. S. Zubairy, *Quantum Optics* (Cambridge University Press, 1997).

[266] S. H. Rice (2015).

[267] J. A. Sherman, M. J. Curtis, D. J. Szwier, D. T. C. Allcock, G. Imreh, D. M. Lucas, and A. M. Steane, *Phys. Rev. Lett.* **111**, 180501 (2013).

[268] E. Brion, L. H. Pedersen, and K. Mølmer, *Journal of Physics A: Mathematical and Theoretical* **40**, 1033 (2007).

[269] W. Chen, M. Abbasi, B. Ha, S. Erdamar, Y. N. Joglekar, and K. W. Murch, *Physical Review Letters* **128**, 110402 (2022), publisher: American Physical Society.

[270] J. P. Garrahan and I. Lesanovsky, *Physical Review Letters* **104**, 160601 (2010), arXiv:0911.0556 [cond-mat, physics:quant-ph].

[271] M. Esposito, U. Harbola, and S. Mukamel, *Rev. Mod. Phys.* **81**, 1665 (2009).

[272] J. L. Lebowitz and H. Spohn, *Journal of Statistical Physics* **95**, 333–365 (1999).

[273] M. Cech, I. Lesanovsky, and F. Carollo, *Physical Review Letters* **131**, 120401 (2023).

[274] A. Tilloy, M. Bauer, and D. Bernard, *Phys. Rev. A* **92**, 052111 (2015).

[275] A. Sherry, C. Bernardin, A. Dhar, A. Kundu, and R. Chetrite, *Phys. Rev. A* **111**, 042215 (2025).

[276] M. Motta, C. Sun, A. T. K. Tan, M. J. O’Rourke, E. Ye, A. J. Minnich, F. G. S. L. Brandão, and G. K.-L. Chan, *Nature Physics* **16**, 205 (2020), publisher: Nature Publishing Group.

[277] B. Barch and D. Lidar, en “Computational Complexity of Non-Hermitian Quantum Systems,” (2025), arXiv:2506.03435 [quant-ph].

[278] M. Krbálek and P. Seba, *Journal of Physics A: Mathematical and General* **33**, L229–L234 (2000).

[279] S. Rawal and G. Rodgers, *Physica A: Statistical Mechanics and its Applications* **346**, 621–630 (2005).

[280] A. Abul-Magd, *Physica A: Statistical Mechanics and its Applications* **368**, 536–540 (2006).

[281] P. Šeba, *Journal of Statistical Mechanics: Theory and Experiment* **2009**, L10002 (2009).

[282] G. Akemann, M. Baake, N. Chakarov, O. Krüger, A. Mielke, M. Ottensmann, and R. Werdehausen, *Journal of Theoretical Biology* **509**, 110475 (2021).

[283] M. C. Gutzwiller, *Journal of Mathematical Physics* **12**, 343 (2003), https://pubs.aip.org/aip/jmp/article-pdf/12/3/343/10951718/343_1_online.pdf.

[284] J. H. Hannay and A. M. O. D. Almeida, *Journal of Physics A: Mathematical and General* **17**, 3429 (1984).

[285] M. Sieber, *Journal of Physics A: Mathematical and General* **35**, L613–L619 (2002).

[286] S. Müller, S. Heusler, P. Braun, F. Haake, and A. Altland, *Phys. Rev. Lett.* **93**, 014103 (2004).

[287] S. Heusler, S. Müller, A. Altland, P. Braun, and F. Haake, *Phys. Rev. Lett.* **98**, 044103 (2007).

[288] B. Bertini, P. Kos, and T. c. v. Prosen, *Phys. Rev. Lett.* **121**, 264101 (2018).

[289] B. Bertini, P. Kos, and T. c. v. Prosen, *Phys. Rev. Lett.* **123**, 210601 (2019).

[290] B. Bertini, P. Kos, and T. c. v. Prosen, *Phys. Rev. X* **9**, 021033 (2019).

[291] P. B. Kahn and C. E. Porter, *Nuclear Physics* **48**, 385 (1963).

[292] A. Y. Abul-Magd and M. H. Simbel, *Physical Review E* **60**, 5371 (1999).

[293] W.-J. Rao, *Physical Review B* **102**, 054202 (2020), publisher: American Physical Society.

[294] D. Engel, J. Main, and G. Wunner, *Journal of Physics A: Mathematical and General* **31**, 6965 (1998).

[295] T. A. Brody, *Lettere Al Nuovo Cimento Series 2* **7**, 482–484 (1973).

[296] A. Y. Abul-Magd and M. H. Simbel, *Physical Review E* **62**, 4792 (2000), publisher: American Physical Society.

[297] P. J. Forrester, *Communications in Mathematical Physics* **285**, 653 (2009).

[298] J. Sakhr and J. M. Nieminen, *Physical Review E* **73**, 047202 (2006).

[299] S. H. Tekur, U. T. Bhosale, and M. S. Santhanam, *Physical Review B* **98**, 104305 (2018).

[300] J. B. French, P. A. Mello, and A. Pandey, *Annals of Physics* **113**, 277 (1978).

- [301] S. P. Mirevski and L. Boyadjiev, *Computers & Mathematics with Applications Advance in Fractional Differential Equations*, **59**, 1271 (2010).
- [302] D. A. Abanin, E. Altman, I. Bloch, and M. Serbyn, *Rev. Mod. Phys.* **91**, 021001 (2019).
- [303] K. Joel, D. Kollmar, and L. F. Santos, *American Journal of Physics* **81**, 450 (2013), arXiv:1209.0115 [cond-mat, physics:quant-ph].
- [304] R. Nandkishore and D. A. Huse, *Annual Review of Condensed Matter Physics* **6**, 15–38 (2015).
- [305] P. Sierant, M. Lewenstein, A. Scardicchio, L. Vidmar, and J. Zakrzewski, *Reports on Progress in Physics* **88**, 026502 (2025).
- [306] J. Z. Imbrie, *Journal of Statistical Physics* **163**, 998–1048 (2016).
- [307] W. D. Roeck, L. Giacomin, F. Huveneers, and O. Prosnak, “Absence of normal heat conduction in strongly disordered interacting quantum chains,” (2025), arXiv:2408.04338 [math-ph].
- [308] M. Schiulaz, E. J. Torres-Herrera, F. Pérez-Bernal, and L. F. Santos, *Physical Review B* **101**, 174312 (2020), arXiv:1906.11856 [cond-mat].
- [309] J. T. Edwards and D. J. Thouless, *Journal of Physics C: Solid State Physics* **5**, 807 (1972).
- [310] M. L. Mehta and F. J. Dyson, *Journal of Mathematical Physics* **4**, 713 (1963).
- [311] M. Winer, S.-K. Jian, and B. Swingle, *Physical Review Letters* **125**, 250602 (2020), arXiv:2006.15152 [cond-mat, physics:hep-th].
- [312] Y. Liao, A. Vikram, and V. Galitski, *Physical Review Letters* **125**, 250601 (2020), arXiv:2005.08991 [cond-mat, physics:hep-th].
- [313] D. V. Vasilyev, A. Grankin, M. A. Baranov, L. M. Sieberer, and P. Zoller, *PRX Quantum* **1**, 020302 (2020), publisher: American Physical Society.
- [314] L. K. Joshi, A. Elben, A. Vikram, B. Vermersch, V. Galitski, and P. Zoller, *Physical Review X* **12**, 011018 (2022).
- [315] A. K. Das, C. Cianci, D. G. A. Cabral, D. A. Zarate-Herrada, P. Pinney, S. Pilatowsky-Cameo, A. S. Matsoukas-Roubeas, V. S. Batista, A. del Campo, E. J. Torres-Herrera, and L. F. Santos, *Phys. Rev. Res.* **7**, 013181 (2025).
- [316] H. Dong, P. Zhang, C. B. Dağ, Y. Gao, N. Wang, J. Deng, X. Zhang, J. Chen, S. Xu, K. Wang, Y. Wu, C. Zhang, F. Jin, X. Zhu, A. Zhang, Y. Zou, Z. Tan, Z. Cui, Z. Zhu, F. Shen, T. Li, J. Zhong, Z. Bao, H. Li, Z. Wang, Q. Guo, C. Song,

F. Liu, A. Chan, L. Ying, and H. Wang, *Phys. Rev. Lett.* **134**, 010402 (2025).

[317] L. Sá, P. Ribeiro, and T. Prosen, *Physical Review X* **10**, 021019 (2020).

[318] J. Cornelius, Z. Xu, A. Saxena, A. Chenu, and A. del Campo, *Phys. Rev. Lett.* **128**, 190402 (2022).

[319] A. S. Matsoukas-Roubeas, F. Roccati, J. Cornelius, Z. Xu, A. Chenu, and A. del Campo, *Journal of High Energy Physics* **2023** (2023), 10.1007/jhep01(2023)060.

[320] A. M. García-García, L. Sá, and J. J. Verbaarschot, *Physical Review D* **107**, 066007 (2023).

[321] F. Roccati, F. Balducci, R. Shir, and A. Chenu, *Phys. Rev. B* **109**, L140201 (2024).

[322] M. Massaro and A. del Campo, *Phys. Rev. Res.* **7**, 023107 (2025).

[323] S. Sachdev and J. Ye, *Phys. Rev. Lett.* **70**, 3339 (1993).

[324] C. Sünderhauf, L. Piroli, X.-L. Qi, N. Schuch, and J. I. Cirac, *Journal of High Energy Physics* **2019** (2019), 10.1007/jhep11(2019)038.

[325] F. Minganti, A. Miranowicz, R. W. Chhajlany, I. I. Arkhipov, and F. Nori, *Phys. Rev. A* **101**, 062112 (2020).

[326] H. Tang, “Brownian gaussian unitary ensemble: non-equilibrium dynamics, efficient k -design and application in classical shadow tomography,” (2024), arXiv:2406.11320 [hep-th] .

[327] J. M. Renes, R. Blume-Kohout, A. J. Scott, and C. M. Caves, *Journal of Mathematical Physics* **45**, 2171–2180 (2004).

[328] A. Klappenecker and M. Roetteler, “Mutually unbiased bases are complex projective 2-designs,” (2005), arXiv:quant-ph/0502031 [quant-ph] .

[329] C. Dankert, R. Cleve, J. Emerson, and E. Livine, *Phys. Rev. A* **80**, 012304 (2009).

[330] E. Onorati, O. Buerschaper, M. Kliesch, W. Brown, A. H. Werner, and J. Eisert, *Communications in Mathematical Physics* **355**, 905–947 (2017).

[331] M. Aifer, K. Donatella, M. H. Gordon, S. Duffield, T. Ahle, D. Simpson, G. Crooks, and P. J. Coles, *npj Unconventional Computing* **1** (2024), 10.1038/s44335-024-00014-0.

[332] P. E. Kloeden and E. Platen, *Numerical Solution of Stochastic Differential Equations*, edited by P. E. Kloeden and E. Platen, Applications of Mathematics (Springer, Berlin, Heidelberg, 1992).

List of Figures

1	Conceptual map of the main results of the thesis	xvii
1.1	Quality of the numerical unfolding for GOE	30
1.2	Level spacing distribution for the Kicked Top	31
1.3	SFF for the RMT ensembles	36
2.1	Pictorial representation of the Stochastic Operator Variance and its difference with the quantum mechanical variance	48
2.2	Introducing chaos in the pictorial depiction of the SOV	50
2.3	Illustration of the SOV	53
2.4	Replica interpretation of the SOV	56
2.5	Illustration of the SOV-OTOC connection	68
2.6	Evolution of the SOV eigenvalues and OTOC for LMG	75
2.7	Eigenvalues of SOV for LMG with non-commuting Hamiltonian and Jump	75
2.8	Short time behavior of OTOC in LMG	76
2.9	Visualization of the SOV evolution for LMG	77
2.10	Lyapunov exponent for classical sLMG	83
2.11	Visualization of the sLMG model	85
3.1	Purity evolution for SDQ	114
3.2	λ_0 is the largest eigenvalue	116
3.3	Liouvillian spectrum for SDQ	117
3.4	Spectral and steady state phase diagram	119
3.5	Non-orthogonality of Liouvillian eigenstates	125
3.6	Non-orthogonality of eigenvectors 2	126
3.7	Non-orthogonality of Liouvillian eigenstates as function of Γ	126
3.8	Streamlines in the Bloch sphere of SDQ	128
3.9	Nullclines of the radial coordinate	131
3.10	Area of purifying region in Bloch sphere	133
3.11	Angular nullclines for SDQ vector field	134

3.12	z coordinate as function of Γ in SDQ	135
3.13	Convergence to PTb and NI phases of SDQ	136
3.14	z coordinate dynamics in SDQ	141
3.15	Dynamics of z coordinate in SDQ 2	142
3.16	Dynamics of the Bloch y coordinate	143
3.17	Evolution of Purity in SDQ in different methods	144
3.18	Fidelity between time evolved and steady state in SDQ	145
3.19	Single Trajectories of the SDQ	149
3.20	Evolution of Bloch coordinates from single trajectories	150
3.21	Single trajectory steady state phase diagrams for the SDQ	150
3.22	No pump dynamics of the SDQ	152
3.23	Fitting strategy to experimental data of DQ	157
3.24	Residual damping: antidephasing & dephasing models	159
3.25	Comparison between real and imaginary noise models	160
4.1	Time evolution of the kn SFF for RMT and Poisson	182
4.2	k -th neighbor Spectral Form Factor for the disordered XXZ spin chain	185
4.3	Minimum time for the kn SFF for RMT and Poisson	186
4.4	Minimum value of the kn SFF and scaling of the deepest kn SFF for RMT and Poisson	188
4.5	Justification for lack of correlation hole in the Poisson ensemble	190
4.6	Minimum of the kn SFF and deepest kn SFF for disordered XXZ in the transition from chaos to integrability	191
4.7	Relative variance of the plateau of the kn SFF	194
4.8	Visualization of Thouless and dip times	197
4.9	Dip and Thouless times in RMT	198
4.10	Dip and Thouless times in XXZ	199
4.11	Even vs odd contributions to the SFF	200
4.12	Full Spectral Form Factor for RMT	202
4.13	kn SFF for GSE and ratio of plateau time and with of envelope	204
4.14	Approximate vs numerical vs connected SFF for RMT	205
4.15	Cosine vs sine contributions to the SFF	207
4.17	SFF for the toy model with correlations only to nearest neighbors	210